(Silico-) Aluminophosphates:

Synthesis and Application for Heat Storage and

Transformation

Hendrik van Heyden

aus

Kassel

2008

Erklärung

Diese Dissertation wurde im Sinne von § 13 Abs. 3 der Promotionsordnung vom

29. Januar 1998 von Herrn Prof. Dr. Thomas Bein betreut.

Ehrenwörtliche Versicherung

Diese Dissertation wurde selbstständig, ohne unerlaubte Hilfe erarbeitet.

München, am 20.03.2008

(Unterschrift des Autors)

Dissertation eingereicht am 20.03.2008

1. Gutachter: Prof. Dr. Thomas Bein

2. Gutachter: Prof. Dr. Helmut Knözinger

Mündliche Prüfung am 05.05.2008

Danksagung

Diese Arbeit entstand im Arbeitskreis von Prof. Thomas Bein am Institut für Physikalische Chemie der Ludwig-Maximilians-Universität München. Hier durfte ich drei in jeder Hinsicht lehrreiche, spannende und intensive Jahre verbringen. Dazu hat wesentlich die Hilfe meiner Kollegen, Freunde und Verwandten beigetragen.

Bei meinem Doktorvater, Herrn Prof. Thomas Bein, möchte ich mich ganz herzlich für die Aufnahme in seine inzwischen stark angewachsene Gruppe bedanken. Seine immer freundliche Unterstützung und Anleitung, und der durch ihn bereitgestellte Gerätepark haben mir eine Arbeit in wissenschaftlichem Luxus ermöglicht.

Bei Frau Doktor Svetlana Mintova möchte ich mich für die Einführung in die Welt der Zeolithe bedanken. Ihr stetes Fördern und Fordern hat mich immer sehr motiviert und die diversen Reisen mit ihr zu unseren Projekttreffen waren stets angenehm und interessant.

Bei Dr. Hans-Martin Henning, Dr. Ferdinand Schmidt, Gunther Munz und Lena Schnabel möchte ich mich für die hervorragende und jederzeit freundliche Zusammenarbeit ihm Rahmen des BMBF-Netzwerkes bedanken.

Ganz besonderer Dank gilt meinen Kollegen, von denen viele zu echten Freunden geworden sind, besonders Camilla Scherb, Enrica Biemmi, Lea Mühlstein, Monika Plabst, Johannes Kobler, Johann Kecht, Andreas Keilbach, Stephan Steinlein und Ralf Köhn. Ihr habt die Zeit im AK Bein durch unzählige

lustige Tage und Abende, und bei den zahlreichen Ausflügen und Konferenzen unvergesslich für mich gemacht.

Sehr herzlich möchte ich mich auch bei unseren Sekretärinnen, Frau Dagmar Hiltermann und Frau Regina Huber, bedanken. Sie waren wirklich die guten Seelen in unserer Gruppe und haben dafür gesorgt, dass die Dinge in geregelten Bahnen verlaufen. Dagmar wünsche ich von Herzen alles Gute für den Kampf mit ihrer schweren Krankheit.

Bedanken möchte ich auch meinen ehemaligen Praktikanten Andreas Esterbauer, Mirjam Dogru und Sonja Herdlicka, die hervorragende Arbeit geleistet haben. Es freut mich sehr, dass wir Mirjam inzwischen als Mitglied unserer Gruppe gewinnen konnten.

Abschließend möchte ich ein liebes Dankeschön an meine Frau Ank, an meine Eltern und an meine ganze Familie für deren unerschöpfliche Unterstützung und Ermutigung in den vergangenen drei Jahren aussprechen.

Abstract

This work is focussed on the synthesis of microporous aluminophosphates and silicoaluminophosphates, which are potentially useful for heat exchanger applications. More specifically, SAPO-34 (CHA structure) and AlPO-18 (AEI structure) were prepared in the form of nanosized crystals (<200 nm), which can provide decreased diffusion pathways and increased outer surfaces. To obtain nanocrystals, clear colloidal synthesis mixtures were used, and hydrothermally treated at elevated temperatures using either conventional or microwave ovens. The effect of synthesis composition, time and temperature was studied, and it was found that a high supersaturation in the precursor, and a large degree of homogeneity in composition and temperature are of crucial importance. Additionally, very concentrated systems gave rise to a faster growth phase and increased crystal sizes. The use of microwave energy led to smaller crystals and increased monodispersity in both the AlPO and the SAPO system.

AlPO-18 was tested for its suitability in heat exchanger applications. Therefore, layers of increasing thickness of up to ~600 µm were prepared by coating and drying. The aqueous coating suspensions consisted of the calcined AlPO-18 powders and polyvinyl alcohol as a binder component. Homogeneous and mechanically stable layers were obtained. The kinetics of water adsorption were studied by means of a specially designed measuring setup, which allowed for both canonical (number of particles constant) and isobaric measuring modes. The setup provided conditions close to applications in real heat exchangers. Films with thicknesses of up to ~150 µm allowed for fast mass and heat

transport (<2 min), whereas thicker films showed decreased rates. The process was faster in films comprising nanosized AlPO-18 powders due to a decreased heat resistance in the film matrix.

Gel syntheses using high-throughput methods were conducted aimed at cost-efficiency in the AlPO-18 (AEI) system. Therefore, two strategies, namely template substitution and decrease of template concentration were followed. By substitution of tetraethylammonium by triethylamine pure AlPO-18 could be synthesized under specific conditions. The use of unconventional templates, especially urea, led to the discovery of a new aluminophosphate phase. The reduction of the tetraethylammonium content did not lead to the AEI structure, but AlPO-5 (AFI) was formed under most synthesis conditions.

Table of Contents

1   Introduction

1.1   Climate change and -protection

1.1.1   The Nobel Peace Price 2007

"The Norwegian Nobel Committee has decided that the Nobel Peace Prize for 2007 is to be shared, in two equal parts, between the Intergovernmental Panel on Climate Change (IPCC) and Albert Arnold (Al) Gore Jr. for their efforts to build up and disseminate greater knowledge about man-made climate change, and to lay the foundations for the measures that are needed to counteract such change."[1]

Not only since the awarding of this year's Nobel Peace Price the global community's focus on climate protection has sharpened.[2] Today, a broad consensus prevails that our climate is apparently changing, and the IPCC and Al Gore have contributed to this public awareness. Only some consequences of global warming shall be mentioned here. The retreat and disappearance of the Earth's glaciers can be measured and followed in terms of mass balances and satellite monitoring, and a steady average decrease in mass and length was observed in the past 50 years.[3, 4] This has a major impact on the Earth's water cycle as the glacier retreat is assumed to have drastic effects on the sea level rise and the heat transport by oceanic streams. Extreme weather conditions like hurricanes are correlated to a global rise in temperature and CO_2 – level,[5-8] and less-predictable periods of droughts and floods are already occurring, especially on the warmest continents, Africa[9] and Australia. Many ecosystems

around the world are strongly affected by a changing climate, e.g.,, birds are changing their annual migration and many other species including plants are forced out of their habitats.[10-12] The consequences of global warming on agriculture, insurances, migrations etc. will result in serious damage to the global economy, and the former chief economist of the world bank, Nicholas Stern, stated in his famous review for the British government in 2006 that "the benefits of strong, early action on climate change outweigh the costs".[13]

The attribution of the detected global warming to human influence is difficult as the Earth's global climate is naturally variable on century time-scales. Therefore, critics of the debate still doubt human influence. However, the 2007 Fourth Assessment Report of the IPCC,[14-16] which represents consensus in the scientific community, has concluded that the increase in globally averaged temperature can be attributed mainly to the increase in anthropogenic greenhouse gas concentrations. Especially, Chapter 9 of "The Contribution of Working Group 1"[16] is concerned with the reasons for the detected extremes in global climate. On 84 pages a detailed summary of scientific statements is given, which provides the strongest evidence so far that the current warming trend is the increasingly dangerous result of human activity. Therefore, a coherent political response is urgently demanded.[17]

Nearly ten years ago, in March 1998, the Kyoto Protocol was opened for signature. This agreement was an amendment to the "United Nations Framework Convention on Climate Change", held in Rio de Janeiro in 1992. The protocol was ratified by a total of 169 countries, which have agreed that

"industrialized countries will reduce their collective emissions of greenhouse gases by 5.2 % compared to the year 1990". This would represent a 29 % cut compared to the expected global emissions without the protocol. However, notable countries such as the United States and Australia have not ratified the agreement, and other important countries such as India and China are not required to reduce carbon emissions under the present protocol. Additionally, no sanctions will be imposed on those countries which will not fulfill their own goals concerning the reduction of the main greenhouse gases, namely carbon dioxide, methane, nitrous oxide, sulfur hexafluoride, hydrofluoro- (HFCs), and perfluoro compounds (PFCs). As a consequence, the protocol has not led to a change of the increasing trend of greenhouse gas emissions yet, and leading politicians are aiming on an improved successive agreement. The various processes contributing to the global greenhouse gas emissions are shown in Figure 1-1.[18]
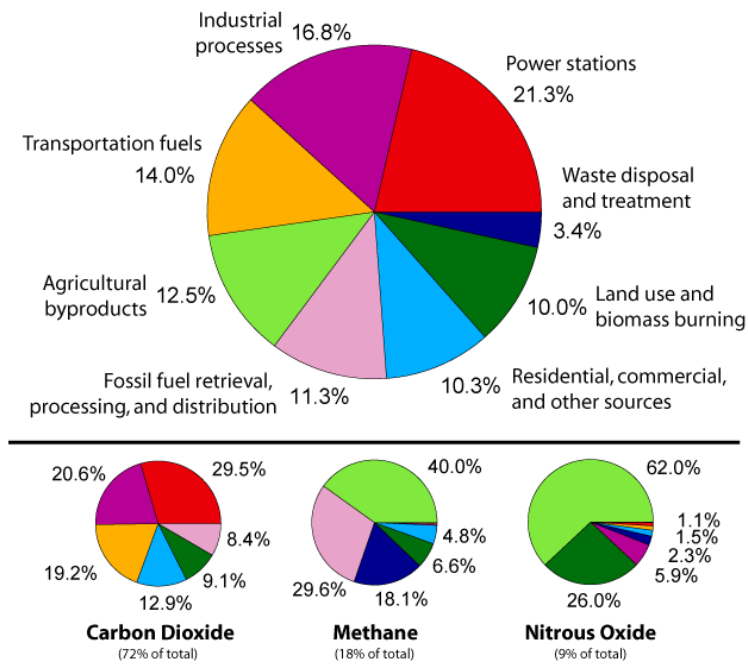
Figure 1-1. Relative fraction of man-made greenhouse gases coming from each of eight categories of sources, as estimated by the Emission Database for Global Atmospheric Research in 2000. The top panel shows the sum over all greenhouse gases, weighted by their global warming potential over the next 100 years. This consists of 72% carbon dioxide, 18% methane, 8% nitrous oxide and 1% other gases. Lower panels show the comparable information for each of these three primary greenhouse gases, with the same coloring of sectors as used in the top chart. Segments with less than 1% fraction are not labeled.[18]

The mechanisms contributing to the Earth's atmospheric and surface temperature are radiation, convection and evaporation/condensation of water vapor. In a simplified model, the radiative atmospheric greenhouse effect causes a net warming. The spectrum of incoming wavelengths is determined by the sun's surface temperature, whereas the outgoing spectrum is determined by the surface and atmospheric temperature of the Earth. According to Wien's displacement law the spectrum is shifted to longer wavelengths, which are absorbed by greenhouse gases and therefore causing a so-called positive radiative forcing. The main greenhouse gases are water, carbon dioxide and ozone, and a distinction concerning the importance of the individual gases is

difficult.[19] However, especially carbon dioxide concentrations have significantly risen since human industrialization. In the Earth's atmosphere it is present as a trace gas and the present average concentration is ~380 ppm (volumetric). This value is 38 % above the levels of 1832 (284 ppm), which can be measured in ice cores.[20] Carbon dioxide absorbs infrared radiation at 4.26 μm (asymmetric stretching mode) and 14.99 μm (bending mode). Natural sources of atmospheric carbon dioxide are volcanic activities, combustion processes of organic matter and respiration of living organisms. The main anthropogenic source is the burning of fossil fuels for energy generation, heating and transport. Therefore, industrialized countries are the major contributor to increasing CO_2 emissions with China being the global leader since 2006, followed by the United States and the European Union.[21]

1.1.2 *Private, industrial and technological measures*

It is the duty of politics to define world-wide legal requirements forcing the industrialized nations to reduce their greenhouse gas emissions, but the change to a "cleaner" future must proceed on a daily life basis within the world's cultures.

As discussed above, the main reason for anthropogenic CO_2 emissions is the burning of fossil fuels for energy production, heating and transport. It is not a "lucky coincidence" that fossil fuels are not infinite. Therefore, mankind must sooner or later become independent from natural oil, gas and coal reserves. Hence, renewable energy sources have to be used and the most prominent ones are solar energy, wind, water and geothermal technologies. The use of

biofuels preserves fossil fuel reserves, but their utilization for energy production is again coupled to greenhouse gas emissions. In fact, their greenhouse balance is worse than for the burning of fossil fuels,[22] due to the release of N_2O from N fertilization, the clearing of woodlands for biofuel production, and the use of fossil fuels on the farms. However, as petroleum is the raw material for many other chemical products, renewable primary products have to substitute crude oil in the future. Especially in the transport sector, a secondary energy source must replace petrol; hydrogen as carrier molecule seems to have the greatest potential in the long term as the energy density in hydrogen systems is higher compared to electricity stored in batteries.[23] However, there are major technical problems to be overcome for the realization of a so-called hydrogen economy. In terms of greenhouse gas emissions it is necessary to produce the needed hydrogen with emission-free technologies, e.g., electrolysis.[24] Nuclear power is generally not considered as renewable energy although future breeder reactors could significantly elongate the potential use of this energy form.[25] However, the disposal of nuclear waste and the reactor security renders nuclear energy a critical future technology.

Renewable energy sources can only facilitate a reduction in greenhouse gas emissions if the global consumption of primary energy does not increase parallel to economy. Therefore, energy efficiency and renewable energies are called the "twin pillars" of sustainable energy policy. However, the world consumption of primary energy has increased in the past 26 years from 6.65 billion tons oil equivalent to over 11 billions, which corresponds to 65.4 % or an

average annual increase of 2.5 %.[26] Although more energy was consumed in every region, the rate of increase varies remarkably. Whereas China had a 51.3 % increase between 1994 and 2005, the economically developed countries, e.g., the U.S. or Germany, could decrease their rates. Efficient energy use describes those measures which reduce energy consumption without reducing the energy service, e.g., insulation of houses could reduce the consumed energy by one third until 2050 without decreasing the room temperatures[27]. In contrast, heating a room less in winter would be an example of energy conservation.

The Princeton researchers Stephen Pacala and Robert Socolow proposed several industrial and political measures to stabilize the climate with today's technologies.[28] The potential for efficient energy use is indeed enormous. In private households most energy is used for heating or cooling, followed by hot water generation. Both items together represent approximately 25 - 33 % of the consumption of primary energy in Germany.[29] Apart from technological improvements like insulation and the use of efficient heating systems (e.g. geothermal heat pumps, which will be discussed below), personal customs can strongly contribute to private energy consumption. Examples are careful adjustment of the heating system, closing doors between living and sleeping rooms, proper room ventilation and showering instead of bathing. Further contributions to energy consumption are electrical household aids and illumination. Here, several per cent can be saved, e.g., by abandonment of laundry dryers, disconnection of stand-by apparatuses or use of energy-saving

lamps. The list of personal measures can be further extended, and it is necessary to improve the transparency of personal energy flows and to economically stimulate energy-efficient behavior of personal households. The industrial sector contributes to greenhouse gas emissions by both consuming energy for production processes or transport, and by directly emitting the gases.[30] Prominent examples for CO_2 emitting processes are the production of cement and steel.[31] The cement industry produces 5 % of global man-made CO_2 emissions, of which 50 % is from the chemical process, and 40 % from burning fuel.[32] Industrial energy consumption is counteracted by so-called energy management activities, by which a specific company is trying to analyze its individual energy flows in order to utilize its savings potentials. The BASF network site in Ludwigshafen, for example, covers 47 % of its heat demand by heat recovery from its own production processes.[33] Another 7 % is generated by burning waste chemicals, e.g., from the production of isophytol. The emission of process-related greenhouse gases can be reduced by optimization of process parameters and the use of efficient filter ("end-of-pipe") technologies. The long-term storage of CO_2 in geological formations or oceans is called CO_2-sequestration, but there are major concerns referring leakage of such reservoirs.[34-37] To stimulate reductions of CO_2 emissions in industry, the European Union has introduced an EU-wide emission trading scheme in 2005. In a market-oriented "cap-and-trade"-system, certificates on a plant basis are allocated and traded. Additionally, national politics have implemented climate-political goals in their respective laws, e.g., the ecological tax reform in

Germany. Several industrial sectors have announced voluntary commitments and set their own emission goals.

The knowledge that Earth's climate is changing in a potentially dangerous manner is founded on the scientific work of researchers all around the world. More than 2500 scientific expert reviewers, more than 850 contributing authors, and more than 450 lead authors contributed to the IPCC's Fourth Assessment Report. But science must not only document the climate change, but also provide new insights and technologies to facilitate a climate revolution.[38] On top of everything, there is virtually no scientific area that can not add a contribution. As climate protection is one of the world's dominant future concerns, one could even consider it a scientist's duty to be conducive to the problem in the field of his scientific interest. To cope with global warming, questions related to economic damages, insurance issues, environmental sociology, impacts on ecosystems, health risks and political consequences have to be answered. Engineers, physicists and chemists can provide technological responses, e.g., in car development, energy generation or materials science. In the latter field the introduction of nanotechnology bears additional potentials. The renowned Stanford futurist Ray Kurzweil predicted in 2006 that "nanotechnology will eliminate the need for fossil fuels within 20 years".[39] Kurzweil was referring to the potential of nanotechnology to harvest solar power, just one of a whole set of nano-applications that may come to the rescue just in time.

1.1.3 Solar energy

In 2004, the worldwide energy consumption of the human race was 15 TW (= 1.5×10^{13} W) which is equivalent to 0.5 ZJ (= 5×10^{20} J) per year.[26] The world's energy resources were or are generated by sunlight hitting the Earth's surface. The absorption of solar energy by atmospheric convection (sensible heat transport) and by the evaporation and condensation of water vapor (latent heat transport) drives the winds and the water cycle. Upon reaching the surface, sunlight is absorbed by the oceans, earth and plants. The energy captured in the oceans is ultimately responsible for temperature driven ocean currents such as the thermohaline cycle and wind driven currents such as the Gulf Stream.[40] The energy absorbed by the Earth in conjunction with that recycled by the greenhouse effect warms the surface to an average temperature of approximately 14°C.[16] The small portion of solar energy captured by plants and other phototrophic organisms is converted to chemical energy via photosynthesis. Some of the latter has been conserved in fossil fuels over periods of million years. The amount of incoming solar electromagnetic radiation per unit area, measured on the outer surface of Earth's atmosphere in a plane perpendicular to the rays, is called the solar constant.[41] It includes all types of solar radiation, and is measured by satellite to be roughly 1.37 kW m^{-2}, though it fluctuates by about 6.9% during a year - from 1.41 W m^{-2} in early January to 1.32 W m^{-2} in early July, due to the Earth's varying distance from the sun, and by a few parts per thousand from day to day. For the whole Earth, with a cross

section of $1.3 \cdot 10^9$ km², the power is 1.74×10^{17} W, which is more than 10^4-fold of human energy consumption.

There are numerous technologies for the utilization of solar energy, and they can be classified in active or passive systems. An example for the latter is "solar architecture", i.e. orientation of a building's lengthwise axis in the east/west direction, a reasonable ratio of southwards windows to floor space and the use of energy efficient materials for window coatings and insulation. Another possibility is solar lighting to reduce the amount of electricity used for illumination. Active harvesting of solar energy is subdivided in solar electrical and solar thermal systems. Solar electrical systems convert sunlight into electrical energy, and the most prominent example is the use of photovoltaic (PV) cells.[42] A PV system consists of a material which absorbs sunlight to generate charge carriers (electrons and holes) integrated in a cell design, which allows for the separation and transport of the charges to a conductive contact. Most often semiconductors, especially silicon, are used, but the production of highly efficient silicon based PV cells is expensive. The key issue involves the trade-off between material purity and device performance. A certain thickness of the material is needed in order to absorb >90 % of the incoming radiation; therefore, the photo-excited charge carriers must live sufficiently long to arrive at the electrical junction, which in turn demands high material purities. Therefore other concepts for PV cells ("third generation") are under investigation, which involve concepts to separate the direction of absorbance from the direction of charge transport, e.g., by the use of silicon nanorods.[43, 44] A related concept is

the dye-sensitized solar cell, in which a random, disordered network of inexpensive TiO_2 particles is used to collect the charge carriers. The light absorption is performed by an adsorbed dye molecule, and the interfacial contact distance is kept small by use of a liquid or conductive polymer.[45] The future of PV cells for primary energy production is coupled to cheap and effective storage capabilities as the intensity of sunlight varies and much energy is needed especially in the winter periods.

Active solar thermal technologies make up the most widely used category of solar energy technology.[46] Various concepts are used, which can provide heat for buildings, processes and warm water generation. The contribution of solar thermal systems to the global energy production can be measured in terms of installed collector area. The annual collector yield of all solar thermal systems installed by the end of 2003 was 55 TWh (200 PJ = $0.2 \cdot 10^{-3}$ ZJ). This corresponds to an oil equivalent of $8.8 \cdot 10^9$ L and an annual avoidance of $24.1 \cdot 10^6$ t of CO_2. The simplest concept of using solar thermal energy is by the use of solar collectors for providing warm water. These systems are able to provide 60 – 70 % of the needed annual energy demand. If solar thermal systems are designed to provide room heat, heat storage systems are needed, as the maximum heat demand occurs in colder months. Heat storage systems are commonly based on large isolated water tanks (storage of sensitive heat). These systems provide a high power density during charge/discharge, are cheap and non-poisonous. However, the storage density is relatively low; therefore, large volume tanks are needed. Other technologies for heat storage

application are the storage of latent heat, e.g., with phase-change materials (PCM), or thermochemical systems, e.g., by physisorption. Additonally, solar thermal heating in winter, cooling in summer and hot water generation can be combined by the use of low temperature sources, e.g., geothermal energy. For that purpose, the temperature level must be transformed with the help of a heat pump. Most commonly, compression heat pumps are used, which utilize critical greenhouse active gases. The drawbacks of common heat storage and exchange systems can be overcome by the use of other concepts, especially sorption technologies. These technologies will be discussed in detail in the following chapter.

1.1.4 *Heat storage and –transformation with sorption technologies*

Adsorption of gases into porous materials can be used for both heat storage and transformation. The underlying adsorption/desorption cycle is identical for both purposes (Figure 1-2).[47]
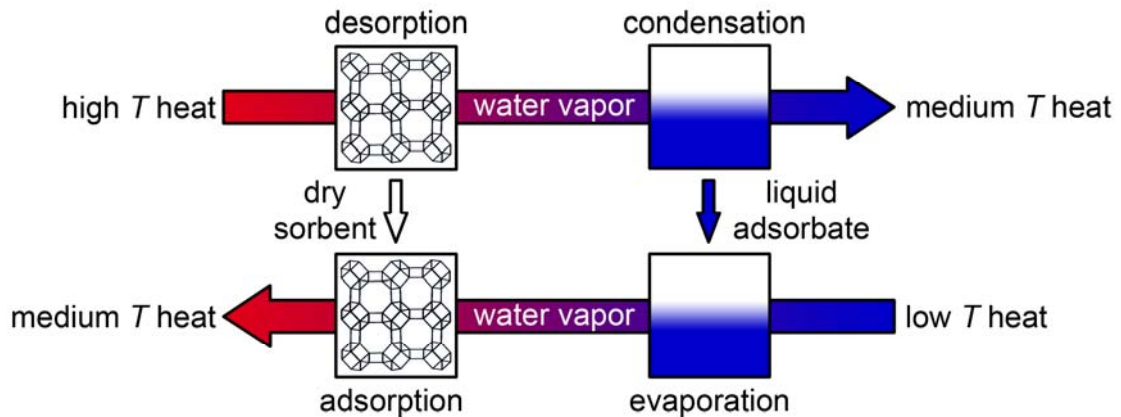
Figure 1-2. Scheme of a single heat transformation cycle. 1. A high temperature source is used for desorption of a suited adsorbent and the released adsorptive is transferred to a condenser. 2. A low temperature source is used to evaporate the adsorbate, which is transferred to the dry sorbent, thereby releasing the stored heat of adsorption (after Henning et al.[47]).

However, the cycle time varies between several months for storage applications, and minutes for heat exchange. In the desorption step the loaded adsorbent is desorbed by the supply of driving heat, which is provided on a high temperature level. For solar thermal systems this temperature is maintained by the solar collector, and is typically around 140 °C. For industrial applications process heat is commonly applied. The bound adsorbate, most often water, is transferred into its gaseous state, and condensed within a condenser unit. The condensation of free liquid adsorbate releases the corresponding useable enthalpy of evaporation on a medium temperature level. The temperature of the condenser determines the pressure of the desorption step, and is related by the vapor pressure curve of the adsorbate. During the desorption step, the working fluid is evaporated by heat from a low temperature source, typically geothermal or groundwater energy. The gaseous adsorbate is transported to the adsorption

unit of the system and adsorbed on the dry porous adsorbent. This is an exothermic process, which releases the corresponding useable heat of adsorption on a medium temperature level. The adsorption pressure is determined by the temperature within the evaporation unit.

An idealized transformation cycle of an adsorption pair (e.g. zeolite/water) is shown in Figure 1-3.
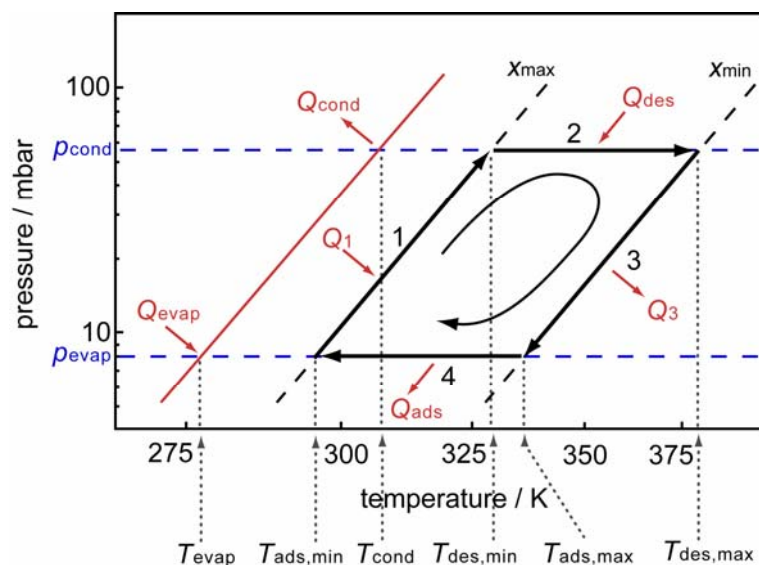
Figure 1-3. Basic heat transformation cycle of an adsorption pair (e.g. zeolite/water) plotted in a Clapeyron diagram. 1. Isosteric heating of the pair. 2. Desorption. 3. Isosteric cooling. 4. Adsorption. The red line represents the adsorbate saturation curve.

The vapor pressure curve of the adsorbate is shown in red on the left-hand side of the diagram. Red arrows are indicating the employed and released heats at the different steps. Step 1 corresponds to an isosteric heating of the adsorbent, i.e. the loading is kept approximately constant. The adsorbate pressure is increasing, corresponding to the equilibrium of the adsorption pair with increasing temperature and constant loading, until the pressure level of the condensor is reached. An additional heat input (e.g. from solar energy) leads to

the desorption of the sorbent at nearly constant pressure (step 2). The free adsorbate releases its enthalpy of condensation in the condenser unit. The temperature of the adsorption pair increases with decreasing loading at constant pressure until the temperature of the driving source is reached. Step 3 corresponds to an isosteric cooling of the adsorption pair at constant loading to the evaporator pressure level. During step 4 the working fluid is evaporated by means of the corresponding supply of evaporation energy (e.g. from a geothermal source). The temperature decreases with increasing loading at constant pressure according to the equilibrium of the adsorption pair. This temperature is given by the minimum useable temperature of the respective application. Afterwards, a new cycle is started.

The above described process can be used to realize a long-term or seasonal heat storage system. The desorption step corresponds to the loading of the unit, whereas discharge is accomplished by adsorption. The needed desorption energy can be provided by means of solar thermal collectors, and the released heat during condensation is either dissipated to the environment or used for low temperature applications. For adsorption the working fluid is evaporated by supply of heat from a solar collector at low irradiation or by geothermal heat. The released heat of adsorption is then usable for heating purposes. An adsorption system offers two main advantages over conventional systems (e.g. storage of sensitive heat). On the one hand the volumetric and mass-specific storage density is larger. Whereas sensitive heat storage and latent heat storage exhibit densities of around 60 kWh m^{-3} and <120 kWh m^{-3}, respectively,

thermochemical system can provide densities between 200 – 500 kWh m^{-3}.[48]

However, the more important factor is that the heat can be stored over long

periods with extremely low losses. In contrast to warm water tanks, those losses

only emerge during charge and discharge. After desorption, only sensitve heat

stored in the material and system can be lost. A far larger part of the stored heat

can be maintained over long periods, if the adsorbent is kept under vacuum

without moisture. The concept of such a system and the interconnections to the

peripheral devices are shown in Figure 1-4.
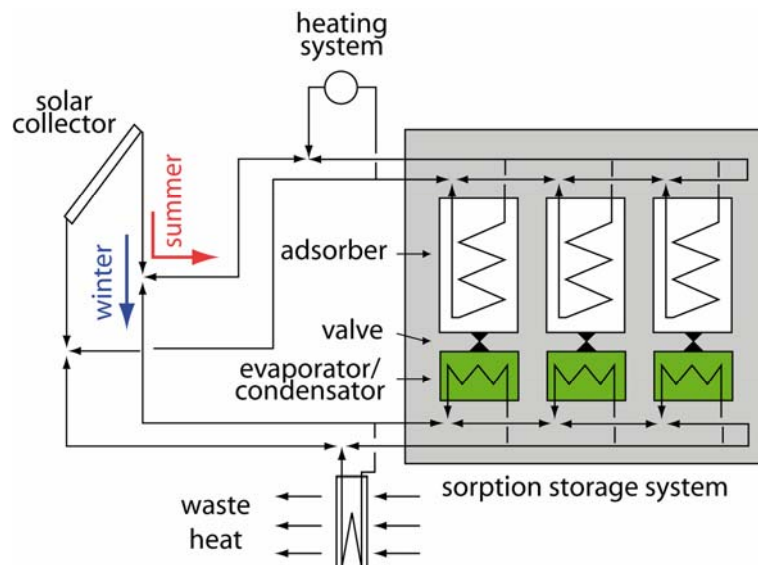
Figure 1-4. Scheme of a seasonal adsorption heat storage system. Solar thermal energy is used for desorption (summer) or evaporation (winter), respectively. Opposing arrows represent two or three way valves.

An adsorption heat pump is able to utilize environmental heat, which is free of

costs and on a non-usable low temperature level, by raising the temperature to

a level suitable for heating applications. The actuator for this process is a

thermal heat source with temperatures typically between 80 – 250 °C. The

components of such a device are in principle identical to the above described

storage systems but the dimensions are different. According to the individual configuration, combined or separate evaporators and condensators, two or more adsorbers and a hydraulic control unit are incorporated into the setup. Unlike in storage applications the times for a full cycle are in the range of several minutes.

Figure 1-5 shows a cycle of an adsorption heat pump consisting of two adsorbers, an evaporator and a condenser. In phase 1 the sensitive heat used for desorption of adsorber 2 is recycled and exchanged with adsorber 1. For the latter the indicated phases are equivalent to the numbered steps in Figure 1-3. In phase 2 the working fluid is evaporated from the evaporator by means of low temperature heat and transported to adsorber 2 where the released heat of adsorption provides heating energy on a medium level. In the same phase adsorber 1 is desorbed and the free working medium is condensed in the condenser unit to provide additional heating energy. Phases 3 and 4 are equivalent to phases 1 and 2 with exchanged working modes of the two adsorber units.
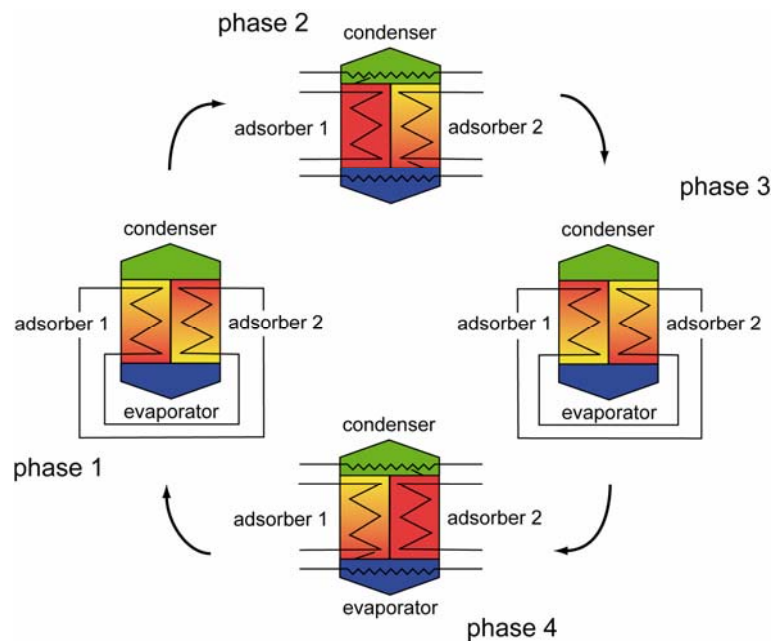
Figure 1-5. Scheme of a full cycle of an adsorption heat pump working with 2 adsorber units allowing a continuous operation mode. Note the valves as small lines above and below the adsorbers. The zig-zag lines indicate heat transfer to/from evaporator/condenser.

Adsorption heat pumps are a highly efficient means for the reduction of CO_2 emissions. A comparable potential for the utilization of heat of the same temperature level can only be provided by absorption techniques, which are the main competitive technology. The two most important absorption pairs are ammonia / water and water / aqueous lithium bromide solution. Ammonia bears risks when used in domestic systems due to its toxicity. Lithium bromide as sorbent can crystallize at low operational temperatures, which leads to disruption of the process. Generally, these systems achieve comparable coefficients of amplification (COA = usable heat / driving heat) to adsorption techniques of up to 4. The potential of adsorption technologies for the reduction of CO_2-emissions has been investigated.[49, 50] Accordingly, the largest potential is given in room heating applications by the use of gas fired adsorption heat

pumps. Systems with COAs of a least 1.5 can lead to a CO_2 reduction of 30 – 40 % compared to state-of-the-art condensing boilers.

An adsorption cooling machine is generally constructed in the same manner.[51] However, it is different in the hydraulic connections and the peripheral components. The cooling effect is provided by the evaporator of the systems, which serves as the physical heat sink. The released heats of adsorption and condensation need to be removed to the environment, which is typically achieved by the use of cooling towers or air-water heat exchangers with ventilators. Thermally driven cooling devices are very efficient due to the temporal correlation of large cooling demands and large solar irradiation. Nowadays, solar cooling systems for the industrial sector (>50 kW) and the private sector (5 – 50 kW) are commercially available.

As adsorption heat pumps and cooling machines are constructed following practically identical concepts, it is possible to use primary energy sources in a highly efficient manner by including free environmental heat, and to provide cooling by solar thermal energy corresponding to the seasonal demands with a single instrument. Consequently, this requires a tradeoff in terms of the used adsorbent due to the different heating and cooling operational modes. Figure 1-6 schematically shows the devices of such a combined system including solar collectors, an adsorption heat pump, geothermal probe and other typical components.
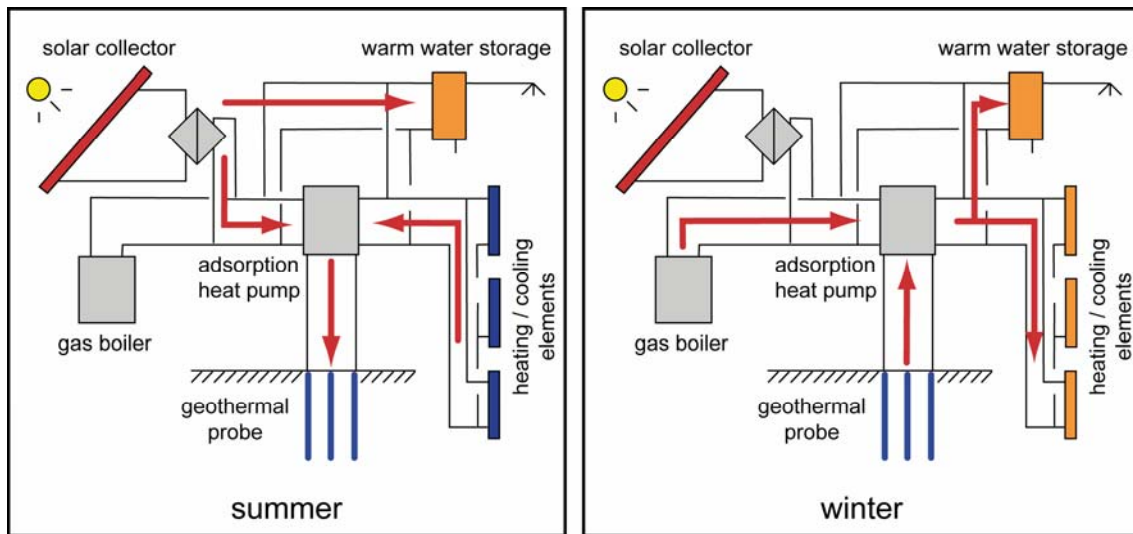
Figure 1-6. Scheme of an adsorption heat pump setup including peripheral devices during summer (left) and winter (right) operation. The main heat flows are indicated with red arrows (the diamond-shaped device is a heat exchanger).

During summer (left) the solar collector serves for hot water generation with nearly complete coverage, if sufficient storage volume is provided. Additionally, the heat pump is driven by solar thermal energy and the evaporator provides the heat sink for the cooling elements. The released heat from adsorption and condensation is transported to the geothermal probe. During winter (right) the systems utilizes heat from a gas boiler for heating and warm water purposes in a highly efficient way by converting geothermal energy from the ground probe. This concept creates only low additional costs compared to a monovalent system, which are easily compensated due to the all-season operational concept.

1.1.5 The BMBF network project

Applied sciences have contributed both nationally and internationally to the above-mentioned issues by numerous activities concerning systems

engineering and product development. However, the used materials, the concepts for heat and mass transport and the heat exchanger design more or less remained the same. On the other hand, much knowledge exists in fundamental chemical research institutions for the rational design of materials in order to optimize specific properties for technical processes. So far, a lack of systematic cooperation between the two mentioned groups – applied science / systems engineering and basic research / materials design – in the subject area of the mentioned storage and heat transformation technology was obvious. However, it is known from adsorption thermodynamics that a fundamental optimization of adsorbent materials for a given heat exchanger or storage cycle needs to be performed on a nanostructural basis. There is an obvious contradiction between the shared opinions that such optimizations could lead to significant improvements of subsequent applications, and the lack of such contributions in terms of publications and conference lectures.[52] As mentioned above, this situation is partly due to the different backgrounds of heat pump engineers and materials synthesis experts. Additionally, this process is difficult as there are numerous parameters to be varied in a specific synthesis and it is extremely time-consuming to characterize the effect of each specific variation. It is suggestive, to overcome this problem by additionally using theoretical approaches based on statistical thermodynamics and computer simulation. Therefore, a joint network project of 11 research institutions under the supervision of the Fraunhofer-Institute for Solar Energy Systems (ISE) in Freiburg was launched by the Federal Ministry of Education and Research

(BMBF) in 2003. In this project, groups having the above mentioned backgrounds – system engineering, materials synthesis and theoretical chemistry – were included. The participating institutional partners were the following:

- Fraunhofer-Institute for Solar Energy Systems (ISE)

- Institute for ventilation and refrigeration engineering (ILK) Dresden

- Johannes-Gutenberg-University Mainz

- Hermsdorf Institute for Technical Ceramics (HITK)

- Friedrich-Alexander-University Erlangen-Nürnberg

- Bauhaus-University Weimar

- University of Dortmund

- Albert-Ludwigs-University Freiburg

- University of Leipzig

- Ruhr-University Bochum

- Ludwig-Maximilians-University Munich (LMU)

The three work groups with expertise in the design of zeolitic materials were the groups of Klaus Unger (Mainz), Wilhelm Schwieger (Erlangen) and our own group. Within the scope of the coordinated network Prof. Unger's group concentrated on the synthesis of metal-organic frameworks (MOFs) and the group in Erlangen on layered silicates, e.g., clays. Our group was engaged in

the synthesis of three-dimensional microporous networks, e.g., zeolites, which was part of work package 2 of the project. Especially, we were interested in synthesizing relevant adsorbents in nanocrystalline form. Additionally, we also engaged in work package 5, which dealt with the connection of specific adsorbents to a heat exchanger surface, typically aluminium. In the latter, we contributed through the preparation of thick post-synthesis coatings on two-dimensional and porous three-dimensional supports.

1.2   Nanoscience and nanotechnology

As mentioned above, nanoscience is expected to have a great impacton issues related to climate change and energy supply. Within the scope of this thesis and the BMBF network project the materials of interest are "nanomaterials" in various contexts. On the one hand, the processes of mass and heat transport proceed on the nanoscale, e.g., the pores of the used adsorbents have diameters ranging between less than one and several nanometers. On the other hand, the microporous crystals themselves can have dimensions between 50 and several hundred nanometers, and their size can influence heat and mass transport. Therefore, a brief introduction into nanoscience research areas shall be given below.

1.2.1   What is nanoscience?

Various slightly differing definitions of the terms "nanoscience" and "nanotechnology" can be found in the literature but consensus exists that both deal with very small objects on the "nanometer scale". A nanometer is equal to

one-billionth of a meter. A human hair is approximately 80,000 nm wide, and a red blood cell approximately 7000 nm wide. Figure 1-7 shows the nanometer in context.[53] Atoms are below a nanometer in size, whereas many molecules, including some proteins, range from a nanometer upwards.
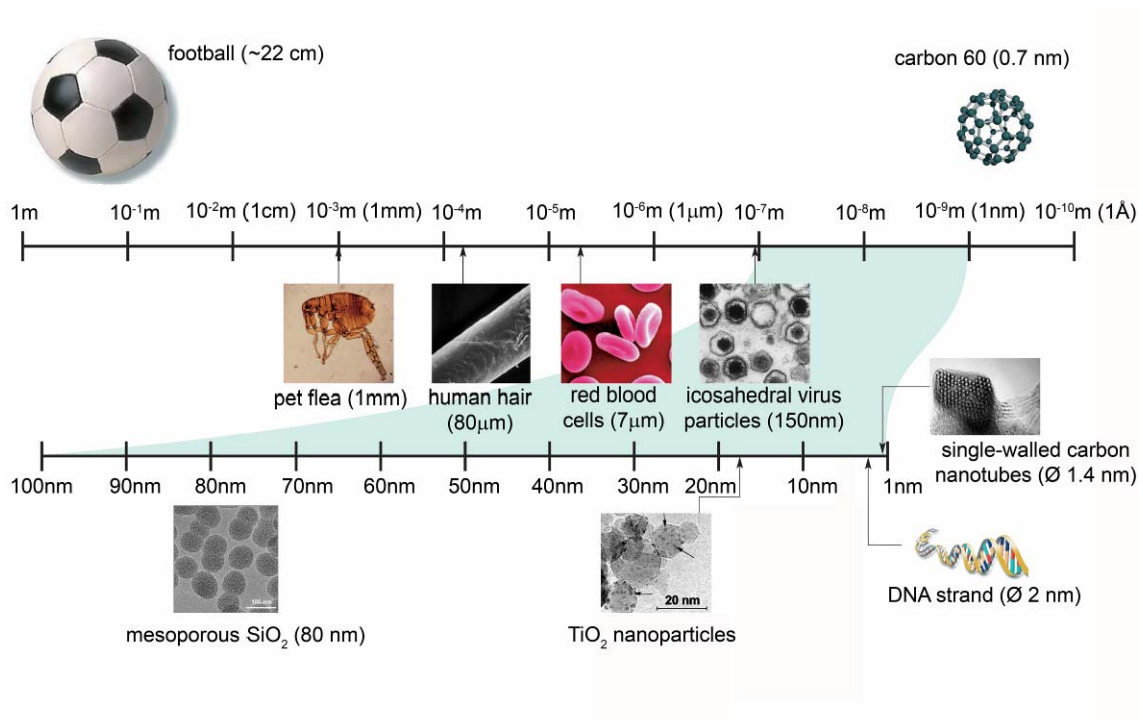
Figure 1-7. Length scales showing the nanometer in context. The length scale at the top ranges from 1 m to 10^{-10} m, and illustrates the size of a football compared to a carbon 60 (C_{60}) molecule, also known as a buckyball. The section from 10^{-7} m (100 nm) to 10^{-9} m (1 nm) is expanded below. The length scale of interest for nanoscience and nanotechnologies is from 100 nm down to the atomic scale - approximately 0.2nm (after The Royal Society[53]).

According to the illustration, "nanoscience" is the science of objects that are intermediate in size between the largest molecules and the smallest structures that can be fabricated by current photolithograpy (a technique used to process semiconductor wafers, e.g., for processor production).[54] Historically, this range of sizes has been associated in chemistry with colloids, micelles or polymer

molecules. Nowadays, particularly interesting nanostructures are formed by silicon nanorods, carbon nanotubes or semiconductor quantum dots. In physics, nanoscience is most often associated with quantum behavior and the behavior of electrons and photons in nanoscale structures. Many biological or biochemical structures – from DNA and viruses to subcellular organelles – are highly interesting nanostructures.

The term „nanotechnology" has a somehow overlapping meaning, but corresponds more specifically to the design, characterization, production and application of structures, devices and systems by controlling shape and size at the nanometer scale. Actual applications in this context will be given below. The word "nano" itself has become a giant among today's buzzwords, and its public and political impact has become so large (e.g. governmental organizations keep a share of their science and technology budget for all the nano applications) that many scientific communities are focusing on "nano" topics.[55] As the understanding, the synthesis and characterization of every scientific field of interest have become more and more precise, it is a logical evolution that the nano regime is today's frontier in an increasingly large fraction of research areas. However, nanoscience has also provided the basis for completely new, and often highly interdisciplinary areas, e.g., in semiconductor nanocrystal synthesis and characterization.

Nanostructures are interesting for numerous reasons. First, many nanoprocesses, e.g., the movement of electrons through organometallic wires,[56] are not fully understood today. Additionally, nanostructures are difficult

to make, and it is challenging to find out the governing mechanisms, e.g., of nanoparticle crystallization. Third, many nanoscale systems show new properties compared to bulk materials. The two main reasons for this change in behavior are an increased relative surface area (A/R increases with ~1/r), and the dominance of quantum effects. An increase in surface area per unit volume will result in a corresponding increase in chemical reactivity, making some nanomaterials useful as catalysts to improve the efficiency of fuel cells and batteries. As the size of matter is reduced to tens of nanometers or less, quantum effects can begin to play a role, and these can significantly change a material's optical, magnetic or electrical properties. Quantum phenomena are, of course, the ultimate basis of the properties of atoms and molecules, but are largely hidden behind classical behavior in macroscopic matter and structures.[54]

1.2.2 Materials and properties

Only some of the most interesting materials and effects in the nanoscience field shall be briefly mentioned here.

Nanomaterials

C_{60} fullerene (also called Buckminster fullerene or buckyball) was discovered as the first discrete, graphite-like nanostructure by Kroto, Curl and Smalley in 1985 (Nobel Price in Chemistry 1996). They were followed by carbon nanotubes, which are beginning to find commercial uses, e.g.,, as additive to polymers to increase conductivity in order to allow electrostatic spray-painting. They have a

range of remarkable properties such as metallic electrical conductivity, semiconductivity with very high carrier mobility, and extraordinary mechanical strength.[57] Some types of nanomaterials including carbon, zeolite and gold are shown in Figure 1-8.

| (a) | (b) | (c) | (d) |
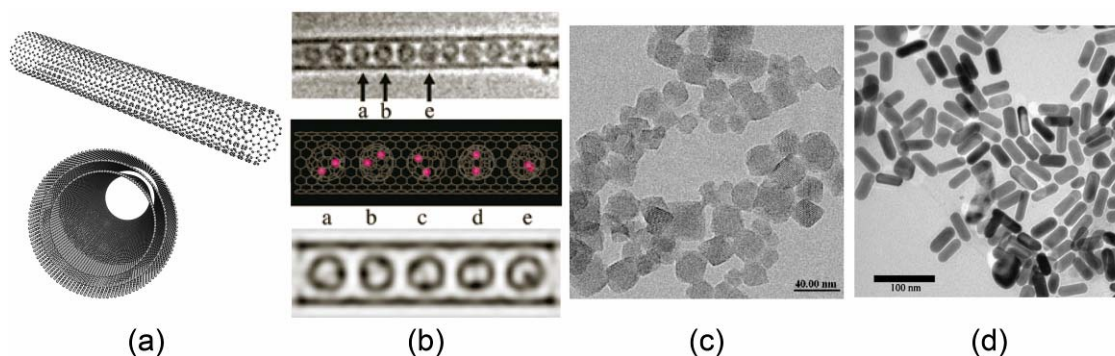
Figure 1-8. Different kinds of nanomaterials. (a) Models of single- (top) and multi-walled (bottom) carbon nanotubes (SWCNT, MWCNT).[53] (b) HRTEM image of $Sc_2@C_{84}$ metallofullerene particles inside of a SWCNT (top) and a model (middle) used for the simulation (bottom).[58] (c) Zeolite Y nanoparticles. (c) gold nanorods.[59]

Catalyst performance can be sensitive to particle size because the surface structure and electronic properties can change greatly in this size range. For example, the heat of adsorption for CO and the activation energy for CO dissociation both change with the increasing size of Ni particles, a phenomenon that affects the performance of Ni nanoparticles in the Fischer-Tropsch synthesis of hydrocarbons from synthesis gas (a mixture of CO and H_2).[60] Titania-supported Au nanoparticles have been found to be active at ambient conditions for the oxidation of CO to CO_2, and can be used to reduce the levels of CO pollution in buildings by being incorporated into the paint used to cover the interior walls.[61] Nanoparticles of vanadia supported on various oxides (ZrO_2, Al_2O_3, and MgO) are active catalysts for the oxidative dehydrogenation

(ODH) of alkanes to olefins.[62] An increasing amount of microporous and mesopourous materials, e.g., zeolites, which will be described in detail below, can be synthesized in a nanocrystalline form today.[63] The surface acidity, which is related to crystal size, is of importance when zeolites are used in catalysis, and smaller zeolite crystals have reduced diffusion path lengths within their micropores. Additionally, the synthesis of colloidal zeolite suspensions opens up a route for the fabrication of thin films, composite materials and hierarchical structures. From a fundamental point of view, these systems are convenient for studying the zeolite crystallization mechanism by methods not applicable in conventional zeolite syntheses. Many other materials, e.g., polymers, can be synthesized in nano dimensions, and the size reduction leads to altered or even new properties.

Quantum dots

A quantum dot is a nanostructure that confines the motion of conduction band electrons, valence band holes, or excitons (bound pairs of conduction band electrons and valence band holes) in all three spatial directions.[64, 65] The initial products that incorporate quantum dots are nanometer-sized grains of semiconductor materials, e.g., cadmium selenide, which are stabilized against hydrolysis and aggregation by coating with a layer of zinc oxide and a film of organic surfactant.[54] The significance of the spatial confinement of the electronic carriers can be seen in a plot of the density of states for each low-dimensional structure. Depicted in Figure 1-9 is the change in the density of

states that occurs as a material evolves from a completely unconfined state to the three-dimensionally confined state.
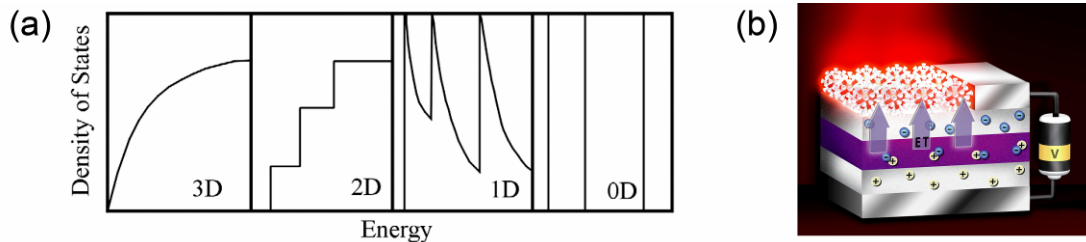
Figure 1-9. (a) Density of states vs. energy for a bulk material (3D), quantum well (2D), quantum wire (1D), and quantum dot (0D).[66] (b) CdSe nanocrystals caused to emit size-dependent wavelenghts when placed on top of a nearby InGaN/GaN quantum well, which acts as energy source, eliminating the need to put wires directly on the nanocrystals. The energy transfer efficiency is greater than 50 %.[67]

This complete quantization of energy states makes the quantum dot a very unique structure for research, e.g., CdSe particles absorb light of different energy dependent on their size, and therefore appear in size-dependent colors. Such spectral tunability, together with large photoluminescence quantum yields and high photostability, make nanocrystals attractive for use in a variety of light-emitting technologies, e.g., displays, solid-state lighting and lasers (Figure 1-9).

Self-assembly

Self-assembly is the autonomous organization of components into patterns or structures without human intervention. Self-assembling processes are common throughout nature and technology, and can be divided into different types, e.g., static, dynamic or templated self-assembly.[68] The most well-known example for a static process are self-assembled monolayers (SAMs).[69] They consist of chain-like molecules with specific functionalities (e.g. long alkane chains with a thiol group at one end), which form ordered arrays by bonding to a surface (e.g.

gold) with the functional group and alignment of chains by Van-der-Waals forces. Based on this process highly structured films of nanometer thickness can be prepared and used to provide biocompatibility, control of corrosion, friction, wetting and adhesion. Moreover, SAMs can be used as a basis for further surface processes, e.g., oriented growth of crystalline matter.[70, 71] As an example a SAM from decanethiol on gold is shown in Figure 1-10.

(a)   (b)   (c)
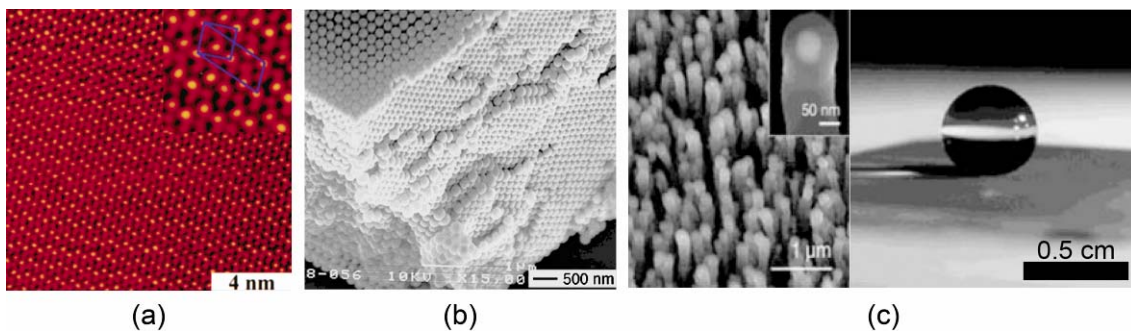
Figure 1-10. Self-assembly and surface modifications. (a) Scanning tunneling microscope image of a self-assembled monolayer (SAM) of decanethiol on gold.[72] (b) SEM images of 3D crystalline arrays that were assembled in 12 mm thick packing cells from ~220 nm polystyrene (PS) beads. It is possible to obtain highly ordered arrays over several square centimeters in area.[73] (c) A drop of water resting on a PTFE-coated carbon nanotube forest. (left: an electron micrograph of the same ultrahydrophobic surface).[74]

The formation of regular, crystalline lattices is a fundamental process in self-assembly, and is a method to convert 100 nm particles into photonic materials (Figure 1-10). A photonic crystal consists of periodically structured materials having different dielectric constants. Such a crystal can influence the propagation of electromagnetic waves in a similar way as a semiconductor does for electrons, i.e. it provides a band gap that excludes the passage of photons with a certain range of frequencies. This principle is technologically important as it can be used to produce light-emitting diodes (LEDs) that display coherence

properties, to fabricate threshold-less semiconductor diode lasers, and to significantly enhance the performance of many other types of optical, electro-optical, and quantum electronic devices.

Nanocoatings

Nanotechnology provides valuable tools for the modification of surfaces, not only by means of self-assembly. For example, the tuning of a surface wettability is used for so-called self-cleaning coatings. One possibility is the use of hydrophobic coatings, which lead to high water contact angles, resulting in almost spherical droplets which readily roll away, carrying dust and dirt with them. Dirty water falling onto the hydrophobic coating is removed before it can evaporate. Over 200 species of plant are known to utilize rolling droplets of water to keep clean, most famously the Lotus plant native to south-east Asia. For a self-cleaning hydrophobic surface very high contact angles of >160 ° are necessary; this can be reached by the use of fluorinated polymers in conjunction with micro patterned surface topologies. In Figure 1-10 such a surface is shown. Vertically aligned CNTs were deposited via plasma enhanced chemical vapor deposition (CVD) and modified with a fluorinated polymer. Interestingly, hydrophilic surface coatings can also provide self-cleaning, and the most prominent example are thin transparent films of nanocrystalline titanium dioxide for windows. This coating acts by two distinct properties: Photocatalysis causes the coating to chemically break down organic dirt (including aromatics, polymers, dyes and surfactants) adsorbed onto the window; hydrophilicity causes water to form "sheets" rather than droplets and

contact angles are reduced to very low values in sunlight and dirt is washed away. The latter effect is called super-hydrophilicity. Both mechanisms are based on the semiconductive nature of TiO_2. Light-generated electron-holes can migrate to the surface and cause oxidation or combine with atmospheric oxygen to give superoxide radicals, which quickly attack the nearby organic molecules. If the holes oxidize lattice oxygen at the surface of the material, this results in oxygen vacancies, which can be filled by adsorbed water, leading to surface hydroxide groups that make the wetted surface more favorable compared to the dry surface. This mechanism lowers the static contact angle to almost 0 ° after irradiation.

Drug delivery

An important prerequisite for designing efficient drugs for many diseases, most-importantly cancer, is the use of an efficient drug delivery system. Today's anti-cancer agents, cisplatin or carboplatin, most-often are injected intravenously, thereby rendering the therapy less cell specific. Therefore, research has focused on the development of suitable nanocontainers with the ability to transport the desired guest molecules to the targeted site and release the cargo in a controlled manner. Such containers open up completely new therapy concepts, e.g., gene therapy. Various types of nanocontainers have been envisaged for this purpose. These include liposomes (spherical vesicles surrounded by a phospholipid bilayer) and other lipid-based carriers such as micelles[75] and polymer microspheres.[76] Several drug delivery systems have reached the market, and the majority of the currently approved systems fall into

the category of liposomal or lipid based formulations. Inorganic nanoparticles, such as functionalized mesoporous silica nanoparticles, offer several unique features, such as stability, large surface areas, tunable pore sizes and volumes, and well-defined surface properties for site-specific delivery and for hosting molecules with various sizes, shapes, and functionalities.[77] However, these more ambitious systems are at a relatively far state from commercialization today.

Nanoelectronics

Moore's Law describes an important trend in computer hardware history, stating that the number of transistors that can be inexpensively placed on an integrated circuit is increasing exponentially, doubling approximately every two years.[78] It might be expected – in an optimistic scenario - that Moore's law is going to continue another ~20 years before the size of a transistor has to approach the size of a single atom, which is thought to be a fundamental barrier.[79] Nanoelectronics can possibly provide a means to extend Moore's Law beyond the foreseen limits of small-scale conventional silicon integrated circuits, which are fabricated nowadays by photolithography. Therefore, they are considered as disruptive technology because present candidates are significantly different from traditional transistors. These candidates include hybrid molecular/semiconductor electronics, one-dimensional nanotubes/nanowires, or advanced molecular electronics.

Nanorobots

Nanoscience has inspired so-called futurists – people who imagine how the future might be. The imaginative projection of nanoscience into the future has produced ideas both exciting and terrifying. One of these ideas is that someday so-called nanorobots, devices ranging in size from 0.1-10 micrometers and constructed of nanoscale or molecular components, could fulfill specific tasks in various research fields. Most often, the term is used in the context of medical applications, i.e. those devices could for example find tumor cells in a human body and destroy them. So far, nanorobots are more fiction than science. However, first attempts have been made, e.g., the development of a so-called nanocar, whose wheels consisted of fullerene groups attached to a carbohydrate "chassis".[80]

1.2.3 Synthesis

As discussed above a vast number of different nanomaterials and concepts exist, and each system is prepared or synthesized with a specific procedure. Traditionally, all different routes are classified in two different classes, the top-down and the bottom-up approach. Nanoelectronic devices such as integrated chip circuits are produced by photolithography. It uses light (nowadays deep ultra violet with wavelengths of 248 and 193 nm) to transfer a geometric pattern from a photomask to a light-sensitive chemical, the photoresist. Afterwards, a series of chemical treatments is used to engrave the exposure pattern into the material underneath the photoresist. Photolithography is the prototype of a top-down approach and one of the most important industrial processes. Bottom-up

means to use the chemical properties of atoms and molecules to arrange them into a nanoscale structure. Classically, self-assembly, and more specifically SAMs are mentioned as the most-prominent synthetic example. As already discussed, self-assembly is abundant in chemical synthesis, and crystallization from molecular precursors to three-dimensional crystal structures could be considered just another form of self-assembly. Bottom-up approaches are in principle more precise than top-down approaches as the resolution is given by intermolecular forces, e.g., van-der-Waals forces, rather than by diffraction. That is why they are expected to become an important factor in nanofabrication. For example, technologies very familiar in chemistry – printing or molding – have emerged as potential competitors to photolithography. It should be emphasized that life on Earth, based on the genetic code, can be considered as the most sophisticated form of self-assembly.

1.2.4 Applications

Although there has been much hype about the potential applications of nanotechnology, most current commercialized applications are limited to the use of "first generation" passive nanomaterials. These include titanium dioxide nanoparticles in sunscreen, cosmetics and some food products; silver nanoparticles in food packaging, clothing, disinfectants and household appliances; zinc oxide nanoparticles in sunscreens and cosmetics, surface coatings, paints and outdoor furniture varnishes; and cerium oxide nanoparticles as a fuel catalyst.[53] However, further research on applications which require actual manipulation or arrangement of nanoscale components will

probably change this situation drastically in the future. Moreover, the nanomaterials already used will become more and more sophisticated. There is no doubt that this "evolutionary" nanotechnology in general already has a great impact on many of today's applications. It is still an open question if there will be "revolutionary" applications based on fundamentally new nanoscience in the future. The general enthusiasm for "nano" has produced many vague hopes in this context. However, science and technology should be focused on the "right size" for desired effects – and that size may range from nanometers to millimeters and beyond.

1.2.5 Risks

The physicochemical properties of nanomaterials, especially nanoparticles and nanorods, also bear potential health risks. For instance, shrinkage in size can create discontinuous crystal planes that increase the number of structural defects as well as disrupt the well structured electronic configuration of the material. This can lead to specific surface groups that could function as reactive sites. Such effects (e.g. TiO_2 particles used in coatings, see above) depend strongly on the chemical composition of the material, and are impressive from a physicochemical viewpoint. However, these novel properties raise concerns about adverse effects on biological systems, which at the cellular level include structural arrangements that resemble nanomaterials in terms of their function. Moreover, some nanoparticles readily travel throughout the body, deposit in target organs, penetrate cell membranes, lodge in mitochondria, and may trigger injurious responses. There are currently no conclusive data or scenarios

that indicate that these effects will become a major problem or that they cannot be addressed by a rational scientific approach. Nonetheless, precise safety evaluations for specific materials when produced in nano dimensions are urgently needed.

1.3 Porous materials

Porous materials can be classified by the diameter of their pores. According to IUPAC (International Union of Pure and Applied Chemistry), pores up to 2 nm are called micropores. Mesoporous materials range between 2 – 50 nm whereas macropores have diameters of >50 nm. The most prominent class of microporous materials are 3D structured aluminosilicates, i.e. zeolites, which will be discussed in detail below. Silicates can also be prepared in mesoporous forms, and especially the M41S family (e.g. MCM-41), first discovered by the Mobil Oil Corporation,[81, 82] has to be mentioned here. Apart from pore size, these materials differ substantially from zeolites with respect to their 3D structure and the synthesis mechanism. Whereas zeolites represent fully crystalline materials, MCMs are only crystalline in terms of pore structure; the walls between them consist of amorphous silicon dioxide. This structure arises from micelles, which are formed during the synthesis, and silica only condenses around these micelles. Other mesoporous materials include metal oxides and non-oxides (e.g. sulfides), carbons or metals (normally not structured).[83] Macropores can be formed in oxides, activated carbons, polymer resins or metals.[84, 85]

1.3.1 Zeolites

Zeolites are aluminosilicates consisting of a three-dimensional network of connected $[SiO_4]$ and $[AlO_4]^-$ tetrahedra, forming channels and cavities of molecular dimensions (about 3 – 15 Å).[86] As zeolites represent fully crystalline materials the pore system is perfectly ordered and homogeneous (Figure 1-11). The incorporation of $[AlO_4]^-$ tetrahedra leads to a negatively charged network, which is balanced by metal ions, typically alkali or earth alkali cations. The charge-balancing ions occupy specific sites within the channel system. The negative charge of the framework can also be balanced by protons connected to the oxygen bridges resulting in Brønsted acid sites. These sites can be used as size-selective catalytic centers; therefore, zeolites are among the industrially most important heterogeneous catalysts. The pores can be filled with water or other guest molecules, rendering zeolites highly efficient adsorbents with large internal surface areas of up to ~800 $m^2 g^{-1}$. These unique properties make zeolites highly interesting for many applications, and some of them shall be mentioned below (Applications section). 48 naturally occurring zeolite minerals are known, some of the more well-known include analcime, chabazite, faujasite, heulandite, natrolite, phillipsite and stilbite. Natural zeolites form at elevated temperatures when volcanic magma and ash reacts with alkaline groundwater or under surface conditions, e.g., in alkaline saline lake deposits, where they have been formed in geological time periods.[87] Additionally, they can be found in specific marine environments formed at low temperatures. Naturally occurring zeolites are rarely pure and are contaminated to varying degrees by other

minerals, metals, quartz or other zeolites. For this reason, naturally occurring zeolites are excluded from many important commercial applications where uniformity and purity are essential. More than 150 zeolite types can be formed synthetically, the majority of them in alkaline media under hydrothermal conditions at temperatures between 100 – 200 °C. The product properties, such as Si/Al – ratio, included ions and crystal morphology can be tuned by adjustment of the reaction mixture composition, pH of the system, operating temperature, pre-reaction "seeding" time, reaction time as well as the templates used. These templates (or structure-directing agents, SDA) are generally required in order to produce a certain pore structure, which appears to form around the SDA. Some zeolites can be made by using only inorganic reactants, but the majority of recipes use organic molecules such as amines. Also other framework elements, e.g., titanium can be incorporated. Details to the various syntheses and the corresponding reaction mechanisms will be discussed below.
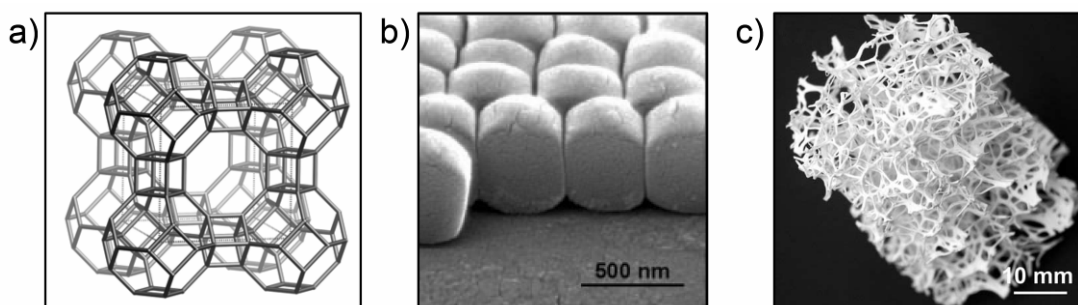
Figure 1-11. (a) T-atom representation of Zeolite A (LTA). Each corner of the shown network represents a T-atom (Si,Al), each connection a T-O-T bond.[88] (b) self-assembled monolayer of individual silicalite-1 nanocrystals.[89] The crystals were grown on a functionalized glass surface. (c) Silicalite-1 self-supporting (calcined) zeolite replica of a *Luffa* sponge resulting in a hierarchical 3D pore structure.[90]

The term "zeolite" (from Greek: *zeein*, "to boil"; *lithos*, "stone") was founded by the Swedish mineralogist Axel Fredrik Cronstedt in 1756.[91] Richard Barrer from the imperial college in London and Robert Milton from the Linde Corporation can be called the founders of synthetic zeolite research. The Barrer group synthesized the first zeolites not known in nature, namely zeolites P an Q, in 1948.[92-94] In the years 1949 and 1950, the Linde group prepared the zeolites A, B (now NaP), C (hydroxyl sodalite), X, and synthetic chabazite for the first time.[95, 96] Both groups were especially interested in the latter material as it was known to be industrially useful for air separation and purification. Again, the Barrer group,[97] in addition to G. K. Kerr and G. T. Kokotailo,[98] first reported on the use of organic amines as structure-directing agent. This discovery opened up the field for a whole group of new zeolitic materials. Silicalite[99] was the first purely siliceous zeolite (an analogue to ZSM-5) discovered in 1978. Since then, a growing number of nearly Al-free zeolites became accessible. These results have consequently led to the possibility of tuning parameters such as hydrophilicity and acidity. Since the 1990s, improved characterization techniques like high resolution transmission electron microscopy (HRTEM), small angle X-ray scattering (SAXS) or dynamic light scattering (DLS) have been used to investigate the mechanism of zeolite formation on a molecular level,[100, 101] and these investigations have led to the synthesis of zeolites in colloidal form.[63] Here, zeolite science became also nanoscience. Nowadays, advanced functional molecular sieves are accessible by means of nanozeolites and other techniques, e.g., hierarchical pore systems, which allow for an

improved mass transfer within the pores of the material (Figure 1-11). The zeolites themselves can be decorated with functional organic groups and nanocrystals can be self-assembled on various surfaces[89, 102] or grown upon self-assembled monolayers.[70, 71]

1.3.2 (Silico)aluminophosphates

Stephen T. Wilson and coworkers working at Union Carbide reported a new class of microporous materials in 1982.[103, 104] Their crystalline aluminophosphates represented the first family of framework oxide molecular sieves synthesized without silica. This discovery opened up the field for a large number of open-framework inorganic materials. The new materials, designated AlPO-n (or AlPO$_4$-n), were prepared with a wide range of pore sizes using organic template molecules under hydrothermal conditions. The AlPO structures are based on strict alternation of $[AlO_4]^-$ and $[PO_4]^+$ tetrahedra leading to a non-charged framework in contrast to most zeolitic frameworks, and similar to all-silica zeolites. However, charge can be induced into AlPO frameworks, either by an Al/P – ratio of >1, or by partial replacement of aluminium and/or phosphorus by silicon or other elements. The introduction of hetero framework elements is balanced by protons, resulting in Brønsted acid sites, and/or generates catalytically active metal centers. If other metals are incorporated, the compounds are called MeAPO or MeAPSO. As in aluminosilicate structures, aluminophosphates avoid Al-O-Al bonds (Löwenstein's rule[105]), and additionally P-O-P bonds, which leads to even-numbered rings within the structures. Metal hetero elements normally substitute Al atoms in the framework

(SM1 substitution) whereas Si atoms predominantly substitute P atoms (SM2). Additionally, Si can adopt both Al and P positions (SM3), which leads to silicon islands.

Some AlPO-based molecular sieves have structures analog to known zeolites, but many compounds have no zeolite counterpart. The discovery of AlPOs has lead to a greater flexibility in possible frameworks compared to traditional zeolite research, e.g., the incorporation of many new framework elements (V, Cr, Ni, Li, Be, B, Mg, Ti, Mn, Fe, Co, Zn, Ga, As, Cu), the availability of pore sizes larger than 12-membered rings (Figure 1-12), and the primary building unit not only limited to a tetrahedral coordination.[106, 107]
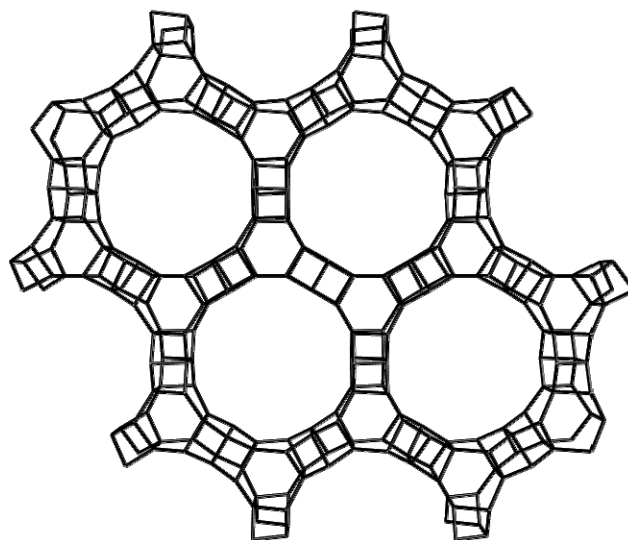
Figure 1-12. Perspective t-atom representation of VPI-5 (VFI structure type code) showing the 18-ring pore openings along [001].[88]

As the solution chemistries of silicon and phosphorus are different the synthesis conditions of zeolites and AlPOs are different, too. Zeolites are formed primarily in alkaline media whereas AlPOs can be obtained within a broad pH ranging

approximately from 3 – 10. Bonding is also different in the two types of molecular sieves. Comparing isostructural silica and AlPO molecular sieves, the silica polymorph consists of covalently connected SiO_4 units; AlPOs, in contrast, have a molecular-ionic character with idealized discrete Al^{3+} and PO_4^{3-} ions.[108] The ionic character of AlPOs can serve as an explanation for the finding of a larger variety and concentration of hetero elements compared to zeolites, and also for larger enthalpies of adsorption for polar adsorbates.

Over 100 different organic molecules are known to act as structure-directing agents for AlPO syntheses, e.g., quaternary ammonium cations, amines (primary, secondary, tertiary or cyclic),[109] alkanolamines, and some metal complexes.[110, 111] Recently, ionic liquids have been used as both template and solvent.[112, 113] The templating effect appears to be different from zeolite chemistry. This is expected as a porous neutral framework generally is likely to form by the use of a template with a high volume-to-charge ratio because less framework charges have to be compensated. Under this aspect, the used templates act primarily as so-called pore fillers, rather than providing a specific geometrical pattern for the pore system. Therefore, it is not surprising that many different templates can possibly result in the same AlPO structure (this is especially the case for AlPO-5, which can be synthesized with over 25 different molecules). On the other hand, the same template can lead to the formation of a variety of structures. For example, di-n-propylamine has been used in the synthesis of at least ten different AlPO structure types, such as AlPO-11, -31, -39, -41, -43, -46, -47, -50, H3/MCM-1, and H1/VPI-5/MCM-9, exhibiting low

structure specificity. A few AlPO structures, however, exhibit high specifity, e.g., AlPO-18 or -20. For the above mentioned reasons purely inorganic synthesis mixtures are not leading to porous aluminophosphates. A prominent exception is the 18-membered ring compound VPI-5 which can be synthesized without addition of any organic additive.[114, 115]

1.3.3 Synthesis and mechanism of molecular sieve synthesis

Traditionally, zeolites are synthesized by mixing appropriate sources for aluminium and silicon with a cation source, and most often an organic template in a basic medium (Figure 1-13). In case of (silico)aluminophosphates, reactants containing aluminium, phosphorus and eventually silicon are mixed with a suitable template. Afterwards, the aqueous reaction mixture is heated in a sealed autoclave at temperatures usually between 100 – 200 °C. For some time after raising the synthesis temperature, the reactants remain amorphous or in their pre-synthesis phase. After this "induction period" crystalline products can be detected. Gradually, all the precursor material gets converted into an approximately equal mass of zeolite / aluminophosphate crystals. The products are recovered by filtration or centrifugation, washing and drying.

The framework elements are typically introduced in an oxidic form, sometimes metal organic molecular precursors are used, which hydrolyze in solution to an oxidic species. Phosphorus can be introduced in form of phosphorus oxide, but more commonly phosphoric acid is used. The precursors contain Al/Si/P-O bonds which are converted to e.g. Si-O-Al bonds during the hydrothermal reaction by hydrolysis and condensation reactions. The bond types of educts

and products are very similar in bond energy, therefore, the overall free energy change during the synthesis is small, and the process is usually kinetically controlled. Thus, the desired product is frequently metastable, and care needs to be taken that an elongated synthesis time does not lead to re-dissolution of the product.
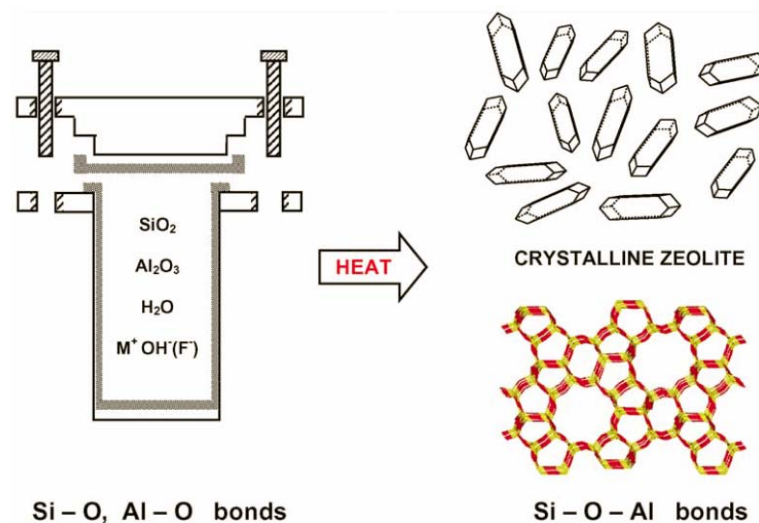
Figure 1-13. Hydrothermal zeolite synthesis. The starting materials (Si-O and Al-O bonds) are converted by an aqueous mineralizing medium (OH and/or F) into the crystalline product (Si-O-Al bonds), whose microporosity is defined by the crystal structure.[116]

Many researchers have investigated the mechanism by which the transformation from the left to the right side in Figure 1-13 proceeds.[116] Most of the investigations were concerned with zeolite synthesis, only relatively few with aluminophosphates.[117, 118] In general, it is important to note that the crystallization mechanism varies for either zeolites or aluminophosphates, just as each specific synthesis mixture will result in different reactions under the given conditions. Nonetheless, some general mechanistic considerations shall be discussed here, which are accepted for most of the different molecular sieve

systems. The overall process is generally divided into three different periods, namely the induction, nucleation and growth period. After mixing of the reactants and subsequent heating, dissolution and condensation processes progress, and a gel phase is formed. An increasing number of zeolitic structures have been synthesized nowadays from optically clear precursor solutions. In these cases, the individual gel particles are present as colloidal particles with nanometer dimensions. The gel phase normally becomes increasingly ordered after mixing in a way that alternating types of T-atoms become connected and an increasing state of condensation arises. Hydrolysis leads to the generation of so-called secondary building units (SBU) in the liquid phase within and around the gel particles. Typically, these units comprise a small number of alternating connected TO_4 tetrahedra. The molecular order of the gel can be detected by NMR and IR techniques. It is very important to note that all these processes represent a dynamic non-equilibrium system which is governed by the kinetics of the contributing hydrolysis and condensation reactions. The moment when the first particles with long-range order appear in the synthesis mixture is called nucleation. This type of order can be detected by diffraction techniques like XRD or electron-diffraction, which is not possible for the short-range order during the induction period. Nucleation proceeds by the assembly of a certain number of SBUs to a periodically ordered domain of a certain size. Therefore, a certain degree of supersaturation of the SBUs must be present in the mixture. To form the nucleus from the precursor phase, energy must be expended to generate a surface, and the cohesive energy gain from bond formation must be

large enough to outweigh this surface energy. Thereby, a stable nucleus is formed and provides the structural basis for further growth to the final particle size. In the case of zeolite nucleation, it is reasonable to suppose that the construction of the nucleus is a more complex assembly process compared to simpler dense materials. The assembly of SBUs to nuclei is assumed to be sterically directed by the present template (either inorganic or organic). Heterogeneous nucleation is probably more important than homogeneous nucleation, however, both processes can simultaneously take place. The first contribution was beautifully demonstrated by HRTEM investigations in conjunction with in situ DLS to examine the formation and growth of zeolites A and Y from clear sols.[100, 101] Single zeolite Y crystals were observed to nucleate within amorphous gel particles of 20 – 80 nm in size within 3 days at 100 °C (Figure 1-14). After nucleation, the individual nuclei grow by further addition of nutrients from solution. Predominantly, these nutrients are delivered in form of monomeric units to the surface of the crystals, where they find positions with maximum bonding possibilities, e.g., at topological steps on the zeolite surface.
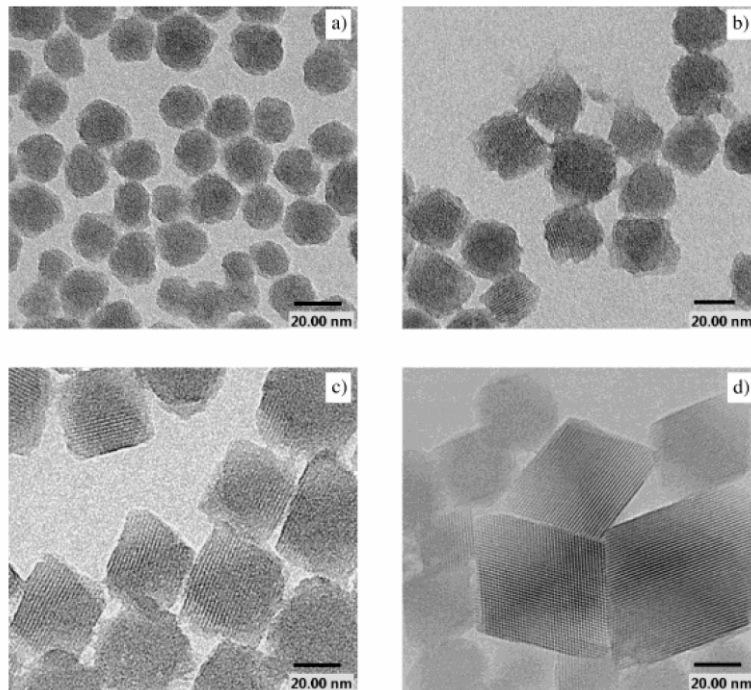
Figure 1-14. Observation of nucleation within colloidal particles in a) freshly prepared aluminosilicate solution for the synthesis of zeolite Y and after hydrothermal treatment at 100 °C for b) 28, c) 48, and d) 75 h.

Certainly, the presented mechanism represents an idealized case, and in each system the situation can vary to a certain degree. For example, in most synthesis mixtures the different steps will not be separated strictly in time over the whole synthesis volume. Formed nuclei will tend to grow straight after nucleation, and nucleation can still proceed in other parts of the system. This is more likely to happen in large and unstirred batches. Especially during and after the growth phase, other processes can proceed depending on composition and temperature. As zeolite formation is a dynamic process, re-dissolution processes can occur and lead to re-crystallization of other zeolite or dense phases, or large crystals grow at the expense of smaller crystals (Ostwald

ripening). Additionally, individual crystals can grow together and form agglomerates, or they can aggregate depending on their surface charge.

1.3.4 Applications

Natural zeolites are used as additives in the cement and paper industry, where they serve for the reduction of processing temperatures and as fillers, respectively. Clinoptilolite is used in agriculture as a soil treatment to provide a source of slowly released potassium. Additionally, natural zeolites are used for sewage water treatment in order to reduce the levels of soluble heavy metals.

Synthetic zeolites have become available in commercial quantities in the 1950s, and since then the world consumption of these materials has greatly increased. Starting from a few hundred tons this became 60×10^3 t/a in 1975, 460×10^3 t/a in 1987, and ca. 1.2×10^6 t/a in 1994.[119] The main application in terms of quantity is the use as so-called "builders" in detergent compositions. Their function is to enhance the surfactant effect by removing ions causing water hardness, i.e. calcium and magnesium. 90 % of the used builder additives are Zeolite NaA and 10 % NaP. These compounds have effectively substituted previously used pentasodium tripolyphosphate, which led to eutrophication of many lakes and rivers. 1 050 000 t/a or almost 90 % of all zeolites produced in 1994 have been used for this purpose.

Zeolites are very efficient catalysts for many organic reactions. Although considerably smaller amounts (1994: 115 000 t/a) are used for catalytic processes, this is the industrial application with the largest addition of value.

The majority of the world's gasoline is produced with zeolite catalysts. The largest contributor in this area is zeolite Y used as component of the FCC (fluid catalytic cracking) catalyst for oil refinery. The process converts vacuum distillates and residues into gaseous alkenes, gasolines, and diesel fuel. Alternatively, zeolites can promote hydrocracking to convert high-boiling oils into kerosene and diesel. The catalytic conversion of gases into petrochemical products is also of great industrial relevance. A very prominent example is the conversion of methanol to olefins (MTO). Possible catalysts for this purpose are ZSM-5 or SAPO-34. The latter is now used in the UOP/Hydro MTO process in a large plant in Nigeria.[106] Other examples of industrial scale organic reaction catalyzed by zeolites are the production of ethylbenzene from benzene and ethylene[120] or the synthesis of cumene from benzene and propene.

Zeolites are important industrial adsorbents for a number of applications, together with silica gel, alumina or activated carbons. However, the homogeneity of the pore structure and diameter, and the resultant size selectivity towards varying adsorbates makes zeolites the materials of choice for many adsorption applications. In particular, the adsorption of water is used in order to dry gases (e.g. air, natural gas, cracked gas) and liquids (i.e. organic solvents). For these processes the zeolites need to be desorbed between process cycles, and the preferred methods are temperature-swing or pressure-swing adsorption (TSA, PSA). The large amount of heat generated during water adsorption can be used for heat storage and transformation applications (see section 1.1.4). An exotic example which makes use of water adsorption in

zeolites is emergency blood clotting.[121] Many other molecules can be adsorbed in zeolites, and most often zeolites A, X and Y are used. In purification processes contaminants like CO_2, H_2S, dioxine or mercury can be removed from crude gases like natural gas or waste air (from plants). Prominent examples of so-called separation processes are the production of O_2 from air, ozone production from O_2/O_3 mixtures or the separation of n-alkanes from iso-alkanes on 5A zeolites, which is of importance in the mineral oil industry. In the nuclear waste industry zeolites are used to trap nuclear fission products, and the zeolite-waste composite can be hot pressed into an extremely durable ceramic form, closing the pores and trapping the waste in a solid stone block.

1.4 Goals and Motivation

This work was part of the joint BMBF network "New highly porous materials and systems for energy storage and heat transformation". In this context, a broad range of materials was tested at the Fraunhofer ISE, in order to find potentially interesting adsorbents, which were not previously used for the above mentioned applications. The best performance in terms of water capacity and adsorption/desorption temperature-range was found for the aluminophosphate AlPO-18 and the silicoaluminophosphate SAPO-34, but other adsorbents, e.g., metal organic frameworks and fibrous carbon, also showed promising water adsorption characteristics. As comprehensive knowledge about the synthesis of zeolitic materials exists in our workgroup, this thesis was focused on the two former materials, whereas the latter ones were investigated in other network groups.

A key factor for heat transformation with adsorptive systems is the realization of short adsorption/desorption cycle times, which are governed by two main transport resistances, namely mass transport into the adsorbent pores, and heat transport from the material to the heat exchanger. The mass transport within the micropores can be influenced by employing nanocrystals of the materials of interest, whereas the heat transport is dependent on the combination of a suitable adsorbent with a metallic heat exchanger matrix.

Therefore, the first goal of this thesis was two investigate the possibility of synthesizing the above mentioned materials in form of nanocrystals in order to reduce the diffusion pathways within the microporous structure. Secondly, the materials should be combined with metallic supports and tested for their suitability for the final application in a specially designed measuring setup.

The mentioned investigations were conducted under the aspect of fundamental research in order to increase the potential for the use of new materials for heat exchanger applications. However, the feasibility of such an utilization is strongly dependent on materials cost. Therefore, cost-efficient syntheses for microporous aluminophosphates were investigated in the last chapters of this work.

2 Methods

2.1 X-ray diffraction

X-ray diffraction (XRD) is one of the most powerful tools to identify the crystalline phases in a material and to determine properties like phase composition, domain size, and preferred orientation.[122] XRD is a non-destructive technique, which allows for the structural characterization of materials containing any element. However, heavier elements give rise to larger diffracted intensities. In a typical experiment, the diffracted intensity is measured as a function of the diffraction angle 2Θ and the orientation of the specimen, which yields the diffraction pattern.

Crystals consist of planes of atoms with a certain distance d to each other, and can be resolved into many groups of atomic planes, each with a different d-spacing. The atomic planes can be described by introduction of a suitable coordinate system. The reciprocal intercepts of the planes with the coordinate axes, the so-called Miller indices (h, k, l), are used to distinguish the planes. For a simple cubic crystal, the d-spacing is

$$d_{hkl} = a_0 \: / \: \sqrt{(h^2 + k^2 + l^2)} \tag{2-1}$$

where a_0 is the lattice constant of the crystal. Constructive interference of the scattered X-rays leads to the observation of diffraction peaks. The diffraction of X-rays can be described according to a reflection at the atomic planes. Hence, the condition for constructive interference is given by the Bragg equation:

$$\lambda = 2d_{hkl} \sin\Theta_{hkl} \qquad\qquad (2\text{-}2)$$

where Θ is the angle between the atomic planes and the incident (and diffracted) X-ray beam (Figure 2-1).
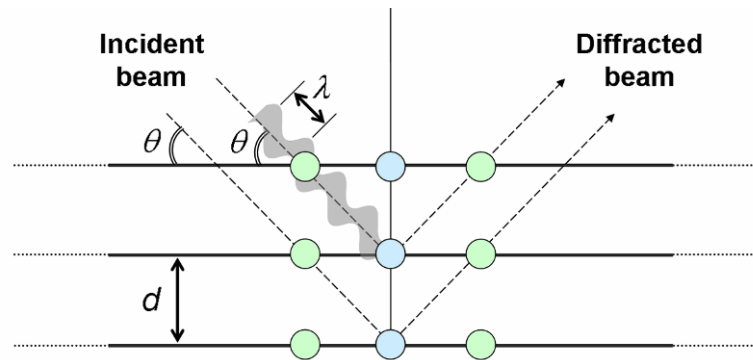
Figure 2-1. Scheme of the reflection of X-rays at the atomic planes of a crystal.

With given incident direction, monochromatic wavelength, and d-spacing, each plane fulfils the Bragg equation for a specific angle between detector and incident beam. In a powdered sample the crystals are randomly orientated, which leads to constructive interference along a so-called Laue cone. When the detector is positioned at an intercept with the Laue cone, a reflection is recorded. The intensity of the reflections is proportional to the product of the intensity of the incident beam and the density of electrons in the lattice plane that is reflecting the beam. This leads to a specific "powder pattern" for a certain crystalline compound. Hence, powder diffraction is commonly used to identify unknown substances, by comparing diffraction data against a database maintained by the International Centre for Diffraction Data (ICDD). Additionally, information about the crystal domain size can be obtained by means of the line

broadening in the diffraction pattern. A simple relationship for the domain size D is given by the Scherrer equation

$$D = (K \lambda) / (\beta \cos \Theta) \tag{2-3}$$

where λ is the wavelength, K is the Scherrer constant, whose value is approximately 0.9, β is the integral width of a reflection (in radians 2θ) located at 2θ, and Θ is the Bragg angle.

2.2 Electron microscopy

The maximum resolution of an optical microscope is limited by the use of visible light to objects separated by a distance of ~0.2 μm. Therefore, electron microscopy is the first choice to investigate smaller features with respect to their morphological appearance. However, compositional, structural, and electronic information can also be obtained with modern electron microscopes. The wavelength of electrons, accelerated by 100 kV, is 0.004 nm and ~10^5 times smaller than visible light. Two different microscopic techniques are commonly used, namely Scanning Electron Microscopy (SEM) and Transmission Electron Microscopy (TEM). Whereas SEM detects backscattered or secondary electrons emitted from the sample, TEM uses transmitted electrons. Therefore, sample preparation is crucial for TEM, as the electron beam can only penetrate thin samples of up to ~200 nm thickness. For SEM, sample preparation is easier, however, non-conducting samples need to be coated with a thin conducting film (C or Au), in order to prevent charging of the sample. Figure 2-2 shows the different interactions between the electron beam and the sample. If

an incident electron undergoes inelastic scattering with atomic electrons, these

"secondary electrons" (SE) can exit the material if their energy exceeds the

work function of the material. During a measurement, the electron source is

focused into a fine probe, which is rastered over the sample surface. The signal

generated by the detection of secondary electrons is amplified, and a pixel

proportional to the number of emitted electrons is printed on the screen.
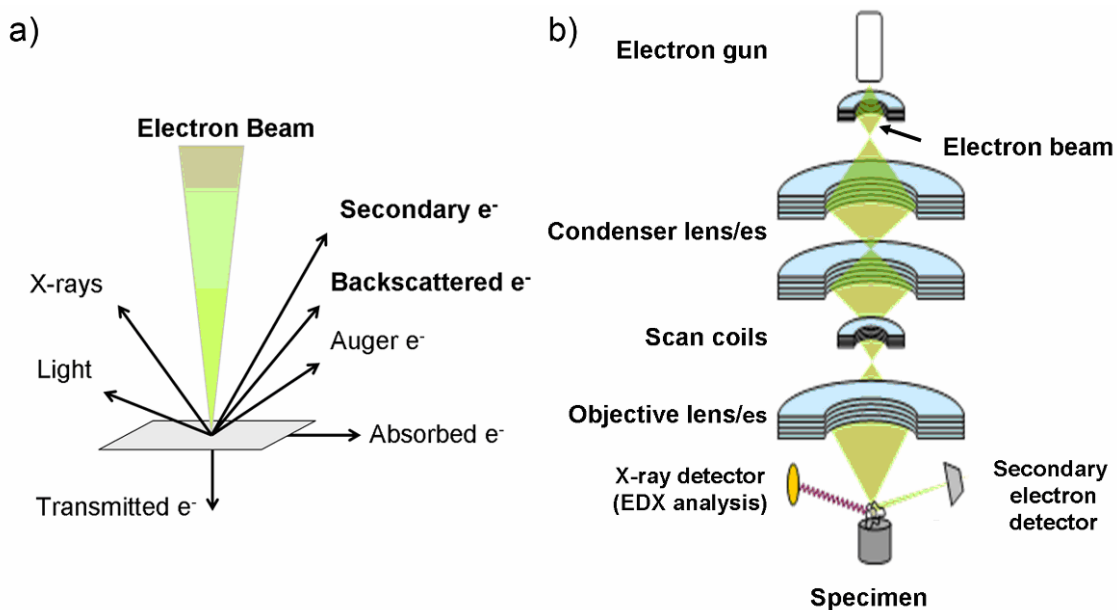
Figure 2-2. Schematic representation of an Scanning Electron Microscope (SEM). a) Sample-electron beam interactions. b) Electron pathway from electron generation to the sample surface (after [122]).

Additionally, backscattered electrons (BSE), which result from elastic scattering

with the atomic nucleus, can provide information about the composition of the

scanned material. The efficiency of production of backscattered electrons is

proportional to the sample material's mean atomic number. If the collision of the

electron beam with the atoms of the sample causes an inner shell electron to be

ejected, the re-occupation of the vacancy by an outer shell electron leads to

emission of element specific X-ray radiation. If the instrument is equipped with an energy dispersive X-ray detector, this radiation can be used to obtain both qualitative and quantitative elemental information.

2.3   Thermogravimetric analysis and Differential Scanning Calorimetry

Thermogravimetric analysis (TGA) is a method to monitor the mass change of a sample as a function of temperature/time. Therefore, the sample is heated in an inert thermostable crucible to temperatures of up to 1600 °C. The crucible is fixed on a thermobalance and a thermocouple close to the sample registers the actual temperature. Different temperature-programs and different gas atmospheres can be chosen with modern instrumentation. Quantitative information about processes like oxidation, reduction, evaporation, or sublimation can be obtained. In case of zeolitic materials, most commonly the evaporation of water, the decomposition of the template, and phase transformations are observed.

A valuable complementary method to TGA is Differential Scanning Calorimetry (DSC). This method measures the heat flux from/to a sample as a function of sample temperature. For this purpose, an empty reference crucible is heated on the same sample holder (disc type measuring system), and a sensor underneath the sample/reference measures the occurring heat fluxes, which are dependent on the heat capacity, and endo- or exothermic processes. Thereby, phase transformations like melting, which proceed without any mass change,

can be observed. Additionally, specific mass changes can be distinguished in terms of their endo- or exothermic nature. All processes investigated with TGA/DSC are strongly dependent on the exact measuring conditions, which consequently have to be chosen very carefully.

2.4 Physisorption

Adsorption of gases within the pores of a material is a widely used method to determine properties like porosity, surface area, or pore diameter. Adsorption is measured either by gravimetrical or volumetric methods, and two different types of adsorption, chemisorption and physisorption, can be distinguished. Chemisorption involves the formation of chemical bonds between the gas molecule and the pore surface, whereas physisorption is mediated by loose interactions, like Van-der-Waals forces. In contrast to chemisorption, physisorption is a completely reversible process. Therefore, the measured adsorbed volume as a function of relative pressure p/p_0 gives equilibrium isotherms. Volumetric physisorption isotherms are obtained by dosing a certain gas volume into the sample chamber, and by measuring the pressure decrease due to adsorption in the pores. Depending on the types of pores present in the material, the measuring temperature, and the probe molecule, different types of isotherms are obtained. They can be classified according to IUPAC into six different types shown in Figure 2-3.[123] Microporous materials commonly show isotherms of type I. They are characterized by a steep increase of adsorbed volume at very low relative pressures, typically below 0.1. This step corresponds to the formation of an adsorbate monolayer within the micropores

of the material. As the dimensions of the pores are in the range of the adsorbate, the monolayer formation is equivalent to a complete filling of the pores, and no further increase of adsorbed volume is observed until a high pressure close to $p/p_0 = 1$ is reached. If the adsorbent particles have nano-scale dimensions, the interparticle voids can fall into the mesoporous range, leading to textural porosity. Hence, a steady increase in adsorbed volume is observed after micropore filling.
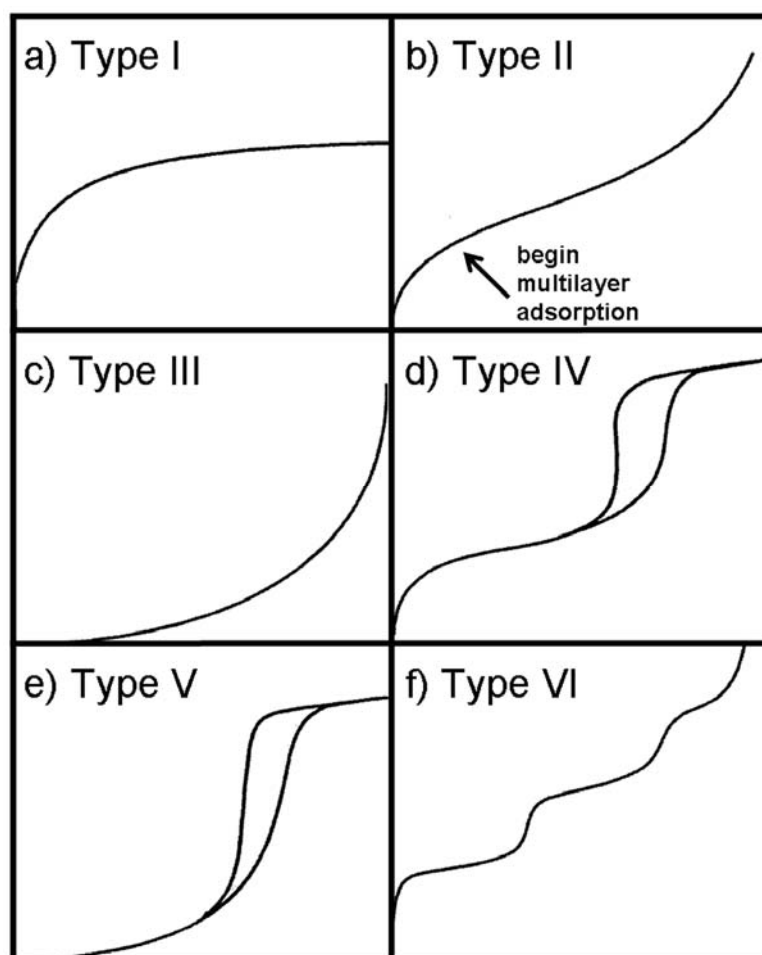
Figure 2-3. IUPAC classification of sorption isotherms. a) Microporous material. b) Non-porous material with a high energy of adsorption. c) Non-porous material with a low energy of adsorption. d) Mesoporous material. The hysteresis loop is associated with the occurrence of pore condensation. e) Mesoporous material with a low energy of adsorption. f) Stepwise multilayer adsorption on uniform non-porous surface.[123]

Mesoporous materials exhibit type IV isotherms, characterized by the formation of adsorbate multilayers in the range p/p_0 ~0.05 – 0.25. Above this pressure condensation of the adsorbate within the mesopores takes place leading to a step in adsorbed volume. As the mechanisms of mesopore filling and desorption are different, a hysterisis loop between the adsorption and desorption branches of the isotherm is typically observed (Figure 2-3 d). The p/p_0 range of multilayer formation can serve for the calculation of the surface area. Most often, the Brunauer-Emmett-Teller (BET) method is used for this purpose:

$$\frac{p}{n(p_0 - p)} = \frac{1}{n_m C} + \frac{C-1}{n_m C} \cdot \frac{p}{p_0} \qquad (2\text{-}4)$$

n is the number of adsorbed molecules, n_m the monolayer capacity, p_0 is the saturation pressure and the constant C depends on the difference between adsorption energy of the first layer and the liquefaction energy of the adsorbate. From the monolayer capacity n_m the surface area A_s can be calculated according to

$$A_s \text{ (BET)} = n_m \text{ N}_A \ a_m \qquad (2\text{-}5)$$

where N_A is the Avogadro constant, and a_m is the cross-sectional area of the probe molecule (0.162 nm^2 for N_2). The BET method is widely used for porous materials, including microporous solids, although there it is strictly not applicable, as no multilayer formation is found in micropores. However, the BET value is a useful comparative measure. Nowadays, powerful modern analysis tools have become available for the investigation of microporous materials,

especially Density Functional Theoretical (DFT) models.[124] In the DFT approach the density of the adsorbate as a function of location in the pore is calculated. These equilibrium density profiles are obtained by minimizing a free-energy functional, which is the grand free energy for a pore system in equilibrium with a bulk phase (i.e. the situation when an adsorption experiment is performed). This is a major advantage to classical models, which assume the adsorbate to exist in either the bulk gas or liquid state. Based on the calculated density profiles, isotherms in model pores can be determined. Experimental isotherms can then be fitted to the model by applying the Generalized Adsorption Isotherm (GAI) equation:

$$N(p/p_0) = \int N(p/p_0, W)\, f(W)\, dW \qquad (2\text{-}6)$$

where $N(p/p_0)$ is the experimental adsorption isotherm data, W is the pore width, $N(p/p_0, W)$ is the isotherm on a single pore of width W, and $f(W)$ is the pore size distribution function. The GAI equation reflects the assumption that the total isotherm consists of a number of individual "single pore" isotherms multiplied by their relative distribution, $f(W)$, over a range of pore sizes. The validity of the DFT method has been shown using various reference materials. Therefore, it has become the method of choice if corresponding DFT data are available for the respective material.

2.5 Vibrational Spectroscopy

Molecules in solution or atoms in a crystalline arrangement can be approximated by balls (atoms) connected with springs (chemical bonds).[122]

The vibrations of these systems give rise to certain resonance frequencies determined by the mass of the balls (atomic weights), and by the stiffness of the springs (bond force constants). The frequencies are in the infrared range of the electromagnetic spectrum from 10^{12} to 10^{14} Hz (3 – 300 µm), and the vibrational bands can be assigned to specific motions of pairs or groups of atoms. To obtain an infrared spectrum the sample is irradiated with infrared light, and the intensity of the absorbed, transmitted, or reflected light is analyzed according to its wavelength. Modern instruments use polychromatic light, and the spectral analysis is performed by Fourier Transformation of the signal obtained by a Michelson interferometer and a suitable detector. The various peaks apparent in the spectrum can be analyzed according to their positions, intensities and widths. By comparison with functional group tables or online databases, the different positions give information about the chemical groups present in the sample. The peak intensities allow a relative or absolute quantification of the concentration of the specific groups, whereas the peak width can be related to the degree of bond homogeneity within the investigated material. Therefore, amorphous materials give rise to peak broading.

Raman spectra arise from indirect coupling of the incident light with electrons making up the chemical bonds of a material. Therefore, the sample is illuminated with monochromatic light generated with a laser (typically Ar, or He-Ne lasers), and the scattered light is analyzed by a detector situated at an angle, for example 90° to the incident beam. Most of the scattered light has the wavelength of the incident beam (elastic Raleigh scattering), but a small portion

of the energy is transferred to the material, exciting the vibrational modes (Figure 2-4). The corresponding energies are deducted from the incident beam energy, which leads to small sidebands in the spectrum at lower energies (higher Raman shifts) than the Rayleigh line. This effect is called (inelastic) Stokes scattering, whereas the opposite effect, where vibrations excited by thermal processes lead to scattering with larger energies, is called anti-Stokes scattering. Anti-Stokes intensities are strongly temperature-dependent, whereas the Stokes intensities are only weakly temperature-dependent. Therefore, commonly only Stokes scattering is measured.
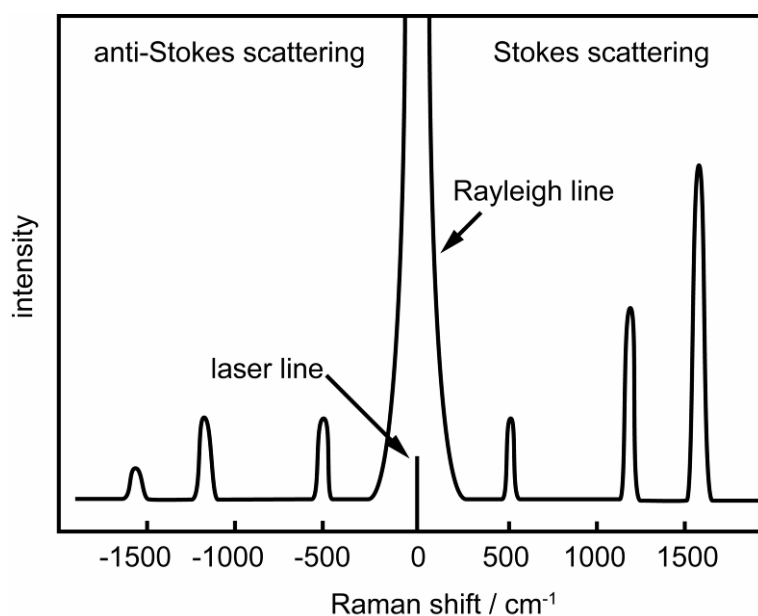
Figure 2-4. Schematic Raman scattering spectrum showing Rayleigh line, Stokes Raman scattering and anti-Stokes Raman scattering (after [122]).

IR absorption is the result of a change of the dipole moment during the corresponding vibration, whereas Raman scattering involves a change in the bond polarizability, as the two mechanisms are different. Therefore, IR and Raman can give complementary information.

2.6 Dynamic Light Scattering

Dynamic light scattering (DLS) is the time-dependent modulation of the light scattering intensity due to Brownian movement of the particles in a colloidal suspension.[125] If the particles are much smaller in diameter than the wavelength of the laser light, the scattering intensity is independent of the detection angle (Rayleigh scattering). In contrast, the scattering intensity is a function of the viewing angle if the particle diameter is in the same range as the laser wavelength (Mie scattering). As the Brownian motion is size-dependent, the particle diameter can be calculated from the variation in dynamic light scattering. A device, called digital auto correlator is used for the analysis. It generates a correlation function, which correlates the intensity of the scattered light at a certain time delay τ to the intensity at $t = 0$:

$$G(\tau) = <I(t)\ I(t+\tau)> \tag{2-7}$$

For very short delay times, the correlation will be large as the particles have moved only a short distance, whereas there will be no correlation for very long delay times. A correlation curve typically shows an exponential decay (Figure 2-5).
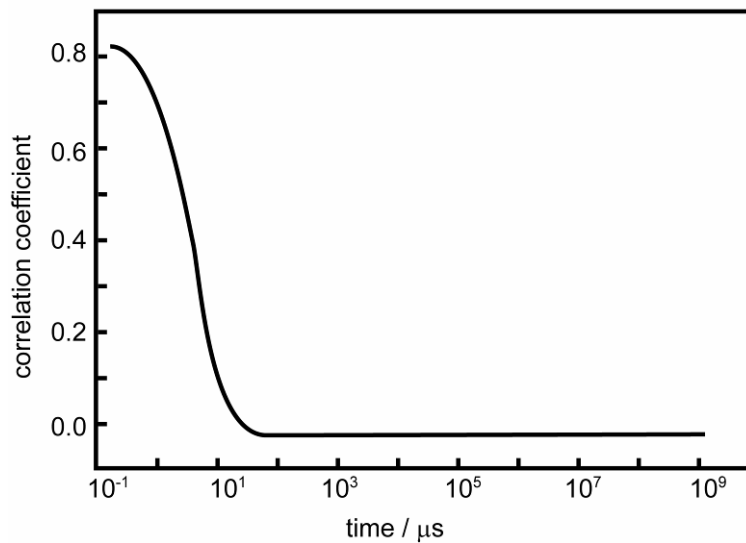
Figure 2-5. Scheme of a typical correlogram from a sample containing small particles in which the correlation of the signal decays rapidly.

In case of a monomodal colloidal suspension, the correlation curve can be fitted to a single exponential function in the so-called Cumulants analysis:

$$G(\tau) = A[1 + B \exp(-2\Gamma\tau)] \qquad (2\text{-}8)$$

with

$$\Gamma = Dq^2 \qquad (2\text{-}9)$$

$$q = (4\pi n / \lambda_0) \sin(\theta/2) \qquad (2\text{-}10)$$

D is the translational diffusion coefficient, n the refractive index of the dispersant, λ_0 the wavelength of the laser, and θ the scattering angle.

For polydisperse systems, a multi-exponential fit (Contin analysis) is used. From the obtained diffusion coefficient the particle diameter can be calculated using the Stokes-Einstein equation:

$$d(H) = kT / 3\pi\eta D \qquad (2\text{-}11)$$

Here, d(H) is the hydrodynamic diameter, D the translational diffusion coefficient, k is the Boltzmann constant, T the absolute temperature, and η the viscosity of the surrounding medium.

Using the Mie theory, the obtained intensity distributions can be transformed to volume- or number-weighted distributions, if the density of the material is known.

2.7 Zeta-potential measurements

In contrast to a solution, finely dispersed particles forming a colloidal suspension scatter visible light when being illuminated (Tyndall effect). Between the particles act attractive Van-der-Waals and repulsive Coulomb forces. The sum of these forces defines the stability of the suspension versus aggregation and subsequent sedimentation. To avoid these effects two possibilities for stabilization exist. Steric stabilization can be achieved by adsorption of polymers onto the surface of the particles, which prevent aggregation. Alternatively, the suspension can be electrostatically stabilized by altering the surface charge of the particles and the Coulomb forces acting between them. If a particle possesses a surface charge, it is surrounded by a relatively rigid layer of counter ions, the so-called Stern-layer (Figure 2-6). Around this layer a diffuse layer of ions, which are less firmly associated, exists. Ions within within a certain boundary, which is called the slipping plane move together with the particle, those further away from the particle stay with the bulk dispersant. The charge at this plane is called the zeta potential (ζ-potential), which is

experimentally available.[125] The ζ-potential is a measure of the electrostatic Coulomb forces between the particles, and typically the suspension is considered stable if the ζ-potential is > | 30 mV | .
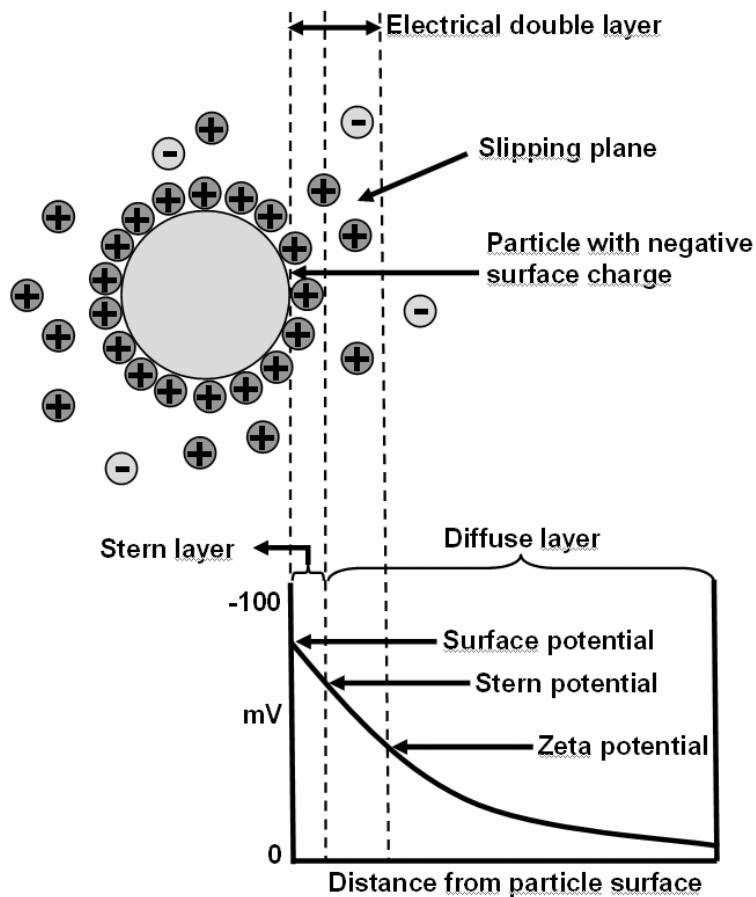
Figure 2-6. Schematic representation of the ζ-potential.

To measure the ζ-potential the suspension is put into a capillary cell and subjected to an electrical field. The particles move within the field and their velocity is dependent on the field strength, the dielectric constant of the medium, the viscosity of the medium, and the ζ-potential. The movement is detected by illuminating the particles with a laser source and detecting the scattered light. Compared to a reference beam, the scattered light fluctuates

with a frequency proportional to the velocity of the particles. From the velocity, the ζ-potential can be calculated using the Henry equation:

$$U_E = 2\,\varepsilon\,\zeta\,F(\kappa a)\,/\,3\eta \qquad\qquad (2\text{-}12)$$

U_E is the electrophoretic mobility, ζ the zeta potential, ε the dielectric constant of the dispersant, η its viscosity, and $F(\kappa a)$ is called the Henry function. In aqueous media and at moderate electrolyte concentrations the Henry function can be approximated to be 1.5 (Smoluchowski approximation).

2.8 High-throughput instrumentation

The reactions occurring during hydrothermal synthesis of zeolitic materials are complex and often poorly understood. This makes the targeted discovery of new zeolites, or the optimization of existing molecular sieves a tedious mission. Often, a large number of experiments is needed for a systematic screening of all crucial synthesis parameters. This difficulty is known from other scientific areas, especially in pharmaceutical research. Therefore, high-throughput methods have been developed, which allow for the rapid synthesis of a large number of potentially biologically active substances, and their parallel identification and testing. In the last ten years, high-throughput methods have also been adopted by materials researchers.[126, 127]

In the ideal case, every step during a high-throughput screening – experiment scheduling, reactant mixing, synthesis, work-up, and characterization – is designed in a parallel and automatic way. This is crucial as each serial step

represents a bottle-neck, and depending on the scope of the experiments, this can lead to large delays.

In our work group a semi-automatted high-throughput system for the parallel hydrothermal synthesis of porous materials has been developed, and has been used in this work. The reaction system consists of a multiclave including either 24 or 48 reaction vessels (Figure 2-7). Depending on the investigation and the reactants, the synthesis mixtures are either prepared manually or by use of a liquid dosing robot. After hydrothermal treatment, the reactants are transferred to a multiple-filter block for work-up and washing. Afterwards, the reactants are automatically characterized by means of X-ray diffraction with a STOE Stadi P diffractometer equipped with a automatic xy-sample-stage. Data analysis can be performed using the STOE Win XPOW Combinatorial analysis software.
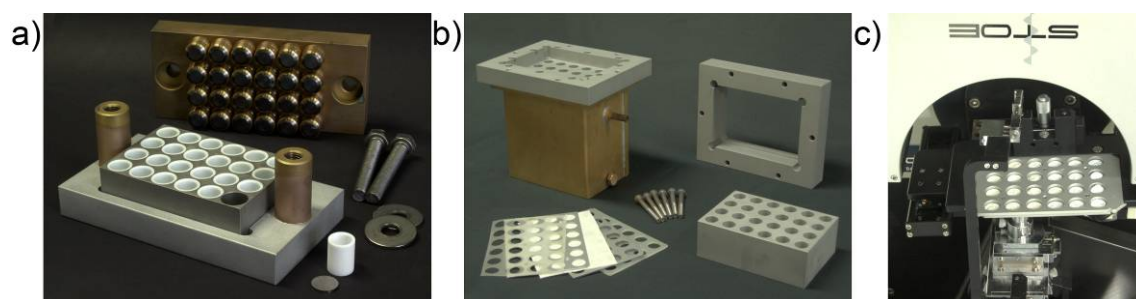
Figure 2-7. High-throughput instrumentation used for the synthesis of molecular sieves. a) 24-experiment multiclave lined with Teflon inlets. b) Filter block for parallel work-up of the experiments. c) XRD stage for the automatic X-ray analysis of the 24 samples.

3   Nanosized SAPO-34 synthesized from colloidal solutions

This chapter is based on a publication in the ACS (American Chemical Society) journal "Chemistry of Materials".[128]

3.1   Introduction

The reduction of zeolite crystal size has been a major research field for the past 10 years as the decrease of dimension leads to substantial changes in the properties of the materials.[63] Primarily, this has an impact on the performance of zeolites in traditional application areas such as catalysis and separation.[129-131] Additionally, this development has led to new synthesis strategies yielding nanomaterials with narrow particle size distributions. Moreover, the possibility of stabilizing these nanoparticles in suspensions has facilitated the production of thin-to-thick films, which are interesting for membrane and sensing applications.[102, 132-138] The most promising route for the preparation of microporous and particularly zeolite nanocrystals is the use of clear solutions or colloidal suspensions as precursor media. An excellent review summarizing the systems studied was published by Tosheva and Valtchev.[63] This article mainly deals with zeolite syntheses, but aluminophosphate systems are also discussed, namely AlPO-5 (AFI), AlPO-11 (AEL) and AlPO-18 (AEI). The AlPO-18 system is a thoroughly investigated colloidal aluminophosphate due to its interesting water sorption properties.[139] A structurally related system is AlPO-34 with chabazite structure (CHA); the silicon-substituted form SAPO-34 is one of the widely investigated molecular sieves due to its use in catalysis, especially

in the methanol-to-olefin (MTO) process.[140] Furthermore, SAPO-34 shows unique water sorption properties, which can be used for the thermochemical storage of heat.[141-143] Among the approximately 600 publications concerning the SAPO-34 material, only a few shall be mentioned here. Originally discovered at Union Carbide Corporation,[144, 145] the crystal structure of SAPO-34 and its analogy to natural chabazite was firstly reported by Ito et al.[146] (the analogy to the CHA structure was already reported with the discovery). Numerous groups have investigated the SAPO-34 material with respect to further applications, and mainly the performance in the MTO reaction.[147] Apart from its pore structure, the short- and long-term hydrothermal stability, which is dependent on the degree and homogeneity of the silicon incorporated in the CHA framework, is of importance.[148-150] The samples with relatively low amounts of silicon show high stability. It was found that the silicon distribution is dependent on the choice of template used during the synthesis, and the most stable samples are obtained from tetraethylammonium-containing precursor suspensions.[151] The mechanism of SAPO-34 crystallization using morpholine as structure-directing agent was studied in detail by Vistad et al.[152-154]

Other factors investigated include the acid-site strength[155] and the influence of incorporated transition metals on the stability and performance of SAPO-34 materials.[156] The effect of crystal size on the MTO process was investigated by Chen et al.[157-160] They separated fractions of different crystal sizes by centrifugation and found the best performance for crystals of sizes smaller than 500 nm. Below this diameter no diffusion limitations are observed during the

catalytic reaction. Therefore, a synthesis route to SAPO-34 crystals with diameters lower than 500 nm with the tetraethylammonium ion as templating agent seems very desirable. Lesch et al. synthesized SAPO-34 from very diluted solutions, but did not include any data concerning particles size.[161] Additionally, Mertens et al. claimed the reduction of particle size by either using tetraalkyl orthosilicate as the silicon source,[162] or by dissolving the silicon in organic bases prior to mixture with other reagents.[163] Here, particles of sizes <100 nm are claimed based on SEM and XRD line width. Yao et al. made an attempt to synthesize SAPO-34 in confined polymer spaces.[164] However, the products contained large amounts of micrometer-sized crystals and their reduced crystallinity led to reduced surface areas.

This chapter reports on the synthesis of nanosized SAPO-34 crystals with narrow particle size distributions by using colloidal precursor solutions. The influence of the initial composition, temperature and source of heating on crystal dimensions was studied.

3.2 Experimental

Clear precursor solutions were prepared with the following molar compositions: $1\ Al_2O_3 : 2-4\ P_2O_5 : 0.6-1\ SiO_2 : 2-4\ TEA_2O : 75-147\ H_2O$. The synthesis conditions and the resultant phases from different batches are summarized in Table 3-1. Aluminium isopropoxide (e.g. sample 160/180_4: 6.00 g, 29 mmol, Aldrich), colloidal silica (1.72 g, 9 mmol, Ludox HS-30, 30 wt.%, Aldrich) and tetraethylammonium hydroxide solution (48.45 g, 115 mmol, 35 wt.%, Aldrich)

were mixed at RT and stirred at 450 rpm for at least 2 h in 180 mL PP-bottles. To the resultant solution, phosphoric acid (13.28 g, 115 mmol, 85 wt. %, Aldrich) was added drop-wise over a period of 60 – 150 min to avoid the formation of dense gel particles. It is important to note that the latter step is crucial for the overall process (special care is needed for the solution with the ratio of Al_2O_3 : TEA_2O = 1 : 2, and after the complete dissolution of the Al/Si-sources the acid was added very slowly). If not, the obtained mixtures were not clear, but white suspensions were formed. At low concentrations of Al_2O_3 : TEA_2O = 1 : 4, the obtained precursor solutions did not show a Tyndall-effect (the scattering of light by the suspended particles). The mixture was stirred another 30 min prior to HT treatment. 10 g of the solution were filled into a 23 mL Teflon-lined stainless steel autoclave (Parr Instrument Company) and heated in a conventional oven. To study the kinetics of crystal growth of SAPO-34, simultaneously 5 autoclaves were used for each precursor solution, and the experiments were quenched after varying synthesis times. Additionally, microwave syntheses were performed using 100 mL autoclaves (Synthos 3000, Anton Paar GmbH). After the synthesis, the suspensions containing nanosized crystals were purified in a series of three steps consisting of high-speed centrifugation (43000 g (RCF), 20 min), removal of the supernatant and re-dispersion in aqueous KOH solution (pH = 8) using an ultrasonic (US) bath. If no material was separated by centrifugation, aqueous NaCl solution (15 mM) was used to achieve coagulation prior to centrifugation. The samples were freeze-dried in order to avoid aggregation for further characterization.

3.3 Characterization

All samples were investigated by means of Dynamic Light Scattering (DLS) in a Zetasizer Nano-ZS (Malvern Instruments) directly after HT treatment and after the subsequent washing cycles. Zeta potential measurements, giving information about the stability of the suspensions, were performed using the same instrument. Prior to these analyses, one drop of the final suspensions was added to 1 mL of buffer solution (Hydrion®, Aldrich, pH = 2 – 11), equilibrated for 30 min and checked for pH using a gel electrode (Mettler Toledo). Powder X-ray diffraction (XRD) patterns of the freeze-dried samples were recorded using a Stoe STADI-P diffractometer (transmission mode, Cu Kα radiation). The elemental composition of the products was determined by atomic absorption spectroscopy with a Varian Vista RL CCD instrument. To investigate the size and morphology of the products, scanning electron microscopy (SEM) images were recorded using a JEOL JSM-6500F microscope. Diffuse Reflectance Infrared Fourier Transform (DRIFT, Bruker Equinox 55) and Raman (Horiba Jobin Yvon LabRAM-HR, Bruker Equinox 55 & FRA Raman module 106 /S) spectroscopy was used to investigate the short-range order within the materials during the crystallization process. Thermogravimetric analyses (TGA) and Differential Scanning Calorimetry (DSC) were performed on the as-synthesized samples using a Netzsch STA 440 C Jupiter thermobalance. The samples (10 mg) were heated in a stream of synthetic air (50 ml min^{-1}) with a heating rate of 10 K min^{-1} in an alumina crucible in the temperature range 25 – 900 °C. Selected samples were investigated by means of volumetric argon

physisorption experiments (Quantachrome Autosorb MP) at 87 K. Prior to the adsorption experiments, the samples were calcined in air at 550 °C for 24 h (heating rate: 1 °C min^{-1}) and out gassed under vacuum at 350 °C overnight.

3.4 Results and discussion

3.4.1 Synthesis

To obtain colloidal precursor solutions for the synthesis of nanosized silicoaluminophosphates, the following strategy previously employed in AlPO-18 (AEI structure type code) syntheses was used (Chapter 4). First, the molecular or colloidal sources for aluminum and silicon are dissolved in basic media in the presence of tetraethylammonium hydroxide as solvent. The lower threshold in order to obtain a clear solution was a molar ratio of Al_2O_3 : TEA_2O = 1 : 2 (based on a 35 wt.% TEAOH solution). Afterwards, the same molar amount (as the base) of phosphorus is added in the form of concentrated phosphoric acid in order to maintain the solution as concentrated as possible, and to neutralize the synthesis solution, as the SAPO-34 phase crystallizes most preferentially under slightly acidic or neutral conditions.[165] According to La Mer at al.,[166] the synthesis of nanocrystals is favored by a high degree of supersaturation at the end of the induction period, which leads to fast nucleation of a high number of nuclei with ideally monomodal size distribution. In a conventional gel system, heterogeneous nucleation often results in the formation of particles with broad size distributions. Therefore, the ideal precursor solution should be as concentrated as possible, but still colloidal to guarantee a real solution with a

high degree of supersaturation during the induction heating period. The concentration of the precursor systems was varied and the temperature of HT treatment was changed gradually in order to optimize the nucleation and crystallization process. A highly dilute system with Al_2O_3 : TEA_2O : H_2O – ratios of 1 : 4 : 147 was the starting point. This system guaranteed clear solutions during the whole synthesis procedure; the corresponding precursor solutions did not show a Tyndall effect. Afterwards the concentration of the reactants was increased stepwise to Al_2O_3 : TEA_2O : H_2O = 1 : 2 : 75, which was the upper limit for the preparation of colloidal precursor solutions. The formation of the colloidal suspension was also very sensitive to parameters such as room temperature aging (typically ~30 min), speed (450 rpm) and time of stirring during initial dissolution (~2 h) and addition rate of H_3PO_4 (~0.2 mL min^{-1}), etc. (these parameters were not systematically investigated and presented in this chapter).

All precursor systems were subjected to HT treatment with varying times of crystallization. The heating rate in the used setup is typically ~2.5 ° K min^{-1} (estimated from the cooling behaviour), quenching to RT was performed under flowing water in ~10 min. All samples quenched after short heating times, even the concentrated ones (see Table 3-1), yielded no solid material after centrifugation or flocculation in low-density solvents like methanol or ethanol. Instead, the systems represented perfectly clear solutions showing no Tyndall effect. However, by adding dilute NaCl solution to these solutions, flocculation was observed, and subsequent centrifugation was possible, and some of the

resulting amorphous products were subjected to further characterization (see below).

At 160 °C, AEI was detected in various amounts as a competing phase in the final crystalline products according to XRD. Extensive reporting of CHA/AEI intergrowths is present in the ExxonMobil patent literature. However, based on our XRD and SEM data, the phases and their typical crystal morphologies appear to be largely separated. AEI forms sheet-like hexagonal crystals, whereas CHA is obtained in form of cubic crystals. The SAPO-18 phase (AEI-type structure) is structurally related to the chabazite structure.[88] Both include sheets of connected double six-membered rings (D6R). The sheets are connected along the z-axis (via O-bridges) to form stacked sheets. The lateral shift between the sheets is zero for the CHA structure, whereas a rotation of 180 ° about the z-axis gives the AEI structure. The connection gives rise to a three-dimensional channel system with eight-membered pore openings of 3.8 Å diameter. This close relationship apparently gives rise to similar energies for both microporous materials and both AEI and CHA-type materials can nucleate at 160 °C in the investigated systems. The appearance of side products is also very common for the analogous aluminosilicate chabazite structure. Additionally, re-crystallization from AEI to CHA was observed in the reacting systems with increasing the time of heating (see samples 160_3 and 160_4). The rate of re-crystallization is dependent on the initial composition and temperature; however the re-crystallization in the opposite direction is not observed (from CHA to AEI). The experiments performed at 160 °C do not show

a steady trend in nucleation times, and this is attributed to the occurrence of two different phases in the final products.

For the experiments at 180°C, it was observed that the induction time increased from less than 2 to less than 4.5 h with decreasing concentrations of Al, P and Si. In the more diluted systems, the diffusion pathways for the reactive components are increased, which apparently results in slower reaction kinetics.

Table 3-1. Synthesis conditions and resulting products.

Sample name	Precursor comp. (Al$_2$O$_3$: P$_2$O$_5$: SiO$_2$: TEA$_2$O : H$_2$O)	T (°C)	t (h)	Structure type code	Size (nm)*	Product composition			
						Al	P	Si	P+Si
160_2_1	1 : 2 : 0.6 : 2 : 75	160	0.50	amorphous					
160_2_2	1 : 2 : 0.6 : 2 : 75	160	1.00	amorphous					
160_2_3	1 : 2 : 0.6 : 2 : 75	160	1.50	AEI	230	0.51	0.45	0.04	0.49
160_2_4	1 : 2 : 0.6 : 2 : 75	160	2.00	AEI	240	0.51	0.47	0.02	0.49
160_3_1	1 : 3 : 0.6 : 3 : 111	160	1.30	amorphous					
160_3_2	1 : 3 : 0.6 : 3 : 111	160	2.50	amorphous					
160_3_3	1 : 3 : 0.6 : 3 : 111	160	3.50	amorphous					
160_3_4	1 : 3 : 0.6 : 3 : 111	160	5.75	CHA (AEI)	320	0.50	0.45	0.05	0.50
160_3_5	1 : 3 : 0.6 : 3 : 111	160	20.0	CHA	356	0.49	0.43	0.08	0.51
160_4_1	1 : 4 : 0.6 : 4 : 147	160	2.50	amorphous					
160_4_2	1 : 4 : 0.6 : 4 : 147	160	3.50	AEI	299	0.50	0.47	0.03	0.50
160_4_3	1 : 4 : 0.6 : 4 : 147	160	5.00	AEI	329	0.51	0.46	0.03	0.49
160_4_4	1 : 4 : 0.6 : 4 : 147	160	13.5	AEI	340	0.50	0.46	0.04	0.50
160_4_5	1 : 4 : 0.6 : 4 : 147	160	15.0	CHA	417	0.50	0.42	0.08	0.50
180_2/1_1	1 : 2 : 1 : 2 : 77	180	0.50	amorphous					
180_2/1_2	1 : 2 : 1 : 2 : 77	180	1.00	amorphous					
180_2/1_3	1 : 2 : 1 : 2 : 77	180	1.50	CHA (low yield)	181				
180_2/1_4	1 : 2 : 1 : 2 : 77	180	2.00	CHA	285	0.51	0.43	0.06	0.49
180_2/1_5	1 : 2 : 1 : 2 : 77	180	2.50	CHA	272	0.51	0.42	0.07	0.49
180_2_1	1 : 2 : 0.6 : 2 : 75	180	0.50	amorphous					
180_2_2	1 : 2 : 0.6 : 2 : 75	180	1.00	amorphous					
180_2_3	1 : 2 : 0.6 : 2 : 75	180	2.00	CHA	286	0.51	0.42	0.07	0.49
180_2_4	1 : 2 : 0.6 : 2 : 75	180	4.25	CHA	316	0.52	0.42	0.06	0.48
180_3_1	1 : 3 : 0.6 : 3 : 111	180	2.00	amorphous					
180_3_2	1 : 3 : 0.6 : 3 : 111	180	3.00	CHA	264	0.50	0.47	0.03	0.50
180_3_3	1 : 3 : 0.6 : 3 : 111	180	4.00	CHA	265	0.50	0.46	0.04	0.50
180_3_4	1 : 3 : 0.6 : 3 : 111	180	6.00	CHA	276	0.49	0.45	0.05	0.51
180_3_5	1 : 3 : 0.6 : 3 : 111	180	18.5	CHA	507	0.49	0.44	0.08	0.51
180_4_1	1 : 4 : 0.6 : 4 : 147	180	2.00	amorphous					
180_4_2	1 : 4 : 0.6 : 4 : 147	180	3.00	amorphous					
180_4_3	1 : 4 : 0.6 : 4 : 147	180	4.50	CHA	308	0.51	0.46	0.03	0.49
180_4_4	1 : 4 : 0.6 : 4 : 147	180	5.50	CHA	350	0.51	0.46	0.03	0.49
180_4_5	1 : 4 : 0.6 : 4 : 147	180	7.00	CHA	368	0.51	0.45	0.04	0.49
180_2_MW	1 : 2 : 0.6 : 2 : 75	180	7.25	CHA	206	0.50	0.41	0.09	0.50

*Particle diameters are given as Z-average values of the corresponding Cumulants algorithm.[167, 168]
Sample code: (Temperature)_(Molar ratio of P$_2$O$_5$/Al$_2$O$_3$)_(Increasing Exp.-No. with synthesis time).

The sizes of the particles after HT treatment increased with synthesis time for all investigated samples. Comparing the different concentrations in the precursor solutions, no clear trend with respect to particle size can be seen (Table 3-1). This might be expected, as there are several contributing processes. The smallest primary particles nucleate from the most concentrated precursor solutions. However, after nucleation, growth of primary particles takes place and the growth rate is faster in more concentrated systems. Additionally, the growth phase is longer if the system is more concentrated or the amount of nuclei is lower (which is the case for less concentrated precursor solutions). Therefore, the size of the resulting particles depends on the elapsed time between nucleation and quenching during the HT treatment. In case of sample 180_2/1_3, the quenching obviously was very shortly after nucleation and the particles showed an average size of 180 nm. However, the yield at that time was very low (~10 % of final yield). Between 1.5 h and 2.0 h a large increase in size (>50 %) was observed for this sample and the growth phase was completed, as no further increase in size was observed after 2.5 h. Similarly, sample 180_2_3 was quenched relatively late, and a fast growth process had already taken place. The resultant size (285 nm) is identical to the system 180_2/1 after the same synthesis time (2 h). In order to synthesize particles of small size, it is therefore necessary to balance the size of primary particles and the subsequent growth rate by careful adjustment of synthesis conditions. In the system 180_3 (lower concentration) this balance is obviously better. After 3 h of aging, the particles are nucleated and have grown to a Z-average size of

264 nm, and further growth was very slow (180_3_3 – 180_3_5). Therefore, the final crystals were smaller in diameter than the 180_2 series of samples.

The yields of the syntheses were similar for all investigated systems. Typically, yields of ~60 % were found relatively shortly after nucleation. For long synthesis times (>6 h) the yields increased to ~75 %. A third contributing process, which is affecting the size of the products, can be deduced from the 180_3 series, but was also observed for all systems (not shown). If the synthesis time is further prolonged, particles with sizes of up to ~1 µm are obtained although the yield and degree of crystallinity do not increase. Most probably these large particles result from aggregation of primary particles as the zeta potential is very low (see DLS and ζ-potential section). However, Ostwald ripening cannot be ruled out.

The pH of the synthesis solutions was monitored prior to and after HT treatment. All precursor solution showed neutral pH, and due to the relatively high dilution, the pH raised to 7.1, 7.5 and 8.5 with increasing the concentration after the complete condensation process.

All crystalline samples were subjected to elemental analysis after freeze-drying to gain information about the degree of silicon incorporation. The relative molar fractions of the T-elements are shown in Table 3-1. With increasing the synthesis time, the silicon content increased, but none of the investigated samples reached the Si/Al -ratio in the precursor solution of 0.3. A similar result was found earlier by Ashtekar et al.[148] Those samples that were hydrothermally treated for relatively long times (>6 h) reach a Si molar fraction of 0.08, which corresponds to a composition of $Al_6P_5SiO_{24} \cdot x\ TEA^+ \cdot n\ H_2O$ (or one silicon atom

per chabazite cage containing 12 T-atoms). Obviously, only P-positions of the hypothetical CHA-framework are substituted by Si-atoms. Tan et al.[150] showed by means of MAS NMR data that a large part (~80 %) of the final silicon fraction is incorporated during nucleation in the gel systems and later substitution of phosphoros atoms only takes place to a minor extent. In our clear precursor systems the situation is slightly different. The products quenched shortly after nucleation show approximately 40 % of the final Si substitution, and the remaining Si is incorporated during crystal growth. However, the fraction of silicon by weight in the total mass of the analyzed products is relatively low (~1 %) resulting in a rather large uncertainty in the shown elemental ratios. This can account for the unexpected values for the samples 160_2_4 and 180_2_4.

3.4.2 DLS and ζ-potential

DLS data of the series 180_4 are shown in Figure 3-1. The same sample series has been depicted in the following graphs (the results for all investigated samples were similar).
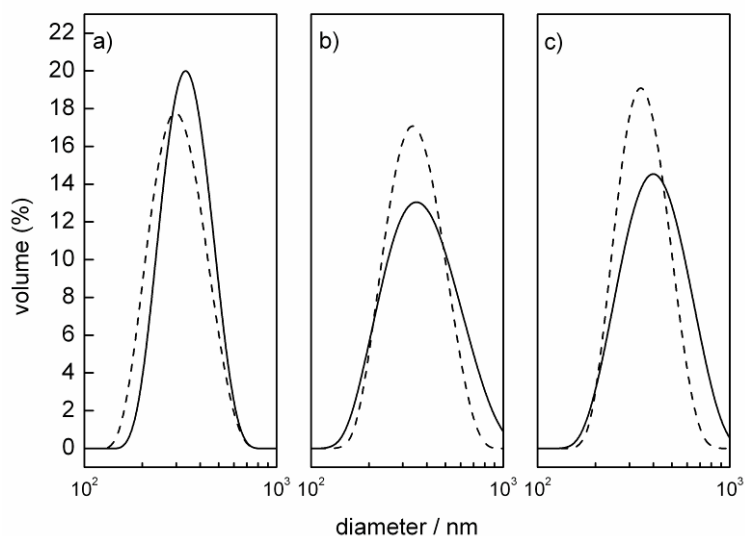
Figure 3-1. DLS curves of samples 180_4_3 – 180_4_5 after hydrothermal treatment (solid) and after 3 purification cycles in aqueous KOH solution (dashed). The data are expressed as volume-weighted Contin distributions.

All products showed monodisperse particle size distributions after HT treatment with polydispersity indexes of below 0.1 (This parameter is calculated during the Cumulants analysis[167, 168] of the DLS correlation function. If one were to assume a single size population following a Gaussian distribution, then the polydispersity index PdI would be related to the standard deviation (σ) and the average mean size (Z_D) of the hypothetical Gaussian distribution: PdI = σ^2 / Z_D^2). However, if the samples were washed in doubly distilled water, they showed varying degrees of polydispersity due to aggregation. The stability of the suspensions was investigated by means of pH-dependent zeta potential measurements of particles stabilized in water (Figure 3-2). The isoelectric point of the SAPO-34 particles is at pH ~ 4 due to the acidity of the molecular sieve which is dependent on the degree and distribution of silicon in the CHA framework structure. Consequently, suspensions of SAPO-34 react acidic. The

zeta potential reaches values of < -40 mV when the suspensions have pH values above 6. Therefore, we chose slightly basic (pH = 8) aqueous KOH solution for the washing cycles after the complete crystallization of the SAPO-34 samples. Hence, the washed suspensions showed the same or even narrower monomodal size distributions than after HT treatment (Figure 3-1). At pH > 9 the synthesized samples started to decompose and therefore showed irreproducible zeta potential values.
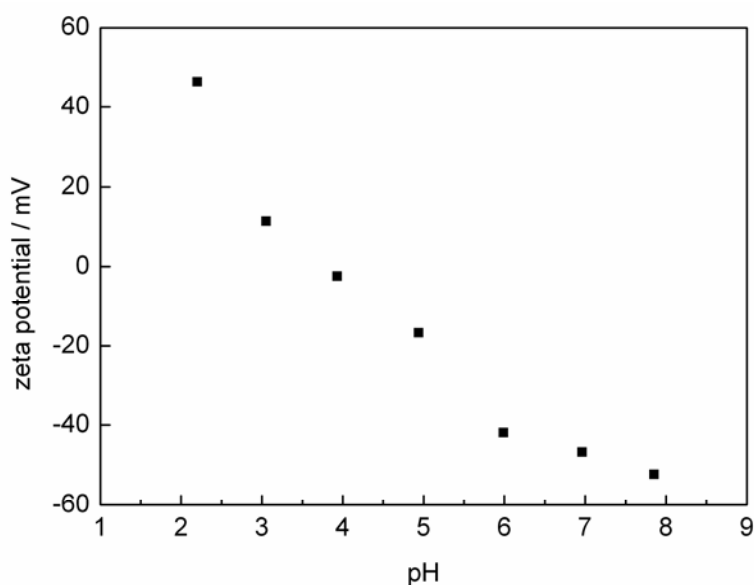
Figure 3-2. pH dependence of zeta potential value for sample 180_4_5 (the samples were equilibrated in Hydrion® buffer solutions and checked for pH with a gel electrode prior the measurements).

3.4.3 XRD and SEM investigations

Figure 3-3 shows X-ray diffraction patterns of the samples 180_4. The flocculated samples 1 – 2 appear X-ray amorphous after purification and drying.
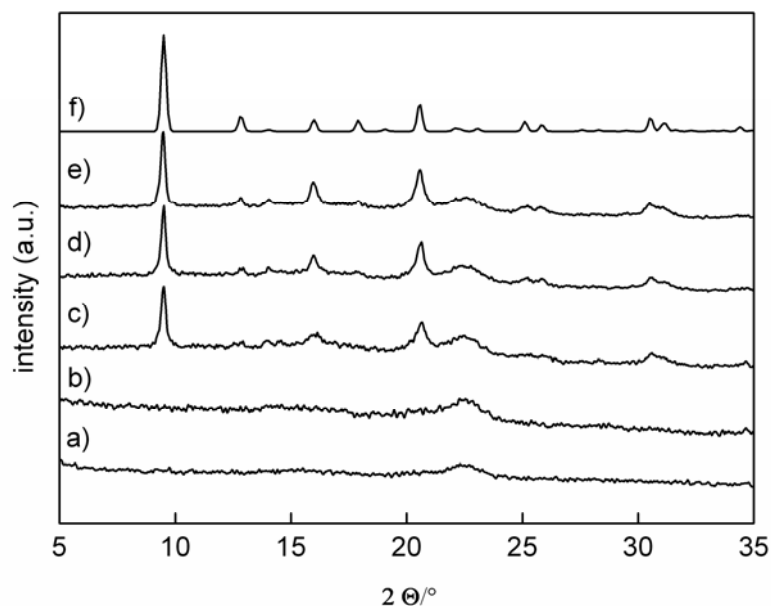
Figure 3-3. Powder X-ray diffraction patterns of samples 180_4_1 – 180_4_5 (a-e) and simulated SAPO-34 XRD data (f).[146] The broad peak at ~22.5° is due to the sample support (filter paper) in the used measuring set up.

Consequently, SEM images of the freeze-dried samples (Figure 3-4 a-b) show aggregated particles with undefined morphology. At higher magnification (50000x, not shown) the size of the individual flocculated gel particles can be estimated to be about 100 nm. The samples 3 to 5 represent crystalline materials with the typical SAPO-34 (CHA) pattern. No phase impurities were detected in this series and in the other experiments conducted at 180 °C, whereas samples treated at 160 °C contain SAPO-18 impurities (AEI). With increased crystallization time, the particles become bigger in size (Figure 3-4 c-e). Additionally, the morphology of the crystals is better defined, and a flattened cube-like habit is dominant for the particles. Especially the SEM images of sample 180_4_3 show a relatively large amount of material with undefined morphology.
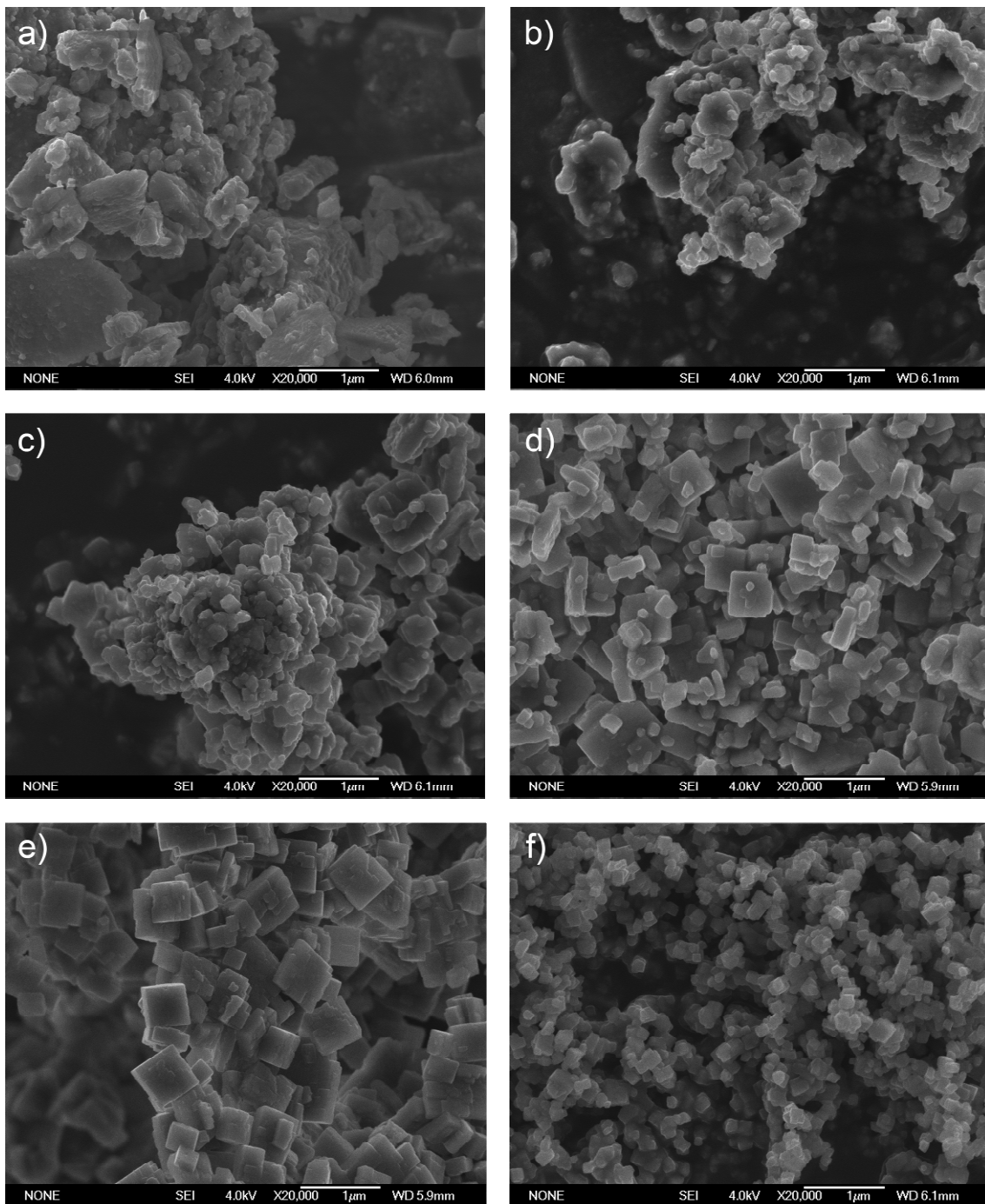
Figure 3-4. SEM images of samples 180_4_1 – 180_4_5 (a-e) and 180_2_MW (f) (Magnification: 20 000x, Scale bar: 1 μm).

3.4.4 Vibrational spectroscopy

In Figure 3-5 the Raman spectra of the sample series 180_4 and of aqueous TEAOH are shown. The assignments of Raman and IR bands were based on relevant reports[148, 150, 165, 169-173] and the data are summarized in Table 3-2.
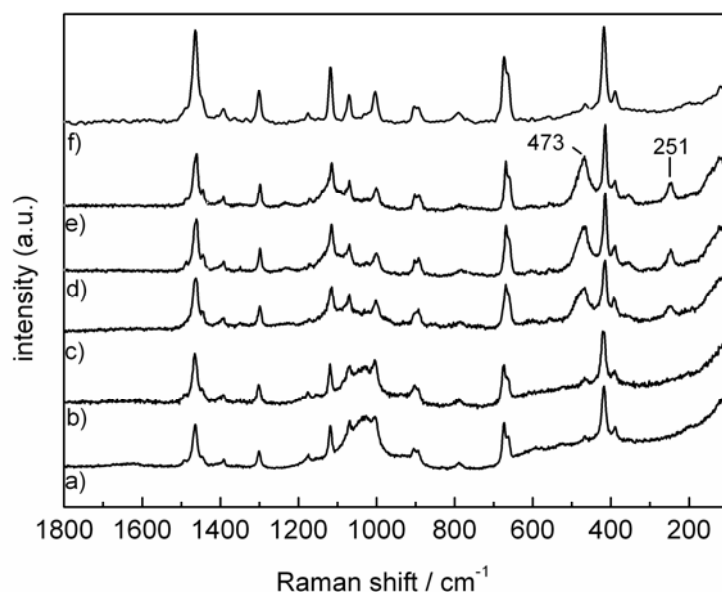
Figure 3-5. Raman spectra of samples 180_4_1 – 180_4_5 (a-e) and of aqueous tetraethyl ammonium hydroxide solution (f).

All bands of the template are present in the solid products indicating that TEA$^+$ ions interact with the silicoaluminophosphate network at all stages of the crystallization process. However, the samples 1 and 2 represent X-ray amorphous coagulated condensation products and the template is likely to be captured inside of the amorphous gel, rather than specifically interacting with any gel structure. This results in a shift of ~2 cm^{-1} to higher wavenumbers for the template-specific Raman bands. Tan et al.[150] observed a gradually increasing amount of included template in the silicoaluminophosphates with

increasing the synthesis time of the gel systems. The crystalline samples 3 – 5 showed two structure-sensitive bands at 251 and 473 cm^{-1}. The origin of the first mode is rather unclear. Marchese et al.[170] attributed it tentatively to a mode involving both the template and the framework in morpholine-containing SAPO-34. The latter band was assigned to the motion of an oxygen atom in a plane perpendicular to the T-O-T bonds.[174]

Table 3-2. Assignments of vibrational bands in the SAPO-34 material.[148, 150, 165, 169-173]

IR bands (wavenumbers/cm^{-1})	Raman bands (wavenumbers/cm^{-1})	Assignment
1213		v_A P-O-Al
1122		v_A O-P-O
1005		v P-O
644		δ T-O (D6R)
571		δ T-O (PO4)
532		δ T-O (Si/AlO4)
488		δ T-O (SiO4)
	473	δ T-O-T
390		δ T-O
	251	δ "T-N"[170]

IR spectra (Figure 3-6) of the three crystalline samples are dominated by a broad band at ~1100 cm^{-1} assigned to an O-P-O asymmetric stretching vibration. In the T-O-bending region characteristic framework vibration bands are observed at 644, 571, 532, 488 cm^{-1}, and 390 cm^{-1}. The increasing degree of crystallinity for the shown SAPO-34 samples is reflected by increasing Kubelka Munk functions for all observed bands.
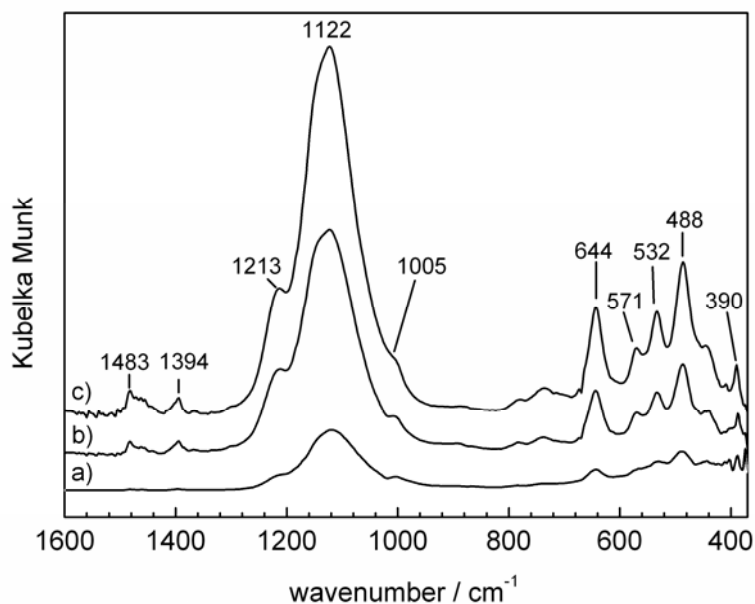
Figure 3-6. Diffuse reflectance infrared Fourier spectroscopy (DRIFT) data for samples 180_4_3 to 180_4_5 (a-c).

3.4.5 TGA and DSC data

In Figure 3-7 TGA and DSC data of the samples 180_4_1 to 5 are shown. The samples 4 and 5 show nearly identical TGA behavior. These samples lose ~4 % of water upon heating to 100 °C and a small endothermic peak is observed in the DSC curve. The exothermic decomposition of the template molecules proceeds in two steps at 400 °C (14 %) and 520 °C (2 %). These weight losses correspond to 2 H_2O molecules and 1 TEA^+ molecule per chabazite cage (the TEA^+ molecule is expected for the charge compensation of 1 Si atom, see elemental analysis). The water loss in the samples 1 – 3 is much larger (14, 16 and 8 %, respectively) due to a higher fraction of non-condensed hydroxyl groups, which is expected for the amorphous samples (1 and 2). These data suggest that a substantial fraction of sample 180_4_3 is not in a fully condensed/crystalline state. The amorphous samples lose 12 and 9 % of their

weight upon further heating to 240 °C. This weight loss is attributed to the decomposition of weakly connected template with the inorganic matrix. Sample 3 also loses 4 % at this temperature, but a larger fraction (14 %) of template is removed at higher temperature, indicating a stronger interaction of the template within the crystalline framework structure. Interestingly, the samples 1 – 3 show large exothermic DSC signals at ~600 °C, which is due to a phase transformation to the tridymite phase (shown by XRD).

3.4.6 Microwave synthesis

One of the major goals in the synthesis of nanosized molecular sieves is to render the synthesis mixture as homogeneous as possible in terms of composition and temperature. Additionally, for the investigated systems a very fast heating rate can avoid the formation of AEI impurities. These parameters can only be controlled to a limited degree in conventional autoclaves and ovens. Therefore, we used microwave (MW) energy for heating of different precursor systems. The most successful experiment performed in the MW oven, coded as sample 180_2_MW, is listed in Table 3-1. The precursor solution of molar composition 1 Al_2O_3: 2 P_2O_5: 0.6 SiO_2: 2 TEA_2O: 75 H_2O was treated at 180 °C (heating rate of 32 °C min^{-1} for a duration of 7.25 h). The obtained particles had an average particle diameter of 100 nm based on DLS (PdI = 0.090) and no AEI impurities were detected in the XRD pattern (not shown). This particle diameter is exceptionally small for (silico)aluminophosphate systems.[63] SEM images (Figure 3-4 f) show particles with a homogeneous cube-like morphology.

Furthermore, a large fraction of the powder consists of particles with diameters around 100 nm.
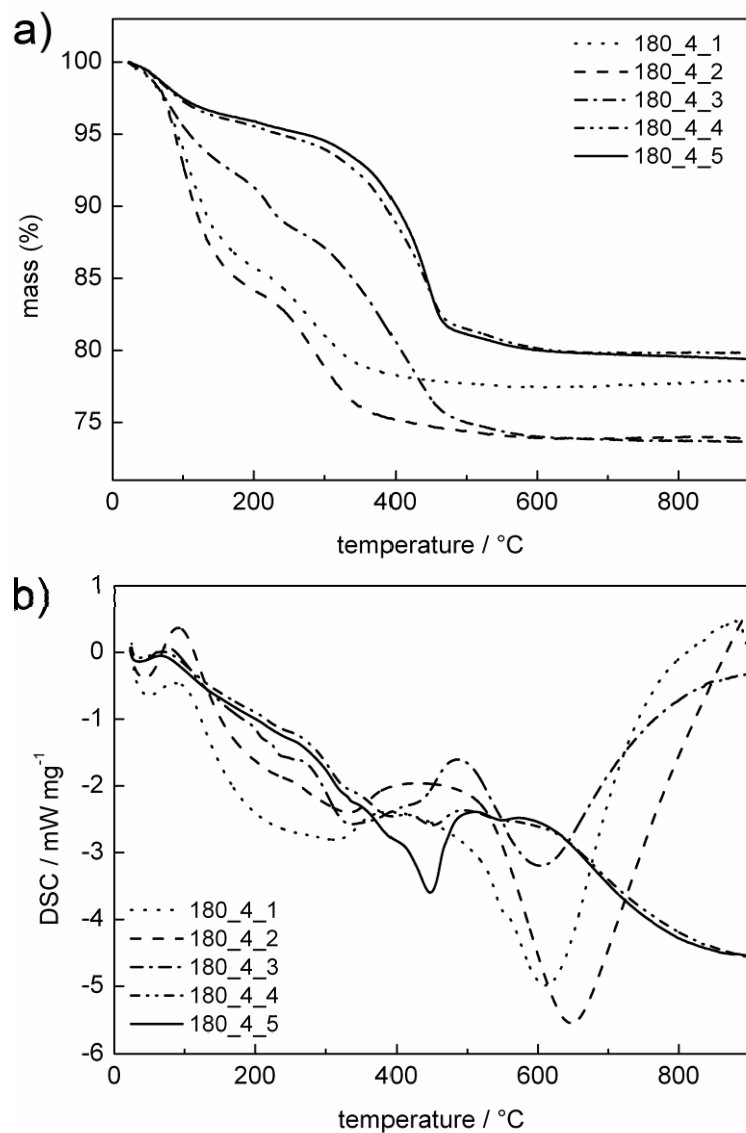
Figure 3-7. Thermogravimetric (a) and differential scanning calorimetric (b) data of samples 180_4_1 to 180_4_5.

3.4.7 Sorption properties

To evaluate the effect of crystal size on the sorption properties of the nanosized crystals, a reference material according to the original work by Lok et al.

(Example 35) was prepared.[144] The resulting sample synthesized from a conventional gel was highly crystalline and had particle sizes above 1 µm. Figure 3-8 shows the argon physisorption isotherms of sample 180_2_MW in comparison with the reference sample. In this case, argon was used as the probe molecule (diameter: 3.42 Å[175]) as the CHA structure has pore openings of 3.8 Å. The graphs (logarithmic scale, right image in Figure 3-8) show that the micropores of both materials are starting to be filled at a relative pressure of $1 \cdot 10^{-5}$ and the process is completed at $1 \cdot 10^{-4}$ p/p$_0$. This exceptionally steep loading curve is typical for CHA and AEI (silico)aluminophosphates (and also for other adsorptives, e.g., water).
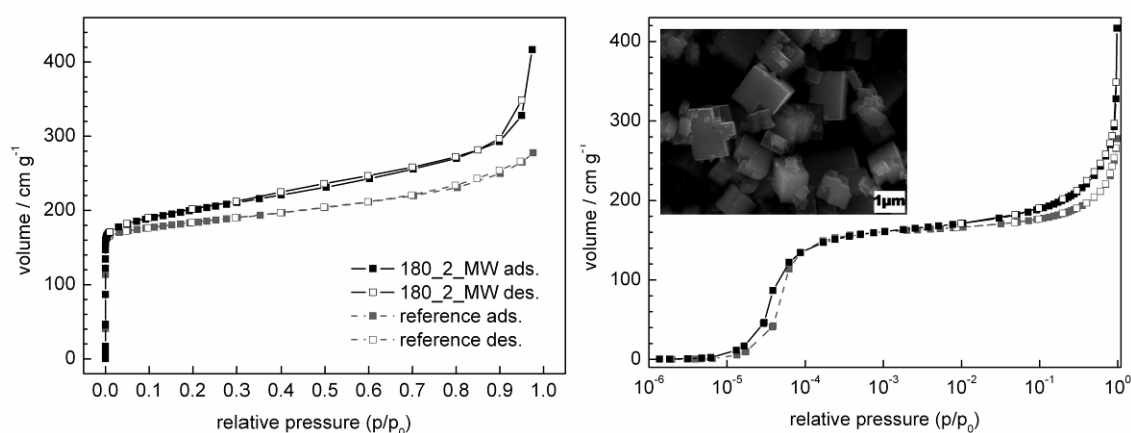
Figure 3-8. Argon physisorption isotherms of sample 180_2_MW (black) and a micron-sized reference sample (grey). Left: linear scale; right: logarithmic scale. Inset: SEM image of the reference sample with magnification of 15000.

As expected, the nano- and micronsized samples show the same micropore volume, as both are fully crystalline. At higher relative pressure, adsorption in the interparticle voids of the material takes place (left image). The degree of textural porosity is much larger in the nanosized samples and another

125 cm^3 g^{-1} (43 % of total adsorbed amount of argon, 34 % for the reference sample) are adsorbed.

3.5 Conclusion

The use of colloidal precursor solutions made it possible to synthesize SAPO-34 particles with diameters smaller than 300 nm. By means of microwave hydrothermal treatment the diameter was further reduced to 100 nm, and the resultant material was fully crystalline with a well-defined cube-like morphology. All investigated products showed narrow particle distributions and the resultant suspensions could be electrostatically stabilized in basic media. In the precursor solutions, tetraethylammonium hydroxide was used as the structure-directing agent and the final chemical composition was varied in the following range: 1 Al_2O_3 : 2 – 4 P_2O_5 : 0.6 – 1 SiO_2 : 2 – 4 TEA_2O : 75 – 147 H_2O.   The   kinetic study suggests the following mechanism of crystallization: upon heating of the clear precursor mixtures the dissolved Al-, P- and Si – sources start to react and form precursor species until a certain degree of supersaturation is reached, which is dependent on composition and temperature of heating. Subsequently, nucleation of primary particles takes place within the amorphous species. These particles grow by further addition of nutrients from the synthesis solution until they reach their final size. Additionally, at a relatively later stage of heating, aggregation and condensation of secondary particles or Ostwald ripening may take place.

4 AlPO-18 nanocrystals synthesized under microwave irradiation

This chapter is based on a publication in the "Journal of Materials Chemistry", published by the Royal Society of Chemistry (RSC).[139]

4.1 Introduction

There is a growing interest in nanosized molecular sieves due to the fact that the reduction of particle size from the micrometer to the nanometer scale leads to substantial changes in the properties of the materials.[63] As the particle size decreases the external surface area increases. A high number of external acid sites, reduced diffusion pathways and an improved access to the internal pore volume are the consequences. In the past decade a number of zeolites in the nanosized range were prepared, e.g.,, FAU,[100, 134, 176-181] LTA[101, 182, 183] or BEA.[133, 134, 184, 185] However, only a small number of nanosized microporous aluminophosphate materials have been reported. For instance, AlPO-11 nanocrystals with AEL-type structure (crystal size: 65 nm) have been synthesized by heating of gel systems in conventional ovens,[186] nanosized AlPO-5 (AFI) was obtained from gel systems[187] (crystal size: 500 – 800 nm) or clear precursor solutions[188] (crystal size: 100 – 600 nm) in microwave ovens. Recently, we reported the synthesis of colloidal AlPO-18 (AEI) from aluminophosphate solutions under conventional heating.[135, 136]

The framework topology of the latter aluminophosphate is characterized by a three-dimensional pore system possessing eight-membered intersecting channnels with a diameter of 3.8 Å.[189] The framework density (14.8 T/1000 Å^3) of the AEI topology is among the lowest in the family of aluminophosphate microporous materials.[190] The high hydrophilicity of this molecular sieve accounts for exceptionally high water sorption capacities (27.8 wt.% at 22 °C and 24 mbar),[104] which make the material particularly interesting for heat storage, heat exchange and humidity sensing applications. Heat curves and sorption isotherms of the AlPO-18 system were earlier reported for conventional AlPO-18 crystals synthesized from aluminophosphate gels.[141, 191]

In order to induce fast and homogeneous crystallization of aluminosilicate and aluminophosphate species, the replacement of conventional ovens by microwave systems is of growing interest. Various studies have demonstrated that the synthesis of molecular sieves can be significantly improved and extended when microwave energy is employed.[192] In most cases, the time for synthesis is extremely reduced and some products can be obtained in more uniform dimensions and element distributions. Additionally, products with more variable compositions can be produced. The reasons for these "microwave effects" are not well understood yet. However, many different factors seem to influence the results. Among them are the used microwave frequency (most often 2.45 GHz), the pH, the permittivity of the synthesis solution and the reactor design. A comprehensive review concerned with the synthesis of

zeolites, mixed oxide and mesoporous molecular sieves by employing microwave energy has recently been published by Tompsett et al.[193]

This chapter focuses on the microwave synthesis of nanosized AlPO-18 crystals, their morphological appearance and their stabilization in aqueous suspensions by adjusting the pH. In addition the sorption properties of the AlPO-18 nanocrystals in comparison to micron-sized crystals obtained from conventional heating of gel precursors have been investigated.

4.2 Experimental

4.2.1 Synthesis of AlPO-18 nanosized crystals

Clear precursor solutions for the synthesis of nanosized AlPO-18 crystals were prepared with the following molar composition: $1\,Al_2O_3$: $3.16\,P_2O_5$: $3.16\,(TEA)_2O$: $186\,H_2O$. Aluminium-sec.-butoxide (5.0 g, 20 mmol, Aldrich), tetraethylammonium hydroxide (26.7 g, 63 mmol, 35 wt.%, Aldrich) and water (13.4 g, 741 mmol) were mixed under vigorous stirring for 20 min and then the phosphoric acid (7.3 g, 63 mmol, 85 wt.%, Aldrich) was added in a drop-wise fashion in order to avoid the formation of dense gels. The resulting solution was stirred for an additional hour at ambient temperature. Prior to heating, the solution was filtered with a 450 nm PTFE filter to remove bigger amorphous particles and ensure a monomodal particle size distribution in the amorphous precursor solution. For the hydrothermal (HT) treatment, 20 g of the precursor solution were filled in a 100 ml teflon lined microwave autoclave, and then heated at 130 °C in a QWave 3000 microwave oven (Questron Technologies

Corp.). Crystallization times were varied from 5 to 60 min in 5 min steps. After the synthesis, the suspensions containing nanosized crystals were purified in a series of three steps consisting of high-speed centrifugation (19 000 rpm, 20 min), removal of the supernatent and re-dispersion in water using an ultrasonic (US) bath. For the investigation of the stability of the colloidal suspensions, pre-defined amounts of diluted hydrochloric acid and sodium hydroxide were added to the purified samples and checked with a pH-meter prior to the measurements. A part of the samples was freeze-dried and then calcined in air at 550 °C for 6 h with a heating rate of 15 °C min $^{-1}$ for further characterization.

4.2.2   Synthesis of AlPO-18 micron-sized crystals

The synthesis of micron-sized AlPO-18 crystals was performed following the method of Wendelbo et al.[194] The molar composition of the gel system was: 1 Al_2O_3 : 1 P_2O_5 : 0.9 $(TEA)_2O$: 60 H_2O. Aluminium-iso-propoxide (13.3 g, 65 mmol, Aldrich), phosphoric acid (7.5 g, 65 mmol, 85 wt.%, Aldrich) and water (18.2 g, 1 mol) were mixed and shaken vigorously for 1 min and then tetraethylammonium hydroxide (24.5 g, 58 mmol, 35 wt.%, Aldrich) was added. The mixture was shaken additional 5 min to produce a uniform gel. For the HT treatment, 60 g of the precursor gel were loaded into 100 ml teflon-lined stainless steel autoclaves, aged at ambient temperature for 6 h and heated in a conventional oven at 215 °C for 69 h. The solid product was freeze-dried and calcined according to the procedure described above for the nanosized aluminophosphates.

4.3   Characterization

The crystallinity of the AlPO-18 crystals was examined by X-ray diffractometry (XRD) using a Stoe StadiP diffractometer (transmission mode, CuKα radiation). To confirm the phase purity, the powder patterns were compared with literature data.[104] Dynamic light scattering (DLS) and zeta potential investigations of AlPO-18 suspensions were performed with a Malvern Zetasizer Nano-ZS. The morphologies of the nano- and microcrystalline powders were examined using a transmission (TEM, JEOL JEM 2011) and a scanning electron microscope (SEM, JEOL JSM-6500F). Thermogravimetric (TG) investigations were performed with a Netzsch STA 440 C Jupiter thermobalance. Prior to the TG measurements, all samples were stored in a descicator over saturated ammoniumchloride solution for 2 days. For all measurements, samples (10 mg) were heated in a stream of synthetic air (50 ml min^{-1}) with a heating rate of 10 K min^{-1} in an alumina crucible. The sorption isotherms for N_2 and H_2O were collected on a Quantachrome Autosorb-1 MP instrument equipped with a vapor sorption facility. The bath temperatures were kept at 77 K and 293 K for nitrogen and water sorption, respectively.

4.4   Results and discussion

4.4.1   Nano- and micron-sized AlPO-18

In conventional ovens AlPO-18 crystals are usually synthesized at temperatures over 150 °C.[104] In the present study the syntheses were performed in a microwave oven at 130 °C in order to ensure controlled nucleation in a

precursor solution with minimal temperature gradients. The crystallization time was varied from 5 to 60 min in 5 min steps (see Experimental section). Up to 25 min heating no crystallites could be recovered from the mother liquor. After that period, crystallization of AlPO-18 propagated very fast. AlPO-18 nanocrystals with an average particle diameter of 265 nm were recovered from solutions heated for 30 min. The size of the suspended particles was determined by DLS (Figure 4-1) and confirmed with TEM (Figure 4-2).
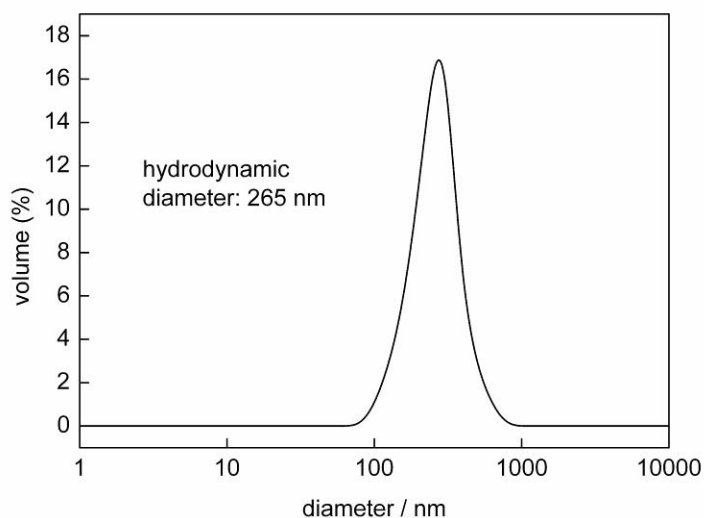
Figure 4-1. Volume-weighted dynamic light scattering (DLS) data of purified AlPO-18 nanocrystals in aqueous suspension.

Further increase of the synthesis time up to 60 min did neither change the mean size of the particles nor the total crystalline yield (~45 %). A similar observation was already reported for HT treatment of AEI type molecular sieve in conventional ovens.[136] According to X-ray analysis, the product obtained after 30 min MW treatment is crystalline and exhibits the typical AEI-type XRD

pattern (Figure 4-3). Neither other crystalline phases nor amorphous material were detected at this stage of crystallization in the clear precursor solutions.
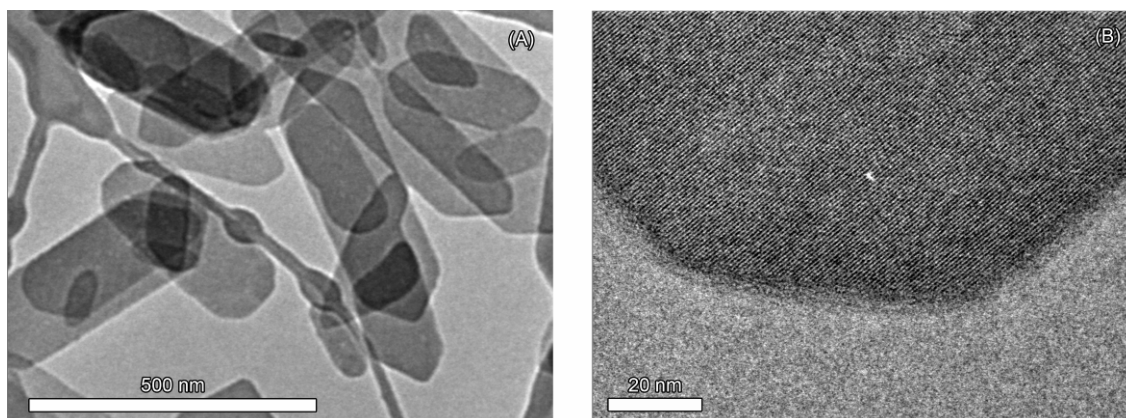
Figure 4-2. Transmission electron micrographs of nanosized AlPO-18 crystals: (A) Scale bar = 500 nm and (B) scale bar = 20 nm.

For comparison, AlPO-18 crystals were synthesized by heating of precursor gel systems in a conventional oven at 215 °C (see Experimental section). Heating of the precursor gel at lower temperatures, for instance 130 °C, did not lead to the formation of crystalline material. Therefore the recipe provided in reference[194] was followed literally. The XRD pattern of AlPO-18 micron-sized samples is identical with that of the nanosized products (Figure 4-3).
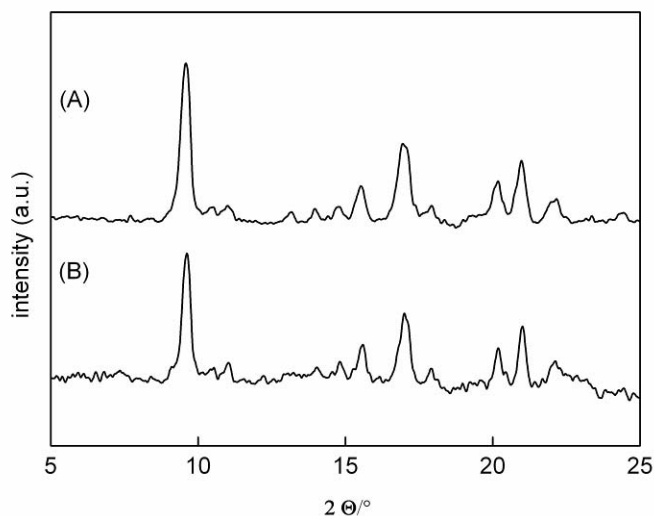
Figure 4-3. Powder diffraction patterns of (A) nanosized and (B) micronsized AlPO-18 molecular sieves.

4.4.2   Size and morphology

The morphological features of the nanosized AlPO-18 differ substantially from those of the micron-sized crystals. The nanocrystals generally appear as well-shaped single crystals with narrow particle size distributions (Figure 4-1 and Figure 4-4), whereas crystals from gel precursors vary in size over a broad range, i.e., 0.3 – 3 µm (Figure 4-4). The size distributions of nanosized aluminophosphates are typically not as narrow as for zeolitic nanoparticles.[187, 188] The TEM images (Figure 4-2) reveal that the AlPO-18 nanoparticles are growing as thin elongated hexagons with average sizes of 265 x 85 nm and well-developed faces. Crystal fringes observed in the TEM images confirm the crystalline structure of the aluminophosphate particles, and demonstrate the formation of single crystals since no penetration and misalignment between different fringes is visible. The morphology of micron-sized crystals obtained

from conventional aluminophosphate gels is typically not that well-defined. Square-shaped plate-like crystals were observed predominantly in the samples, in combination with smaller particles forming aggregates (Figure 4-4b).
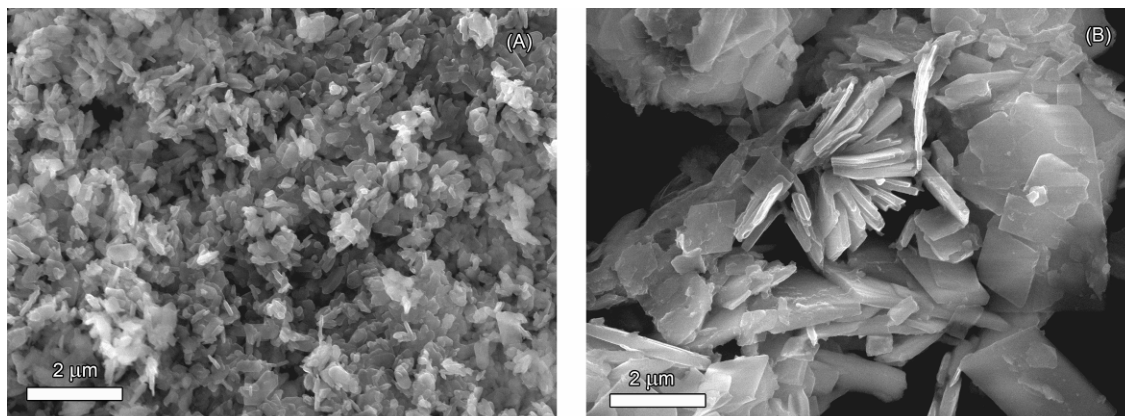
Figure 4-4. Scanning electron micrographs of (A) nanosized and (B) micronsized AlPO-18 crystals.

4.4.3 AlPO-18 nanocrystals stabilized in water suspensions

The stability of nanosized particles with respect to aggregation depends on the balance between attractive London-Van der Waals and repulsive electrostatic forces.[195] The electrostatic repulsion depends on the ionic strength and on the surface potential (Nernst potential), which can be altered by adjusting the pH value of the suspension. While the Nernst potential is experimentally not accessible, the electrokinetic potential at the shear plane, the zeta (ζ) potential, can be monitored. Dispersions are typically regarded to be stable when the zeta potential is higher than ca. |30 mV|, whereas particles tend to form aggregates near the isoelectric point (IEP), which is defined as the pH at which the zeta potential is zero. Therefore, the zeta potential measurements in suspensions containing nanosized AlPO-18 crystals were investigated at controlled pH

values (Figure 4-5). The S-shaped curve for AIPO-18 nanocrystals in aqueous suspension demonstrates that effective stabilization by adjustment of the pH with diluted hydrochloric acid to pH < 4 can be achieved. Typically, the suspensions of aluminophosphate nanocrystals show pH ~ 5 after purification. The stabilized AIPO-18 suspensions showed no sedimentation for at least two weeks, which allows further applications and the formation of 3D and 2D constructs.

Clear colloidal solutions showing a Tyndall-effect could not be obtained as the particles are too large. The micron-sized crystals could not be stabilized electrostatically and were not studied in that manner.
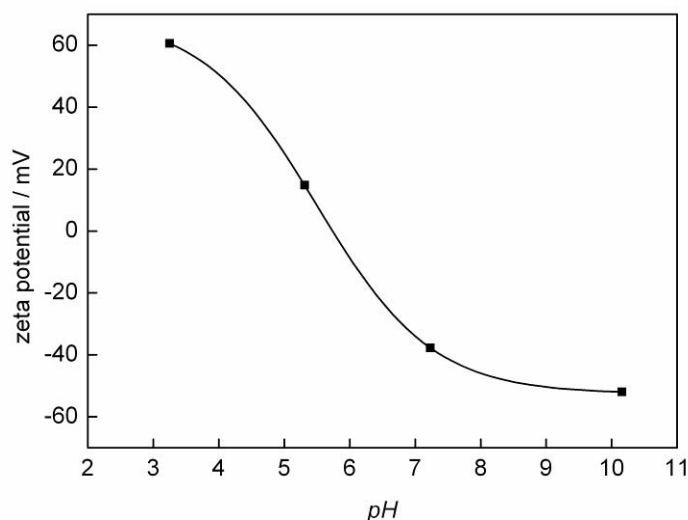
Figure 4-5. Effect of pH on the zeta potential of purified non-calcined AIPO-18 nanocrystals in water suspensions.

4.4.4 Sorption properties

For an estimation of the AlPO-18 nanocrystal capacity towards water, all samples were stored in high humidity atmosphere (see Experimental section) and subsequently subjected to TG analysis (Figure 4-6). For comparison, the micron-sized AlPO-18 crystals and also commercial samples of zeolite X and Y were investigated. The high water capacity of the latter molecular sieves is well known, and therefore they have been chosen as references in the current study. The TG curves for the AlPO-18 samples show a steeper loss of water at 100 °C, in comparison with zeolites X and Y. Moreover, the H_2O was desorbed more slowly and up to 250 °C in the reference samples. The nature of the water-framework-interaction is different due to the more polar, but neutral AlPO framework, the very small pore diameters, and the possibility of forming five- and six-coordinated Al^{3+} atoms. Moreover, AlPO-18 shows greater weight-losses: Nanosized AlPO-18 crystals loose up to 26 wt.%, which is 5 wt.% more than micron-sized AlPO-18 crystals.
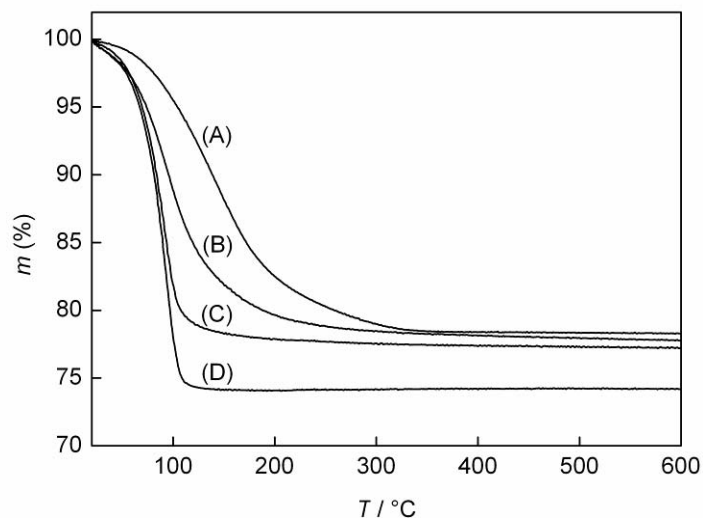
Figure 4-6. Thermogravimetric analyses of (A) commercial zeolite X (UOP, USA), (B) zeolite Y (Grace, USA), (C) micron-sized AlPO-18 and (D) nanosized AlPO-18 stored under high humidity atmosphere for 48 h prior to measurements.

In addition to the TG analysis, nitrogen and water sorption experiments on the

same samples were performed (Figure 4-7 and Figure 4-8).
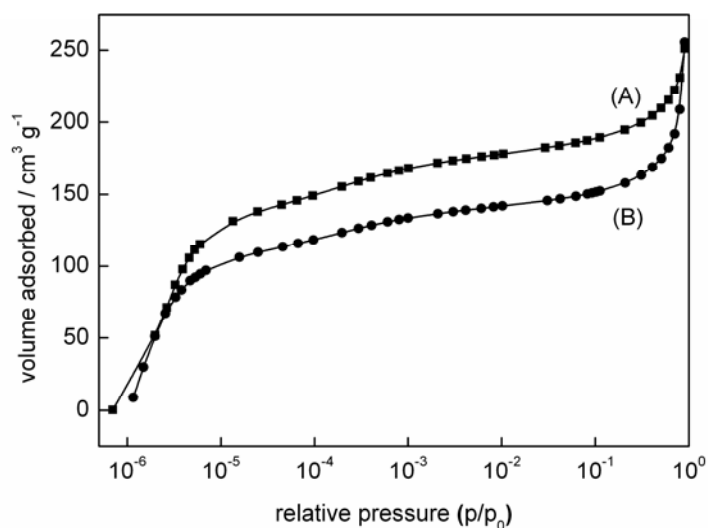
Figure 4-7. Nitrogen adsorption isotherms of (A) nanosized and (B) micronsized AlPO-18 molecular sieve.

Nitrogen sorption isotherms typical for microporous molecular sieves were obtained for both types of AlPO-18 crystals. Nanosized AlPO-18 crystals possess a higher accessible pore volume compared to micron-sized crystals (t-plot: $\Delta V = 35$ cm^3 STM g^{-1}). This observation is attributed to the more perfect crystal morphology of the nanocrystals in comparison with the micron-sized AlPO-18. In the latter case, fault planes, intergrowth, and amorphous deposits can contribute to the lower accessible pore volume. The difference in pore volume is even more pronounced when water is used as the probe molecule (Figure 4-8). The water sorption curves showed typical characteristics of small pore microporous hydrophilic molecular sieves. The desorption of water at 20 °C is kinetically inhibited, leading to non-equilibrated sorption measurement for both nano- and micron-sized powders. An increase of equilibrium temperature is not possible in the used setup.
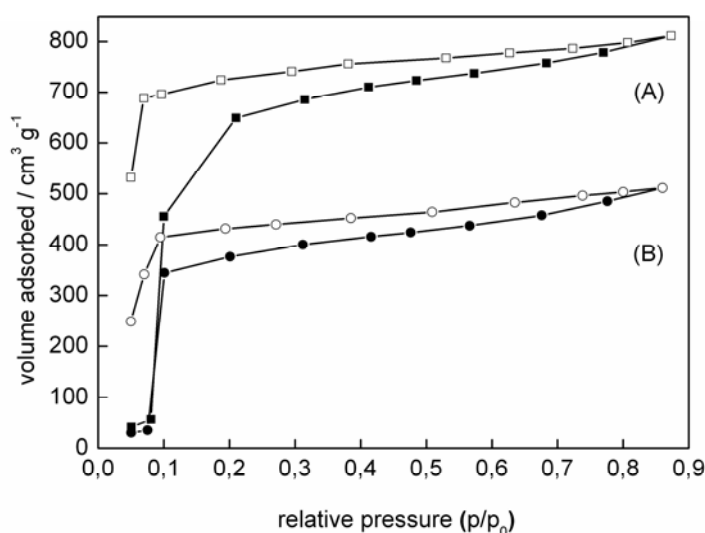
Figure 4-8. Water sorption curves of (A) nanosized and (B) micron-sized AlPO-18 molecular sieve (full symbols: adsorption, open symbols: desorption).

4.5   Conclusion

The work presented in this chapter reports on a fast and efficient route for the synthesis of AlPO-18 nanocrystals by utilization of microwave energy. At 130 °C the crystallization process was completed in 30 min and a further increase of the synthesis time up to 60 min did not alter size, morphology and yield of the final crystalline product. The plate-like nanosized particles had an average size of 265 x 85 nm. After purification, suspensions containing AlPO-18 nanocrystals could be stabilized for several weeks by adjusting the pH of the suspensions to pH < 4. A stabilization above pH = 7 is difficult due to aggregation and sedimentation of the nanoparticles near the isoelectric point. The accessible pore volume in nanosized AlPO-18 crystals is larger compared to conventional micron-sized crystals. Therefore they can adsorb larger amounts of nitrogen and especially water, which confirms the high water capacity of nanosized AlPO-18 hydrophilic material.

5 Kinetics of water adsorption in thick aluminophosphate layers

5.1 Introduction

Adsorption heat pumps utilizing waste heat or solar energy can be based on various solid-vapor working pairs. The three combinations that have received the most attention during the last decade are zeolite/water, activated carbon/ammonia and silica gel/methanol. A comprehensive review of the various concepts for regenerative adsorption systems was given by Lambert et al.[196] Solid/vapor adsorptive systems are very promising for heat transformation applications as they can utilize efficiently solar energy or waste heat as driving force and they can render the burning of fossil fuels for heating much more effective compared to modern condensing boiler heating systems.[197] Therefore, a significant amount of environmental pollution could be avoided. Additionally, non-polluting working media (e.g. water) can be used and the machines are nearly noiseless, as they contain no moving parts (except valves). The core of the machine is the adsorber unit, which is composed of the adsorbent and a heat exchanger. To work efficiently, the heat released during adsorption must be quickly transported to the exchanger to ensure minimum cycle times. If the released heat leads to increased temperatures of the adsorbent, its capacity is decreased.[198] Therefore, the design of the adsorber unit is of crucial importance to guarantee fast mass and heat transport. Three different concepts can be distinguished:

- fine powders distributed in exchangers with large metal surface areas

- consolidated powders

- compact layers prepared on the heat exchanger walls

The first method has a major drawback, as extra material is included in the design, and that leads to an extra thermal capacity. Consolidated grains contribute to good vapor transport, but the heat transport is limited due to the point contacts between the individual grains and the heat exchanger wall. The thermal conductivity of the grains themselves can be enhanced by the addition of conductive components. Coating methods improve the heat transfer between the adsorbent and the metal support to a great extent. However, the resistivity within the layer is comparable to consolidated grains and the mass transport is dependent on the structure of the layer. Another problem is the mechanical stability of the coatings, and cracking is observed very frequently.

Two concepts used for the preparation of thick layers on metal supports are:

- the metal support is directly immersed in a synthesis solution thus leading to direct growth[199-202]

- the material is synthesized in a separate step prior to coating[203]

In the latter case the use of additional compounds, e.g., a binder component is necessary in order to enhance adhesion between the particles and the support. However, coating methods offer advantages over growth methods. The adsorbent can be calcined prior to coating to remove the pore-forming organic

template. Calcination of grown layers at temperature around 500 – 600 °C can again lead to cracking, as the support and the adsorbent layer generally possess different thermal expansion coefficients. Additionally, grown layers are limited in thickness as the material-specific synthesis solution only contains a limited amount of nutrients. Futhermore, coating techniques can be easily transferred to larger scale industrial processes, as various methods are known from other surface treatment industries, e.g., spray- or dip-coating.

Various adsorbent materials can be used in heat exchanger applications. Most commonly, molecular sieves, in particularly zeolites such as zeolite A (LTA),[199, 201, 202, 204, 205] Y (FAU)[206] or ZSM-5 (MFI)[200] are employed. These materials are commercially available and their sorption characteristics can be tuned by controlling the Si/Al – ratio and by post-synthesis ion exchange However, (silico)aluminophosphates, e.g., SAPO-34 or AlPO-18, show superior sorption behavior, which is depending on their composition and morphology. They have improved effective water vapor capacities as the temperature/pressure difference needed for adsorption/desorption is lower.[139, 141, 142] Other promising materials include supported salt hydrates[207-212] and metal-organic frameworks. In addition to the improved sorption properties, the stability of the used material under process conditions is of importance. The BMBF project mentioned in the Introduction chapter was focused on closed adsorber units working with water as refrigerant. In order to enhance the COP (coefficient of performance) as well as the power density of state-of-the-art systems both thermodynamic and kinetic parameters of the materials have been investigated. One of the most

promising adsorbent materials in terms of equilibrium data was found to be the microporous aluminophosphate AlPO-18 (AEI structure type code).[139] Under relatively mild conditions, e.g., adsorption at 35 °C (1.23 kPa) and desorption at 90 °C (5.67 kPa), it shows useful loadings of up to 28 wt.% depending on the synthesis procedure.[213] Besides equilibrium data kinetics play a crucial role for the overall performance of the adsorber unit. As discussed above, there can be various limiting factors to achievable cycle times. Therefore, we aimed at the preparation of compact layers of various molecular sieves which should reduce limitations due to heat transport to a great extent. Experimental and theoretical investigations concerning kinetics of adsorptive materials for energy applications have been carried out by Knoche and coworkers[203] and other authors. They investigated compact layers of zeolite A and achieved improved mass transfer by addition of melamine as a pore-forming agent. Erdem-Senatalar, Tatlier and coworkers developed an improved method for direct synthesis of zeolite A and ZSM-5 on metal surfaces[199, 200, 202, 214] and also investigated the diffusivities in layers having different thicknesses.[201, 204, 205] Aristov and coworkers worked on the kinetics of water adsorption on impregnated silica gel pellets.[207-209, 211, 215] Major efforts have been extended on modeling various kinetic effects, mainly in adsorber beds of pelletized zeolites. Among others, the groups of Ruthven,[216-218] Kast[219-222] and Mersmann[223, 224] have simulated the effects of mass and heat resistances as well as non-isothermal adsorption processes. Models for layered geometries

were presented by Knoche and coworkers,[203] Tatlier et al.[225] and Dawoud et al.[198, 215].

Kinetic measurements with different adsorptive composite samples were performed at the Fraunhofer Institute for Solar Energy Systems. Composite samples are combinations of adsorbent and metal layer, joined together by different technologies. The experimental characterization of composite samples therefore gave information not only about the heat and mass transfer characteristics of the adsorbent layer, but also about the heat transfer resistance between adsorbent layer and metal layer. Thus, a realistic evaluation for heat exchanger applications becomes possible. A one-dimensional model has been developed in order to describe properly the behavior of the used experimental setup.[226]

This chapter reports on the experimental data concerning sorption kinetics of water vapor in microporous aluminophosphate (AlPO-18) material deposited in the form of thick layers on aluminum supports.

5.2   Theoretical comments

The overall process of water vapor adsorption in thick layers of microporous adsorbents can be divided into several non-independent processes. For the described applications adsorption is initiated by pressure gradients between a vapor source and a desorbed, empty adsorber unit. The final pressure of the adsorption is defined by the evaporation pressure and the adsorber temperature, which define the final loading. The initial loading of the sample at a

given temperature defines the initial pressure of the adsorbent layer and, in combination with the vapor pressure, the maximal pressure difference. Starting the adsorption by connecting evaporator and adsorber, the vapor instantaneously flows to the layer surface. Then the vapor needs to be transported to the adsorption sites within the microporous crystals. Generally, the composite matrix of microporous crystals, polymeric binder and void volume is considered to represent an idealized macroporous system. This is a critical simplification as the investigated systems are generally not ordered. However, a more or less monomodal distribution of pore diameters with upper limits in the range of the crystal dimensions is assumed. In this model the walls of the system consist of the microporous AlPO-18 crystals. After vapor transport to the pores, diffusion within the channels of the AlPO-18 takes place. Finally, the adsorption process leads to the release of the corresponding heat of adsorption. In the ideal isothermal case this heat is quickly dissipated to the boundary of the individual crystal, then to the adjacent particle and finally to the heat exchanger wall, i.e. the metal support. For a mathematical description the whole system is normally seen as a network of capacities and resistances. Additionally, one needs to describe the type of diffusion processes at different stages. In the following, the contributing processes are qualitatively described.

5.2.1 Macropore diffusion

The structure of an amorphous network of macropore channels generated during the coating process is difficult to investigate. Sometimes mercury intrusion is used, but standard data interpretation normally assumes bundles of

straight capillaries, which is a rather strong simplification. Additionally, SEM data can serve for a rough estimation of pore diameter and porous structure. Most often the diameter of the pores lies in the macroporous range (> 50 nm) and does not exceed the diameter of the crystals. At 17 mbar the free path length Λ for water is 7.6 µm resulting in a Knudsen number (Eq. 5-1):

$$Kn = \Lambda/d_{map} \approx 7.6 - 76 \tag{5-1}$$

Kn Knudsen number

Λ free path length

d_{map} macropore diameter

for pores with diameters of 0.1 – 1 µm. If Kn > 10, the determining mechanism of mass transfer is Knudsen diffusion.[227] Hence, for the investigated samples, free diffusion (described by Fick's law) should only play a minor role (only for the largest macropores at the highest total pressures). The mass flow is then given by (Eq. 5-2):[203, 227]

$$dm/dt = -A_{map} \cdot D_{Kn}/\mu_{map} \cdot dp/ds \tag{5-2}$$

with Eqs. 5-3 and 5-4:

$$A_{map} = A \cdot \Psi_{map} \tag{5-3}$$

$$D_{Kn} = 4/3 \cdot d_{map} \cdot \sqrt{(M_g/2\pi RT)} \tag{5-4}$$

dm/dt mass flow

A_{map} macropore cross sectional area

D_{Kn} Knudsen diffusion coefficient

μ_{map} tortuosity factor

dp/ds pressure gradient

A sample surface area

Ψ_{map} macropore porosity

M_g molecular weight

R gas constant

T temperature

The mass flow is proportional to the pressure gradient, the cross-sectional area (constant for the investigated samples), the macropore diameter and the structure of the macropore system described by the tortuosity factor (μ_{map}). The pressure gradient generally is a function of position, temperature, loading and absolute pressure, which are dependent on the thermodynamic equilibrium.

5.2.2 Micropore diffusion

The diffusion coefficient for intracrystalline diffusion of water (molecule diameter: ~2.75 Å) in CHA type zeolites (AlPO-18: same pore size) is in the order of $10^{-8} - 10^{-7}$ m^2 s^{-1},[175, 228] whereas diffusion coefficients for macropore diffusion in pores with diameter of $10^{-7} - 10^{-6}$ m range between 10^{-4} m^{2}s^{-1} and 10^{-3} m^{2}s^{-1}.[220] However, distances to be covered in micropores are far shorter than those in macropores. The ratio of diffusion times g can serve as an estimation for the relevance of micropore diffusion:

$$g = t_{map}/t_{mip} = (D_{mip}/D_{Kn})\cdot(S^2/s^2) \tag{5-5}$$

t_{map} macropore diffusion time

t_{mip} micropore diffusion time

D_{mip} micropore diffusion coefficient

S macropore length

s micropore length

A value $g > 1$ indicates fast micropore diffusion and limitation by macropore diffusion. Equation 5-5 does not take the tortuosity of the macropores into consideration. If one uses the lowest realistic micropore diffusion coefficient (10^{-8} m^2 s^{-1}), the highest macropore diffusion coefficient (10^{-3} m^2 s^{-1}) and a maximum micropore length of 1 µm (the maximum crystal size in the investigated samples), micropore diffusion can be a limiting mechanism for thin layers below 300 µm. Tatlier et al. have shown that macropore diffusion dominates mass transport for grown coatings of zeolite 4A above a thickness of ~100 µm.[201]

From molecular dynamics simulations it is known that the effect of loading on the effective diffusion coefficient for small molecules in chabazite-related structures is low.[175] Additionally, the effect of absolute pressure on thermodynamics and kinetics of the adsorption process of an individual water molecule is negligible above the saturation limit for AlPO-18. This limit is ~0.1 p/p_0 (~7.4 mbar at 40 °C). This can be deduced from measurements on AlPO-18 powders (see Results and Discussion section).

5.2.3 Non-isothermal effects

If the thermal conductivity between a single microporous crystal and the external heat sink (e.g. the metal support) is poor, non-isothermal effects will be observed, i.e. the crystals heat up during adsorption.[216-218] Higher temperatures lead to lower values of equilibrium loading which results in slower overall kinetics. For many detailed investigations this effect plays a dominant role, especially in packed bed geometries and in compact zeolite layers of relatively high masses and at high pressure. However, for thin layers it is sometimes negligible and the layers become exclusively diffusion limited.[204] Generally, the thermal conductivity of a microporous (zeolite) layer decreases with increasing thickness and void volume. Additionally, the contact area between the microporous crystals, which is dependent on size and morphology of the particles, and the three-dimensional structure of the whole matrix affect the conductivity to a great extent. The non-isothermal effect is often underestimated and can have drastic consequences, e.g., preferential loading of the layer starting at those regions close to the metal surface as was shown by simulation analysis.[203]

5.3 Experimental

5.3.1 Aluminophosphate AlPO-18 synthesis

Nanosized AlPO-18 crystals were prepared from clear precursor solutions by the use of microwave energy. For the synthesis of micron-sized materials

conventional gel syntheses were employed. All powders were calcined in air at 550 °C for 15 h. The two synthesis procedures are described in Chapter 4.

5.3.2 Layer preparation

The calcined AlPO-18 powders were suspended in doubly distilled water; polyvinyl alcohol (PVOH, MW 85000 – 124000, 6 wt.% aqueous solution, Aldrich) was added as binder to the AlPO-18 mixture. The final mixtures were stirred overnight to give homogeneous suspensions with a final composition of 16 wt.% AlPO-18 and 1.6 wt.% PVOH. The 50 x 50 x 0.5 mm aluminum plates (AlMg3 alloy, Al > 94 wt.%) were pre-etched in 2N sodium hydroxide solution for 2 min and rinsed with water. Increasing amounts of the coating suspensions were deposited manually with a pipette on the aluminum plates for the two different AlPO-18 materials. Drying was performed at ambient temperature for 1 to 5 h.

5.4 Characterization

5.4.1 Aluminophosphate powders and layers

Characterization of the AlPO-18 powders was presented in Chapter 4.

The dry layer mass of AlPO-18 layers was determined after heating the samples to 120 °C for 1 h. The average thickness of the layers was calculated based on micrometer screw measurements carried out at four different spots. Additionally, the sample surfaces were investigated by scanning electron microscopy using a JEOL JSM-6500F instrument.

5.4.2 Setup for adsorption kinetic measurements

All AlPO-18 layers were investigated in a standardized procedure in a specially designed measuring setup described below (Figure 5-1 and Figure 5-2).
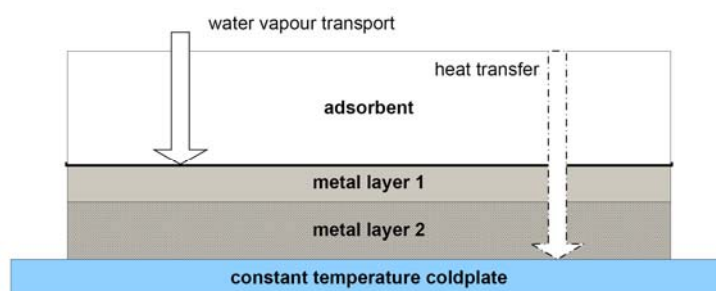
Figure 5-1. Measuring geometry for the kinetic adsorption measurements on AlPO-18 layers.

For the kinetic measurements, AlPO-18 layers on aluminum plates (0.5 mm) were coupled with a special double adhesive tape (3M) to a standardized sample holder, which guarantees a planar surface and a well-defined thermal connection to a cold plate (see Figure 5-1). The thermal connection is ensured with heat-conductive paste. Between the sample holder and cold plate a heat flux sensor is situated (not shown). Figure 5-2 shows the experimental setup used for the kinetic measurements with water.
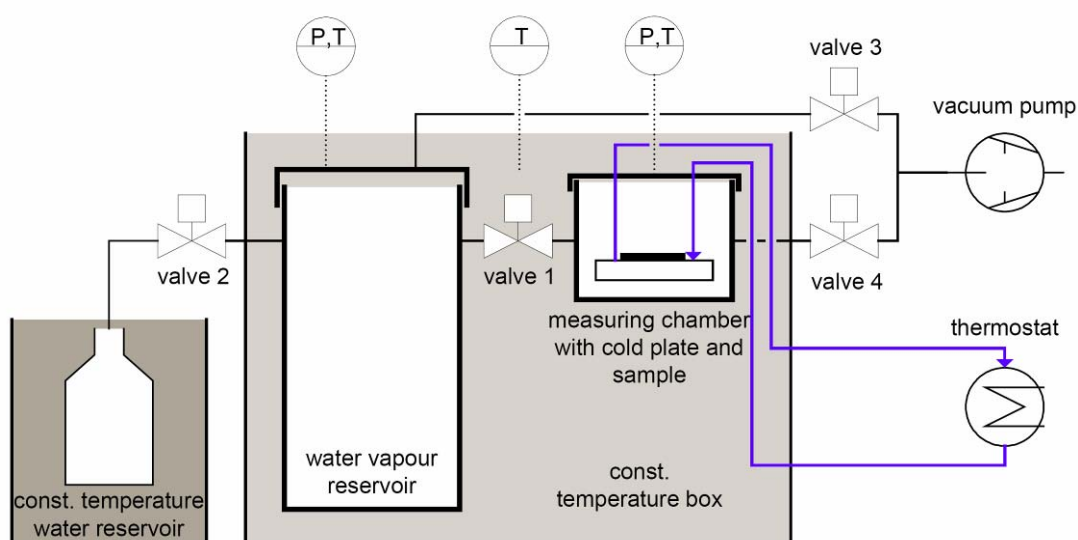
Figure 5-2. Scheme of the kinetic measurement setup.

A measuring chamber working at constant temperature contains the AlPO-18 layers and is connected to a water vapor reservoir. The latter is fed from the water vapor source that is heated to a defined temperature leading to a defined equilibrium pressure. Upon closing this connection (valve 2), the total mass of water vapor in the reservoir can be estimated by the ideal gas law. Prior to measurements, the measuring cell with the sample is heated to 95 °C and connected to a vacuum pump for performing the desorption process. When pressure, temperature and heat flux signal are constant the cold plate is cooled to 40 °C. Parallel to the desorption procedure, the water source is kept at 9 or 15 °C (open valve 2), which corresponds to a vapor pressure of 11.5 or 17 mbar, respectively. Subsequently two different measuring modes, canonical or isobaric, can be performed (in this study, only canonical measurements were made). For the canonical measurements, valve 2 is closed, thus leading to a constant number of gas molecules in the system. After opening the valve

between the measuring chamber and the reservoir (valve 1), the sample instantaneously starts to adsorb, and consequently a decrease in pressure is measured. Since the total volume is known and both vapor pressure and temperature are recorded, the decrease in pressure can be used to calculate the increasing water loading of the adsorber matrix. Besides pressure and temperature, the heat flux between sample and cold plate is measured, and this provides an independent signal to determine the adsorption rate. Data logging runs until the pressure and the heat flux signals become constant. In a subsequent data processing step the amount of water loading is calculated from the measured values of pressures and temperatures and the known volume of the whole device.

5.5   Results and discussion

5.5.1   AlPO-18 powders and layers

The two types of AlPO-18 powders differ substantially in their morphological features.[139] The nanosized powders posses elongated hexagonal plate-like morphology. The monomodal particle size distribution shows an average particle diameter of 250 nm corresponding to the long axis of the non-spherical particles. The powders obtained from gel syntheses show less defined morphologies, most often of cubic plate-like form. The particle sizes vary from ~0.3 µm to 3 µm. The micron-sized crystals show decreased micropore volumes attributed to a less perfect crystal morphology (see Chapter 4).

The layer thicknesses and the corresponding densities of the investigated samples are summarized in Table 5-1. Layers containing nanosized crystals ("type N") are denoted as N1 – N4, whereas those containing micron-sized crystals ("type M") are denoted as M1 – M4. Due to the manual coating process the layers show relatively high degrees of surface roughness of up to 10 %. However, all layers were homogenous over the whole sample area. The two thinnest "type M" layers show increased densities (see Table 5-1). This is attributed to the mechanism of drying under the applied conditions. The coating suspensions "type M" show decreased stabilities with regard to sedimentation. This can lead to an increasing degree of segregation of larger particles from lighter components that deposit on top of the film, i.e. smaller particles and dissolved binder. The effect is expected to be more pronounced when longer drying times are used, i.e. in the case of thicker samples. As a homogeneous particle size distribution leads to a more loose packing of crystals, a higher degree of separation is expected to have the same effect.

Table 5-1. Characteristics of the investigated AlPO-18 layers (per 25 cm^2).

Sample name	Dry layer weight /mg	Effective AlPO-18 mass /mg	Layer thickness /mm	Layer density /mg mm^{-3}	90 % loading /min	90 % heat transfer /min
M1	110	99	0.08	0.55	0.45	1.05
M2	150	135	0.10	0.60	0.65	1.20
M3	350	315	0.44	0.32	3.30	3.50
M4	530	477	0.62	0.34	9.00	9.05
N1	160	144	0.18	0.36	0.65	1.35
N2	370	333	0.44	0.34	2.90	3.15
N3	500	450	0.60	0.33	4.95	5.30
N4	640	576	0.76	0.34	7.95	8.25

SEM images of the layer surfaces are shown in Figure 5-3. Obviously, the interparticle voids or "macropores" are inhomogenenous in size, shape and structure. This fact is not adequately described in the known mathematical models (see the above section). The macropore diameter estimated from the SEM images is 0.1 – 1 µm for both "type N" and "type M" layers. However, "type N" layers tend to form aggregates of nanocrystals during the drying process resulting in relatively large voids between them. "Type M" layers do not show aggregation to the same extent but a rather homogeneous surface. These differences are expected to have an effect on heat and mass transport within the layers.
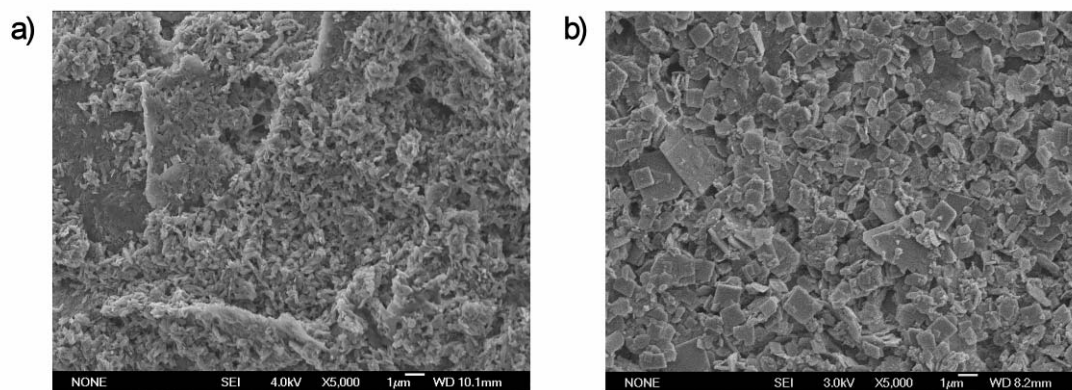
Figure 5-3. SEM images of a) "type N" and b) "type M" AlPO-18 layers (Scale bar: 1 µm).

5.5.2 Kinetic measurements

All statements in the discussion of the kinetic curves account for the varying total adsorbent masses of layers containing nano-/micron-sized AlPO-18 crystals. Layers of comparable total layer masses are plotted in the same color for clarity.

5.5.3 Progression of pressure and mass

Figure 5-4 shows the changes of the vapor pressure within the measuring chamber for the 17 mbar starting pressure.
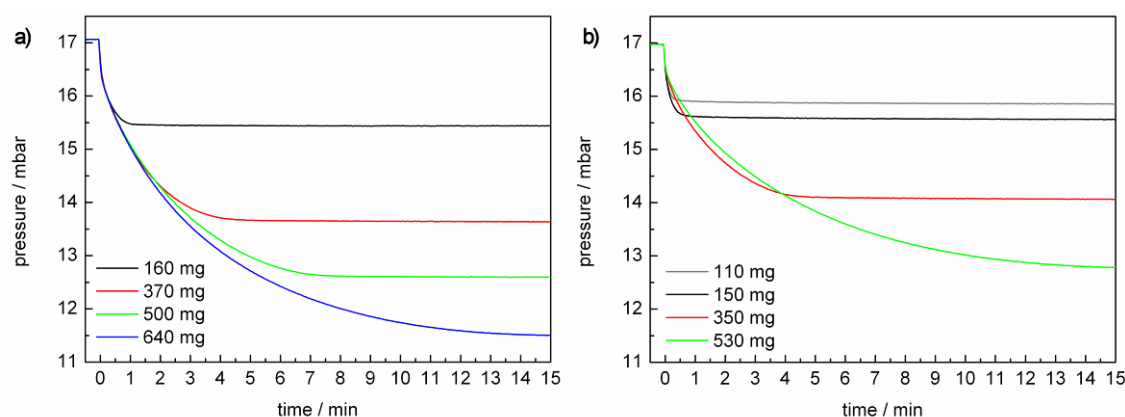
Figure 5-4. Kinetic curves of the pressure within the measuring chamber at 17 mbar starting pressure of a) "type N" and b) "type M" AlPO-18 layers.

With increasing adsorbent masses, the pressure decrease is generally higher for all samples due to the canonical measuring conditions (constant amount of vapor). The increase of the corresponding mass per surface area of the sample is plotted in Figure 5-5. The "type N" layers of comparable masses (same drawing style in the graphs) show larger pressure decreases at 17 mbar than "type M" layers, and therefore higher loadings. This is in a good agreement with the equilibrium sorption data of the corresponding powder samples.
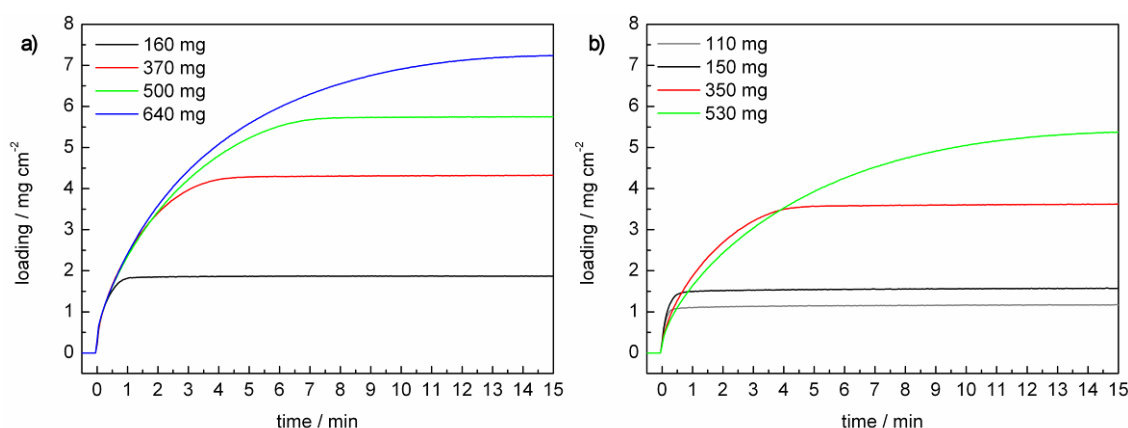
Figure 5-5. Kinetic curves of H_2O mass loading per surface area of the aluminophosphate layers. a) "type N", b) "type M".

In Figure 5-6 the water loading is normalized to the corresponding layer masses resulting in equilibrium loadings of 275 mg g^{-1} and 250 mg g^{-1} for "type N" and "type M" layers, respectively. The water capacities are exceptionally high for microporous molecular sieve materials, thus rendering AlPO-18 a highly interesting compound for heat transformation and storage applications. Additionally, the curves depicted in Figure 5-6 approach the same equilibrium value for all individual materials showing that all films approach saturation under the measuring conditions.
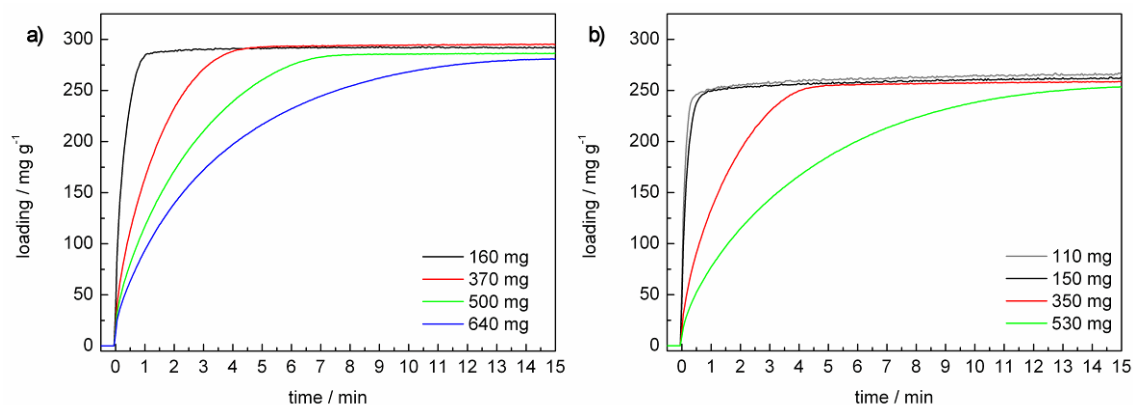
Figure 5-6. Kinetic curves of H$_2$O mass loading per mass of the aluminophosphate layers. a) "type N", b) "type M".

To evaluate the differences in kinetics between the individual samples, one has to account for the differences in adsorbent mass, as the measurements shown here were conducted under canonical conditions. Based on the pressure reached at the end of each measurement, one can calculate the corresponding points in time during the progression of the measurements, where the pressure was 90 % of the final value. These experimental points in time are summarized in Table 5-1, and explicitly shown in Figure 5-7. Based on these 90 % values

one can calculate an average mass and heat flow (although the flows change significantly during the measurement cycles – see slopes in Figure 5-6). The mass and heat flows are plotted against layer mass in Figure 5-7.
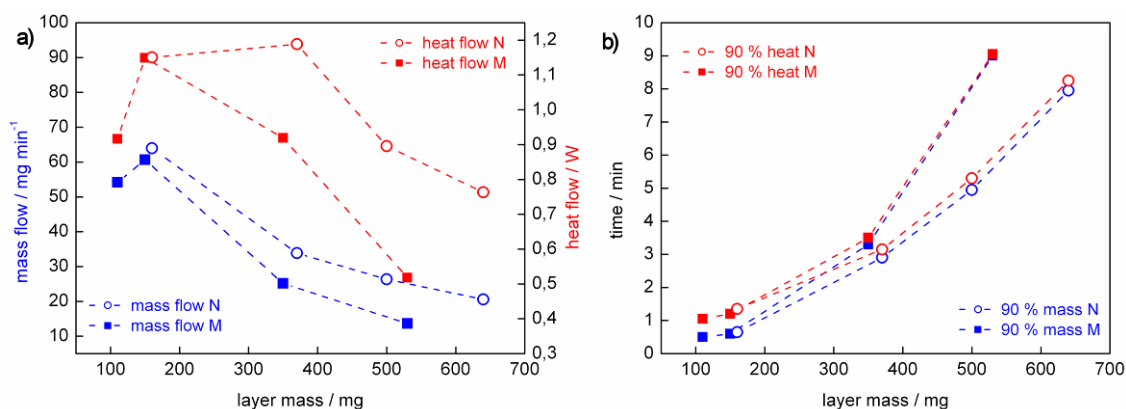
Figure 5-7. a) Average mass flow (blue) at the point in time where 90 % decrease of the final pressure is reached and the corresponding heat flow (red) b) the same 90 % times versus layer mass.

It is found that the water mass flow into the sorbent-binder-matrix decreases significantly with increasing layer thickness. The "type N" layers show higher mass flows than "type M" with comparable masses. A more detailed analysis of the initial stages of the measurements gives rise to the assumption that different layer structures are present in the two types of layers. The pressure decrease of "type N" layers proceeds along decay curves of exponential type until a certain degree of saturation is reached. Hence, the limiting mechanism (most probably heat transport) controls the process to the same degree at the same time intervals. This is in agreement with the assumption that the layers of "type N" with different thicknesses have similar heat transfer characteristics. In contrast, "type M" layers show decreased rates (corresponding to the derivative of pressure, not shown here) with increasing layer masses at the same measuring

times. As discussed in the introduction section, the heat transport is greatly dependent on the structure of the layers, i.e., the porosity, the total number and area of contacts between the single crystals, and the tortuosity of their three-dimensional structure. We attribute the differences in the macropore structure of the two type layers to a variation in the structure of the corresponding coating suspensions. It is found that "type M" suspensions show decreased stabilities on the drying time scale (typically 1 – 4 h) compared to "type N" suspensions due to the smaller crystal dimensions in the latter. As a result, this probably leads to an increased sedimentation rate of larger crystals and a separation of lighter components, e.g., polymeric binder and small crystals, to the upper regions of the layer. The described de-mixing effect is more pronounced for higher sorbent masses as the drying time is increased. Therefore thicker layers are more inhomogeneous along the layer normal axis than the thinner layers. As the "type N" coating suspensions are stable during the time of drying, the resulting layers posses a homogeneous distribution of microporous crystals and macroporous binder matrix. The above considerations strongly suggest that both AlPO-18 crystal size and morphology as well as the overall film morphology have a significant effect on the heat transfer in the films. Of these films, the "type N" samples based on nanoscale AlPO-18 show the best heat transfer, however, the precise origin of this trend is still not understood.

To examine the nature of the limiting mechanism (either Knudsen diffusion or non-isothermal effects/heat transfer limitation) for the thicker layers we performed measurements on ground powders obtained by scratching the layers

off the aluminum support. It is expected that the Knudsen diffusion should be accelerated and heat transfer retarded in these samples. The results for layer M4 are shown in Figure 5-8.
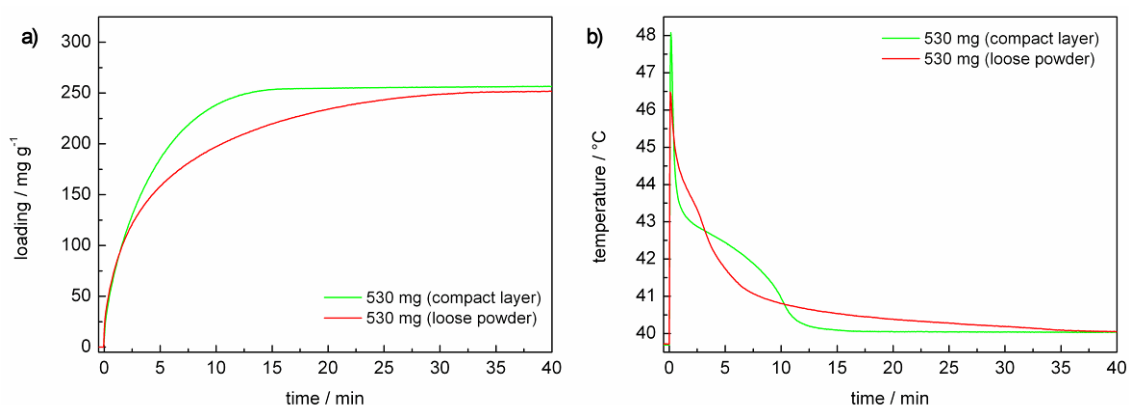
Figure 5-8. Kinetics of water adsorption on layer M4 compared to the same sample in powdered form: a) mass weighted loading curve and b) temperature dependent curve.

The powdered sample reaches the 90 % loading level within 18 min in comparison to 9 min for the corresponding AlPO-18 layer (sample M4). This indicates that non-isothermal effects play a dominant role for the powdered sample. Based on these data, it cannot be estimated how strongly they affect the corresponding compact layer. Therefore, both mass- and heat transfer effects have to be taken into consideration. Additionally, the two effects might change their significance from the start of adsorption until full saturation is reached, which can be seen from the surface temperature curves. It was demonstrated that layered systems might not get loaded continuously from the surface to the bottom due to that reason.[203] It is assumed that after reaching the temperature maximum, the limiting resistance is the heat transport. The material must release heat, and additional water is adsorbed corresponding to

the temperature-dependent equilibrium. Further, we propose that the samples showing nearly symmetrical heating and cooling curves are not controlled by heat transport (Figure 5-9). This is the case for the thin layers (N1, M1-M2). For all other samples the temperature curves featuring a plateau-like decay suggest heat transport limitation.
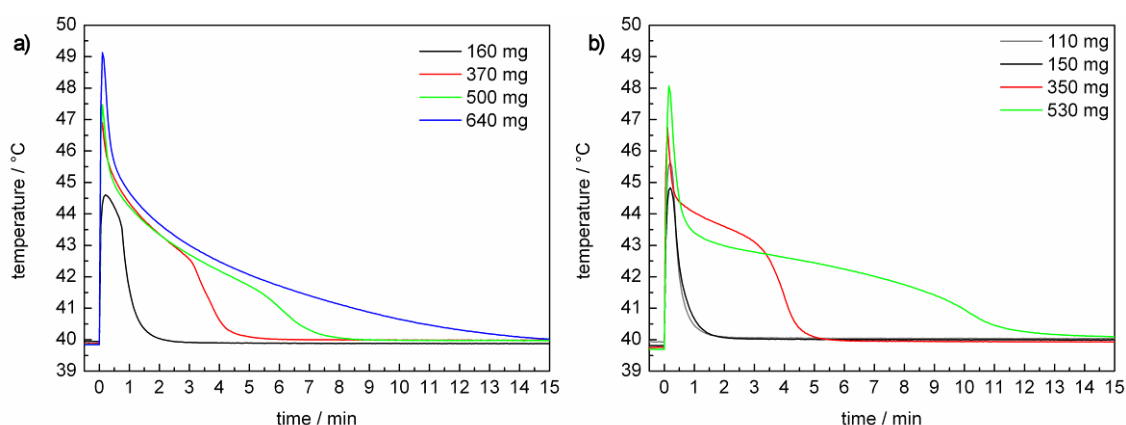
Figure 5-9. Kinetic curves of the temperature near the surface of the aluminophosphate layers: a) "type N" and b) "type M".

As the two effects might change their relative importance during the whole process, additionally the average mass flow for 20 %, 50 % and 70 % and 90 % water loading was calculated (Figure 5-10). The 20 % limit was chosen since the samples approximately reach their heat flux maximum at that time, and the heat transport limitation therefore should be low.
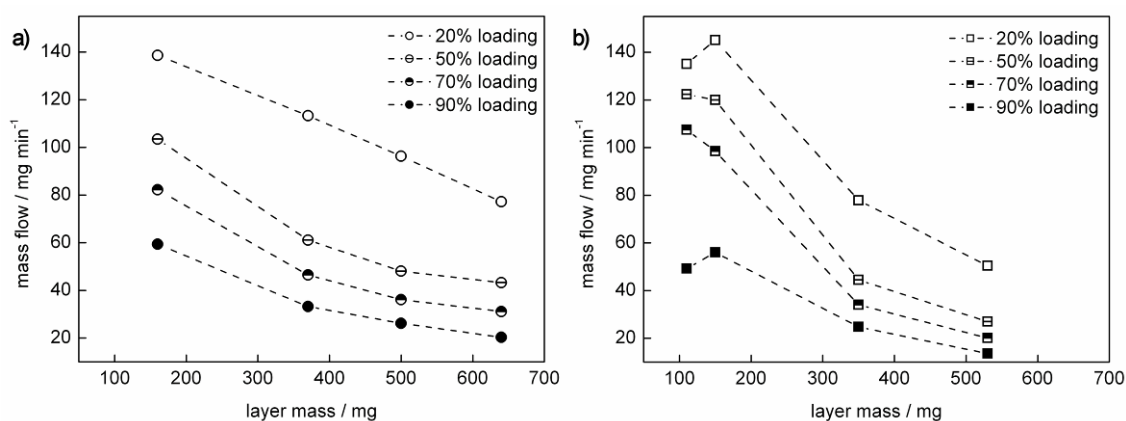
Figure 5-10. Average mass flows for a) „type N" and b) "type M" layers after 20 %, 50 %, 70 % and 90 % water loading.

With increasing the loading limit, the heat flux limitation increases and the mass flow curves are expected to change their shape. Indeed, the decrease in mass flow is nearly linear with layer mass at the 20 % level due to either mass or heat transport limitation (see below). With increasing the loading, the curves show increasing non-linear behavior as heavier layers evolve a larger total heat of adsorption, and are therefore more strongly affected by heat flow limitation.

Comparing the two AlPO-18 crystalline samples, the decrease of mass flow with increasing layer mass and loading limit is more pronounced for "type M" samples. At the 20 % limit, the relatively thin layers M1 and M2 show a higher average mass flow than the corresponding layer N1. This is in agreement with their higher density (see above) and the associated higher heat conductivity. It is suggestive that the heat transport is the limiting mechanism even at 20 % loading as a limiting mass transport should be negatively affected by a higher density. The stronger non-linear behavior of the "type M" layers compared to the

"type N" samples at higher loading levels is attributed to the different three-dimensional structures of the adsorbent matrix (see above).

5.5.4 Progression of temperature and heat flux

Figure 5-9 shows the temperature development within the measuring chamber at a short distance to the sample surface (see Experimental section). The change in the heat flow from the aluminum supports to the constant temperature cold plate is plotted in Figure 5-11. Additionally, the average heat flow at the 90 % time (integral under the heat flow curve divided by time) is shown in Figure 5-7. These curves are a result of the combined effects of mass transport to the microporous crystals, the release of the heat of adsorption and the heat transport to the cold-plate. The different heat transfer resistances during the transport process cannot be separated in the used measuring setup. It can be assumed from the literature data (see Introduction) that the dominant resistance is the transport within the layer rather than intra-crystalline- or metal-metal-transport. The thermal conductivity of the layer generally decreases with increasing layer thickness and macropore volume as discussed before. The temperature above the sample surface rises with increasing sorbent mass for both "type N" and "type M" layers. Obviously, none of the layers shows ideal isothermal behavior (which would be reflected in no temperature change upon adsorption). Relatively thin layers (N1, M1, M2) show fast mass transport. In this case heat transfer, although it is also fast, must be the limiting step for the overall performance. This becomes obvious from the 90 % thresholds for mass and heat transfer dependencies shown in Figure 5-7. For these layers, 90 %

heat transfer is reached within 0.5 min after 90 % mass transfer. As complete loading is established quickly, the heat of adsorption is also released after relatively short times (Figure 5-11) and the temperature goes down to the cold plate level (Figure 5-9). Especially, layer M2 shows efficient transport properties as the temperature at the surface stays relatively low and the heat signal is large. For thicker layers the time difference between 90 % mass and heat transfer is much shorter probably due to decreased capacitive effects of the metal support. These effects result from the weight ratio of adsorbing and non-adsorbing material in the investigated samples. In the thinner samples, the contribution of the metal support to the total specific heat capacity of the system is larger rendering the measuring setup more isothermal. Heavier layers are connected to a relatively lower mass of aluminum which needs to be heated before heat dissipation to the cold plate takes place.
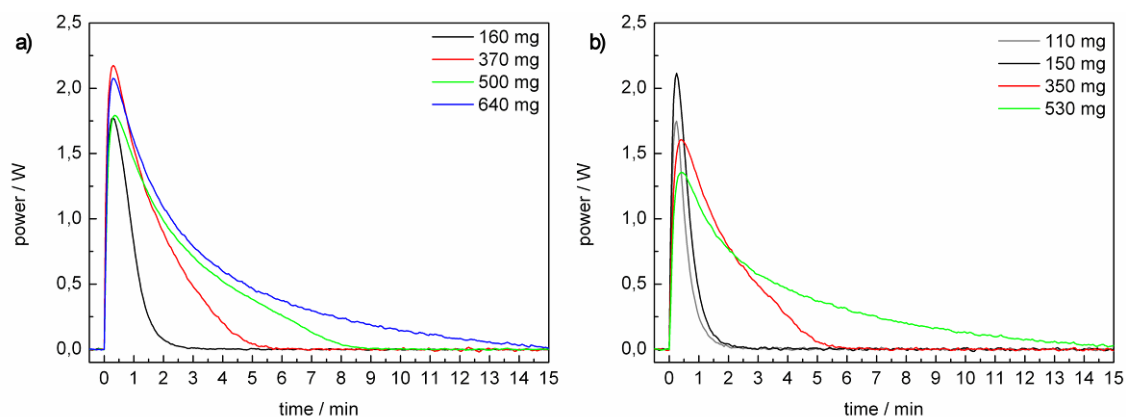
Figure 5-11. Kinetic curves of the heat dissipation from the aluminophosphate layers: a) "type N" and b) "type M".

5.6 Conclusion

Compact, mechanically stable layers of AlPO-18 on aluminum supports were prepared by using polyvinyl alcohol as a binder. The active adsorbent (AlPO-18) was stabilized in an aqueous solution of PVOH to form a homogeneous coating suspension. Two different morphologies, micron-sized crystals from a conventional gel and nanosized crystals, obtained from clear precursor solutions were employed for the preparation of layers.

The mass and heat transfer kinetics of the AlPO-18 layers with different thicknesses were investigated. The results show that the adsorption for layers <200 μm thickness reaches promising values in terms of fast heat and mass transfer characteristics. For layers > 200 μm the thermal output and adsorption rate decreased and the overall process proceeded in more than 2 min. Additionally, layers comprising nanosized AlPO-18 crystals show faster kinetics than the corresponding layers containing micron-sized crystals (for thin layers both crystal sizes show nearly identical kinetics). To account for these differences, most probably non-isothermal effects must be taken into consideration and the degree of transfer limitations also increases with layer thickness. The faster adsorption rates in films based on nanosized crystals are attributed to different layer structures resulting in faster heat transport. Limitation due to micropore diffusion cannot explain the differences in kinetics with increasing film thickness as this limitation is independent from layer thickness. Especially, it was observed that there is nearly no difference in adsorption kinetics in the thin samples. Measurements on AlPO-18 powders of

identical chemical compositions showed that heat transport limitation is much stronger in non-layered geometries. Therefore, layered composite concepts are the first choice to establish efficient mass and heat transport in heat exchanger systems. It is important to note that the binder PVOH does not adsorb significant amounts of water.

The AlPO-18 microporous molecular sieve is a promising material for heat exchanger applications as the useful loading under relatively mild conditions exceeds 25 wt.% and the adsorption kinetics are fast for compact layers up to ~200 μm thickness. For thicker layers attempts have to be undertaken to improve both mass and heat transfer in the composites. A promising adsorber geometry for this purpose is the use of relatively thin coatings in the voids of metal foams.[229]

6 Template substitution in the synthesis of AlPO-18

6.1 Introduction

Zeolites and (silico)aluminophosphates are important materials for many industrial applications, e.g., as catalysts or adsorbents. This is mainly due to their superior properties regarding shape selectivity, large surface area and tunable acidity. However, only a relatively small number of different zeolites is used in large-scale industrial applications, as many synthetic zeolites can only be obtained from expensive synthesis procedures. Cost factors for zeolite synthesis include the use of discontinuously working high-pressure reactors, high-priced reactants, and the need for removing organic templates at high temperatures. Therefore, zeolites that can be synthesized at low temperature and without the addition of expensive organic molecules are industrially preferred. In each specific case production costs have to be balanced by the added value for the industrial application. Therefore, high-priced zeolites are only interesting in those cases where they outperform every other applicable cheaper material. Commercially available molecular sieves comprise the Zeolites A, P, X, Y, β, TS-1, ZSM-5, and SAPO-34, which is used in the UOP / Hydro MTO process.[140]

Low-temperature syntheses can be conveniently designed in a continuous process as no sealed high-pressure reactors are needed. With respect to reactant costs, many attempts have been made to substitute expensive Al- and Si-sources, and organic templates, by low-cost chemicals. For example,

tetraethylorthosilicate (TEOS) was effectively substituted by naturally occurring silica sources, e.g., kaolinite[230] or rice ash.[231-233] However, for many zeolite syntheses the price for the organic template (or structure-directing agent, SDA) by far exceeds all other reagent prices. Template substitution is generally a highly demanding task, especially if a high template-specificity is observed. The possibility for substitution depends on the framework-template interaction, which is often not fully understood. However, some general trends should be considered. In zeolitic frameworks, the Si/Al-ratio governs the degree of framework charge and bond polarity. Highly charged frameworks are often found to be templated by SDAs with a high charge density (=charge/molecular volume). Therefore, zeolites with low Si/Al-ratios can often be synthesized in purely inorganic media, and hydrated alkali cations can act as SDAs in these systems. Especially, MFI, LTA, and FAU structures have been synthesized without organic additives.[234-241] For low-charge frameworks, especially aluminophosphates with an Al/P-ratio of ~1, or similar SAPO frameworks, inorganic cations are not known to act as SDAs. Additionally, template-framework interactions are stronger with decreasing channel/pore diameter. The aluminophosphate AlPO-5 with a pore diameter of 7.3 Å can be synthesized with a variety of over 25 different organic molecules, whereas AlPO-18 (3.8 Å) so far could only be synthesized in the presence of tetraethylammonium ions.

Various strategies can be followed in order to decrease the cost-influence of the template for a specific molecular sieve synthesis. For zeolites, the use of

inorganic cations such as potassium is desirable. If that is not possible, a substitution of the SDA by a less expensive organic molecule can be attempted. Additionally, a decrease in template concentration or the re-use of non-reacted template are possible approaches.[242] Sometimes it is possible to reduce the template concentration if seed crystals of the desired phase are added to the mixtures. Synthesis optimization experiments are generally time-consuming. The complex mechanisms involved in zeolite synthesis are not fully understood, and therefore, a large number of trial-and-error experiments are often needed. Such a large number of experiments can be advantageously performed with high-throughput methodology.

The microporous aluminophosphate AlPO-18 (AEI structure type code) is interesting due to its excellent water sorption properties, which make it a possible material for the use in adsorption heat exchanger and storage applications. The framework topology is characterized by a three-dimensional pore system possessing eight-membered intersecting channels with a diameter of 3.8 Å.[189] The framework density (14.8 T/1000 Å^3) of the AEI topology is among the lowest in the family of zeolitic materials.[190] Various recipes for the synthesis of AlPO-18 can be found in the literature.[135, 136, 139, 189, 194] Interestingly, the material can be synthesized from acidic and basic precursor gels. However, to our best knowledge all published recipes utilize tetraethylammonium hydroxide as the structure-directing agent, which leads to high costs for the synthesis. Vanadium- and cobalt-substituted forms of AlPO-18 have been prepared using N,N – diisopropylethylamine.[243] On the basis of

our experience concerning the competitive crystallization of AlPO-5 (AFI) and AlPO-18 (AEI) in tetraethylammonium-containing synthesis systems (see Chapter 7) we were interested in a new strategy for the synthesis of AlPO-18. As the AFI structure readily forms from triethylamine-containing synthesis mixtures, and this SDA has a geometry similar to the TEA$^+$ ion, we were interested in synthesizing AlPO-18 (AEI) directly with triethylamine as the template.

The goal of this study was to substitute the tetraethylammonium ion in the synthesis of AlPO-18 by triethylamine. Such a substitution gives rise to a decrease in synthesis costs of roughly two orders of magnitude (based on lab scale chemicals prices). In order to cover a broad range of synthesis compositions in a relatively short period, high-throughput methods developed in our laboratory were employed.

6.2 Experimental

The high-throughput setup used in this study is described in detail in the Methods section of this thesis (Chapter 2). Prior to hydrothermal treatment, the precursor gels were mixed in 21 mL closed polypropylene bottles. The reactants were mixed in the following order. Catapal B (Vista) alumina was added to half of the used amount of water and the suspensions were stirred parallel on a multi-stirrer system and only removed from the stirrer for addition of the subsequent reactant. Water, phosphoric acid (85 wt.%, Aldrich), and triethylamine (99 %, Aldrich) were mixed in 8 mL polypropylene bottles and then

added to the alumina suspension. The compositions of the different high-throughput experiments are included in the Results and discussion section below. The time needed for mixing of the chemicals of all experiments was typically ~3 h. The gels were then stirred for another 60 min. Prior to the filling of the multiclave with 1500 µL of each mixture, the pH values of the individual gels were measured. Afterwards, the multiclaves were sealed and heated at different temperatures in a conventional oven. The high-throughput experiments were hydrothermally treated for three different synthesis times. After synthesis, the experiments were quenched to room temperature and checked for mass consistency. After measurement of the post-synthesis pH, the individual experiments were transferred to a filter block. After filtration, the samples were washed twice with doubly distilled H_2O and dried at 60 °C overnight. Some of the as-synthesized samples were calcined for further characterization. For this purpose, they were heated to 550 °C (heating rate 50 °C h^{-1}) and held at this temperature for additional 5 h in a stream of air (150 mL min^{-1}).

6.3 Characterization

After drying, all samples were transferred to a high-throughput XRD holder and the patterns were measured automatically using a Stoe StadiP diffractometer (transmission mode, CuKα radiation). Data processing was performed using a specially developed script for the Origin Pro7 software (OriginLab Corp.). Selected samples were subject to further characterization. Scanning electron microscopy (SEM) images were recorded using a JEOL JSM-6500F microscope. Thermogravimetric analyses (TGA) and Differential Scanning

Calorimetry (DSC) were performed with a Netzsch STA 440 C Jupiter thermobalance. In these measurements, the samples (10 mg) were heated in a stream of synthetic air (50 ml min^{-1}) with a heating rate of 10 °C min^{-1} in an alumina crucible in the temperature range 25 – 900 °C.

6.4   Results and discussion

A high-throughput setup (HT 6.1) was used in order to find suitable crystallization conditions for AlPO-18 (AEI) under the conditions mentioned above. The molar fractions of triethylamine (NEt$_3$) and H$_2$O were varied from 1.0 – 1.5 – 2.0 and 50 – 100, respectively. Two different aluminum sources, boehmite and aluminum hydroxide were used. Additionally, half of the experiments were manipulated after mixing of the reactants by either adjusting the pH to 3 – 4 with HCl, or by addition of seed crystals. The individual compositions are summarized in Table 6-1. The experiments covered a broad range of compositions, and the multiclaves were hydrothermally treated for 1, 4, and 12 days.

Table 6-1. Compositions of the precursor gels in the high-throughput setup HT 6.1 (150 °C, am = amorphous, AFI = AlPO-5, AEI = AlPO-18, APC = AlPO-H3, n.i. = not identified).

	Molar oxide ratio				Mass / g					Total mass /g	pH	Product phase(s)		
No.	Al₂O₃	P₂O₅	NEt₃	H₂O	Catapal B	Al(OH)₃	H₃PO₄, 85 %	TrEA, 99 %	H₂O			1 d	4 d	12 d
1	1.0	1.0	1.0	50.0		1.148	1.480	0.650	4.722	8.000	3.7	AFI	AFI	AFI/n.i.
2	1.0	1.0	1.5	50.0		1.104	1.422	0.937	4.538	8.000	4.4	AFI	AFI/n.i.	AFI/n.i.
3	1.0	1.0	2.0	50.0		1.062	1.369	1.202	4.367	8.000	7.1	am	am	n.i.
4	1.0	1.0	1.0	100.0		0.667	0.859	0.377	6.098	8.000	3.4	AFI	AFI	AFI
5	1.0	1.0	1.5	100.0		0.651	0.839	0.553	5.957	8.000	4.3	AFI	AFI	n.i.
6	1.0	1.0	2.0	100.0		0.637	0.820	0.720	5.823	8.000	6.1	am	AFI	n.i.
7	1.0	1.0	1.0	50.0		1.148	1.480	0.650	4.722	8.000	3.6**	AFI	AFI/n.i.	n.i.
8	1.0	1.0	1.5	50.0		1.104	1.422	0.937	4.538	8.000	3.9*	AFI	AFI	AFI/n.i.
9	1.0	1.0	2.0	50.0		1.062	1.369	1.202	4.367	8.000	3.1*	AFI	AFI	AFI
10	1.0	1.0	1.0	100.0		0.667	0.859	0.377	6.098	8.000	3.3**	AFI	AFI	n.i.
11	1.0	1.0	1.5	100.0		0.651	0.839	0.553	5.957	8.000	3.5*	AFI	AFI	n.i.
12	1.0	1.0	2.0	100.0		0.637	0.820	0.720	5.823	8.000	2.9*	AFI	AFI	n.i.
13	1.0	1.0	1.0	50.0	0.909		1.480	0.650	4.961	8.000	3.1	AFI	AFI	n.i.
14	1.0	1.0	1.5	50.0	0.874		1.422	0.937	4.768	8.000	3.8	AFI	AFI	AFI/n.i.
15	1.0	1.0	2.0	50.0	0.841		1.369	1.202	4.589	8.000	5.6	AFI	AFI/new	n.i.
16	1.0	1.0	1.0	100.0	0.528		0.859	0.377	6.236	8.000	2.9	AFI	AFI	AFI
17	1.0	1.0	1.5	100.0	0.516		0.839	0.553	6.093	8.000	3.5	AFI	AFI	n.i.
18	1.0	1.0	2.0	100.0	0.504		0.820	0.720	5.956	8.000	5.6	**AEI**/AFI	**AEI**/AFI	n.i.
19	1.0	1.0	1.0	50.0	0.909		1.480	0.650	4.961	8.000	3.2**	AFI	AFI	n.i.
20	1.0	1.0	1.5	50.0	0.874		1.422	0.937	4.768	8.000	3.7**	AFI	AFI/n.i.	n.i.
21	1.0	1.0	2.0	50.0	0.841		1.369	1.202	4.589	8.000	3.7*	AFI	AFI/n.i.	AFI
22	1.0	1.0	1.0	100.0	0.528		0.859	0.377	6.236	8.000	2.9**	AFI	AFI	AFI
24	1.0	1.0	2.0	100.0	0.504		0.820	0.720	5.956	8.000	3.5**	AFI	AFI	n.i.
23	1.0	1.0	1.5	100.0	0.516		0.839	0.553	6.093	8.000	2.8*	AFI	AFI/APC	n.i.

*the pH was changed by addition of HCl, 37 %, **10 mg AEI seeds were added

All products were characterized by XRD and the corresponding patterns can be found in the appendix. The analysis of the obtained phases can be summarized as follows. AlPO-5 (AEI) was the major product phase from 1 to 4 days of hydrothermal treatment under all investigated synthesis conditions. Concerning the formation of AlPO-18 (AEI), experiment no. 18 is of special interest. This experiment with molar composition 1 Al_2O_3 : 1 P_2O_5 : 2 NEt_3 : 100 H_2O yielded a 1:1-mixture of AlPO-5 (AFI) and AlPO-18 (AEI) after 1 and 4 days of hydrothermal treatment, respectively. The precursor gel had a relatively high NEt_3/Al_2O_3 – ratio. Additionally, the starting pH of the mixture (pH = 5.6) was relatively neutral compared to all other experiments. However, with a starting pH of 6.1 in the corresponding experiment using aluminum hydroxide (no. 6) pure AlPO-5 was found. Obviously, the crystallization field for AlPO-18 is very narrow in triethylamine-containing systems. Only a small change in peak intensities was found in the XRD patterns of experiment no. 18 from 1 to 4days (Figure 6-1), indicating that no significant re-crystallization (see Chapter 7, HT 7.1) proceeded in this system. However, after an elongated synthesis time of 12 days, complete re-crystallization to another AlPO phase was observed. The same phase was found in nearly all other experiments of the high-throughput setup, but could not be identified by database matching. However, for NEt_3/Al_2O_3 = 1 and H_2O/Al_2O_3 = 100, AFI was found after 12 days of hydrothermal treatment. The reflection intensity ratio for the unidentified phase was identical in all corresponding products indicating phase purity. The most intense XRD reflection is found at 6.7 2Θ. Some experiments showed different

reflection intensities due to a preferred orientation of the crystals in the used

XRD setup (see appendix), which could be removed by grinding the products.
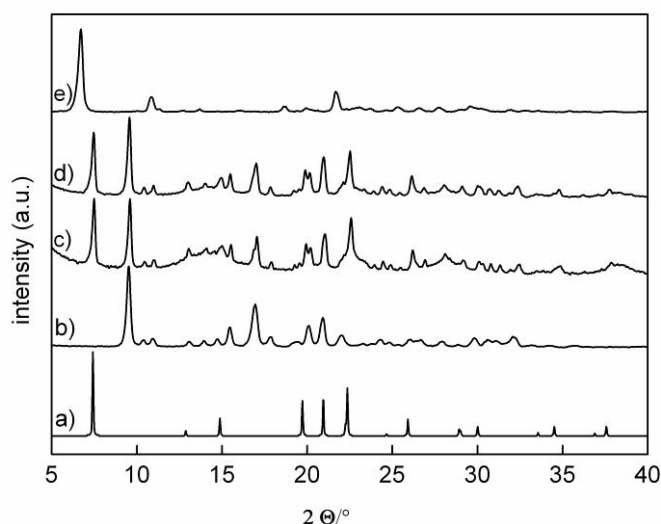
Figure 6-1. XRD patterns of a) simulated AFI, b) hydrated AEI reference, Experiment no. 18 after c) 1 d, d) 4 d, and e) 12 d.

Figure 6-2 shows SEM images of the three different products obtained in

experiment no. 18. The phase mixtures obtained after 1 and 4 days consist of

large crystals of elongated hexagonal morphologies, typical for AlPO-5, and

flattened hexagonal crystals, which are commonly found for AlPO-18 materials.

The unidentified phase obtained after 12 days contained thin (~100 nm) plate-

like crystals with diameters of several microns. No crystal suitable for single-

crystal X-ray analysis could be found in the corresponding samples.
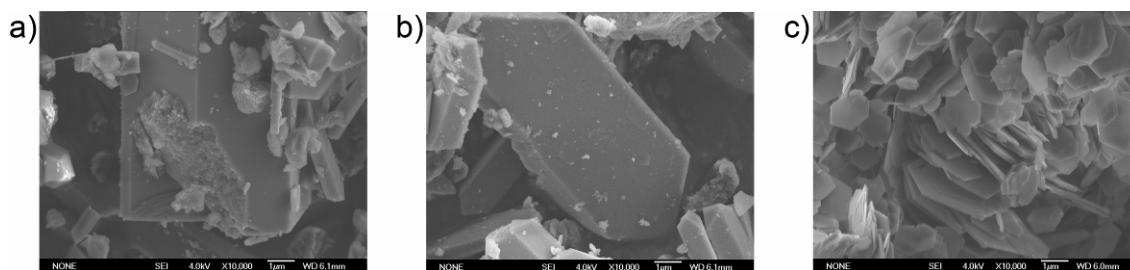
Figure 6-2. Morphologies of the three different phases obtained from a synthesis mixture of molar composition 1 Al_2O_3 : 1 P_2O_5 : 2 NEt_3 : 100 H_2O after a – b) 1 d, and c) 12 d.

The thermogravimetric analysis of the same phase is shown in Figure 6-3. A large weight loss of 14 wt.% between 300 – 500 °C together with two unusual endothermic DSC peaks at 384 and 400 °C was observed.
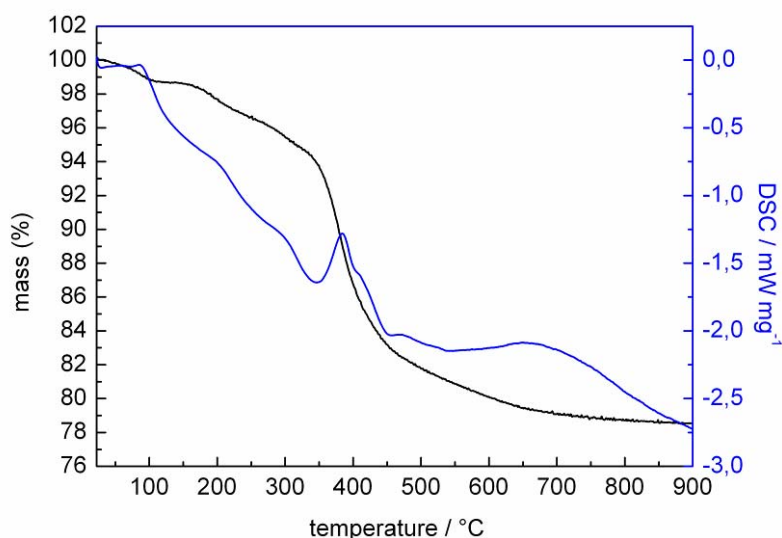
Figure 6-3. Thermogravimetric analyis (TGA) and differential scanning calorimetricy (DSC) data of experiment no. 18 after 12 d of hydrothermal treatment.

To evaluate the stability and potential porosity of the unknown material, the as-synthesized product was calcined in air for 20 h at 400 °C and 500 °C, respectively. The corresponding XRD patterns after calcinations are shown in Figure 6-4. After calcination at 400 °C a gradual decrease in crystallinity and the

transformation to another unidentified phase was observed. The decomposition of the phase at 500 °C led to an X-ray amorphous product.
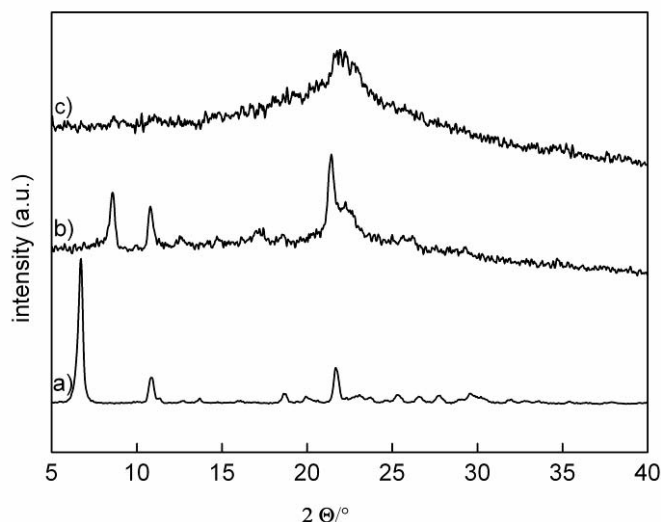
Figure 6-4. XRD patterns of experiment no. 18: a) as-synthesized, b) after calcination at 400 °C, c) after calcination at 500 °C.

The reflection at low 2Θ angles, the plate-like morphology, and the decomposition upon thermal removing of the organic template are indicative for a layered AlPO-NEt$_3$ structure. No further attempts concerning the determination of the crystal structure were undertaken.

Based on experiment no. 18 (HT 6.1), which resulted in the formation of a AFI/AEI mixture, the influence of the molar amount of template, pH, overall concentration, and synthesis temperature was investigated in more detail. It was assumed that triethylamine can only function as SDA for the AEI structure in its protonated ammonium form. Additionally, a relatively low pH and a low molar amount of template were observed to result in AFI as the preferred

product in the previous experiments. Therefore, the H_3PO_4/NEt_3-ratio was varied in a relatively narrow range from 0.75 to 1.25. A molar ratio NEt_3/Al_2O_3 of 2 and 4 was used, respectively. Additionally, the total concentration of the reactants in water was varied from H_2O/Al_2O_3 = 80 - 140. Two identical sets of reagent mixtures were used and hydrothermally treated at 170 °C and 150 °C, respectively. The composition of the individual experiments of the corresponding high-throughput setup (HT 6.2) and the resulting products are summarized in Table 6-2 for the experiments conducted at 170 °C. The product phases obtained at 150 °C in experiment HT 6.3 can be found in Table 6-3. The samples were hydrothermally treated for 1, 3, and 5 days.

Table 6-2. Compositions of the precursor gels in the high-throughput setup HT 6.2 (170 °C, am = amorphous, AFI = AlPO-5, AEI = AlPO-18).

No.	Molar oxide ratio				Mass / g				Total mass / g	pH	Product phase(s)		
	Al_2O_3	P_2O_5	NEt_3	H_2O	Catapal B	H_3PO_4, 85 %	NEt_3, 99 %	H_2O			1 d	3 d	5 d
1	1.00	0.75	2.00	80.00	1.223	1.493	1.748	11.535	16.000	6.68	am	am	am
2	1.00	1.00	2.00	80.00	1.200	1.954	1.715	11.131	16.000	5.34	AFI/**AEI**	AFI/**AEI**	AFI/**AEI**
3	1.00	1.25	2.00	80.00	1.178	2.397	1.684	10.741	16.000	3.42	AFI	AFI	AFI
4	1.00	1.75	4.00	80.00	1.031	2.938	2.948	9.082	16.000	6.18	am	am	**AEI**
5	1.00	2.00	4.00	80.00	1.015	3.304	2.902	8.779	16.000	5.18	AFI	AFI	AFI
6	1.00	2.25	4.00	80.00	0.999	3.659	2.856	8.485	16.000	4.02	AFI	AFI	AFI/am
7	1.00	0.75	2.00	100.00	1.024	1.250	1.464	12.263	16.000	6.58	am	am	AFI/am
8	1.00	1.00	2.00	100.00	1.008	1.640	1.440	11.911	16.000	5.33	**AEI**	**AEI**	**AEI**
9	1.00	1.25	2.00	100.00	0.992	2.019	1.418	11.571	16.000	3.33	AFI	AFI	AFI
10	1.00	1.75	4.00	100.00	0.886	2.524	2.533	10.057	16.000	6.10	am	**AEI**	AFI
11	1.00	2.00	4.00	100.00	0.874	2.845	2.498	9.783	16.000	5.11	AFI	AFI	AFI
12	1.00	2.25	4.00	100.00	0.862	3.158	2.465	9.516	16.000	3.88	AFI	AFI	AFI
13	1.00	0.75	2.00	120.00	0.881	1.075	1.259	12.786	16.000	6.59	am	am	am
14	1.00	1.00	2.00	120.00	0.869	1.414	1.241	12.476	16.000	5.34	**AEI**	**AEI**	**AEI**
15	1.00	1.25	2.00	120.00	0.857	1.743	1.225	12.175	16.000	3.29	AFI	AFI	AFI
16	1.00	1.75	4.00	120.00	0.777	2.212	2.220	10.791	16.000	6.06	am	**AEI**	am
17	1.00	2.00	4.00	120.00	0.767	2.498	2.193	10.542	16.000	5.15	AFI	AFI	AFI
18	1.00	2.25	4.00	120.00	0.758	2.777	2.167	10.298	16.000	3.81	AFI	AFI	AFI
19	1.00	0.75	2.00	140.00	0.772	0.943	1.104	13.181	16.000	6.57	am	am	am
20	1.00	1.00	2.00	140.00	0.763	1.242	1.091	12.904	16.000	5.37	am	**AEI**	**AEI**
21	1.00	1.25	2.00	140.00	0.754	1.534	1.078	12.634	16.000	3.21	AFI	AFI	AFI
22	1.00	1.75	4.00	140.00	0.691	1.969	1.976	11.364	16.000	6.06	am	**AEI**	**AEI**
23	1.00	2.00	4.00	140.00	0.684	2.226	1.955	11.135	16.000	5.09	AFI	AFI	AFI
24	1.00	2.25	4.00	140.00	0.677	2.478	1.934	10.911	16.000	3.73	AFI	AFI	AFI

The analysis of the resulting phases of experiment HT 6.2 (treated at 170 °C) can be summarized as follows. A strong dependence on the pH of the precursor gels was observed. All samples starting at pH < 5.3 yielded pure AlPO-5 (AFI) after 1 day of hydrothermal treatment, irrespective of the molar amount of template or water, and with increasing synthesis time (up to 5 days) no change in the XRD patterns was observed. In contrast, all samples with starting pH > 6.5 did not result in any crystalline product, and the XRD pattern of the nearly amorphous boehmite precursor was observed. Presumably, the solubility of this precursor is too low at this pH leading to either no or extremely slow reaction kinetics. In the region 5.3 < pH < 6.5 AlPO-18 (AEI) was found as the preferred product. Apparently, the lower pH value represents a sharp border between the stability regions of the two different phases. AEI was obtained in a phase-pure form in the experiments no. 4, 10, 15, and 22. These experiments were based on a molar ratio NEt_3/Al_2O_3 of 4/1. Similarly, those experiments with a molar ratio NEt_3/Al_2O_3 of 2/1 (no. 8, 14, and 20) yielded nearly phase pure AlPO-18 (AEI) with a small AFI impurity (<10 %). The amount of the impurity was much larger (~1/1) at the highest total concentration (H_2O/Al_2O_3 = 80). Apparently, a NEt_3/Al_2O_3 – ratio of 2/1 represents a lower threshold for the preferred formation of AlPO-18 over AlPO-5. Additionally, it was observed that the reaction kinetics were slower with increasing pH as the solubility of AlO(OH) is decreased.

The XRD patterns of experiment no. 4 after a synthesis time of 5 days, and those of a reference sample synthesized with tetraethylammonium as the SDA, are shown in Figure 6-5.
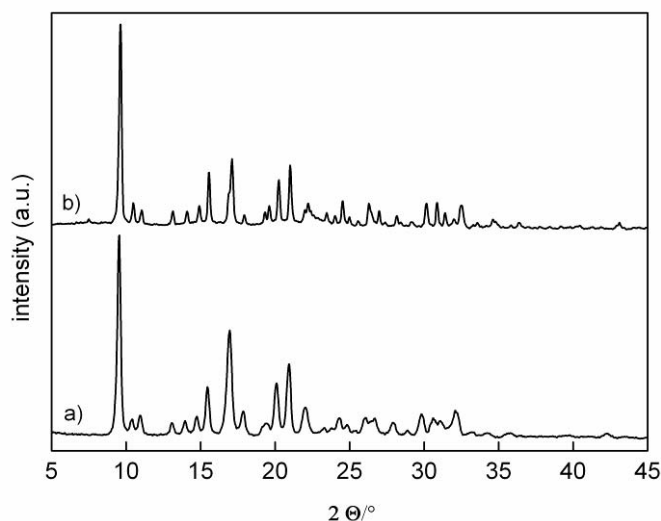
Figure 6-5. XRD patterns of a) AlPO-18 (AEI) synthesized with tetraethylammonium,[194] and b) with triethylamine (HT 6.2 experiment no. 4 after 5 d of hydrothermal treatment) as the structure-directing agent.

In the experiments no. 10 and 18 (NEt_3/Al_2O_3 = 4/1, H_2O/Al_2O_3 = 100,120/1) it was observed that the phase pure AlPO-18 products obtained after 3 days had undergone further reactions after 5 days of hydrothermal treatment. Experiment no. 10 yielded pure AlPO-5 and experiment no. 16 an amorphous product. Re-crystallization processes are very common in aluminophosphate chemistry. However, the reason in the special cases of this study is not clear yet.

Additionally, the crystallinity of the AlPO-18 products was estimated by comparison to a 100 % crystalline gibbsite ($Al(OH)_3$) sample. It was found that the sample synthesized in the most concentrated gel (no. 4) was 100 % crystalline after 5 days of hydrothermal treatment, and the crystallinity at this time decreased gradually with decreasing concentration. The samples with

H_2O/Al_2O_3 = 140/1 showed ~60 % crystallinity. It was not investigated if the latter show full crystallinity after elongated synthesis times.

The thermogravimetric analysis data of sample no. 4 and of an AlPO-18 sample synthesized with the tetraethylammonium ion as the structure-directing agent[194] are shown in Figure 6-6. The samples loose 6 % and 3 % of water upon heating to 100 °C, respectively. The triethylamine occluded in sample b) is removed between 170 °C and 300 °C leading to a weight loss of 14 %. Similarly, the removal of tetraethylammonium in sample a) gives rise to a weight loss of 15 %. However, the latter is removed at much higher temperature (300 – 600 °C).
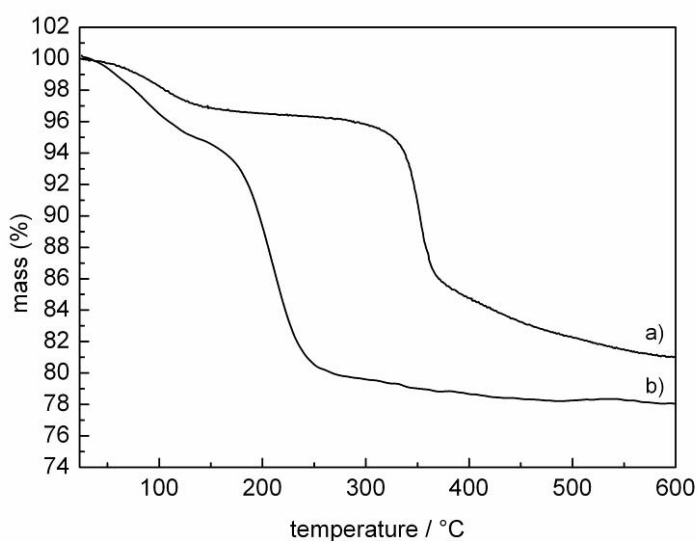
Figure 6-6. Thermogravimetric analysis (TGA) of AlPO-18 (AEI) synthesized with a) tetraethylammonium, and b) with triethylamine as the structure-directing agent.

Apparently, the template-framework interaction is significantly different in the two materials. This could be due to the smaller size of the triethylammonium ion

compared to the tetraethylammonium ion. Furthermore, deprotonation at elevated temperature in the presence of a charge-balancing anion could lead to a more facile removal of the resulting triethylamine in comparison with the charged tetraethylammonium ion.

Figure 6-7 shows SEM images of sample no. 4 (HT 6.2). A large fraction of the material consists of crystals with flattened hexagonal shape. This morphology is typically found for AlPO-18 synthesized with TEA$^+$ as the structure-directing agent. However, the aspect ratio of the long and short axes is increased for the samples synthesized in this study, compared to the morphologies most often found using TEA$^+$.
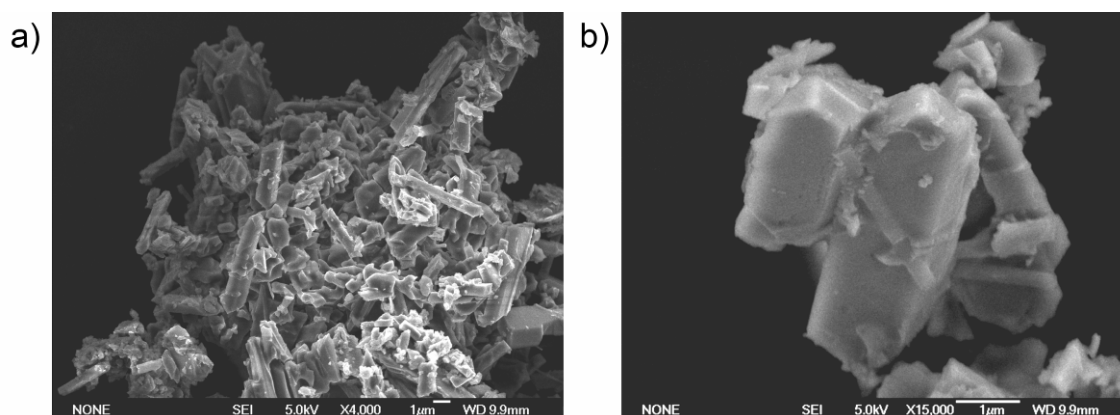
Figure 6-7. SEM images of AlPO-18 (AEI) synthesized with triethylamine as the structure-directing agent (Magnification: a) 4000x, b) 15000x).

Calcined samples were subjected to nitrogen and krypton physisorption to gain information on the porosity of the materials. Figure 6-8 shows typical type I isotherms for both the reference sample (a: TEAOH) and sample no. 4 (b: NEt$_3$). The micropore volume estimated by the t-plot method is 0.254 cm^3 g^{-1} and 0.246 cm^3 g^{-1}, respectively. The reference sample shows a slightly larger

slope of the nitrogen isotherm after filling of the micropores, indicating a higher external surface area (attributed to a smaller average particle diameter). In the krypton isotherms (logarithmic scale, desorption not shown) the NEt$_3$ sample shows slightly higher adsorbed volumes than the reference (the adsorbed volumes (at standard conditions) of krypton are only about one third of those obtained with nitrogen due to the threefold density of Krypton).
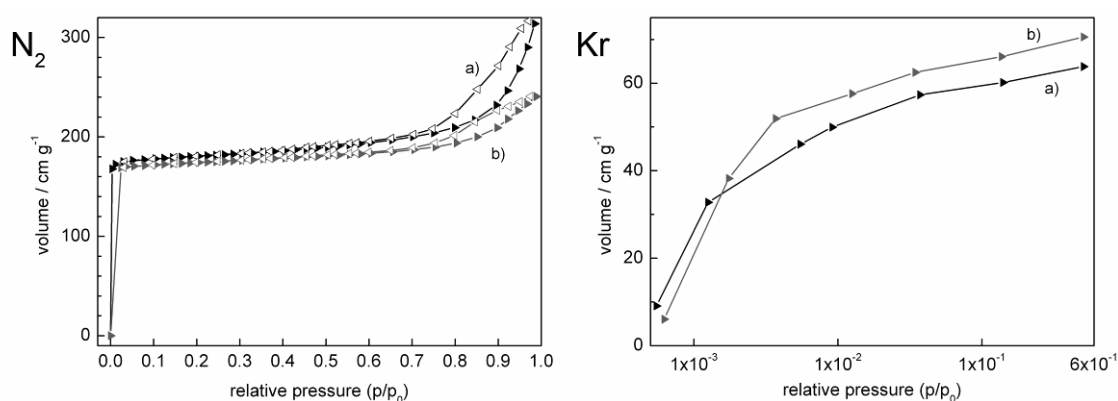
Figure 6-8. Nitrogen (left) and krypton (right) physisorption data at 77 K of a) AlPO-18 synthesized with tetraethylammonium, and b) with triethylamine as the structure-directing agent. Full symbols: adsorption, empty symbols: desorption.

Another high-throughput setup (HT 6.3) was heated at 150 °C for 1, 3, and 5 days using the identical precursor gels as those used in experiment HT 6.2. All corresponding XRD patterns can be found in the appendix and the structure type codes of the obtained products can be found in Table 6-3.

Table 6-3. pH values and obtained phases in experiment HT 6.3 (150 °C, am = amorphous, AFI = AlPO-5, AEI = AlPO-18, APC = AlPO-H3).

	Molar oxide ratio				pH	Product phase(s)		
No.	Al_2O_3	P_2O_5	NEt_3	H_2O		1 d	3 d	5 d
1	1.00	0.75	2.00	80.00	6.68	am	am	am
2	1.00	1.00	2.00	80.00	5.34	am	am	am
3	1.00	1.25	2.00	80.00	3.42	AFI	AFI	AFI
4	1.00	1.75	4.00	80.00	6.18	am	am	am
5	1.00	2.00	4.00	80.00	5.18	am	am	am
6	1.00	2.25	4.00	80.00	4.02	AFI/APC	AFI/APC	APC
7	1.00	0.75	2.00	100.00	6.58	am	am	am
8	1.00	1.00	2.00	100.00	5.33	am	am	am
9	1.00	1.25	2.00	100.00	3.33	AFI	AFI	AFI
10	1.00	1.75	4.00	100.00	6.10	am	am	am
11	1.00	2.00	4.00	100.00	5.11	am	am	AFI
12	1.00	2.25	4.00	100.00	3.88	AFI/APC	AFI/APC	APC
13	1.00	0.75	2.00	120.00	6.59	am	am	am
14	1.00	1.00	2.00	120.00	5.34	am	am	am
15	1.00	1.25	2.00	120.00	3.29	AFI	AFI	AFI
16	1.00	1.75	4.00	120.00	6.06	am	am	am
17	1.00	2.00	4.00	120.00	5.15	am	am	**AEI**/AFI
18	1.00	2.25	4.00	120.00	3.81	AFI/APC	AFI/APC	APC
19	1.00	0.75	2.00	140.00	6.57	am	am	am
20	1.00	1.00	2.00	140.00	5.37	am	am	am
21	1.00	1.25	2.00	140.00	3.21	AFI	AFI	AFI
22	1.00	1.75	4.00	140.00	6.06	am	am	am
23	1.00	2.00	4.00	140.00	5.09	am	**AEI**	**AEI**/AFI
24	1.00	2.25	4.00	140.00	3.73	AFI	AFI	AFI

The analysis of the structural phases can be summarized as follows. Similarly to the gels treated at 170 °C, a strong dependence on the pH of the precursor compositions was observed. As the solubility of the boehmite reagent is further reduced at this temperature, amorphous products were obtained for all experiments that had yielded either amorphous material or AlPO-18 (AEI) at 170 °C. However, AlPO-18 was obtained in experiments no. 17 and no. 23 after 3 and 5 days, together with an AlPO-5 (AFI) impurity of approximately 25 %.

These experiments represent a pH range of 5.1 to 5.2, which is even narrower and slightly lower than the region yielding AlPO-18 at 170 °C. These findings provide strong support for the assumption that a low concentration of aluminum in the precursor solutions leads to the preferred formation of AlPO-18. Additionally, a H_2O/Al_2O_3 ratio lower than 120 did not lead to the formation of AlPO-18 (at 170 °C: lower than 100). Similar to the experiments treated at higher temperature, the experiments showing low pH (<4) prior to the synthesis did not yield AlPO-18, but AlPO-5 (for NEt_3/Al_2O_3 = 2) and/or AlPO-H3 (APC, for NEt_3/Al_2O_3 = 4).

6.5 Conclusion

High-throughput synthesis and characterization methods (a total number of 216 experiments) were performed in order to find suitable synthesis conditions for the preparation of AlPO-18 (AEI) without using tetraethylammonium hydroxide. In a first set of reactions, a broad range of gel compositions was investigated, and the desired phase was only obtained in a single experiment as a 1:1-mixture with AlPO-5, the typical crystallization product under these conditions. After prolonged synthesis times, complete re-crystallization to an unidentified phase (presumably a layered triethylamine-aluminophosphate) proceeded in most experiments of the same high-throughput setup. When using a focussed parameter field of compositions at different temperatures (150 °C and 170 °C) and synthesis times (1 to 5 days), AlPO-18 was synthesized with high purity within a narrow range of gel compositions. A strong dependence on pH was observed, and AlPO-18 crystallized only within the range 5.3 < pH <6.5 at

170 °C. Additionally, a relatively high NEt_3/Al_2O_3 ratio of at least 2/1 and a low total concentration ($H_2O/Al_2O_3 > 100$) were found to be critical to obtain pure AlPO-18. Similar results for the experiments treated at 150 °C suggest that a low solubility of aluminum leads to the preferred formation of AlPO-18 over AlPO-5.

The resulting AlPO-18 powders show morphologies similar to those obtained from known synthesis procedures utilizing tetraethylammonium hydroxide. However, the removal of NEt_3 from the materials proceeds at much lower temperatures and the calcined samples show micropore volumes comparable to those of conventionally synthesized AlPO-18.

7 Strategies for the cost-efficient synthesis of alumino-phosphates

7.1 Introduction

In addition to the studies described in Chapter 6 other concepts for the cost-efficient synthesis of aluminophosphates were followed within the scope of this thesis. Two strategies, namely template reduction and template substitution by extra-ordinary and/or cheap types of templates, were employed. The results of these investigations are discussed in this chapter.

7.2 Experimental

In order to cover a broad range of synthesis compositions the high-throughput methodology described in Chapter 2.8 was used. The preparation of the synthesis gels was performed analogous to the experiments discussed in Chapter 6. The order of mixing was H_2O, H_3PO_4, NaOH/HCl, template, and Al-source, if not otherwise stated. The sealed high-throughput autoclaves were hydrothermally treated at 150 °C for different synthesis times.

7.3 Characterization

All products were characterized using the same methods/instruments mentioned in Chapter 6. Additionally, Raman spectra were recorded using a Horiba Jobin Yvon LabRAM-HR or a Bruker Equinox 55 & FRA Raman module 106 /S.

7.4 Results and Discussion

7.4.1 Cost reduction by decrease of template concentration

A high-throughput setup (HT 7.1) was used in order to find synthesis conditions leading to AEI as the major product phase including a minimum amount of tetraethylammonium hydroxide in the precursor mixture. As a starting point the method described by Simmen et al. was used.[189] This method is the most cost-efficient among the AlPO-18 recipes known in the literature, as it uses boehmite as aluminum source, and the molar composition: 1 Al_2O_3 : 1 P_2O_5 : 0.67 TEA_2O : 0.33 HCl : 35 H_2O. Additionally, the precursor mixture is highly concentrated leading to large volumetric yields. In the setup, the molar ratio of TEA_2O/Al_2O_3 was reduced stepwise to 0.20. Half of the experiments were conducted without adjusting the pH by HCl addition, leading to a relatively broad range of starting pH values. Additionally, half of the experiments were used to investigate the effect of an addition of AEI seeds (2 wt.%) to the mentioned compositions. Details of the individual experiments and the structure type codes of the products can be found in Table 7-1. The reagent mixtures were treated at 150 °C, the time of hydrothermal synthesis was varied in three steps, and the experiments were quenched after 1, 2, and 3 days, respectively. All resulting products were characterized by means of XRD, and the corresponding powder patterns can be found in the appendix. The most important experimental observations are discussed here.

Table 7-1. Compositions of the precursor gels in the high-throughput setup HT 7.1 (150 °C, am = amorphous, AFI = AlPO-5, AEI = AlPO-18, n.i. = not identified).

No.	Molar oxide ratio				Mass / g						Total mass / g	Seed mass / g	pH	Product phase(s)		
	Al_2O_3	P_2O_5	TEA_2O	HCl	H_2O	Catapal B	H_3PO_4, 85 %	TEAOH, 35 %	HCl, 37 %	H_2O				1 d	2 d	3 d
1	1.00	0.99	0.67	0.34	34.91	0.661	1.066	2.624	0.159	0.482	4.991		3.2	AFI	**AEI/AFI**	**AEI**
2	1.00	0.98	0.60	0.34	34.80	0.673	1.079	2.390	0.157	0.675	4.974		2.9	AFI	AFI	AFI
3	1.00	1.20	0.54	0.33	37.08	0.690	1.347	2.192	0.159	0.974	5.362		2.5	AFI	AFI	AFI
4	1.00	0.98	0.40	0.34	34.72	0.711	1.135	1.673	0.166	1.279	4.964		2.3	AFI	AFI	AFI
5	1.00	0.98	0.30	0.34	34.80	0.731	1.162	1.296	0.172	1.607	4.967		1.8	AFI	AFI	AFI
6	1.00	1.19	0.20	0.33	35.80	0.753	1.454	0.892	0.170	1.955	5.225		1.5	n.i.	n.i.	n.i.
7	1.00	1.00	0.67		34.82	0.669	1.091	2.645		0.582	4.987		3.7	AFI	am	am
8	1.00	0.99	0.61		35.10	0.682	1.100	2.457		0.784	5.023		3.5	AFI	am	**AEI**
9	1.00	0.99	0.50		34.85	0.700	1.125	2.074		1.084	4.983		3.1	AFI	AFI	AFI
10	1.00	0.97	0.40		34.61	0.726	1.150	1.722		1.394	4.991		2.9	AFI	AFI	AFI
11	1.00	1.01	0.30		36.49	0.741	1.219	1.313		1.885	5.158		2.5	AFI	AFI	AFI
12	1.00	0.99	0.20		34.94	0.765	1.233	0.903		2.106	5.007		2.4	AFI	AFI	AFI
13	1.00	1.23	0.67	0.31	35.95	0.662	1.329	2.615	0.142	0.486	5.234	0.010	2.8	AFI	AFI	**AEI/AFI**
14	1.00	0.98	0.60	0.33	34.80	0.673	1.079	2.379	0.154	0.684	4.968	0.010	3.0	AFI	am	AFI
15	1.00	1.00	0.50	0.32	34.89	0.693	1.130	2.050	0.152	0.977	5.003	0.010	2.6	AFI	AFI	AFI
16	1.00	0.98	0.40	0.34	34.70	0.720	1.154	1.705	0.169	1.284	5.031	0.011	2.3	AFI	AFI	AFI
17	1.00	0.99	0.30	0.33	34.96	0.731	1.175	1.312	0.167	1.610	4.995	0.011	2.0	am	AFI	AFI
18	1.00	0.98	0.19	0.33	34.62	0.753	1.206	0.865	0.174	1.952	4.949	0.010	1.5	AFI	AFI	AFI
19	1.00	1.01	0.67		58.87	0.663	1.087	2.645		2.588	6.983	0.012	3.8	**AEI/AFI**	**AEI**	**AEI**
20	1.00	0.98	0.60		34.77	0.682	1.089	2.412		0.788	4.970	0.010	3.6	**AEI/AFI**	**AEI/AFI**	**AEI**
21	1.00	0.98	0.49		34.53	0.708	1.130	2.075		1.085	4.997	0.011	3.3	AFI	AFI	AFI
22	1.00	0.97	0.40		34.74	0.722	1.143	1.706		1.404	4.975	0.010	3.0	AFI	AFI	AFI
23	1.00	1.23	0.30		36.40	0.735	1.471	1.321		1.744	5.270	0.010	2.5	AFI	AFI	AFI
24	1.00	1.00	0.20		34.85	0.762	1.236	0.902		2.086	4.986	0.010	2.5	AFI	AFI	AFI

From the XRD data it can be concluded that AlPO-5 represents the preferred product in all experiments containing TEA_2O in molar fractions lower than 0.6. It was obtained in the corresponding experiments after 1, 2, and 3 days of hydrothermal treatment. All experiments containing a molar fraction of TEA_2O of 0.7 (Exp. 1, 7, 13, 19) yielded AlPO-18 (AEI) after 3 days of hydrothermal treatment. Interestingly, the same synthesis mixtures yielded AlPO-5 (AFI) after 1 day, and a steady re-crystallization process with increasing synthesis time could be observed. The corresponding XRD patterns of the products obtained from experiment 1 of the high-throughput setup are shown in Figure 7-1. No other side phases were detected in this experiment, and in all other products of the same high-throughput setup.
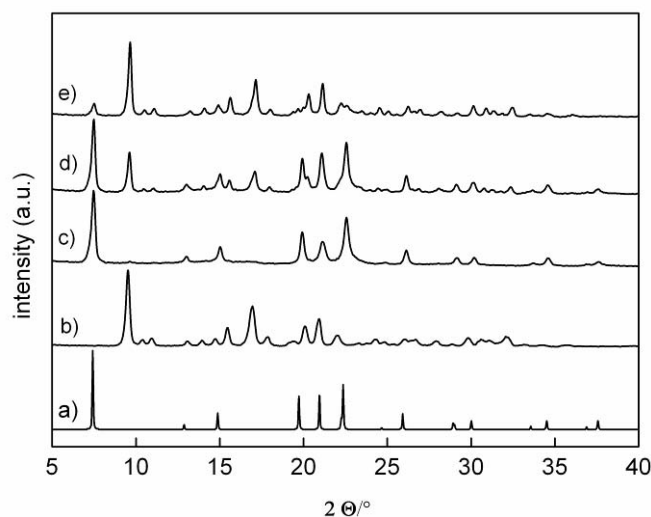
Figure 7-1. Re-crystallization process in synthesis mixtures containing TEAOH: a) simulated XRD pattern of AFI, b) reference XRD pattern of hydrated AEI, Experiment no. 1 after c) 1 d, d) 2 d, and e) 3 d of hydrothermal treatment at 150 °C. Molar oxide ratio: 1 Al_2O_3 : 1 P_2O_5 : 0.67 TEA_2O : 0.33 HCl : 35 H_2O.

A similar re-crystallization behavior was observed when a molar fraction of TEA_2O of 0.6 was used. The corresponding XRD patterns for experiment 8 are shown in Figure 7-2. However, at this concentration it proceeded only if no hydrochloric acid was added to the synthesis gels, resulting in a pre-experimental pH of >3.5. At higher TEAOH concentration, AEI was formed down to a pH of 2.8 in experiment 13.
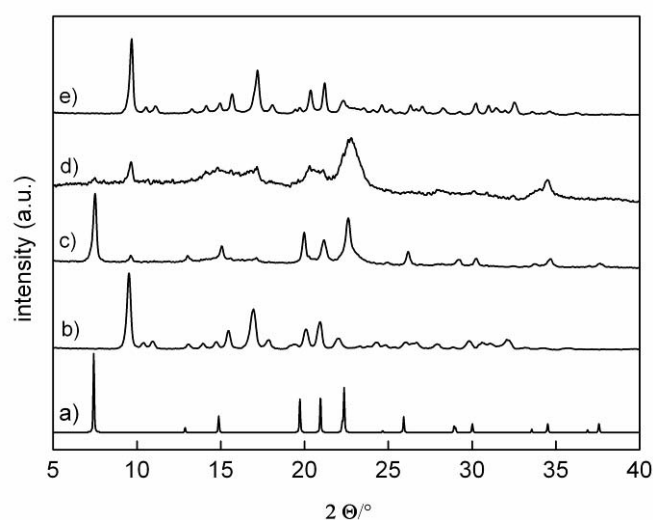
Figure 7-2. Re-crystallization process in synthesis mixtures containing TEAOH: a) simulated XRD pattern of AFI, b) reference XRD pattern of hydrated AEI, Experiment no. 8 after c) 1 d, d) 2 d, and e) 3 d of hydrothermal treatment at 150 °C. Molar oxide ratio: 1 Al_2O_3 : 1 P_2O_5 : 0.60 TEA_2O : 35 H_2O.

Re-crystallization in the reaction system 1 Al_2O_3 : 1 P_2O_5 : 0.67 TEA_2O : 0.33 HCl : 35 H_2O was previously observed by Huang et al.[244] However, the study contains no conclusion concerning the formation mechanism of the two phases. XRD and $^{31}P/^{27}Al$ MAS NMR suggested that the AFI phase is the kinetically favored product, whereas AEI represents the thermodynamically favored phase. This is in agreement with our results as XRD reflections

corresponding to AEI are detected only after fully crystalline AFI has formed. Re-crystallization from one molecular sieve phase to another is known in some aluminosilicate systems, including MOR / ANA to MFI,[245] ANA to KFI,[94, 246, 247] FAU to GIS, and LTA to FAU. Supposedly, the majority of zeolite-zeolite-transformations proceeds via a solution-mediated process,[248] and the rate limiting step is assumed to be the nucleation of the secondary phase. Such a mechanism is in agreement with our findings, i.e., the metastable AFI phase is only transformed to AEI if the surrounding synthesis solution can provoke nucleation of the structure. The two most important properties of the solution were found to be pH and TEA$^+$ concentration. The pH of all synthesis gels was measured before and after hydrothermal treatment. Re-crystallization occurred only if the pH reached values >7 (with TEA$_2$O : Al$_2$O$_3$ = 0.67 : 1) and >7.5 (with TEA$_2$O : Al$_2$O$_3$ = 0.60 : 1) after 2 days of hydrothermal treatment. In addition, a TEA$_2$O molar fraction of ≥0.6 is essential for nucleation of the AEI phase, whereas AFI can be formed in solutions containing much lower concentrations. The pore structure of the two phases can serve as an explanation for the large difference in suitable template concentrations. AlPO-5 (AFI) contains parallel aligned 1-dimensional channels built from 12-membered rings (diameter: 7.3 Å), whereas AlPO-18 (AEI) has a 3-dimensional channel system containing cavities separated by 8-membered rings (3.8 Å). The latter structure gives rise to a lower framework density, and therefore larger amounts of template must be occluded. Additionally, the smaller ring diameter leads to the template being occluded solely in the cavities (and not in channels). This leads to a low

tolerance concerning template geometry compared to the AFI structure. In fact, AlPO-5 can be formed using over 25 different organic molecules. Additionally, water is assumed to be a suitable pore filling agent, and it was found that water can act in this way in other large-pore aluminophosphates, especially for VPI-5 (VFI), a molecular sieve with 18-membered ring channels.[249] A higher degree of water incorporation and the lower degree of template incorporation is also found for the as-synthesized AFI products of the investigated systems. The thermogravimetric analysis of the two different pure phases obtained from experiment 8 after 1 or 3 days of hydrothermal treatment is shown in Figure 7-3.
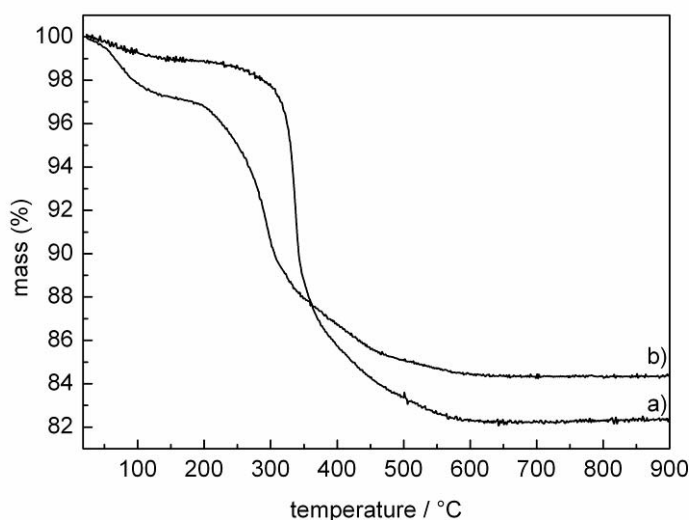
Figure 7-3. Thermogravimetric analysis (TGA) of experiment 8 after a) 3 d (AEI) and b) 1 d (AFI) of hydrothermal treatment at 150 °C.

The AFI phase (b) looses 3 % H_2O at 100 °C, whereas the weight loss at the same temperature corresponds to 1 % in case of the AEI phase (b). At higher temperatures AlPO-5 (AFI) looses another 13 % of its initial weight during the removal of the occluded template. AlPO-18 (AEI) looses 17 %, and the template

removal proceeds within a more narrow temperature range from 300 – 550 °C (a: 200 – 550 °C). Differences in template-framework-interaction can also be investigated by means of Raman spectroscopy, as the vibrational modes of the template change due to the confined space within the pores of the molecular sieve. Raman spectra of the TEA$^+$ ion within the channels of zeolite beta (BEA) have been analyzed by Mihailova et al.[250] The results of the corresponding measurements of the aluminophosphates obtained in the high throughput setup are shown in Figure 7-4.
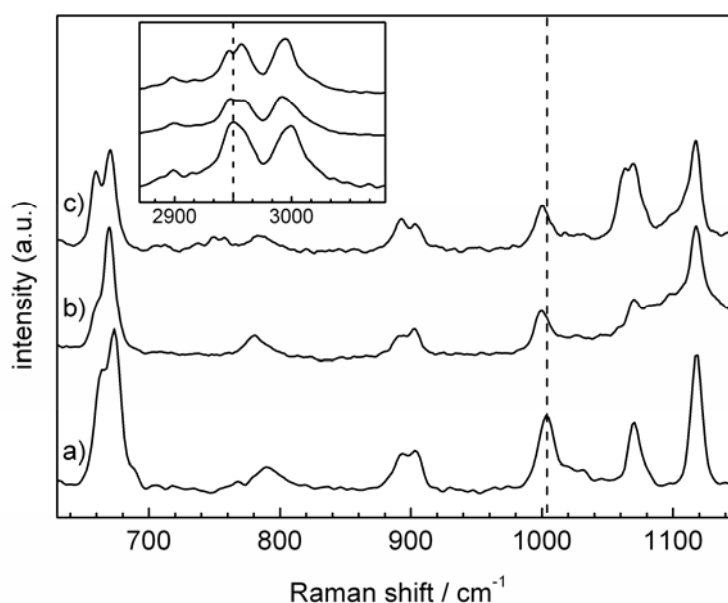
Figure 7-4. Raman spectra of a) TEAOH 35 wt.% in H_2O, as-synthesized product of experiment 8 after b) 1 and c) 3 d of hydrothermal treatment at 150 °C. The inset corresponds to the spectral range generated by C-H bond stretching vibrations. The dashed lines trace positions of the peaks in the TEAOH spectrum that have a detectable red-shift.

The three-dimensional confinement of the TEA$^+$ ion within the cages of the AEI structure (c) leads to a change in the intensity ratio between the peaks at 664 and 674 cm^{-1}, whereas this ratio becomes close to zero in the AFI spectrum (b).

Additionally, the intensity ratio for the two peaks at 890 and 903 cm^{-1} changes contrarily. Most probably, the Raman scattering at 890 cm^{-1} arises from the asymmetrical C-N bond stretching modes of TEA$^+$, whereas the Raman scattering at 660 – 680 cm^{-1} is generated by stretching modes of the whole C-C-N chain. Further, there is a detectable red-shift of the peak at 1003 cm^{-1}, related to CH$_2$ modes, as well as splitting and a red-shift of the band at 2952 cm^{-1}, which originates from a C-H bond stretching mode. These lower-energy shifts are due to the interactions of the H atoms from TEA$^+$ with the surrounding framework atoms.

The addition of seeds to the experiments 13 – 24 resulted in an enhancement of product formation kinetics in those mixtures yielding AEI (experiments 13, 19, 20). No effect was observed at TEA$_2$O molar fractions below 0.6. Apparently, the relatively low pH resulting from the reduced amount of base in these experiments leads to dissolution of the seed crystals, rather than to heterogeneous nucleation on the surface of the added material.

Apart from the observed re-crystallization trend, an interesting feature concerning the morphology of the synthesized AlPO-5 (AFI) phase was observed in the high-throughput setup. Most frequently, AlPO-5 forms crystals of elongated hexagonal form with sizes of 1 – 100 µm. However, the morphology is strongly dependent on the type of SDA and other synthesis conditions. Most often, triethylamine or tri-*iso*-propylamine are used in order to obtain large single crystals which are suited for optical applications.[251-253] The systems in this study differ from most other investigated AlPO-5 gels with

respect to their high reactant concentration. Therefore, high growth rates and relatively small crystal dimensions are expected. SEM images of the samples obtained from the experiments 8 -12 after 1 day of hydrothermal treatment are shown in Figure 7-5. The corresponding experiments differ with respect to the template content (TEA$_2$O molar fraction: 0.6 – 0.2) used for the precursor gel. Accordingly, the pH of the starting gel decreases from experiment 8 – 12 from 3.5 – 2.4. According to XRD, the products contain pure and highly crystalline AlPO-5 (AFI, not shown). It was found that there is an increasing tendency to form spherical agglomerates with decreasing TEAOH content. Both the fraction of the spheres within the sample, and the diameter (~10 – 34 µm) increase in the same direction. SEM images of the interior of these spheres (not shown) reveal a homogeneous aluminophosphate matrix. On the outer surface a mosaic of single crystals with sizes of several microns is found. Therefore, the spheres consist of inter-grown agglomerates, rather than loosely connected aggregates. Apparently, after a certain phase of crystal growth the single crystalline particles aggregate to form spheres, and further growth leads to the final agglomerates.
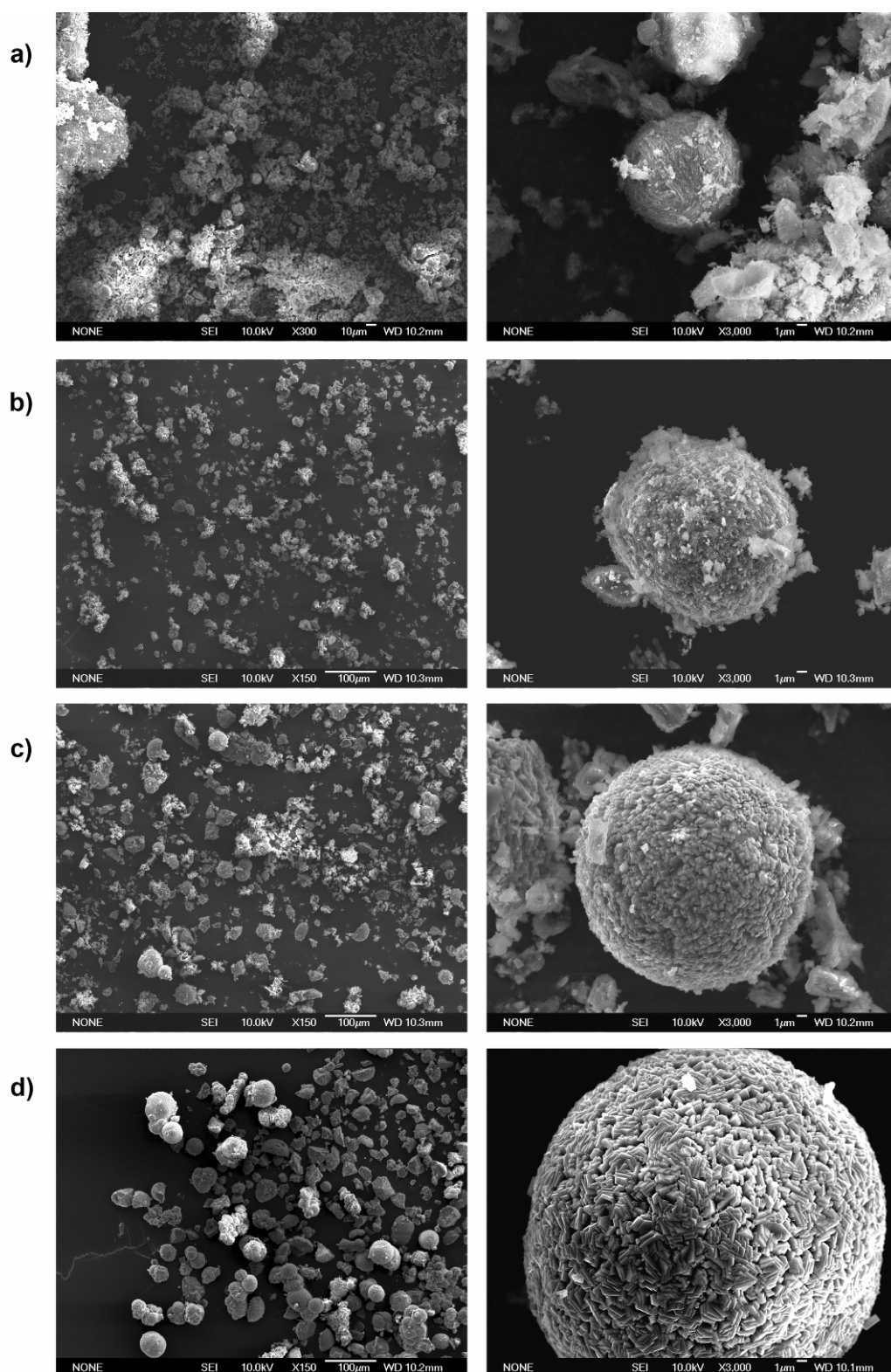
Figure 7-5. SEM images of the experiments 8 (a), 10 (b), 11 (c), and 12 (d) after 1 d of hydrothermal treatment at 150 °C. The images on the left were taken at a magnification of x150 (scale bar: 100 µm, a: x300), images on the right-hand side at a magnification of x3000 (scale bar: 1 µm). The crystalline phase is AFI in each case.

The reason for the aggregation could be the gradual neutralization of pH during the growth phase, and the subsequent decrease of surface charge. When a pH close to the isoelectric point of the material is reached, the particles aggregate to minimize the total surface energy. The degree of aggregation can be lowered sterically by larger amounts of template adsorbed on the particle surface. The effect is assumed to proceed especially in highly concentrated systems as the inter-particle distances within the synthesis mixture are smaller.

7.4.2   Cost reduction by template substitution

Another approach for the establishment of cost-efficient aluminophosphate syntheses is the utilization of organic molecules with a potentially structure-directing effect, which are relatively inexpensive, and/or more or less uncommon in molecular sieve synthesis. In this study, the following molecules were envisaged: triethylamine, morpholine, ammonia, urea, ε-caprolactam, and the tetraammine copper(II)–cation. These compounds were chosen because of their charge-volume-ratio and/or their price. Triethylamine and morpholine are commonly used for molecular sieve synthesis and known to act as templates for AlPO-5 / ZSM-48 and AlPO-34 / ZSM-39, respectively. A detailed study on the use of triethylamine for the synthesis of AlPO-18 is described in Chapter 6. Ammonia is a small-volume molecule known to produce AlPO-15, ECR-5 or phillipsite. Urea and ε-caprolactam are amides (not amines), and were previously not used in aluminophosphate syntheses. The tetraammine copper(II)-complex was investigated as previous experiments in our workgroup yielded porous aluminosilicates with this SDA,[254] and its effect on

aluminophosphate synthesis was of potential interest. For a screening of the template effect of the mentioned molecules a high-throughput experiment with a broad variation of template content was designed (HT 7.2). The molar fraction of the SDA was varied between 0.2 – 1.6 for the six different systems. The compositions of the individual experiments are summarized in Table 7-2. The setup was heated at 150 °C for 1, 3, and 7 d.

All samples were subjected to XRD analyses, and all powder patterns can be found in the appendix. Concerning the structural analysis of the obtained phases, the results can be summarized as follows.

Triethylamine

The experiments using triethylamine as the template led to the formation of AlPO-5 (AFI) in all 4 different template concentrations after 1 day of hydrothermal treatment. Samples 13 and 19 (R = 0.8, 0.2) contained AlPO-H3 (APC) as an impurity, and the ratio of the two phases did not change with increasing synthesis time. At higher template concentrations (R = 1.6, 1.2) complete re-crystallization to AlPO-H3 was observed between a synthesis time of 3 and 7 days. As discussed above, the formation of AlPO-5 (AFI) from NEt$_3$ containing mixtures is known for certain synthesis conditions, but other phases were reported as well.[255-257]

Table 7-2. Compositions of the precursor gels in the high-throughput setup HT 7.2 (150 °C, am = amorphous, AFI = AlPO-5, APC = AlPO-H3, Chr = Christobalite, Tr = Tridymite, A15 = AlPO-15, n.i. = not identified).

No.	Molar oxide ratio				R=	Mass / g									Total mass / g	pH	Product phase(s)		
	Al2O3	P2O5	R	H2O		catapal B	phosphoric acid, 85 %	triethyl amine, 99 %	morpholine, 99.5 %	ammonia, 25 %	urea, 20 %	capro-lactam, 27 %	copper nitrate trihydrate, 45.5 %	water			1 d	3 d	7 d
1	1.0	1.0	1.6	40.0	NEt3	0.754	1.228	0.862						3.156	6.000	3.6	AFI	AFI	APC
2	1.0	1.0	1.6	40.0	C4H9NO	0.770	1.253		0.758					3.220	6.000	3.2	am	am	n.i.
3	1.0	1.0	1.6	40.0	NH3	0.857	1.394			0.658				3.091	6.000	3.4	A15	A15	A15
4	1.0	1.0	1.6	40.0	CH4N2O	0.801	1.304				2.718			1.176	6.000	1.7	am	n.i.	n.i.
5	1.0	1.0	1.6	40.0	C6H11NO	0.742	1.207					3.474		0.577	6.000	1.7	Chr/Tr	Chr/Tr	Chr/Tr
6	1.0	1.0	1.6	40.0	Cu(NO3)2	0.697	1.134						2.613	0.219	6.000	5.0	am	A15	A15
7	1.0	1.0	1.2	40.0	NEt3	0.782	1.273	0.671						3.273	6.000	3.0	AFI	AFI	APC
8	1.0	1.0	1.2	40.0	C4H9NO	0.795	1.294		0.587					3.325	6.000	2.8	Chr	Chr	Chr
9	1.0	1.0	1.2	40.0	NH3	0.863	1.404			0.497				3.236	6.000	3.0	A15	A15	A15
10	1.0	1.0	1.2	40.0	CH4N2O	0.820	1.334				2.086			1.760	6.000	1.7	am	am	am
11	1.0	1.0	1.2	40.0	C6H11NO	0.772	1.257					2.713		1.258	6.000	1.7	Chr/Tr	Chr/Tr	Chr/Tr
12	1.0	1.0	1.2	40.0	Cu(NO3)2	0.697	1.134						2.613	0.219	6.000	5.1	am	A15	A15
13	1.0	1.0	0.8	40.0	NEt3	0.813	1.323	0.465						3.400	6.000	2.6	AFI	AFI	APC/AFI
14	1.0	1.0	0.8	40.0	C4H9NO	0.821	1.337		0.404					3.437	6.000	2.5	Chr	Chr	Chr
15	1.0	1.0	0.8	40.0	NH3	0.869	1.414			0.334				3.384	6.000	2.7	A15	A15	A15
16	1.0	1.0	0.8	40.0	CH4N2O	0.839	1.366				1.424			2.372	6.000	1.8	Chr/Tr	am	am
17	1.0	1.0	0.8	40.0	C6H11NO	0.805	1.311					1.886		1.998	6.000	1.6	Chr/Tr	Chr/Tr	Chr/Tr
18	1.0	1.0	0.8	40.0	Cu(NO3)2	0.697	1.134						2.613	0.219	6.000	5.8	am	A15	A15
19	1.0	1.0	0.2	40.0	NEt3	0.863	1.404	0.123						3.610	6.000	1.9	AFI/APC	AFI/APC	APC/AFI
20	1.0	1.0	0.2	40.0	C4H9NO	0.865	1.408		0.106					3.620	6.000	2.0	Chr/Tr/APC	Chr/Tr/APC	Chr/Tr/APC
21	1.0	1.0	0.2	40.0	NH3	0.878	1.429			0.084				3.609	6.000	2.2	Chr/Tr	Chr/Tr	Chr/Tr
22	1.0	1.0	0.2	40.0	CH4N2O	0.870	1.416				0.369			3.345	6.000	1.8	Chr/Tr	am	Chr/Tr
23	1.0	1.0	0.2	40.0	C6H11NO	0.861	1.401					0.504		3.235	6.000	1.6	Chr/Tr/APC	Chr	Chr/Tr/APC
24	1.0	1.0	0.2	40.0	Cu(NO3)2	0.697	1.134						2.613	0.219	6.000	6.5	am	n.i.	A15

AlPO-H3 is a common impurity in many molecular sieve syntheses as it can be formed from synthesis mixtures containing no organic additives. Therefore, the formation of the structure in NEt_3-containing systems is assumed to be non-specific. The framework consists of PO_4 alternating with AlO_4 tetrahedra and $AlO_4(H_2O)_2$ octahedra. Two-dimensional sheets composed of six-membered rings and two-dimensional sheets of four- and eight-membered rings alternate in the structure.[258] This gives rise to a two-dimensional channel system, and AlPO-H3 was shown to have a reasonable water adsorption capacity. However, the material is thermally unstable above ~250 °C where it transforms into different dense phases.[249, 259]

Morpholine

The use of morpholine under the investigated synthesis conditions did not lead to the formation of porous aluminophosphates, but christobalite and tridymite analog aluminophosphate phases were formed. At low morpholine concentrations AlPO-H3 (APC) was obtained as an impurity. No change in product composition was observed with increasing synthesis time, as christobalite represents a thermodynamically stable dense phase.

Ammonia and tetraammine copper(II) complex

At template concentrations of ≥0.8 pure AlPO-15 was obtained after 1 day of hydrothermal treatment, and the powder patterns did not change with increasing synthesis times. At the lowest template concentration of 0.2 the tridymite analog AlPO was formed after 1 to 7 days. The structure of AlPO-15 consists of

columns of Al-centered corner- and edge-shared octahedra, linked via PO_4 tetrahedra to provide channels approximately parallel to the *b* axis.[260] Ammonium cations occupy the channels and are hydrogen-bonded to framework oxygen atoms and water molecules. The structure collapses upon heating to ~200 °C. AlPO-15 is known to crystallize from NH_3-containing gels between 150 – 200 °C within several hours to days, and seems to be the only stable crystallization product in the investigated NH_3 system.

The same phases obtained with NH_3 as SDA resulted from the corresponding experiments employing Cu^{2+} and NH_3 after 3 to 7 days, indicating that the tetraammine copper(II) complex was not stable in the synthesis mixture or did not act as a structure-directing agent. This was expected, as the complex has a relatively low volume/charge ratio, which is unfavorable for the interaction with near neutral aluminophosphate frameworks.

ε-Caprolactam

From the ε-caprolactam-containing synthesis gels the tridymite analog AlPO phase was obtained in all 4 different mixtures together with variable amounts of AlPO-H3 (APC). No change in product composition was observed with increasing synthesis time, as tridymite represents a thermodynamical stable dense phase.

Urea

The experiments containing urea led to the formation of amorphous AlPO phases together with varying amounts of tridymite AlPOs for template molar

fractions ≤1.2. No change in product composition was observed with increasing synthesis time.

At a molar fraction of urea of 1.6 (no. 4) the evolution of XRD peaks corresponding to an unknown AlPO phase was observed, and a fully crystalline material was obtained after 7 days of hydrothermal treatment.

7.4.3 Urea as structure-directing agent

Based on the latter experiment (no. 4), a high-throughput setup was designed in order to investigate suitable synthesis conditions for the newly found material. In experiment HT 7.3 the molar fraction of urea was varied from 1.6 to 4.8. Additionally, the water content and the aluminum source were varied stepwise. The individual synthesis mixtures are summarized in Table 7-3. The reagent mixtures were heated at 150 °C for 1, 3, and 6 days, respectively.

Table 7-3. Compositions of the precursor gels in the high-throughput setup HT 7.3 (150 °C, am = amorphous, A15 = AlPO-15, n.i. = not identified).

No.	Molar oxide ratio				Mass per experiment / g						Total mass / g	pH	Product phase(s)		
	Al₂O₃	P₂O₅	CH₄N₂O	Na₂O	catapal B	aluminium hydroxide	phosphoric acid, 85 %	urea, 25 %	sodium hydroxide	water			1 d	3 d	6 d
1	1.0	1.0	4.8	0.5	0.517		0.841	4.209	0.146	0.287	6.000	2.8	n.i.	am/n.i.	n.i.
2	1.0	1.0	4.8	0.5	0.389		0.633	3.167	0.110	1.701	6.000	2.8	n.i.	n.i.	n.i.
3	1.0	1.0	4.8	0.5	0.312		0.508	2.539	0.088	2.554	6.000	2.5	n.i.	A15/n.i.	A15/n.i.
4	1.0	1.0	4.8	0.5		0.653	0.841	4.209	0.146	0.151	6.000	3.2	n.i.	n.i.	n.i.
5	1.0	1.0	4.8	0.5		0.491	0.633	3.167	0.110	1.598	6.000	2.1	n.i.	n.i.	n.i.
6	1.0	1.0	4.8	0.5		0.394	0.508	2.539	0.088	2.472	6.000	3.0	n.i.	n.i.	n.i.
7	1.0	1.0	4.8		0.527		0.857	4.290		0.326	6.000	2.0	n.i.	am/n.i.	n.i.
8	1.0	1.0	4.8		0.395		0.642	3.213		1.750	6.000	2.0	n.i.	n.i.	n.i.
9	1.0	1.0	4.8		0.315		0.513	2.568		2.603	6.000	2.0	n.i.	n.i.	n.i.
10	1.0	1.0	4.8			0.665	0.857	4.290		0.187	6.000	2.4	n.i.	n.i.	n.i.
11	1.0	1.0	4.8			0.498	0.642	3.213		1.646	6.000	2.3	n.i.	n.i.	n.i.
12	1.0	1.0	4.8			0.398	0.513	2.568		2.520	6.000	2.3	n.i.	n.i.	n.i.
13	1.0	1.0	3.2		0.560		0.912	3.041		1.487	6.000	1.9	n.i.	n.i.	n.i.
14	1.0	1.0	3.2		0.413		0.672	2.242		2.673	6.000	1.9	n.i.	n.i.	n.i.
15	1.0	1.0	3.2		0.327		0.532	1.775		3.365	6.000	1.9	n.i.	n.i.	n.i.
16	1.0	1.0	3.2			0.708	0.912	3.041		1.340	6.000	2.3	n.i.	n.i.	n.i.
17	1.0	1.0	3.2			0.522	0.672	2.242		2.564	6.000	2.3	n.i.	n.i.	n.i.
18	1.0	1.0	3.2			0.413	0.532	1.775		3.279	6.000	2.2	n.i.	n.i.	n.i.
19	1.0	1.0	1.6		0.598		0.973	1.623		2.806	6.000	1.9	n.i.	n.i.	n.i.
20	1.0	1.0	1.6		0.433		0.705	1.176		3.686	6.000	1.9	am/A15	A15	A15
21	1.0	1.0	1.6		0.340		0.553	0.922		4.186	6.000	1.9	am/A15	am/A15	A15
22	1.0	1.0	1.6			0.755	0.973	1.623		2.648	6.000	2.3	n.i.	n.i.	n.i.
23	1.0	1.0	1.6			0.547	0.705	1.176		3.572	6.000	2.2	n.i.	n.i.	n.i.
24	1.0	1.0	1.6			0.429	0.553	0.922		4.097	6.000	2.3	am	am/A15	am/A15

All products were characterized by means of XRD, and the powder patterns can be found in the appendix. Under nearly all investigated synthesis conditions the previously mentioned unknown phase was obtained. At low template concentrations (R/Al_2O_3 = 1.6, H_2O/Al_2O_3 = 90 – 120) AlPO-15 was obtained after 6 days of hydrothermal treatment. In these experiments the ammonium ion (and not the urea molecule) was found to act as the template for AlPO-15 formation (proven by single crystal X-ray analysis, not shown). Ammonium is known to be a decomposition product of the urea molecule. The powder pattern of the unidentified phase is shown in Figure 7-6. It shows a reflection at 7.6 ° 2Θ, corresponding to a d-value of 11.7 Å. The crystals have plate-like morphologies with undefined geometries (Figure 7-7). The crystal sizes range between 1 and several microns, and intergrowth is observed very frequently.
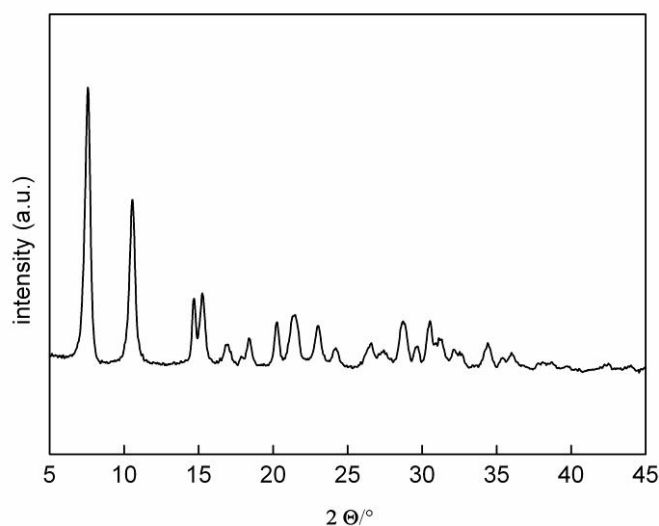
Figure 7-6. XRD pattern of the unidentified phase obtained by using urea as the structure-directing agent (shown: experiment no. 13 of HT 6.1).

No crystals suitable for single crystal X-ray analysis were found in the various products showing the above XRD pattern.
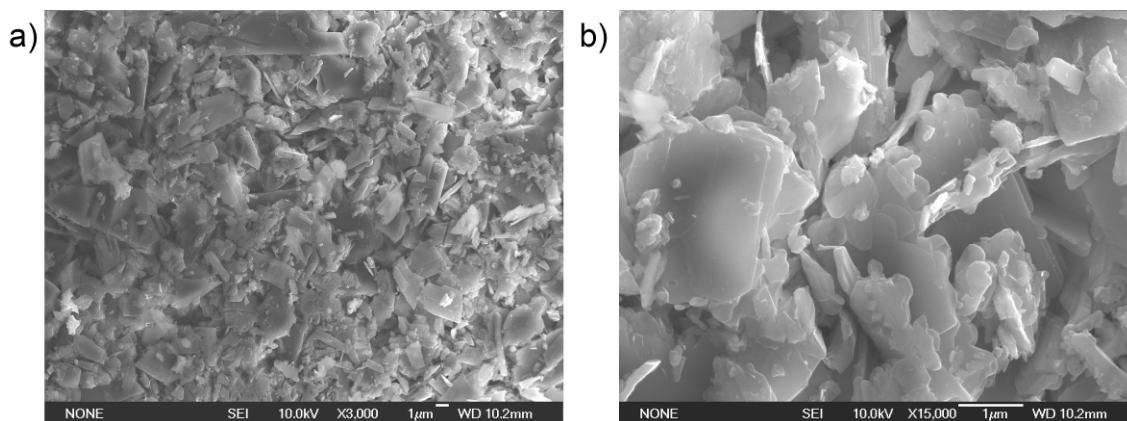
Figure 7-7. SEM images of the unidentified phase obtained by using urea as the structure-directing agent (shown: experiment no. 19 of HT 6.1).

TGA / DSC data are shown in Figure 7-8. A large weight loss of 22 % is observed between ~100 – 400 °C, accompanied by two distinct endothermic peaks in the DSC curve.
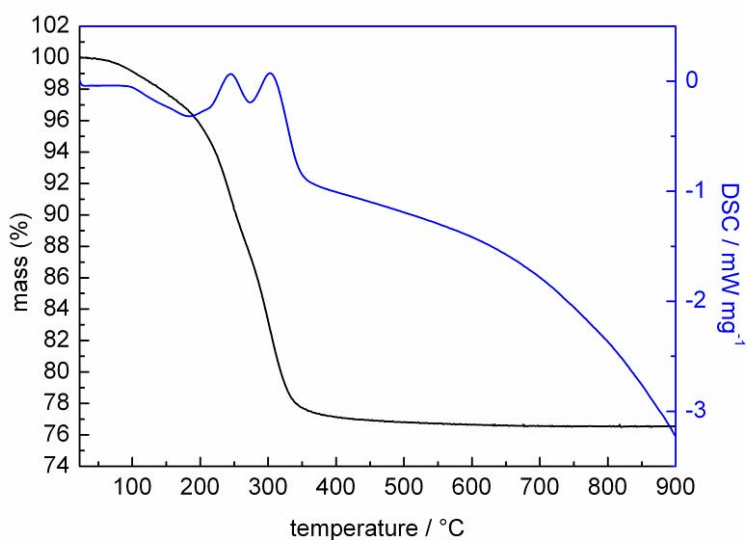
Figure 7-8. TGA / DSC data of the unidentified phase obtained by using urea as the structure-directing agent (shown: experiment no. 19 of HT 6.1).

Upon heating to >400 °C the compound decomposes yielding an X-ray amorphous material. The results of the XRD, SEM, and TG/DSC analyses suggest a layered $AlPO_4 \cdot x \, R \cdot y \, H_2O$ structure.

To investigate the nature of R within the compound Raman spectroscopy was performed (Figure 7-9). Urea shows a very strong peak at 1012 cm^{-1}, assigned to the symmetric C-N-stretching vibration,[261] whereas the compound shows two broad peaks at 1015 cm^{-1} and 1042 cm^{-1}. However, these peaks are unlikely to result from the incorporation of urea, as all other urea-specific peaks were not observed for the unknown compound.
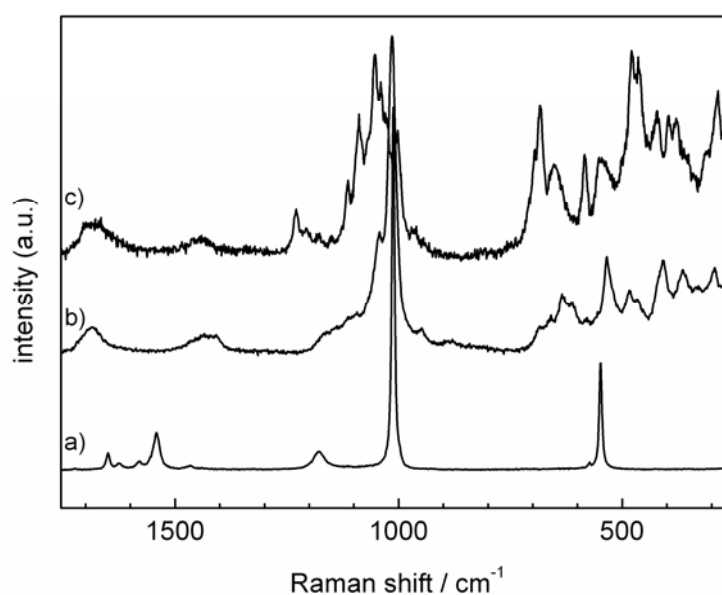
Figure 7-9. Raman spectra of a) solid urea, b) unidentified phase (no. 19 / HT 6.1), c) AlPO-15.

The assignments of the Raman bands for the urea molecule can be found in Table 7-4. Additionally, phosphate groups give rise to one or two bands in the same region (1000 – 1030 cm^{-1}). Therefore, it seems more likely that ammonia

or another decomposition product of urea is present in the structure. In the ^{15}N-MAS NMR (not shown) a peak at -356 ppm, indicative of an amine group, is found. Urea can form different decomposition products upon hydrothermal treatment, e.g., ammonia and cyanic acid or CO_2.[262]

Table 7-4. Assignments of the Raman bands of urea.[261]

Raman bands (wavenumbers/cm^{-1})	Assignment
3434	v_{as} (NH$_2$)
3359	v_s (NH$_2$)
3246	δ_s (NH$_2$)
1649	δ_{as} (NH$_2$)
1624	δ_{as} (NH$_2$)
1580	v (CO)
1542	v (CO)
1466	v_{as} (CN)
1177	ρ_s (NH$_2$)
1012	v_s (CN)
548	δ (CN)

As AlPO-15 was found as a secondary product in experiment 20, after primary crystallization of the unidentified phase, a structural relationship between the two phases is assumed. As the structure collapses upon calcination, no further attempts for the structure determination have been carried out.

7.5 Conclusion

The results of the high-throughput experiment HT 7.1 can be summarized as follows. In the system Al_2O_3 : P_2O_5 : TEA_2O : HCl : H_2O a small reduction of the

molar fraction of TEA_2O to 0.6 is possible whereas a larger reduction leads to crystallization of phase pure AlPO-5. The addition of HCl for pH tuning is not essential. The primary product in all experiments was AlPO-5, and AlPO-18 only appears as a re-crystallization product. With decreasing amounts of template an increased tendency for AlPO-5 to form agglomerated spheres was found, which is attributed to a decreased sterical stabilization by adsorbed template molecules.

In high-throughput experiment HT 7.2, the structure-directing effect of different low-priced templates was investigated. Morpholine and ε-caprolactam did not lead to the formation of porous structures, but the AlPO-analog phases of christobalite and tridymite were formed under all conditions, indicating no templating effect in the investigated systems. The use of ammonia led to AlPO-15 under all conditions, and this phase was previously known to crystallize in such systems. Similarly, the tetraammine copper(II) complex cation led to the formation of AlPO-15, indicating that only the present ammonia could serve as a template. Upon addition of urea to the synthesis mixtures, an unidentified phase with the 100 % XRD reflection at 7.6 ° 2Θ was obtained.

High-throughput experiment HT 7.3 was designed to investigate the synthetic parameters that lead to crystalline AlPO phases when large amounts of urea are present. The unidentified phase was found to crystallize under most investigated conditions. Based on XRD, SEM and TGA data, it seems likely that the phase has a layered AlPO-R structure. At the lowest urea concentrations

(R/Al$_2$O$_3$ = 1.6) AlPO-15 was formed under the templating effect of NH$_4^+$ ions, which result from urea decomposition.

8   General conclusions

The synthesis conditions, leading to nanocrystals of the two (silico)aluminophosphates SAPO-34 and AlPO-18, which are interesting for adsorption heat transformation, were investigated. SAPO-34, a silicoaluminophosphate, which is commercially used as a catalyst for the methanol-to-olefin reaction, was synthesized from clear precursor mixtures. The influence of precursor composition, synthesis temperature, and synthesis time on crystallite size was studied. The products were characterized by means of XRD, SEM, DLS, TGA, IR/Raman, and Argon physisorption. The smallest crystals (<180 nm), having perfect cubic morphology, were obtained from a relatively concentrated mixture at 180 °C using microwave energy for hydrothermal treatment. In order to obtain nanocrystals, a high supersaturation and a high homogeneity of composition and temperature in the synthesis mixture is crucial. After nucleation the remaining nutrients are consumed by crystal growth, and if the system is too concentrated, this process leads to large crystals. Additionally, further processes like agglomeration and Ostwald ripening can proceed. Similarly, the microporous aluminophosphate AlPO-18 was synthesized from colloidal precursor solutions utilizing microwave energy for hydrothermal treatment. Thereby, perfect single-crystalline nanoparticles with plate-like morphology with sizes <260 nm were obtained. The material was characterized by means of X-ray diffraction, electron microscopy, thermogravimetric analysis, and sorption measurements. An increased

micropore volume, compared to AlPO-18 materials from conventional gel syntheses was observed for both nitrogen and water as the probe molecule. This increase is attributed to the more perfect morphology and the avoidance of fault planes and intergrowth.

The suitability of AlPO-18 for heat exchanger applications was tested by preparation of films of increasing thickness (80 – 750 µm) on aluminum supports. Therefore, nanosized and micron-sized AlPO-18 powders were calcined and mixed with polyvinyl alcohol as a binder in aqueous suspensions. Afterwards, the films were prepared by coating and drying at room temperature. The layers were homogeneous and mechanically stable during repeated adsorption/desorption. The kinetics of water adsorption was tested in a specially designed measuring setup, which allowed for both canonical and isobaric measuring modes. The canonical measurements at a starting pressure of 17 mbar showed that the adsorption process is slower with increasing film thickness. Additionally, the kinetics is faster for the nanosized AlPO-18 powders. The averaged mass and heat flow data are indicative for restricted heat flow as the major resistance in the films. Obviously, the larger external crystal surface and differences in the macroprous layer matrix account for increased heat flows when nanocrystals are used.

In order to make AlPO-18 (AEI) applicable for a potential commercial use, synthesis costs, especially those of the tetraethyl ammonium (TEAOH) template have to be decreased. Therefore, high-throughput studies were performed using different strategies, especially template exchange by triethylamine. The

use of this molecule is highly economic as it is produced in large scale industrial production for many organic reactions. It was found that AlPO-18 can be synthesized with triethylamine as the template in a narrow range of synthesis conditions. Most importantly, the pH of the precursor gels needs to be accurately adjusted to a range $5.3 < pH < 6.5$ (at 170 °C). On the one hand, this leads to the template being in its protonated ammonium form. On the other hand, it gives rise to an optimum solubility of the aluminum source. Consequently, amorphous products were obtained at higher pH, and AlPO-5 was formed at $pH < 5$. Additionally, the use of a relatively large template molar ratio ($NEt_3/Al_2O_3 > 2$), a low total reactant concentration ($H_2O/Al_2O_3 > 100$), and a high synthesis temperature ($T > 170$ °C) were found to favor the formation of AlPO-18 over AlPO-5. The obtained material was highly crystalline and porous (after calcination).

Further experiments concerning the reduction of costs for aluminophosphate syntheses were reported in Chapter 7. Reduced amounts of TEAOH led to the formation of AlPO-5 (AFI). At relatively high template concentrations, re-crystallization from the AFI structure to AEI was observed, indicating that high template amounts are crucial for nucleation of AEI. Other investigated templates did not lead to the formation of AlPO-18, but other porous or dense aluminophosphates were obtained. However, the use of urea led to the formation of an unidentified phase, which is assumed to have a layered structure.

9   References

[1]   *Press Release: The Nobel Peace Prize for 2007*, The Norwegian Nobel Committee, Oslo, **2007**.

[2]   R. A. Kerr, E. Kintisch, *Science (Washington, DC, U. S.)* **2007**, *318*, 372.

[3]   M. F. Meier, M. B. Dyurgerov, U. K. Rick, S. O'Neel, W. T. Pfeffer, R. S. Anderson, S. P. Anderson, A. F. Glazovsky, *Science (Washington, DC, U. S.)* **2007**, *317*, 1064.

[4]   M. F. Meier, M. B. Dyurgerov, *Science (Washington, DC, U. S.)* **2002**, *297*, 350.

[5]   K. Emanuel, *Nature (London, U.K.)* **2005**, *436*, 686.

[6]   K. Emanuel, *Nature (London, U.K.)* **2005**, *438*, E13.

[7]   C. W. Landsea, *Nature (London, U.K.)* **2005**, *438*, E11.

[8]   R. A. Pielke, *Nature (London, U.K.)* **2005**, *438*, E11.

[9]   J. Vidal, in *The Guardian*, **2005**.

[10]   J. T. Kerr, H. M. Kharouba, D. J. Currie, *Science (Washington, DC, U. S.)* **2007**, *316*, 1581.

[11]   G.-R. Walther, *Science (Washington, DC, U. S.)* **2007**, *315*, 606.

[12]   G.-R. Walther, E. Post, P. Convey, A. Menzel, C. Parmesan, T. J. C. Beebee, J.-M. Fromentin, O. Hoegh-Guldberg, F. Bairlein, *Nature (London, U.K.)* **2002**, *416*, 389.

[13]   N. Stern, *Stern Review: The Economics of Climate Change*, New Economics Foundation, London, **2006**.

[14] *Climate Change 2007: Impacts, Adaptation and Vulnerability. Contribution of Working Group II to the Fourth Assessment Report of the IPCC*, The Intergovernmental Panel on Climate Change (IPCC), Geneva, **2007**.

[15] *Climate Change 2007: Mitigation. Contribution of Working Group III to the Fourth Assessment Report of the IPCC*, The Intergovernmental Panel on Climate Change (IPCC), Geneva, **2007**.

[16] *Climate Change 2007: The Physical Science Basis. Contribution of Working Group I to the Fourth Assessment Report of the IPCC*, The Intergovernmental Panel on Climate Change (IPCC), Geneva, **2007**.

[17] *Nature (London, U.K.)* **2007**, *449*, 755.

[18] *Emission Database for Global Atmospheric Research 3.2 Fast Track 2000*, The Netherlands Environmental Assessment Agency (MNP), http://www.mnp.nl/edgar/model/v32ft2000edgar/, **2005**.

[19] I. M. Held, B. J. Soden, *Annu. Rev. Energy Environ.* **2000**, *25*, 441.

[20] D. P. Tans, National Oceanic & Atmospheric Administration / Earth System Research Laboratory (NOAA/ESRL), www.esrl.noaa.gov/gmd/ccgg/trends, **2007**.

[21] Carbon Dioxide Information Analysis Center, http://cdiac.ornl.gov/, **2004**.

[22] P. J. Crutzen, A. R. Mosier, K. A. Smith, W. Winiwarter, *Atmos. Chem. Phys. Diss.* **2007**, *7*, 11191.

[23] G. Eisenbeiss, *Physik in Unserer Zeit* **2005**, *36*, 135.

[24] R. F. Service, *Science (Washington, DC, U. S.)* **2007**, *315*, 789.

[25]   B. L. Cohen, *Am. J. Phys.* **1983**, *51*.

[26]   *Statistical Review of World Energy*, BP, London, **2007**.

[27]   *Energy Technology Perspectives*, International Energy Agency (IEA), Paris, **2006**.

[28]   S. Pacala, R. Socolow, *Science (Washington, DC, U. S.)* **2004**, *305*, 968.

[29]   C. Barthel, M. Bunse, W. Irrek, S. Thomas, *Optionen und Potentiale für Endenergieeffizienz und Energiedienstleistungen*, Wuppertal Institut für Klima, Umwelt, Energie GmbH, Wuppertal, **2006**.

[30]   H.-J. Leimkuehler, A. Helbig, *Chem. Ing. Tech.* **2006**, *78*, 367.

[31]   H. M. Aichinger, R. Steffen, *Chem. Ing. Tech.* **2006**, *78*, 397.

[32]   *The cement sustainability initiative*, World Business Council for Sustainable Development (WBCSD), Conches-Geneva, **2002**.

[33]   *Umwelt, Sicherheit und Gesundheit 2006*, BASF AG, Ludwigshafen, **2006**.

[34]   J. Rolker, W. Arlt, *Chem. Ing. Tech.* **2006**, *78*, 416.

[35]   O. Mayer-Spohn, M. Blesl, U. Fahl, A. Voss, *Chem. Ing. Tech.* **2006**, *78*, 435.

[36]   M. Kuehn, C. Clauser, *Chem. Ing. Tech.* **2006**, *78*, 425.

[37]   R. H. Socolow, *Scientific American* **2005**, *293*, 49.

[38]   R. F. Service, *Science (Washington, DC, U. S.)* **2007**, *318*, 730b.

[39]   *Nanotech Could Give Global Warming a Big Chill*, Forbes Inc., New York City, **2006**.

[40]   C. Wunsch, *Science (Washington, DC, U. S.)* **2002**, *298*, 1179.

[41]   P. Foukal, C. Frohlich, H. Spruit, T. M. L. Wigley, *Nature (London, U.K.)* **2006**, *443*, 161.

[42]   N. S. Lewis, *Science (Washington, DC, U. S.)* **2007**, *315*, 798.

[43]   A. P. Goodey, S. M. Eichfeld, K. K. Lew, J. M. Redwing, T. E. Mallouk, *J. Am. Chem. Soc.* **2007**, *129*, 12344.

[44]   J. R. Maiolo, B. M. Kayes, M. A. Filler, M. C. Putnam, M. D. Kelzenberg, H. A. Atwater, N. S. Lewis, *J. Am. Chem. Soc.* **2007**, *129*, 12346.

[45]   M. Gratzel, *Nature (London, U.K.)* **2001**, *414*, 338.

[46]   W. Weiss, I. Bergmann, G. Faninger, *Solar Heating Worldwide - Markets and Contributions to the Energy Supply*, International Energy Agency (IEA), Paris, **2005**.

[47]   H.-M. Henning, *Thermisch aktive Materialien: Grundlagen und Anwendungen*, **2005**.

[48]   P. Feddeck, *Thermochemische Speicher*, Fachinformationszentrum Karlsruhe, Karlsruhe, **2001**.

[49]   F. Meunier, *Clean Technol. Environ. Policy* **2004**, *6*, 187.

[50]   W. Wongsuwan, S. Kumar, P. Neveu, F. Meunier, *Appl. Therm. Eng.* **2001**, *21*, 1489.

[51]   H.-M. Henning, *Appl. Therm. Eng.* **2007**, *27*, 1734.

[52]   M. D. LeVan, *Adsorption processes and modeling: present and future*, Conference on Fundamentals of Adsorption, Giens (France), **1998**.

[53]   *Nanoscience and nanotechnologies: opportunities and uncertainties*, The Royal Society, **2004**.

[54] G. M. Whitesides, *Small* **2005**, *1*, 172.

[55] C. Joachim, *Nat. Mater.* **2005**, *4*, 107.

[56] K. L. Wang, *J. Nanosci. Nanotechnol.* **2002**, *2*, 235.

[57] D. Tasis, N. Tagmatarchis, A. Bianco, M. Prato, *Chem. Rev.* **2006**, *106*, 1105.

[58] K. Suenaga, *AIST Today (Jp. Ed.)* **2003**, *3*, 10.

[59] S. Guo, L. Wang, Y. Wang, Y. Fang, E. Wang, *J. Colloid Interface Sci.* **2007**, *315*, 363.

[60] A. T. Bell, *Science (Washington, DC, U. S.)* **2003**, *299*, 1688.

[61] G. C. Bond, D. T. Thompson, *Catal. Rev. - Sci. Eng.* **1999**, *41*, 319.

[62] T. Blasco, J. M. Lopez Nieto, *Appl. Catal. A* **1997**, *157*, 117.

[63] L. Tosheva, V. P. Valtchev, *Chem. Mater.* **2005**, *17*, 2494.

[64] E. Beham, M. Betz, S. Trumm, M. Kroutvar, Y. Ducommun, H. J. Krenner, M. Bichler, A. Leitenstorfer, J. J. Finley, A. Zrenner, G. Abstreiter, *Phys. Status Solidi C* **2004**, *1*, 2131.

[65] J. Ouellette, *Ind. Phys.* **2003**, *9*, 14.

[66] T. J. Bukowski, J. H. Simmons, *Crit. Rev. Solid State Mater. Sci.* **2002**, *27*, 119.

[67] M. Achermann, A. Petruska Melissa, S. Kos, L. Smith Darryl, D. Koleske Daniel, I. Klimov Victor, *Nature (London, U.K.)* **2004**, *429*, 642.

[68] G. M. Whitesides, B. Grzybowski, *Science (Washington, DC, U. S.)* **2002**, *295*, 2418.

[69]   G. M. Whitesides, J. P. Mathias, C. T. Seto, *Science (Washington, DC, U. S.)* **1991**, *254*, 1312.

[70]   S. Feng, T. Bein, *Nature (London, U.K.)* **1994**, *368*, 834.

[71]   S. Feng, T. Bein, *Science (Washington, DC, U. S.)* **1994**, *265*, 1839.

[72]   G. Yang, G.-Y. Liu, *J. Phys. Chem. B* **2003**, *107*, 8746.

[73]   Y. Xia, B. Gates, Y. Yin, Y. Lu, *Adv. Mater. (Weinheim, Ger.)* **2000**, *12*, 693.

[74]   I. P. Parkin, R. G. Palgrave, *J. Mater. Chem.* **2005**, *15*, 1689.

[75]   R. Savic, L. Luo, A. Eisenberg, D. Maysinger, *Science (Washington, DC, U. S.)* **2003**, *300*, 615.

[76]   T. M. Allen, P. R. Cullis, *Science (Washington, DC, U. S.)* **2004**, *303*, 1818.

[77]   B. G. Trewyn, S. Giri, I. I. Slowing, V. S. Y. Lin, *Chem. Commun.* **2007**, 3236.

[78]   G. E. Moore, *Electronics* **1965**, *38*.

[79]   S. Lloyd, *Nature (London, U.K.)* **2000**, *406*, 1047.

[80]   Y. Shirai, A. J. Osgood, Y. Zhao, K. F. Kelly, J. M. Tour, *Nano Lett.* **2005**, *5*, 2330.

[81]   J. S. Beck, J. C. Vartuli, W. J. Roth, M. E. Leonowicz, C. T. Kresge, K. D. Schmitt, C. T. W. Chu, D. H. Olson, E. W. Sheppard, et al., *J. Am. Chem. Soc.* **1992**, *114*, 10834.

[82]   C. T. Kresge, M. E. Leonowicz, W. J. Roth, J. C. Vartuli, J. S. Beck, *Nature (London, U.K.)* **1992**, *359*, 710.

[83] M. G. Kanatzidis, *Adv. Mater. (Weinheim, Ger.)* **2007**, *19*, 1165.

[84] A. R. Studart, U. T. Gonzenbach, E. Tervoort, L. J. Gauckler, *J. Am. Ceram. Soc.* **2006**, *89*, 1771.

[85] E. S. Toberer, R. Seshadri, *Chem. Commun.* **2006**, 3159.

[86] C. S. Cundy, P. A. Cox, *Chem. Rev. (Washington, DC, U. S.)* **2003**, *103*, 663.

[87] A. Iijima, *Pure Appl. Chem.* **1980**, *52*, 2115.

[88] C. Baerlocher, L. B. McCusker, *Database of Zeolite Structures*, http://www.iza-structure.org/databases/.

[89] J. S. Lee, Y.-J. Lee, E. L. Tae, Y. S. Park, K. B. Yoon, *Science (Washington, DC, U. S.)* **2003**, *301*, 818.

[90] A. Zampieri, G. T. P. Mabande, T. Selvam, W. Schwieger, A. Rudolph, R. Hermann, H. Sieber, P. Greil, *Mater. Sci. Eng., C* **2006**, *26*, 130.

[91] E. M. Flanigen, *Stud. Surf. Sci. Catal.* **2001**, *137*, 11.

[92] R. M. Barrer, *J. Chem. Soc.* **1948**, 2158.

[93] R. M. Barrer, D. W. Riley, *J. Chem. Soc.* **1948**, 133.

[94] R. M. Barrer, *J. Chem. Soc.* **1948**, 127.

[95] R. M. Milton, *Molecular-sieve adsorbents*, US 2882243, **1959**.

[96] R. M. Milton, *ACS Symp. Ser.* **1989**, *398*, 1.

[97] R. M. Barrer, P. J. Denny, *J. Chem. Soc.* **1961**, 971.

[98] G. T. Kerr, G. T. Kokotailo, *J. Am. Chem. Soc.* **1961**, *83*, 4675.

[99] E. M. Flanigen, J. M. Bennett, R. W. Grose, J. P. Cohen, R. L. Patton, R. M. Kirchner, J. V. Smith, *Nature (London, U.K.)* **1978**, *271*, 512.

[100]   S. Mintova, N. H. Olson, T. Bein, *Angew. Chem., Int. Ed.* **1999**, *38*, 3201.

[101]   S. Mintova, N. H. Olson, V. Valtchev, T. Bein, *Science (Washington, DC, U. S.)* **1999**, *283*, 958.

[102]   V. Valtchev, S. Mintova, *Microporous Mesoporous Mater.* **2001**, *43*, 41.

[103]   S. T. Wilson, B. M. Lok, C. A. Messina, T. R. Cannan, E. M. Flanigen, *J. Am. Chem. Soc.* **1982**, *104*, 1146.

[104]   S. T. Wilson, B. M. Lok, E. M. Flanigen, *Crystalline metallophosphate compositions*, EP 043562 B1, **1982**.

[105]   W. Loewenstein, *Am. Mineral.* **1954**, *39*, 92.

[106]   H. O. Pastore, S. Coluccia, L. Marchese, *Annu. Rev. Mater. Res.* **2005**, *35*, 351.

[107]   J. Yu, R. Xu, *Chem. Soc. Rev.* **2006**, *35*, 593.

[108]   F. Cora, C. R. A. Catlow, *J. Phys. Chem. B* **2001**, *105*, 10278.

[109]   P. Feng, X. Bu, T. E. Gier, G. D. Stucky, *Microporous Mesoporous Mater.* **1998**, *23*, 221.

[110]   N. Rajic, *J. Serbian Chem. Soc.* **2005**, *70*, 371.

[111]   X. Bu, T. E. Gier, P. Feng, G. D. Stucky, *Chem. Mater.* **1998**, *10*, 2546.

[112]   E. R. Parnham, P. S. Wheatley, R. E. Morris, *Chem. Commun.* **2006**, 380.

[113]   E. R. Parnham, R. E. Morris, *J. Am. Chem. Soc.* **2006**, *128*, 2204.

[114]   M. E. Davis, *Nature (London, U.K.)* **2002**, *417*, 813.

[115]   M. E. Davis, C. Saldarriaga, C. Montes, J. Garces, C. Crowder, *Nature (London, U.K.)* **1988**, *331*, 698.

[116]   C. S. Cundy, P. A. Cox, *Microporous Mesoporous Mater.* **2005**, *82*, 1.

[117]   S. Oliver, A. Kuperman, G. A. Ozin, *Angew. Chem., Int. Ed.* **1998**, *37*, 46.

[118]   F. Taulelle, *Curr. Opin. Solid State Mater. Sci.* **2001**, *5*, 397.

[119]   E. Roland, P. Kleinschmit, in *Ullmann's Encyclopedia of Industrial Chemistry*, 7th Electronic Release ed., Wiley-VCH, Weinheim, **2005**.

[120]   N. Y. Chen, W. E. Garwood, F. G. Dwyer, *Shape Selective Catalysis in Industrial Applications*, Marcel Dekker Inc., New York, **1989**.

[121]   J. Marshall, *New Scientist* **2006**, *189*, 28.

[122]   *Encyclopedia of materials characterization* (Eds.: C. R. Brundle, C. A. Evans, S. Wilson), Butterworth-Heinemann, Boston, **1992**.

[123]   K. S. W. Sing, D. H. Everett, R. A. W. Haul, L. Moscou, R. A. Pierotti, J. Rouquerol, T. Siemieniewska, *Pure Appl. Chem.* **1985**, *57*, 603.

[124]   S. Lowell, J. E. Schields, M. A. Thomas, M. Thommes, *Characterisation of porous solids and powders: surface area, pore size and density*, Kluwer Academic, Dordrecht, The Netherlands, **2004**.

[125]   P. C. Hiemenz, R. Rajagopalan, *Principles of Colloid and Surface Chemistry*, 3rd ed., Marcel Dekker, New York, **1997**.

[126]   T. Bein, *Angew. Chem.* **1999**, *111*, 335.

[127]   J. N. Cawse, *Acc. Chem. Res.* **2001**, *34*, 213.

[128]   H. van Heyden, S. Mintova, T. Bein, *Chem. Mater.* **2008**, *20*, 2956.

[129]   P. Botella, A. Corma, S. Iborra, R. Monton, I. Rodriguez, V. Costa, *J. Catal.* **2007**, *250*, 161.

[130] P. Waller, Z. Shan, L. Marchese, G. Tartaglione, W. Zhou, J. C. Jansen, T. Maschmeyer, *Chem.--Eur. J.* **2004**, *10*, 4970.

[131] V. H. Grassian, S. C. Larsen, H. Alwy, G. Li, *Development of nanocrystalline zeolite materials as environmental catalysts*, 225th ACS National Meeting, New Orleans, United States, **2003**.

[132] S. Mintova, T. Bein, *Adv. Mater. (Weinheim, Ger.)* **2001**, *13*, 1880.

[133] S. Mintova, M. Reinelt, T. H. Metzger, J. Senker, T. Bein, *Chem. Commun.* **2003**, 326.

[134] B. J. Schoeman, E. Babouchkina, S. Mintova, V. P. Valtchev, J. Sterte, *J. Porous. Mater.* **2001**, *8*, 13.

[135] M. Vilaseca, S. Mintova, K. Karaghiosoff, T. H. Metzger, T. Bein, *Appl. Surf. Sci.* **2004**, *226*, 1.

[136] M. Vilaseca, S. Mintova, V. Valtchev, T. H. Metzger, T. Bein, *J. Mater. Chem.* **2003**, *13*, 1526.

[137] Y. Zhang, F. Chen, W. Shan, J. Zhuang, A. Dong, W. Cai, Y. Tang, *Microporous Mesoporous Mater.* **2003**, *65*, 277.

[138] X. Zhou, T. Yu, Y. Zhang, J. Kong, Y. Tang, J.-L. Marty, B. Liu, *Electrochem. Commun.* **2007**, *9*, 1525.

[139] H. van Heyden, S. Mintova, T. Bein, *J. Mater. Chem.* **2006**, *16*, 514.

[140] J. Q. Chen, A. Bozzano, B. Glover, T. Fuglerud, S. Kvisle, *Catal. Today* **2005**, *106*, 103.

[141] J. Jaenchen, D. Ackermann, E. Weiler, H. Stach, W. Broesicke, *Thermochim. Acta* **2005**, *434*, 37.

[142] H. Kakiuchi, S. Shimooka, M. Iwade, K. Oshima, M. Yamazak, S. Terada, H. Watanabe, T. Takewaki, *Kagaku Kogaku Ronbunshu* **2005**, *31*, 273.

[143] K. Oshima, M. Yamazaki, T. Takewaki, H. Kakiuchi, A. Kodama, *Kagaku Kogaku Ronbunshu* **2006**, *32*, 518.

[144] B. M. Lok, C. A. Messina, R. L. Patton, T. R. Gajek, T. R. Cannan, E. M. Flanigen, *Crystalline silicoaluminophosphates*, US 4440871, **1984**.

[145] B. M. Lok, C. A. Messina, R. L. Patton, R. T. Gajek, T. R. Cannan, E. M. Flanigen, *J. Am. Chem. Soc.* **1984**, *106*, 6092.

[146] M. Ito, Y. Shimoyama, Y. Saito, Y. Tsurita, M. Otake, *Acta Crystallogr., Sect. C: Cryst. Struct. Commun.* **1985**, *C41*, 1698.

[147] S. Wilson, P. Barger, *Microporous Mesoporous Mater.* **1999**, *29*, 117.

[148] S. Ashtekar, S. V. V. Chilukuri, D. K. Chakrabarty, *J. Phys. Chem.* **1994**, *98*, 4878.

[149] F. D. P. Mees, L. R. M. Martens, M. J. G. Janssen, A. A. Verberckmoes, E. F. Vansant, *Chem. Commun.* **2003**, 44.

[150] J. Tan, Z. Liu, X. Bao, X. Liu, X. Han, C. He, R. Zhai, *Microporous Mesoporous Mater.* **2002**, *53*, 97.

[151] M. Briend, R. Vomscheid, M. J. Peltre, P. P. Man, D. Barthomeuf, *J. Phys. Chem.* **1995**, *99*, 8270.

[152] B. Vistad, D. E. Akporiaye, K. P. Lillerud, *J. Phys. Chem. B* **2001**, *105*, 12437.

[153] O. B. Vistad, D. E. Akporiaye, F. Taulelle, K. P. Lillerud, *Chem. Mater.* **2003**, *15*, 1639.

[154] O. B. Vistad, D. E. Akporiaye, F. Taulelle, K. P. Lillerud, *Chem. Mater.* **2003**, *15*, 1650.

[155] L. Regli, S. Bordiga, C. Lamberti, K. P. Lillerud, S. I. Zones, A. Zecchina, *J. Phys. Chem. C* **2007**, *111*, 2992.

[156] D. R. Dubois, D. L. Obrzut, J. Liu, J. Thundimadathil, P. M. Adekkanattu, J. A. Guin, A. Punnoose, M. S. Seehra, *Fuel Process. Technol.* **2003**, *83*, 203.

[157] D. Chen, K. Moljord, T. Fuglerud, A. Holmen, *Microporous Mesoporous Mater.* **1999**, *29*, 191.

[158] D. Chen, H. P. Rebo, A. Holmen, *Chem. Eng. Sci.* **1999**, *54*, 3465.

[159] D. Chen, H. P. Rebo, K. Moljord, A. Holmen, *Ind. Eng. Chem. Res.* **1999**, *38*, 4241.

[160] I. M. Dahl, R. Wendelbo, A. Andersen, D. Akporiaye, H. Mostad, T. Fuglerud, *Microporous Mesoporous Mater.* **1999**, *29*, 159.

[161] D. A. Lesch, R. L. Patton, *Solution synthesis of aluminophosphate crystalline compositions*, EP 293919 A2, **1988**.

[162] M. Mertens, K. G. Strohmaier, *Process for manufacturing a silicoaluminophosphate molecular sieve*, US 6696032 B2, **2004**.

[163] M. Mertens, K. G. Strohmaier, *Process for manufacture of molecular sieves*, US 6773688 B2, **2004**.

[164] J. Yao, H. Wang, S. P. Ringer, K.-Y. Chan, L. Zhang, N. Xu, *Microporous Mesoporous Mater.* **2005**, *85*, 267.

[165] A. M. Prakash, S. Unnikrishnan, *J. Chem. Soc., Faraday Trans.* **1994**, *90*, 2291.

[166] V. K. La Mer, R. H. Dinegar, *J. Am. Chem. Soc.* **1950**, *72*, 4847.

[167] B. J. Frisken, *Appl. Opt.* **2001**, *40*, 4087.

[168] D. E. Koppel, *J. Chem. Phys.* **1972**, *57*, 4814.

[169] P. K. Dutta, K. M. Rao, J. Y. Park, *J. Phys. Chem.* **1991**, *95*, 6654.

[170] L. Marchese, A. Frache, E. Gianotti, G. Martra, M. Causa, S. Coluccia, *Microporous Mesoporous Mater.* **1999**, *30*, 145.

[171] F. Pechar, D. Rykl, *Zeolites* **1983**, *3*, 329.

[172] K.-H. Schnabel, G. Finger, J. Kornatowski, E. Loeffler, C. Peuker, W. Pilz, *Microporous Mater.* **1997**, *11*, 293.

[173] G. Socrates, *Infrared and Raman Characteristic Group Frequencies*, John Wiley & Sons Ltd, Chichester, **2001**.

[174] P.-P. Knops-Gerrits, D. E. De Vos, E. J. P. Feijen, P. A. Jacobs, *Microporous Mater.* **1997**, *8*, 3.

[175] R. Krishna, J. M. van Baten, *Microporous Mesoporous Mater.* **2008**, *109*, 91.

[176] B. A. Holmberg, H. Wang, J. M. Norbeck, Y. Yan, *Microporous Mesoporous Mater.* **2003**, *59*, 13.

[177] B. A. Holmberg, H. Wang, Y. Yan, *Microporous Mesoporous Mater.* **2004**, *74*, 189.

[178] Q. Li, D. Creaser, J. Sterte, *Chem. Mater.* **2002**, *14*, 1319.

[179] V. P. Valtchev, K. N. Bozhilov, *J. Phys. Chem. B* **2004**, *108*, 15587.

[180] B.-Z. Zhan, M. A. White, M. Lumsden, J. Mueller-Neuhaus, K. N. Robertson, T. S. Cameron, M. Gharghouri, *Chem. Mater.* **2002**, *14*, 3636.

[181] G. Zhu, S. Qiu, J. Yu, Y. Sakamoto, F. Xiao, R. Xu, O. Terasaki, *Chem. Mater.* **1998**, *10*, 1483.

[182] J. Hedlund, B. Schoeman, J. Sterte, *Chem. Commun.* **1997**, 1193.

[183] R. A. Rakoczy, Y. Traa, *Microporous Mesoporous Mater.* **2003**, *60*, 69.

[184] M. A. Camblor, A. Corma, A. Mifsud, J. Perez-Pariente, S. Valencia, *Stud. Surf. Sci. Catal.* **1997**, *105A*, 341.

[185] M. A. Camblor, A. Corma, S. Valencia, *Microporous Mesoporous Mater.* **1998**, *25*, 59.

[186] G. Zhu, S. Qiu, F. Gao, G. Wu, R. Wang, B. Li, Q. Fang, Y. Li, B. Gao, X. Xu, O. Terasaki, *Microporous Mesoporous Mater.* **2001**, *50*, 129.

[187] H. Du, M. Fang, W. Xu, X. Meng, W. Pang, *J. Mater. Chem.* **1997**, *7*, 551.

[188] S. Mintova, S. Mo, T. Bein, *Chem. Mater.* **1998**, *10*, 4030.

[189] A. Simmen, L. B. McCusker, C. Baerlocher, W. M. Meier, *Zeolites* **1991**, *11*, 654.

[190] S. T. Wilson, B. M. Lok, C. A. Messina, E. M. Flanigen, in *Proceedings of the 6th International Zeolite Conference (IZC)* (Eds.: D. Olson, A. Bisio), Butterworth, Guildford, **1983**.

[191] S. G. Izmailova, E. A. Vasiljeva, I. V. Karetina, N. N. Feoktistova, S. S. Khvoshchev, *J. Colloid Interface Sci.* **1996**, *179*, 374.

[192] K. J. Rao, B. Vaidhyanathan, M. Ganguli, P. A. Ramakrishnan, *Chem. Mater.* **1999**, *11*, 882.

[193] G. A. Tompsett, W. C. Conner, K. S. Yngvesson, *ChemPhysChem* **2006**, *7*, 296.

[194] R. Wendelbo, D. Akporiaye, A. Andersen, I. M. Dahl, H. B. Mostad, *Appl. Catal. A* **1996**, *142*, L197.

[195] T. Maurer, B. Kraushaar-Czarnetzki, *Helv. Chim. Acta* **2001**, *84*, 2550.

[196] M. A. Lambert, B. J. Jones, *J. Thermophysics Heat Transfer* **2005**, *19*, 471.

[197] S. G. Wang, R. Z. Wang, X. R. Li, *Renewable Energy* **2005**, *30*, 1425.

[198] B. Dawoud, U. Vedder, E. H. Amer, S. Dunne, *Int. J. Heat Mass Transfer* **2007**, *50*, 2190.

[199] A. Erdem-Senatalar, M. Tatlier, M. Urgen, *Microporous Mesoporous Mater.* **1999**, *32*, 331.

[200] M. Tatlier, M. Demir, B. Tokay, A. Erdem-Senatalar, L. Kiwi-Minsker, *Microporous Mesoporous Mater.* **2007**, *101*, 374.

[201] M. Tatlier, A. Erdem-Senatalar, in *Proceedings of the 12th International Zeolite Conference (IZC)*, Baltimore, **1999**.

[202] M. Tatlier, A. Erdem-Senatalar, *Stud. Surf. Sci. Catal.* **1999**, *125*, 101.

[203] R. Lang, T. Westerfeld, A. Gerlich, K. F. Knoche, *Adsorption* **1996**, *2*, 121.

[204] M. Tather, A. Erdem-Senatalar, *Microporous Mesoporous Mater.* **1999**, *28*, 195.

[205] M. Tather, S. B. Tantekin-Ersolmaz, A. Erdem-Senatalar, *Stud. Surf. Sci. Catal.* **2001**, *135*, 3249.

[206] J. Jaenchen, D. Ackermann, H. Stach, W. Broesicke, *Sol. Energy* **2004**, *76*, 339.

[207] Y. I. Aristov, I. S. Glaznev, A. Freni, G. Restuccia, *Chem. Eng. Sci.* **2006**, *61*, 1453.

[208] Y. I. Aristov, I. S. Glaznev, A. Freni, G. Restuccia, *Kinet. Catal.* **2006**, *47*, 770.

[209] Y. I. Aristov, I. V. Koptyug, L. G. Gordeeva, L. Y. Il'ina, I. S. Glaznev, *Kinet. Catal.* **2006**, *47*, 776.

[210] Y. I. Aristov, G. Restuccia, G. Cacciola, V. N. Parmon, *Appl. Therm. Eng.* **2001**, *22*, 191.

[211] Y. I. Aristov, M. M. Tokarev, A. Freni, I. S. Glaznev, G. Restuccia, *Microporous Mesoporous Mater.* **2006**, *96*, 65.

[212] M. A. Stanish, D. D. Perlmutter, *Sol. Energy* **1981**, *26*, 333.

[213] S. Henninger, unpublished thesis, (Freiburg), **2007**.

[214] M. Tatlier, A. Erdem-Senatalar, *Microporous Mesoporous Mater.* **2000**, *34*, 23.

[215] B. Dawoud, Y. Aristov, *Int. J. Heat Mass Transfer* **2003**, *46*, 273.

[216] L.-K. Lee, D. M. Ruthven, *J. Chem. Soc., Faraday Trans.* **1979**, *75*, 2406.

[217] D. M. Ruthven, L.-K. Lee, *AIChE J.* **1981**, *27*, 654.

[218] D. M. Ruthven, L.-K. Lee, H. Yucel, *AIChE J.* **1980**, *26*, 16.

[219] T. Gutermuth, W. Kast, *Chem. Ing. Tech.* **1992**, *64*, 650.

[220] W. Kast, *Adsorption aus der Gasphase - Ingenieurwissenschaftliche Grundlagen und technische Verfahren*, VCH Verlag, Weinheim, **1988**.

[221] W. Kast, *Chem. Ing. Tech.* **2001**, *73*, 1150.

[222] W. Kast, *Waerme- und Stoffuebertragung* **1994**, *29*, 447.

[223] W. Polte, A. Mersmann, *Chem. Ing. Tech.* **1986**, *58*, 600.

[224] W. Polte, S. Scholl, A. Mersmann, *Chem. Ing. Tech.* **1985**, *57*, 789.

[225] M. Tather, B. Tantekin-Ersolmaz, A. Erdem-Senatalar, *Microporous Mesoporous Mater.* **1999**, *27*, 1.

[226] L. Schnabel, H.-M. Henning, *Experimental and simulation study on the kinetics of water vapor adsorption on different kinds of adsorptive material matrices*, International Sorption Heat Pump Conference, Broomfield, Colorado, USA, **2005**.

[227] H.-J. Bart, U. von Gemmingen, in *Ullmann's Encylopedia of Industrial Engineering*, 7th Electronic Release ed., Wiley-VCH, Weinheim, **2005**.

[228] P. D. M. Hughes, P. J. McDonald, M. R. Halse, B. Leone, E. G. Smith, *Phys. Rev. B: Condens. Matter* **1995**, *51*, 11332.

[229] L. Bonaccorsi, A. Freni, E. Proverbio, G. Restuccia, F. Russo, *Microporous Mesoporous Mater.* **2006**, *91*, 7.

[230] C. D. Madhusoodana, R. N. Das, Y. Kameshima, K. Okada, *J. Porous. Mater.* **2005**, *12*, 273.

[231] M. M. Mohamed, F. I. Zidan, M. Thabet, *Microporous Mesoporous Mater.* **2008**, *108*, 193.

[232] R. K. Vempati, R. Borade, R. S. Hegde, S. Komarneni, *Microporous Mesoporous Mater.* **2006**, *93*, 134.

[233] A. V. Rawtani, M. S. Rao, K. V. G. K. Gokhale, *Ind. Eng. Chem. Res.* **1989**, *28*, 1411.

[234] S. Ernst, J. Weitkamp, *Chem. Ing. Tech.* **1991**, *63*, 748.

[235] F. J. Machado, C. M. Lopez, M. A. Centeno, C. Urbina, *Appl. Catal. A* **1999**, *181*, 29.

[236] C. J. Plank, E. J. Rosinski, M. K. Rubin, *Synthetic, crystalline, zeolitic molecular sieves, and their manufacture*, US 4994251, **1991**.

[237] W. Schwieger, K. H. Bergk, D. Freude, M. Hunger, H. Pfeifer, *ACS Symp. Ser.* **1989**, *398*, 274.

[238] M. Smaihi, O. Barida, V. Valtchev, *European Journal of Inorganic Chemistry* **2003**, 4370.

[239] V. Valtchev, S. Rigolet, K. N. Bozhilov, *Microporous Mesoporous Mater.* **2007**, *101*, 73.

[240] V. P. Valtchev, T. Bein, *Synthesis and stabilisation of nanoscale zeolite particles*, WO 0240403 A1, **2002**.

[241] V. P. Valtchev, L. Tosheva, K. N. Bozhilov, *Langmuir* **2005**, *21*, 10724.

[242] O. Larlus, S. Mintova, T. Bein, *Microporous Mesoporous Mater.* **2006**, *96*, 405.

[243] P. Concepcion, T. Blasco, J. M. Lopez Nieto, A. Vidal-Moya, A. Martinez-Arias, *Microporous Mesoporous Mater.* **2004**, *67*, 215.

[244] Y. Huang, B. A. Demko, C. W. Kirby, *Chem. Mater.* **2003**, *15*, 2437.

[245] A. Erdem, L. B. Sand, *J. Catal.* **1979**, *60*, 241.

[246] R. M. Barrer, L. Hinds, E. A. White, *J. Chem. Soc.* **1953**, 1466.

[247] R. M. Barrer, C. Marcilly, *J. Chem. Soc. A* **1970**, 2735.

[248] E. Grujic´, B. Subotic´, L. A. Despotovic, *Stud. Surf. Sci. Catal.* **1989**, *49*, 261.

[249] B. Duncan, M. Stocker, D. Gwinup, R. Szostak, K. Vinje, *Bull. Soc. Chim. Fr.* **1992**, *129*, 98.

[250] B. Mihailova, S. Mintova, K. Karaghiosoff, T. Metzger, T. Bein, *J. Phys. Chem. B* **2005**, *109*, 17060.

[251] O. Weiss, G. Ihlein, F. Schuth, *Microporous Mesoporous Mater.* **2000**, *35-36*, 617.

[252] F. Y. Jiang, J. P. Zhai, J. T. Ye, J. R. Han, Z. K. Tang, *J. Cryst. Growth* **2005**, *283*, 108.

[253] R. A. Rakoczy, S. Ernst, M. Hartmann, Y. Traa, J. Weitkamp, *Catal. Today* **1999**, *49*, 261.

[254] J. Kecht, S. Mintova, T. Bein, *Chem. Mater.* **2007**, *19*, 1203.

[255] Q. Huo, R. Xu, S. Li, Y. Xu, Z. Ma, Y. Yue, L. Li, *Proc. Int. Zeolite Conf., 9th* **1993**, *1*, 279.

[256] Q. Huo, R. Xu, S. Li, Z. Ma, J. M. Thomas, R. H. Jones, A. M. Chippindale, *J. Chem. Soc., Chem. Commun.* **1992**, 875.

[257]   C.-F. Cheng, H. He, J. Klinowski, *J. Chem. Soc., Faraday Trans.* **1995**, *91*, 3995.

[258]   J. J. Pluth, J. V. Smith, *Nature (London, U.K.)* **1985**, *318*, 165.

[259]   K. Kunii, K. Narahara, S. Yamanaka, *Microporous Mesoporous Mater.* **2002**, *52*, 159.

[260]   J. B. Parise, *Acta Crystallogr., Sect. C: Cryst. Struct. Commun.* **1984**, *C40*, 1641.

[261]   R. Keuleers, H. O. Desseyn, B. Rousseau, C. Van Alsenoy, *J. Phys. Chem. A* **1999**, *103*, 4621.

[262]   M. L. Kieke, J. W. Schoppelrei, T. B. Brill, *J. Phys. Chem.* **1996**, *100*, 7455.

10 Appendix

List of abbreviations

AlPO   aluminophsophate

BMBF   Bundesministerium für Bildung und Forschung

DFT   density functional theory

DLS   dynamic light scattering

DSC   differential scanning calorimetry

HT   hydrothermal

ICP/AAS   inductively coupled plasma / atomic absorption spectroscopy

IR   infrared

IUPAC   international union of pure and applied chemistry

MW   microwave

NMR   nuclear magnetic resonance

PVOH   polyvinyl alcohol

RT   room temperature

SAM   self-assembled monolayer

SAPO   silicoaluminophosphate

SDA   structure-directing agent

SEM   scanning electron microscopy

TEAOH   tetraethylammonium hydroxide

TEM   transmission electron microscopy

TGA   thermogravimetric analysis

TrEA   triethylamine

XRD   X-ray diffraction

XRD patterns of high-throughput experiment HT 6.1

Figure 10-1. XRD patterns of high-throughput experiment HT 6.1 after 1 d of HT treatment (170 °C).
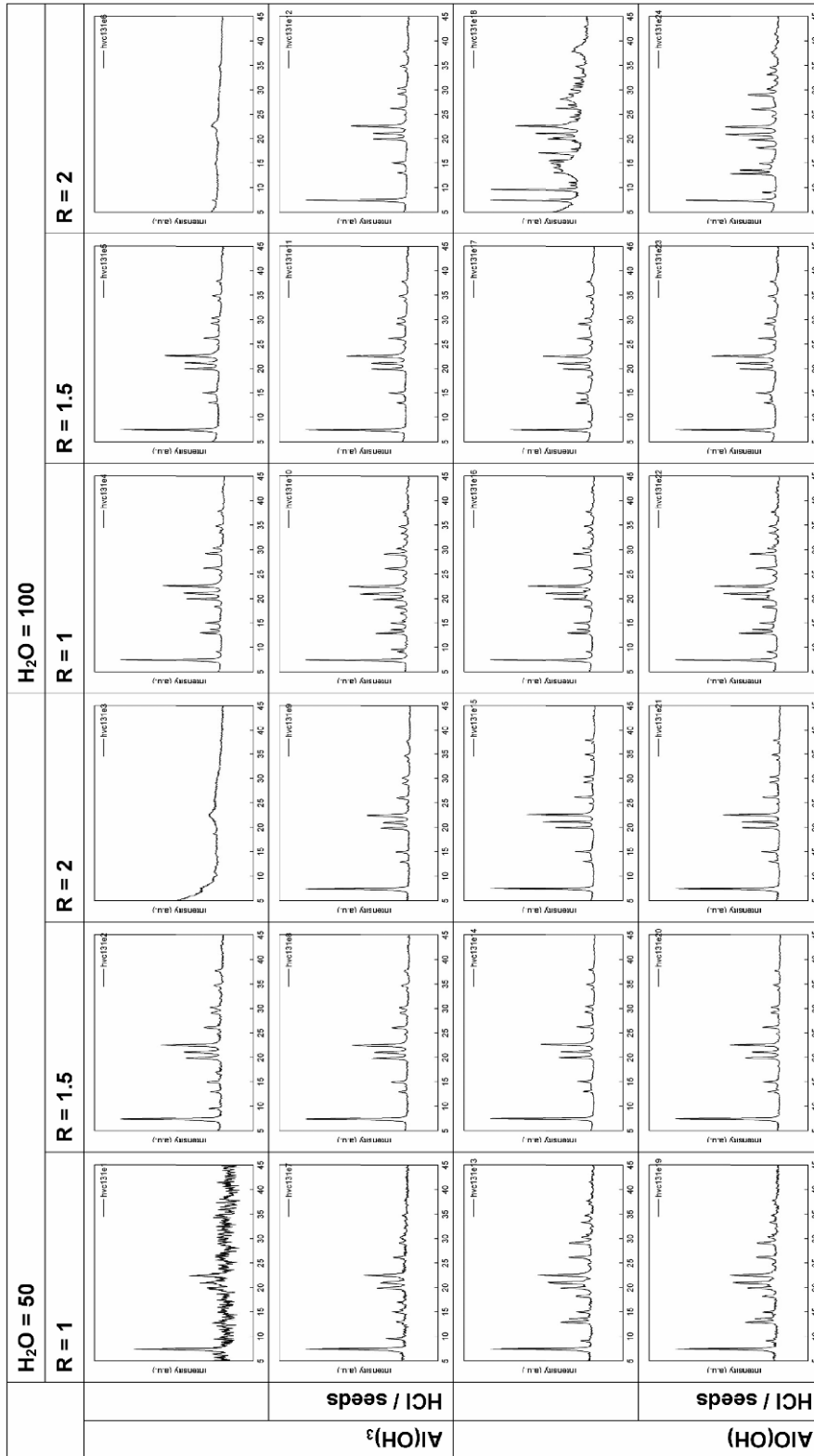
Figure 10-2. XRD patterns of high-throughput experiment HT 6.1 after 4 d of HT treatment (170 °C).
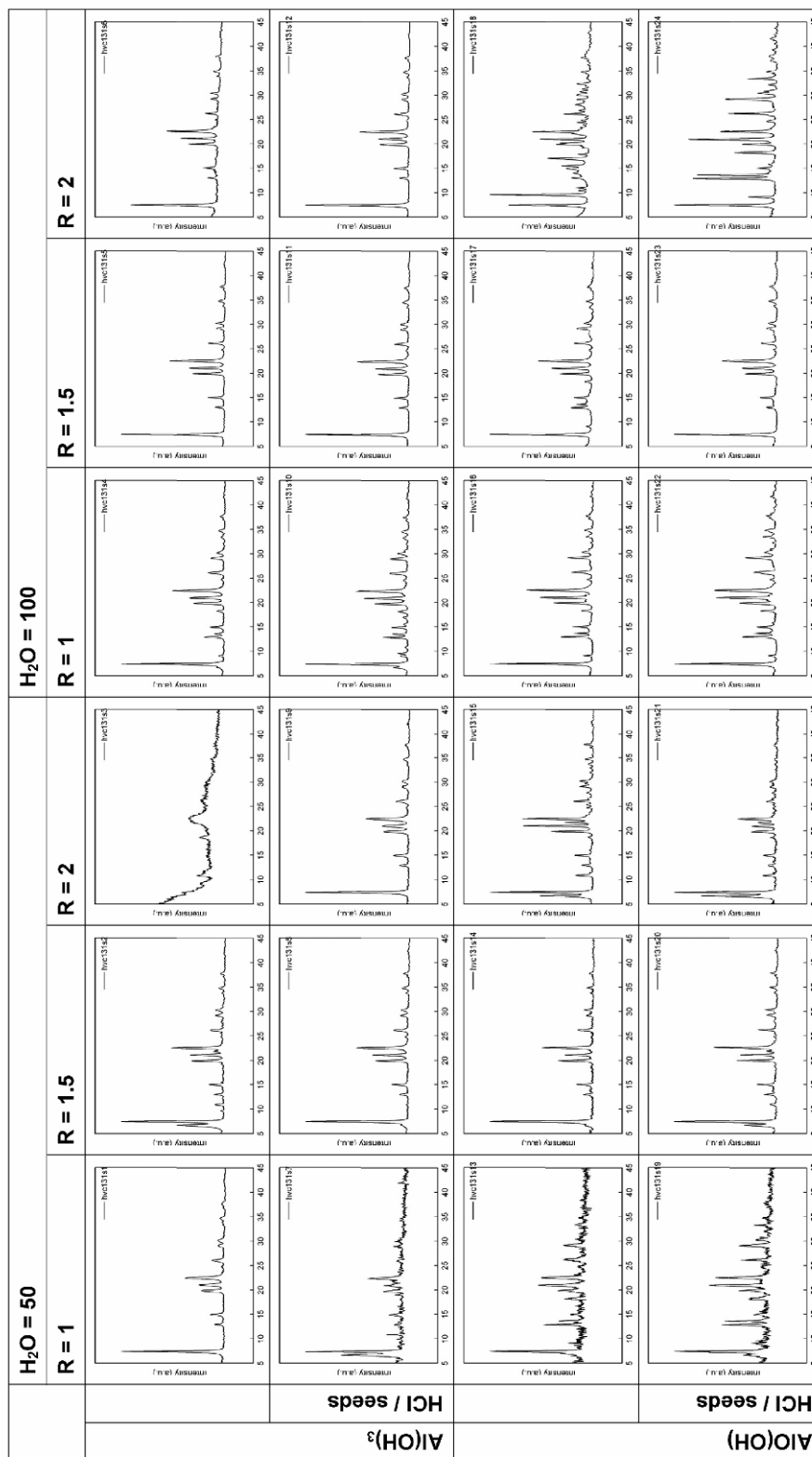
Figure 10-3. XRD patterns of high-throughput experiment HT 6.1 after 12 d of HT treatment (170 °C).
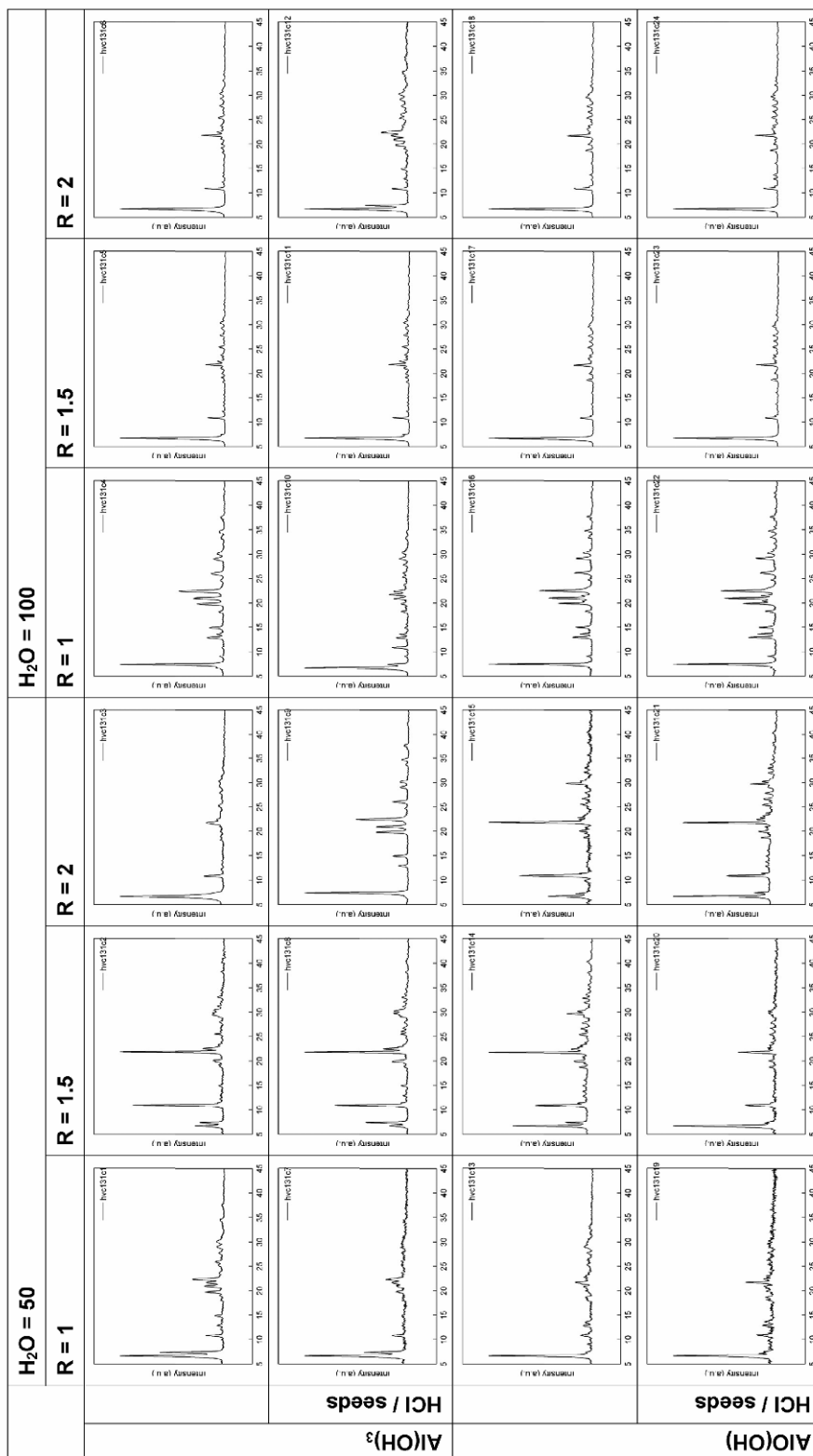
XRD patterns of high-throughput experiment HT 6.2

Figure 10-4. XRD patterns of high-throughput experiment HT 6.2 after 1 d of HT treatment (170 °C).
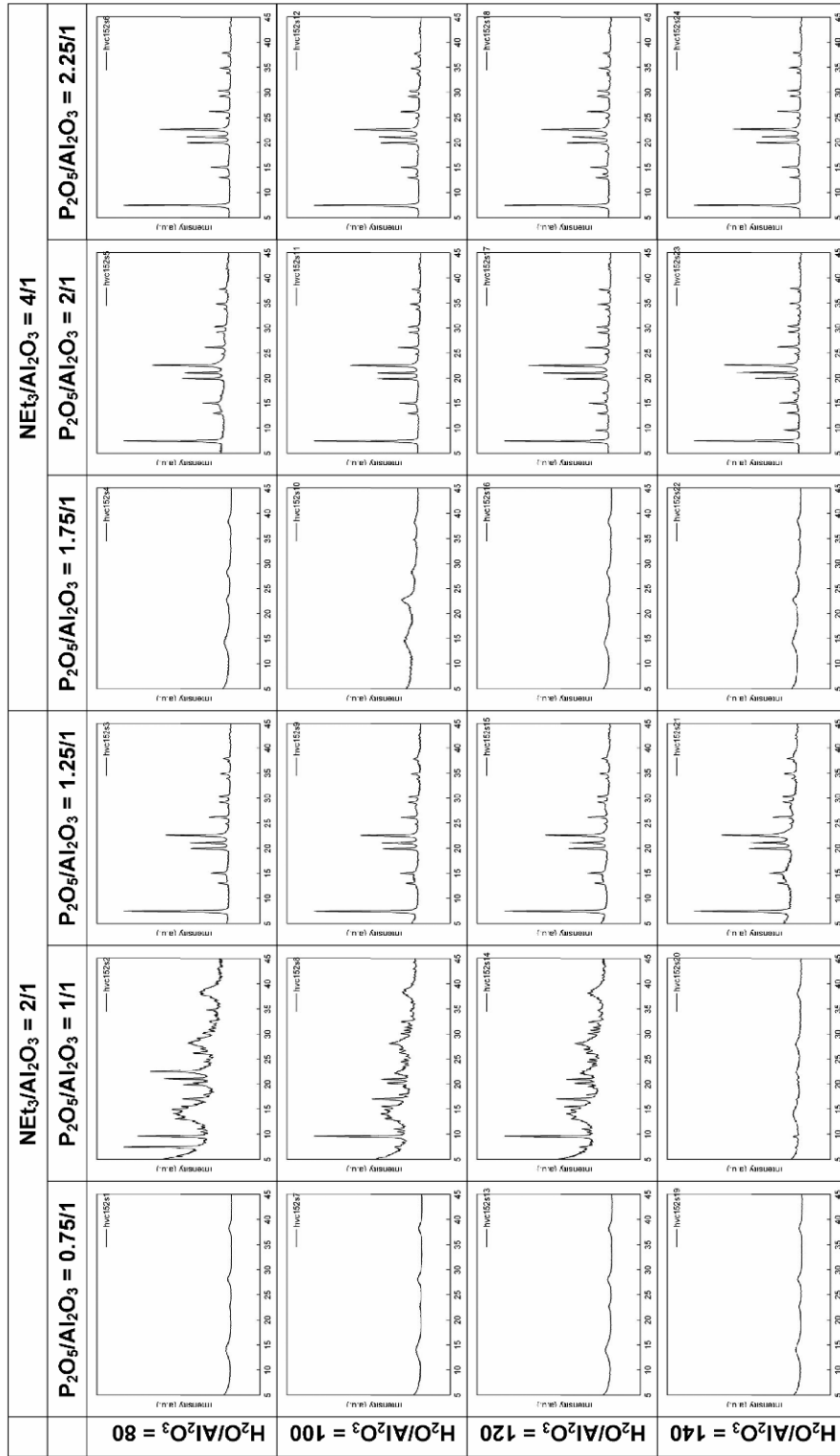
Figure 10-5. XRD patterns of high-throughput experiment HT 6.2 after 3 d of HT treatment (170 °C).
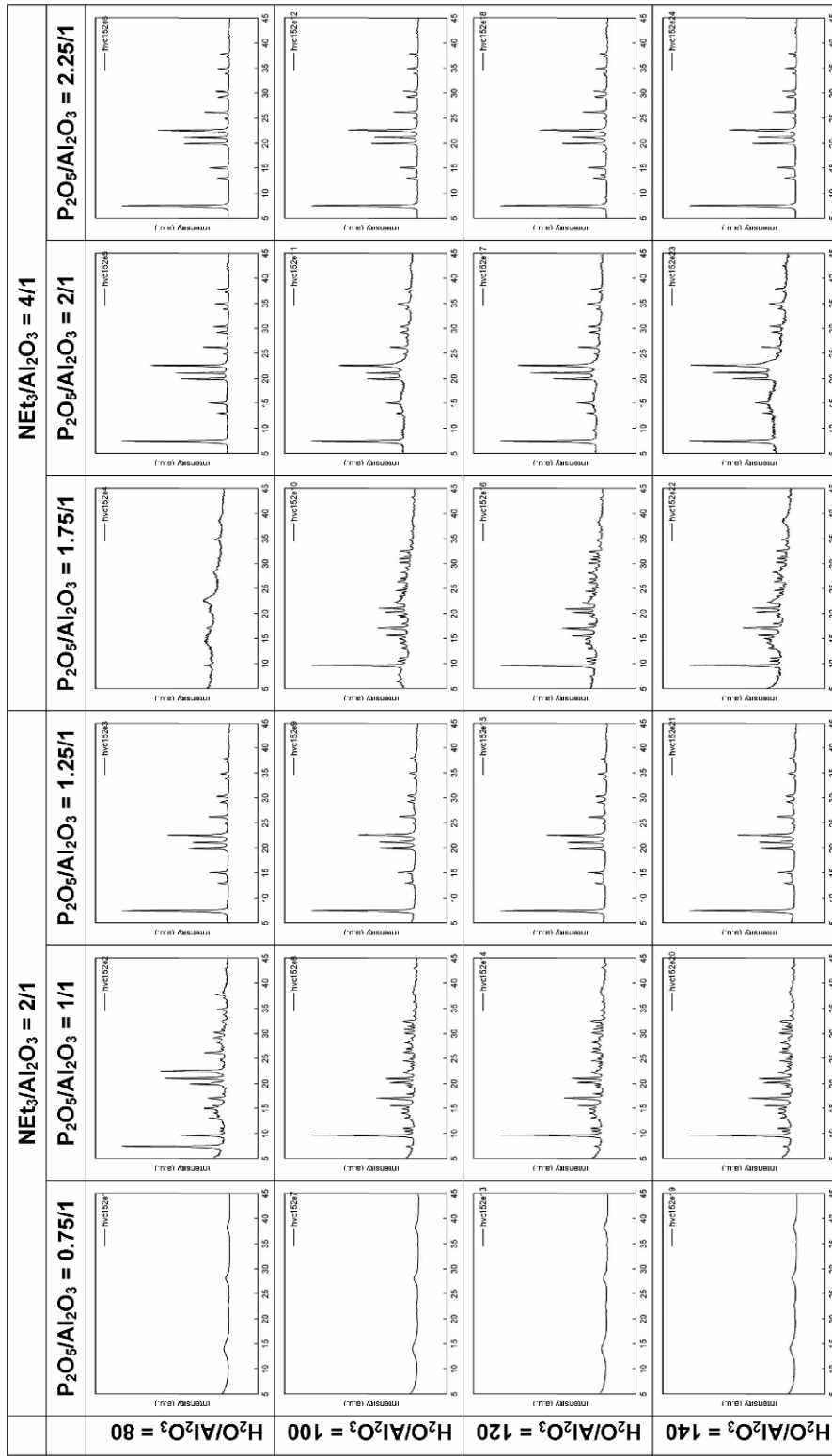
Figure 10-6. XRD patterns of high-throughput experiment HT 6.2 after 5 d of HT treatment (170 °C).
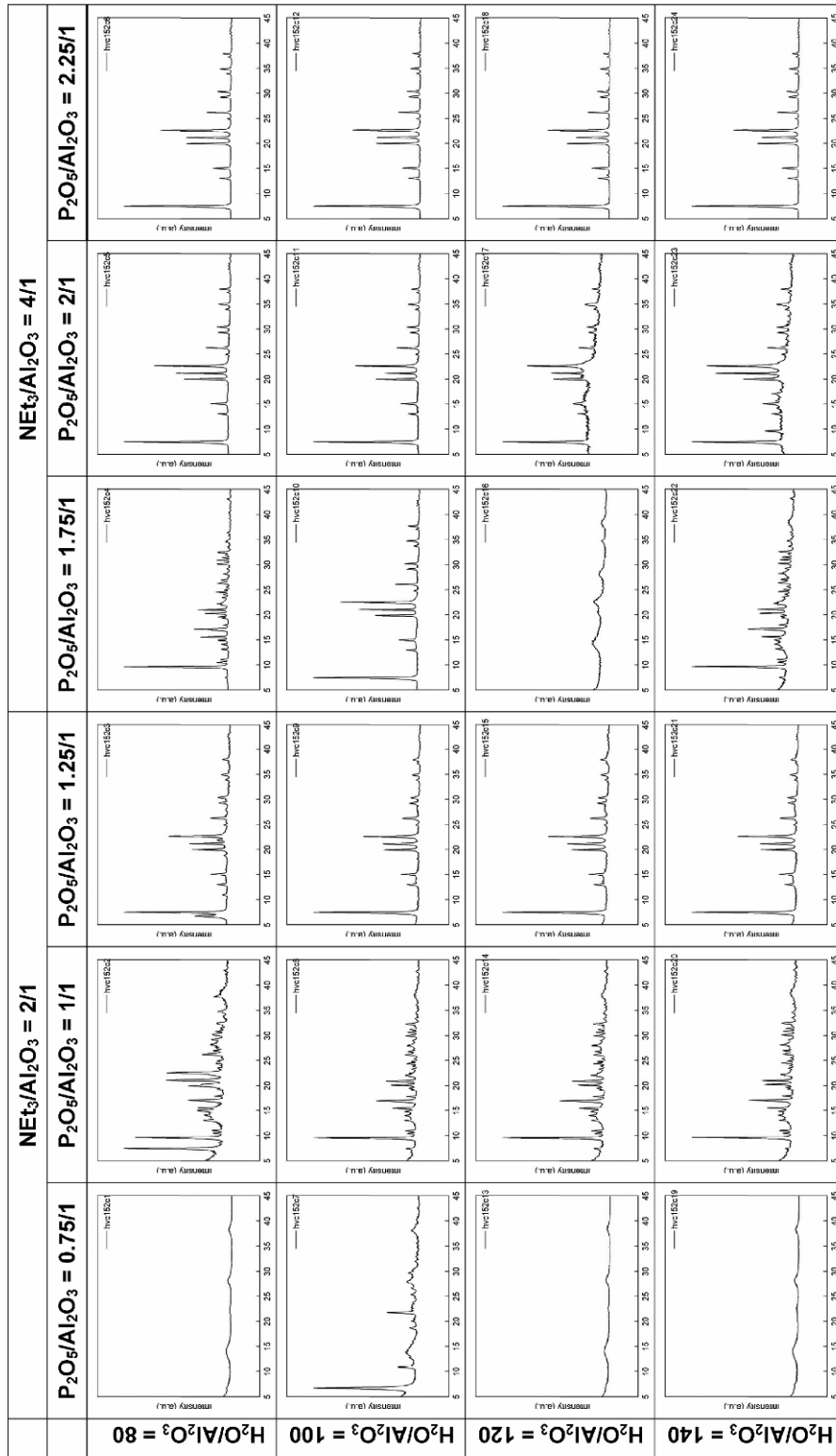
XRD patterns of high-throughput experiment HT 6.3

Figure 10-7. XRD patterns of high-throughput experiment HT 6.3 after 1 d of HT treatment (150 °C).
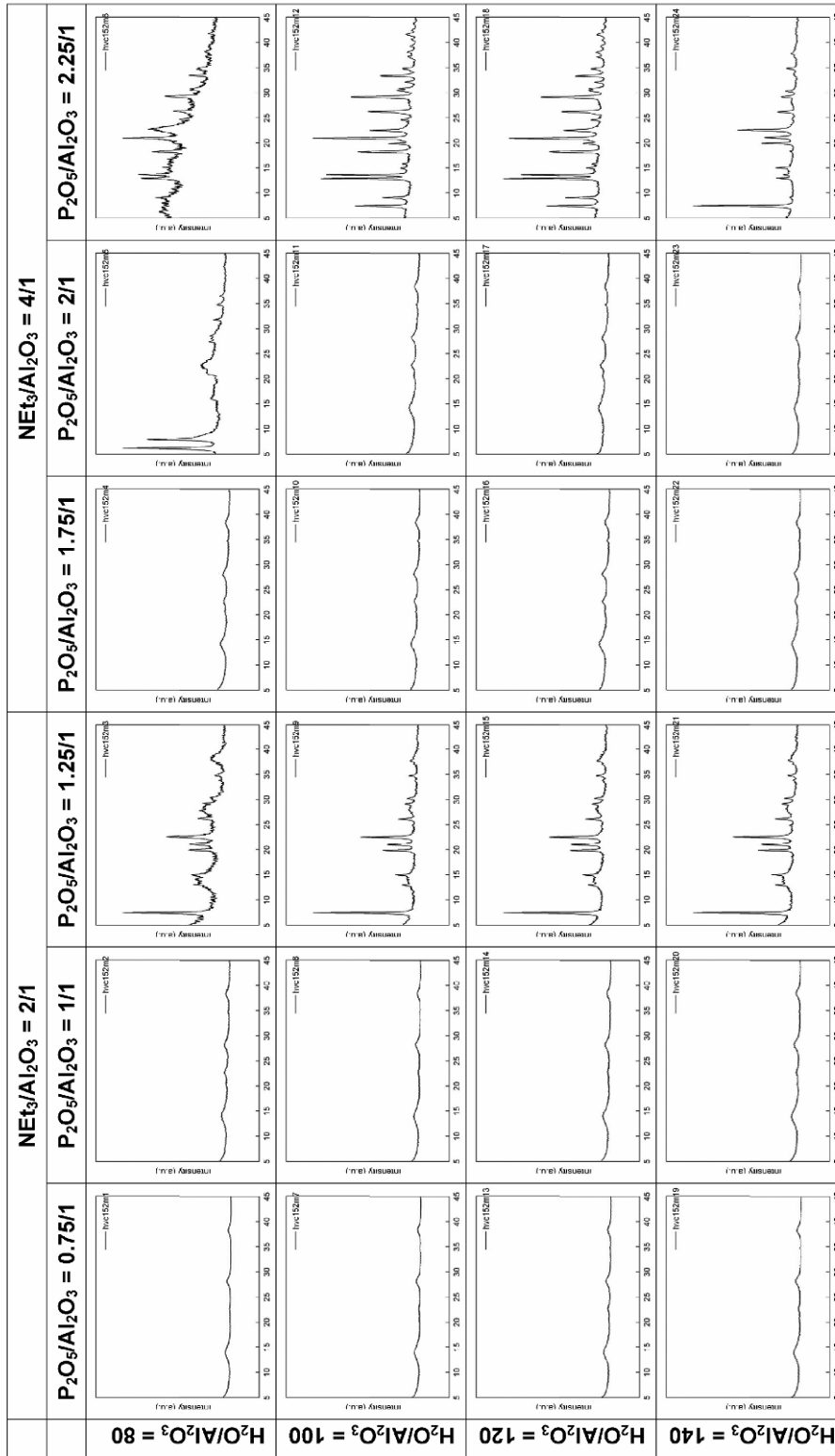
Figure 10-8. XRD patterns of high-throughput experiment HT 6.3 after 3 d of HT treatment (150 °C).
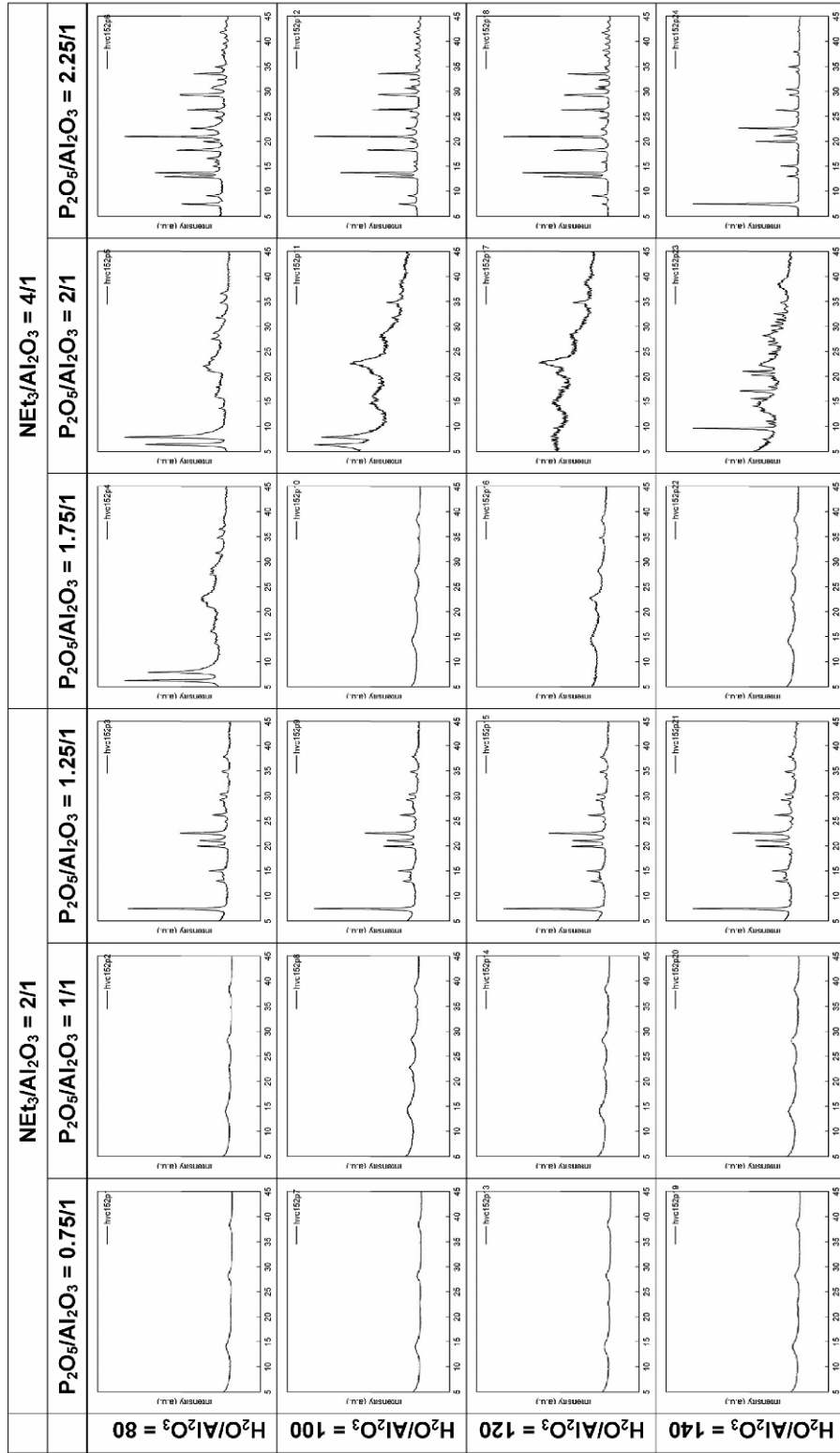
Figure 10-9. XRD patterns of high-throughput experiment HT 6.3 after 5 d of HT treatment (150 °C).
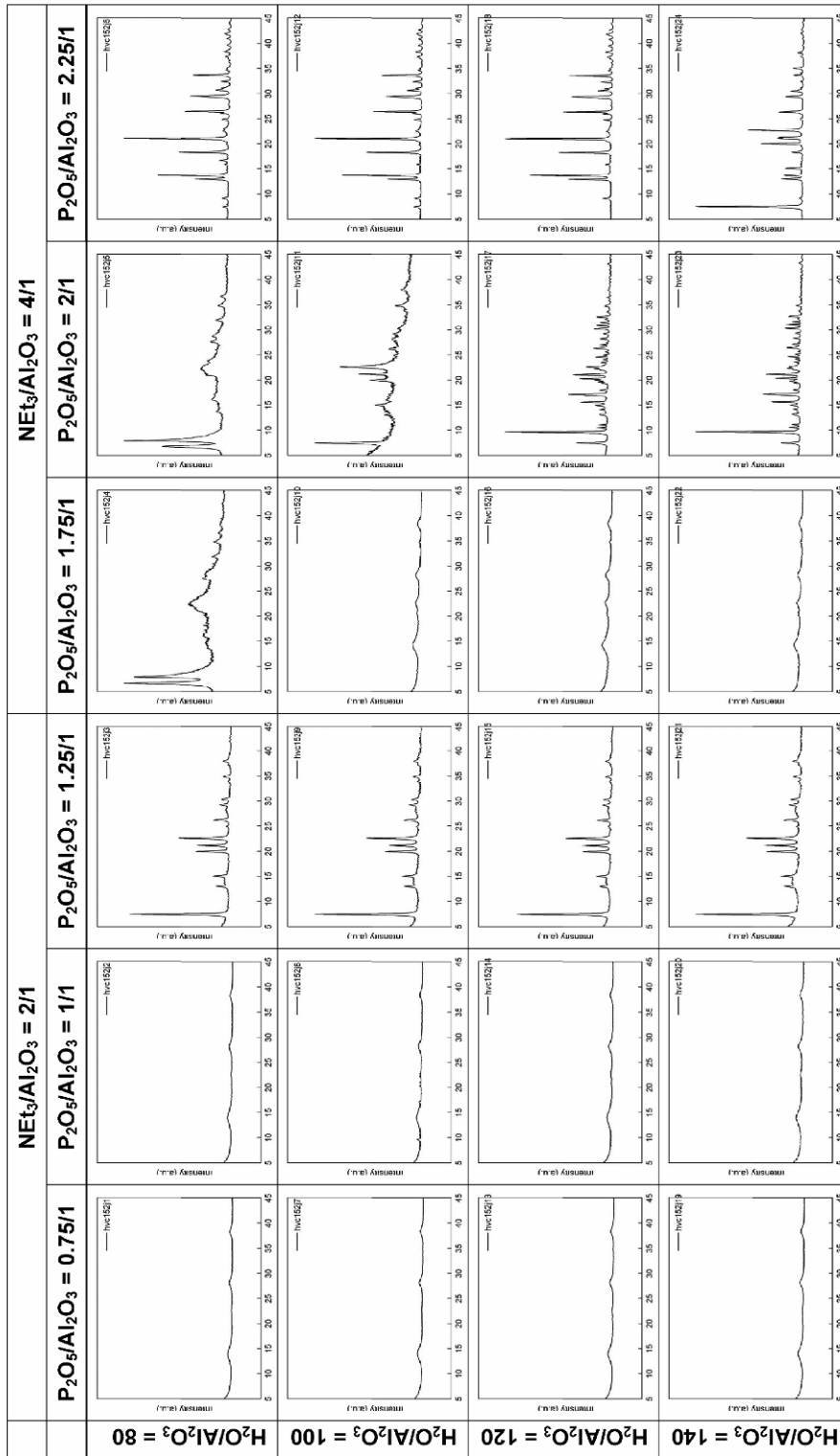
XRD patterns of high-throughput experiment HT 7.1

Figure 10-10. XRD patterns of high-throughput experiment HT 7.1 after 1 d of HT treatment (150 °C).
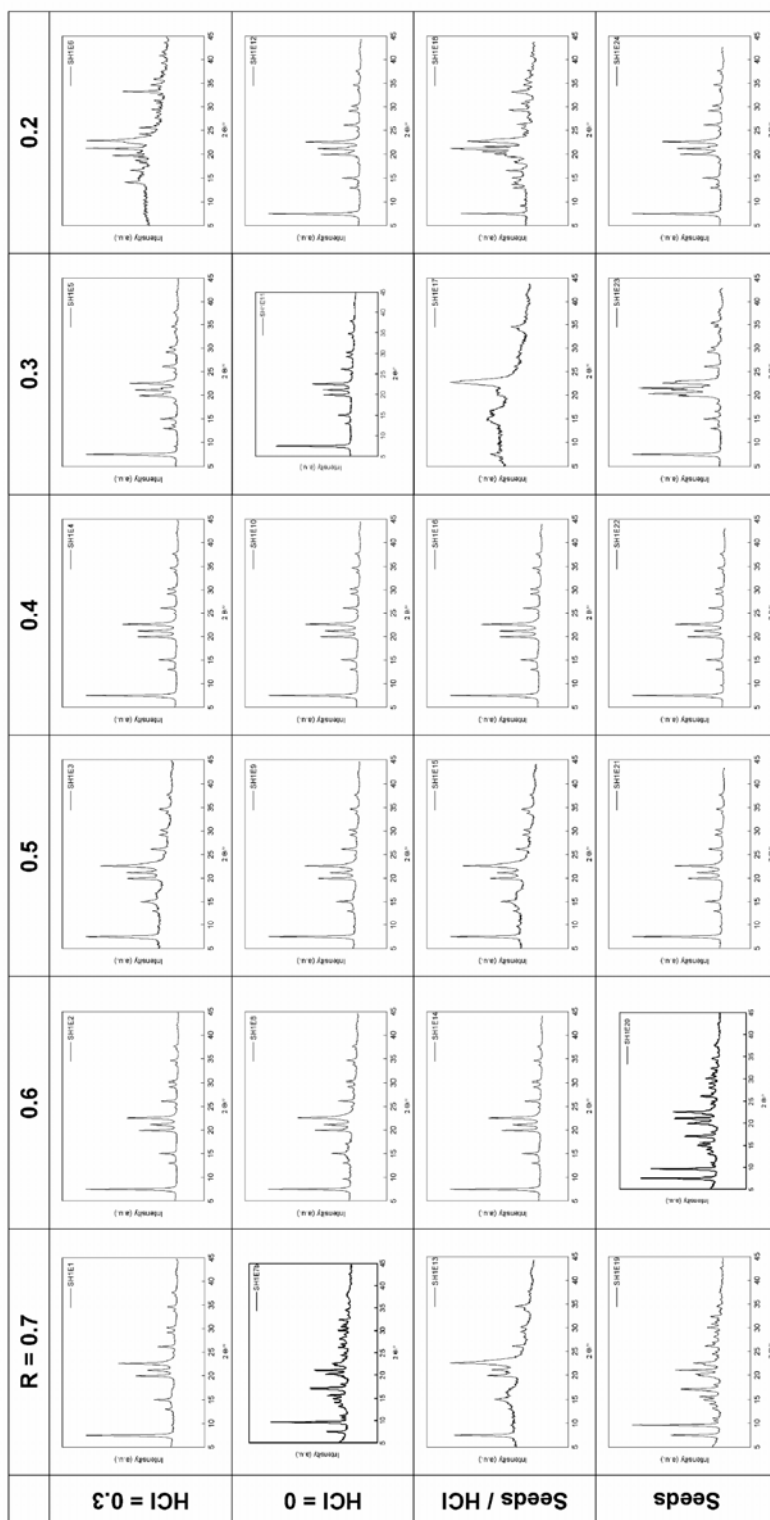
Figure 10-11. XRD patterns of high-throughput experiment HT 7.1 after 2 d of HT treatment (150 °C).
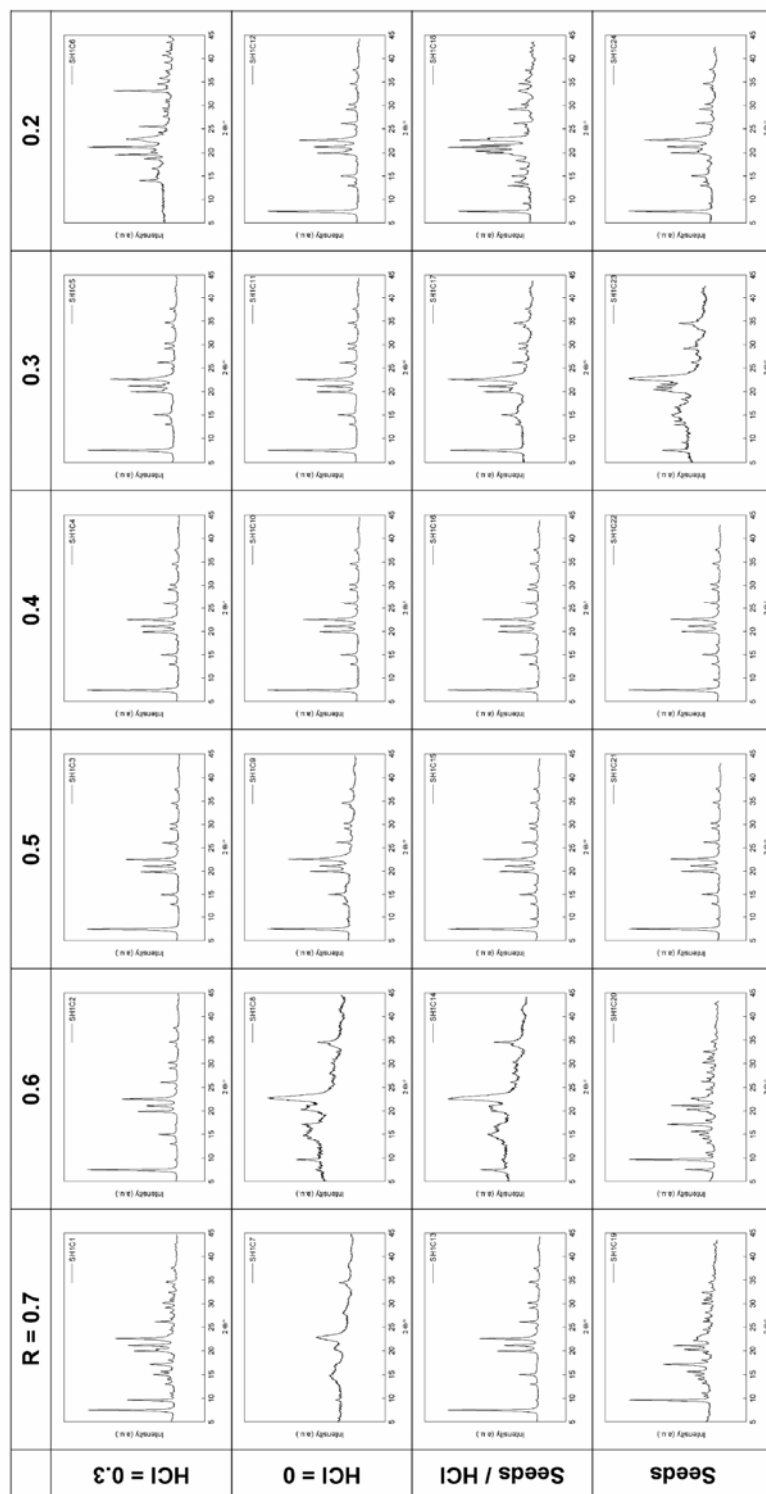
Figure 10-12. XRD patterns of high-throughput experiment HT 7.1 after 3 d of HT treatment (150 °C).
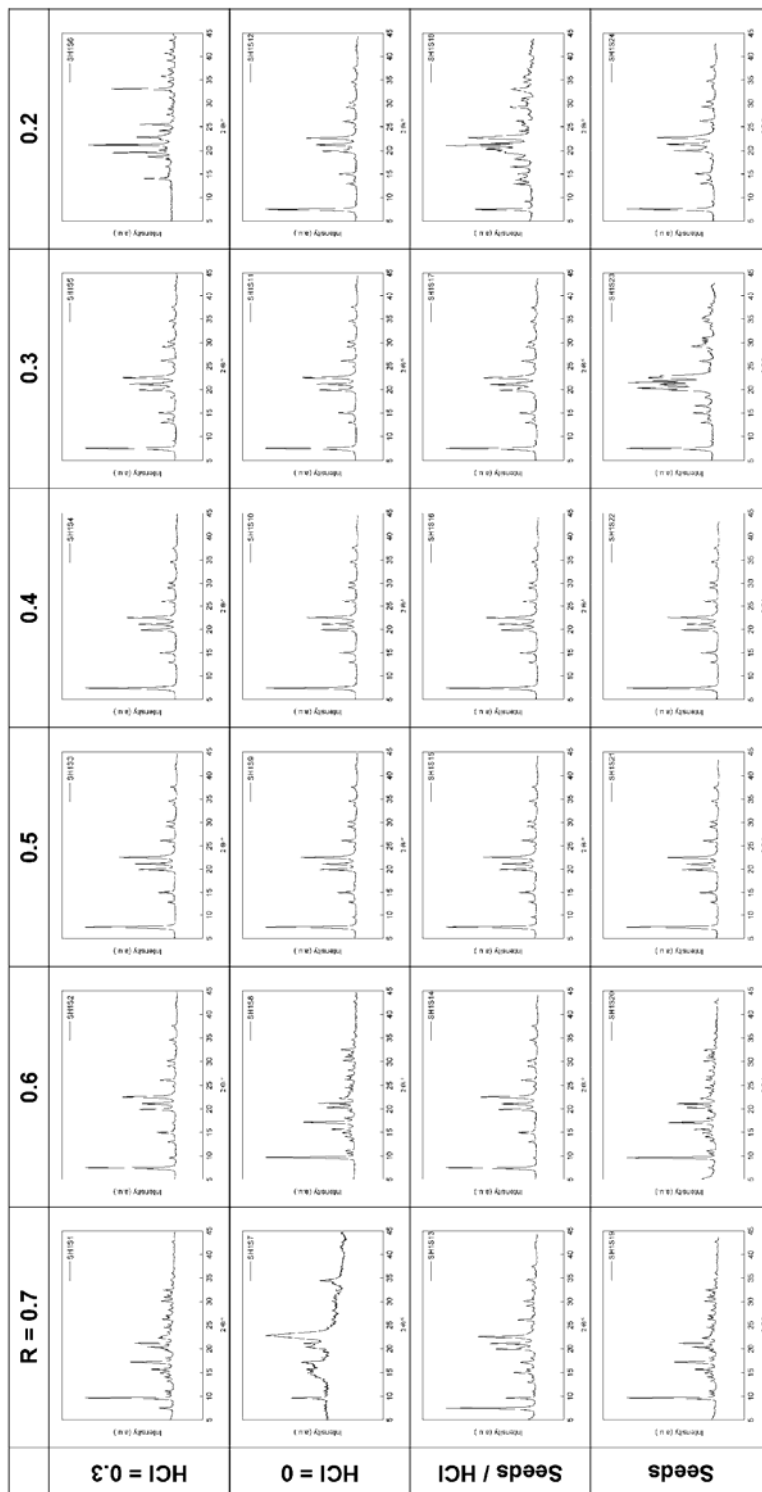
XRD patterns of high-throughput experiment HT 7.2

Figure 10-13. XRD patterns of high-throughput experiment HT 7.2 after 1 d of HT treatment (150 °C).
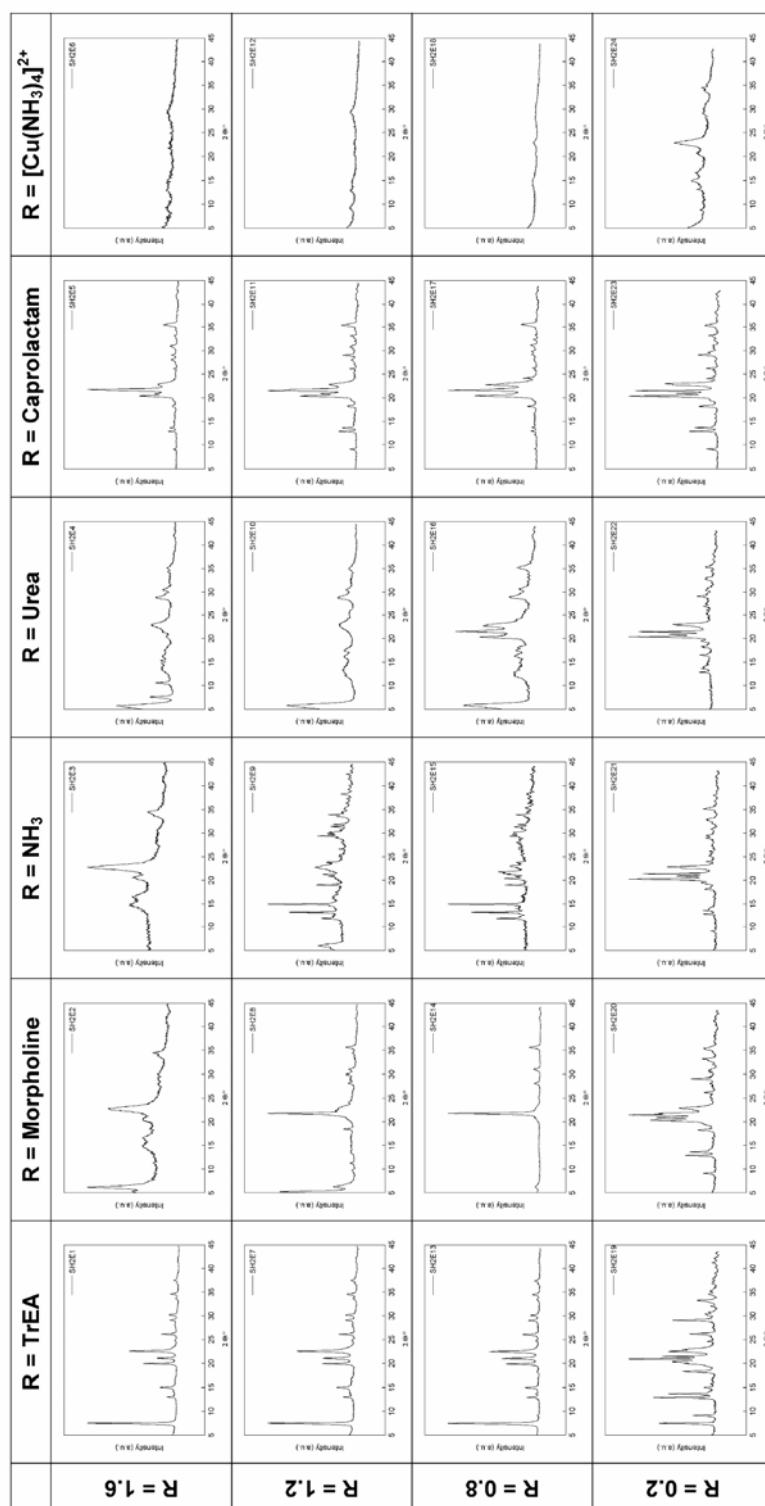
Figure 10-14. XRD patterns of high-throughput experiment HT 7.2 after 3 d of HT treatment (150 °C).
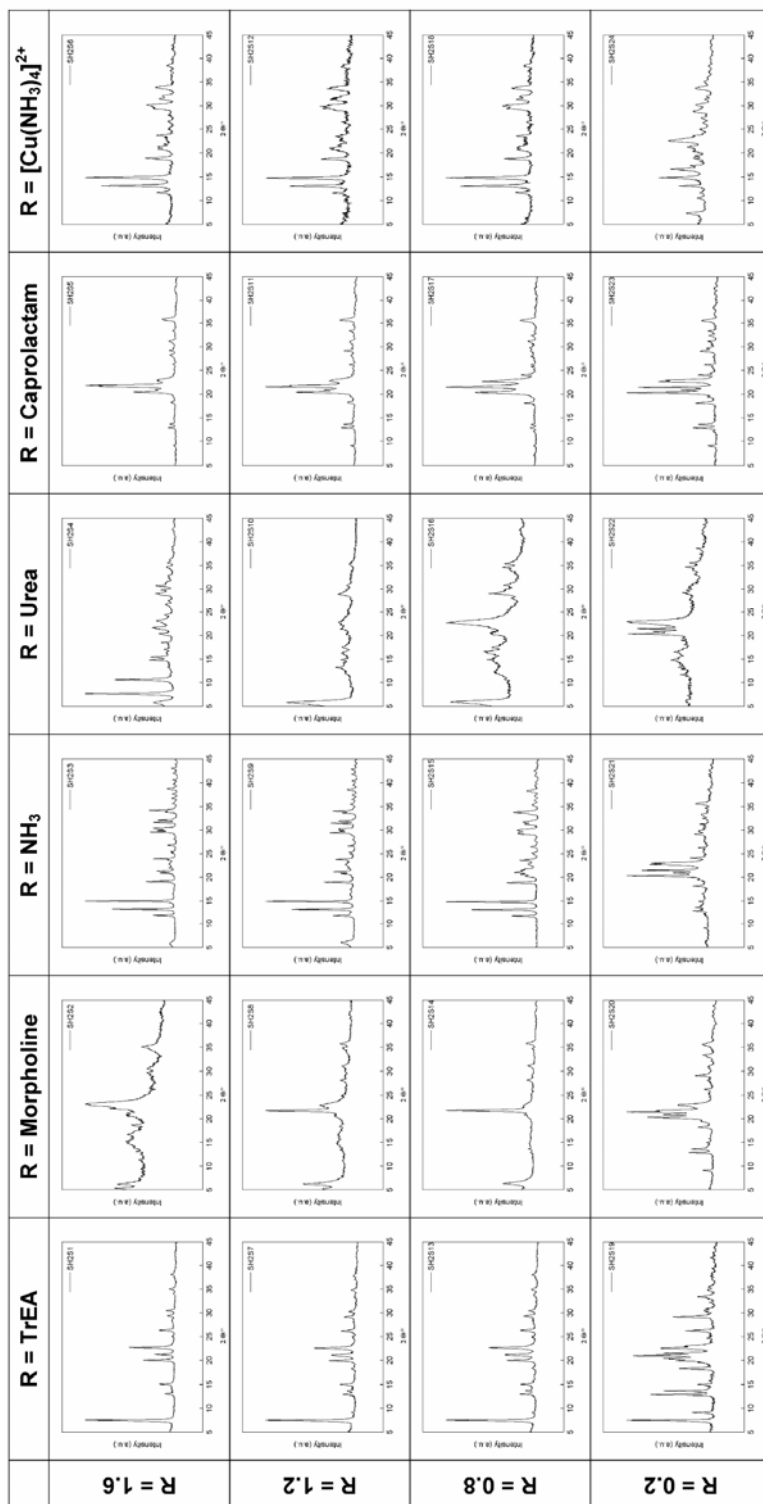
Figure 10-15. XRD patterns of high-throughput experiment HT 7.2 after 7 d of HT treatment (150 °C).
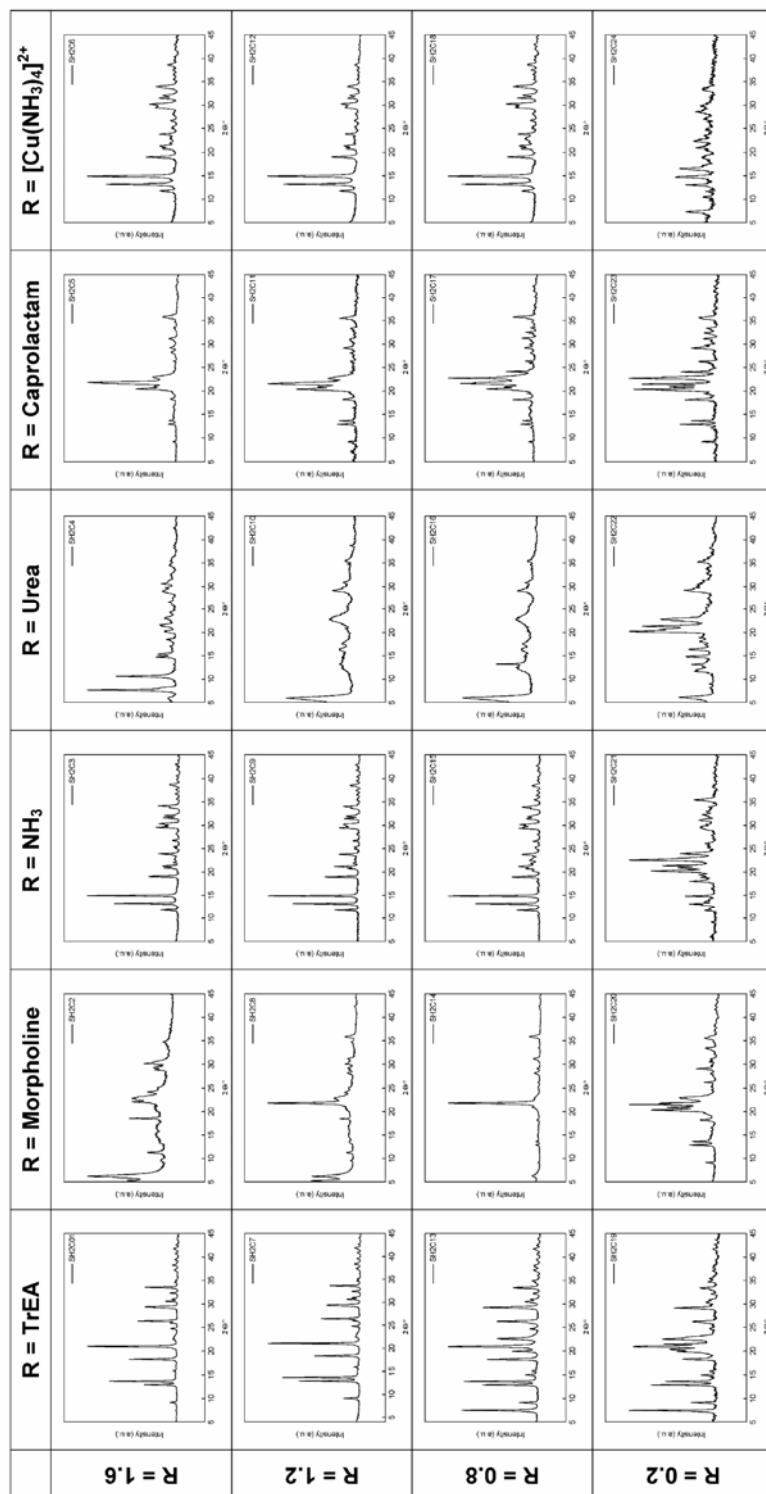
XRD patterns of high-throughput experiment HT 7.3

Figure 10-16. XRD patterns of high-throughput experiment HT 7.3 after 1 d of HT treatment (150 °C).
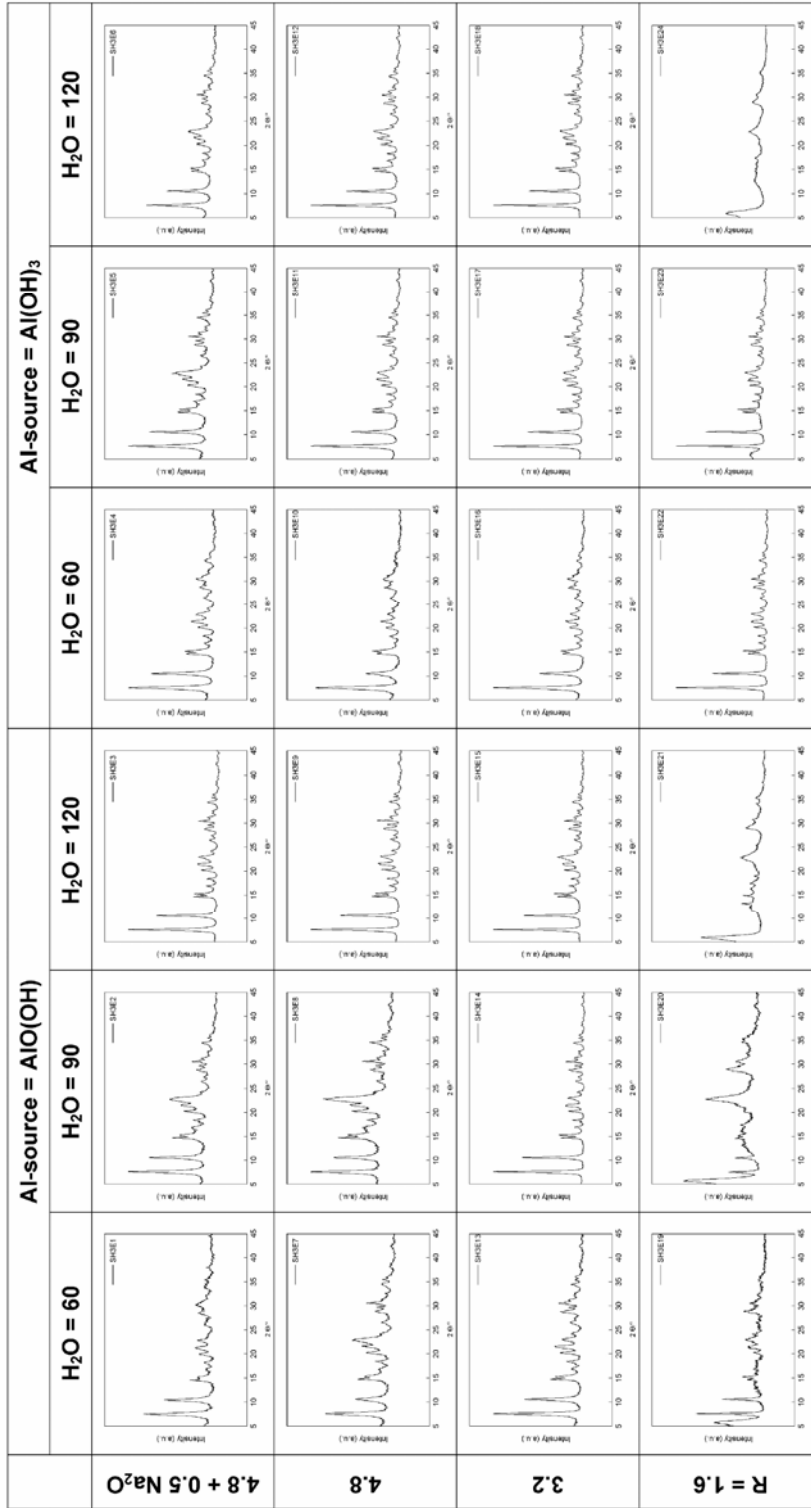
Figure 10-17. XRD patterns of high-throughput experiment HT 7.3 after 3 d of HT treatment (150 °C).
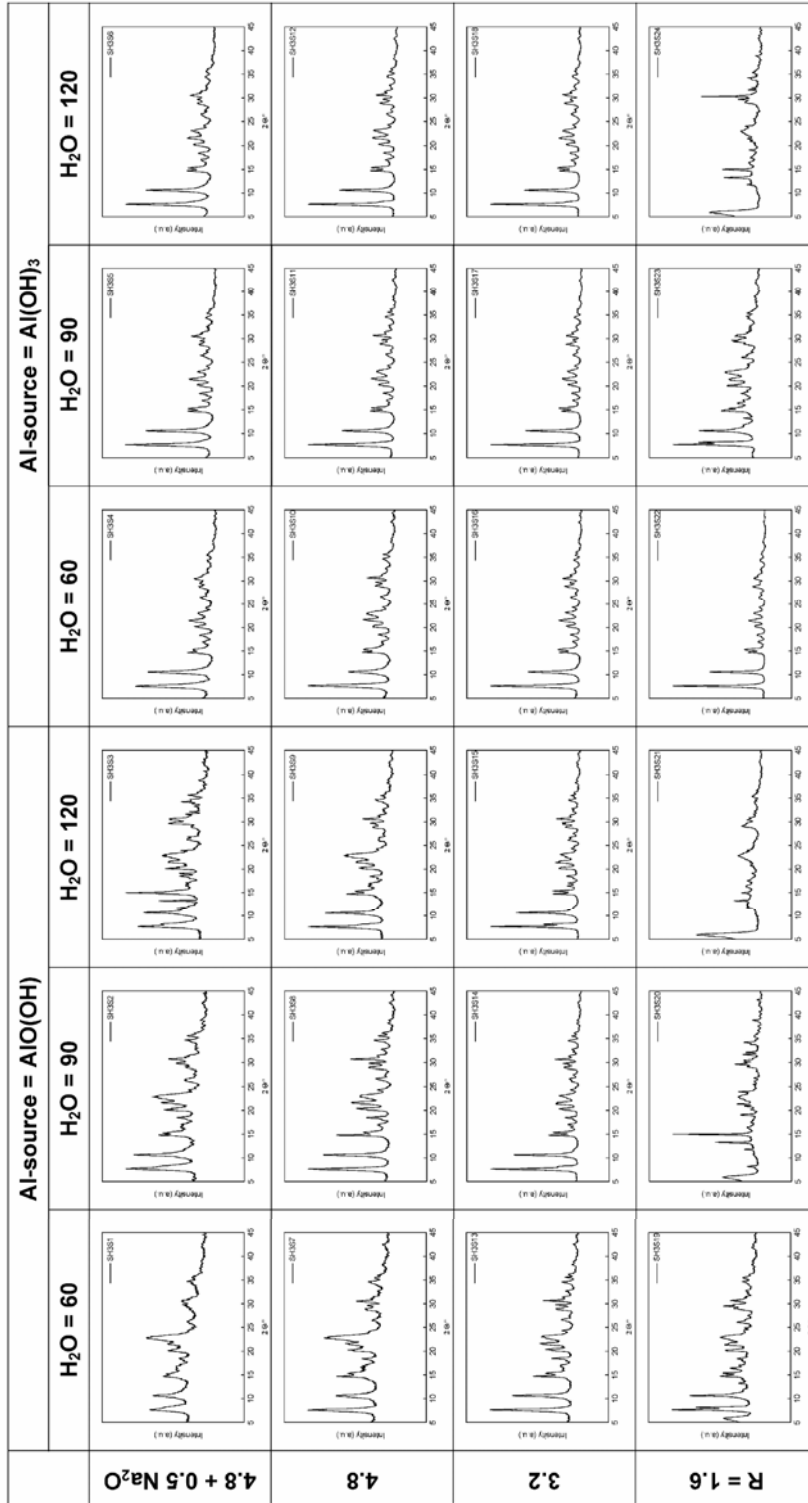
Figure 10-18. XRD patterns of high-throughput experiment HT 7.3 after 6 d of HT treatment (150 °C).
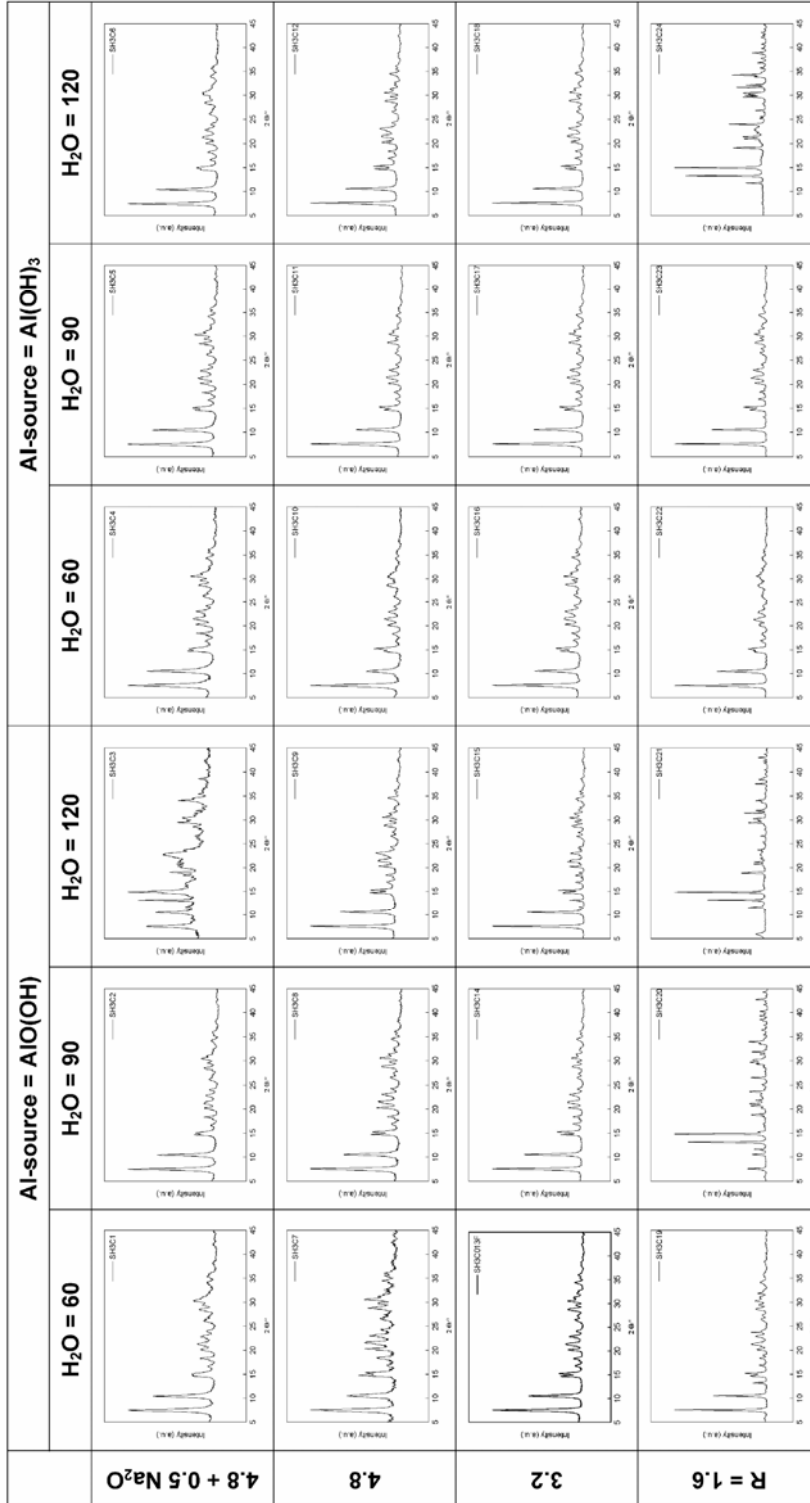
Curriculum Vitae

Zur Person

Hendrik van Heyden, geboren am 02.02.1979 in Kassel, verheiratet, keine Kinder

Studium

Okt 1999 – Feb 2004	Chemiestudium an der LMU München, Wahlfach Biochemie
März 2004 – Sep 2004	Diplomarbeit im Arbeitskreis Prof. T. Bein, LMU München, Titel: „Synthese und Charakterisierung metall-organischer Netzwerke auf Basis von Carboxy-Salen-Komplexen und Tetraphosphonaten"
Okt 2004 – Jan 2005	Bewerbung auf eine industrienahe Promotion, Zusagen von den Firmen BMW und Ciba
Feb 2005 – April 2008	Promotion im Arbeitskreis Prof. T. Bein, LMU München

Zivildienst

Juli 1998 – Juli 1999	Rettungsdienst des Bayerischen Roten Kreuzes, Wertingen

Schulen

1985-1989	Grundschule Wertingen, Zwgst. Gottmannshofen
1989-1998	Gymnasium Wertingen
Mai 1998	Abitur: Leistungskurse Mathematik und Chemie

München, den 29.02.2008

Publications

H. van Heyden, S. Mintova, T. Bein, "AlPO-18 nanocrystals synthesized under microwave irradiation", *J. Mater. Chem.* **2006**, *16*, 514 – 518.

H. van Heyden, S. Mintova, T. Bein, "Nanosized SAPO-34 synthesized from colloidal solutions", *Chem. Mater.*, **2008**, *20*, 2956 – 2963.

H. van Heyden, G. Munz,. L. Schnabel, F. Schmidt, S. Mintova, T. Bein, "Kinetics of water adsorption in microporous aluminophosphate layers for regenerative heat exchangers", *Appl. Therm. Eng.*, submitted.

H. van Heyden, T. Bein, "Template substitution in the synthesis of AlPO-18", in preparation.

Presentations

H. van Heyden, G. Munz, S. Mintova, T. Bein, "Thick films of porous materials for heat storage applications", International Symposium "Catalytic processes on advanced micro- and mesoporous materials" **2005**, Nessebar, Bulgaria.

H. van Heyden, S. Mintova, T. Bein, "Microwave synthesis of nanosized AEI molecular sieve: sorption properties", 3rd International FEZA Conference **2005**, Prague, Czech Republic.

H. van Heyden, G. Munz, S. Mintova, T. Bein, "Kinetics of Water Vapour Adsorption in Thick Aluminophosphate Films", 19. Deutsche Zeolith-Tagung **2007**, Leipzig, Germany.

T. Bein, H. van Heyden, "Microporous Molecular Sieves for heat exchangers", PTJ-Workshop "Wärmespeicherung und –transformation mit mikro- und mesoporösen Adsorbentien – Stand der Entwicklung und zukünftiger FuE-Bedarf" **2006**, Wildau, Germany.

T. Bein, H. van Heyden, Symposium "Nanotechnologie für eine nachhaltige Energieversorgung" **2007**, Berlin, Germany.